In-situ characterization of self-assembled organic layers at anion modified metal/electrolyte interfaces

Thanh Hai Phan

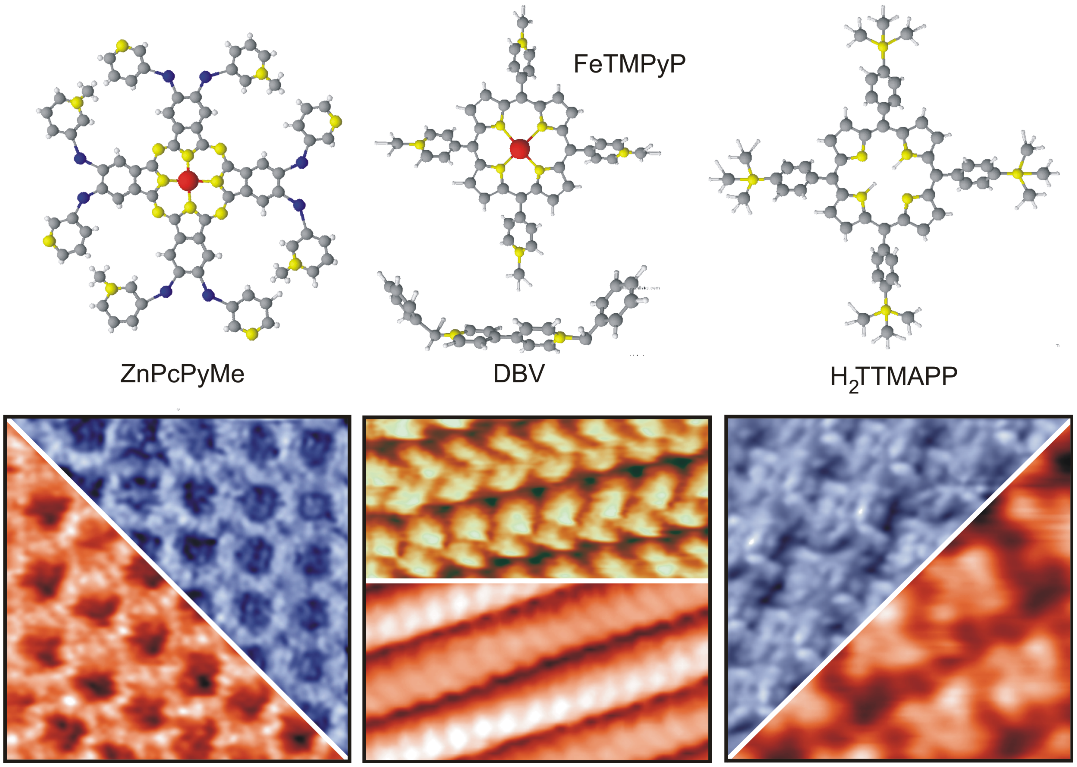

In-situ characterization of self-assembled organic layers at anion modified metal/electrolyte interfaces

Dissertation

zur Erlangung des Doktorgrades (Dr. rer. nat.)

der

Mathematisch-Naturwissenschaftlichen Fakultät

der

Rheinischen Friedrich-Wilhelms-Universität Bonn

vorgelegt von

Thanh Hai Phan

aus

Quang Binh, Viet Nam

Bonn 2012

Angefertigt mit Genehmigung der Mathematisch-Naturwissenschaftlichen
Fakultät der Rheinischen Friedrich-Wilhelms-Universität Bonn

1. Referent: Prof. Dr. Dr.h.c. Klaus Wandelt
2. Referent: Prof. Dr. U. Kubitscheck

Tag der Promotion: Oct. 12th 2012
Erscheinungsjahr: 2013

Dedicated to my families, especially my lovely son An Kiet.

Contents

List of abbreviations

CDR	Copper Dissolution Reaction
CE	Counter Electrode
CV	Cyclic Voltammogram
DBV	Dibenzyl-Viologen
E	Working potential vs RHE BE
E_B	Binding Energy
EC-STM	Electrochemical Scanning Tunneling Microscopy
fcc	face-centered cubic
FeTMpyP	5,10,15,20-Tetrakis-(N-methyl-4-pyridyl)-porphyrin-Fe(III) pentatosylat)
FWHM	Full Width at Half Maximum
HER	Hydrogen Evolution Reaction
HOMO	Highest Occupied Molecular Orbital
HOPG	Highly Ordered Pyrolytic Graphite
H_2TTMAPP	5,10,15,20-Tetrakis(4-trimethylammoniophenyl) porphyrin tetra(p-toluenesulfonate)
H_2PcPy	2,3,9,10,16,17,23,24-Octa(3-pyridyloxy)-5,28:14,19-diimino 7,12:21,26dinitrilotetrabenzo[*c*,*h*,*m*,*r*][1,6,11,16]tetraazacycloeicosinato(2$^-$)-N^{29},N^{30},N^{31},N^{32} zinc(II) (-iodide)

IHP	Inner Helmholtz Plane
LUMO	Lowest Unoccupied Molecular Orbital
ML	Monolayer
NHE	Normal Hydrogen Electrode
NND	Nearest Neighbor Distance
OHP	Outer Helmholtz Plane
RE	Reference Electrode
RHE	Reversible Hydrogen Electrode
SCE	Saturated Calomel Reference Electrode
SHE	Standard Hydrogen Electrode
SoLiAS	Solid/Liquid Interface Analysis System
SXPS	Synchrotron X-ray Photoelectron Spectroscopy
U_{bias}	Bias Voltage
UHV	Ultra High Vacuum
WE	Working Electrode
XPS	X-ray Photoelectron Spectroscopy
ZnPcPyMe	2,3,9,10,16,17,23,24-Octa(3-(N'-methyl)-pyridyloxy)-5,28:14,19 -diimino-7,12:21,26-dinitrilotetrabenzo(c,h,m,r) (1,6,11,16) tetra azacycloeicosinato (2-)-N29,N30,N31,N32 zinc(II))

List of Figures

Chapter 1

Introduction and outline

1.1 Introduction and outline

Supramolecular self-assemblies on well-defined surfaces have attracted much attention in the recent decade due to a wide range of potential applications, such as molecular logic devices, molecular sensors and photodynamic therapy. Therefore, a detailed understanding of their surface structures as well as chemical properties plays a key role for the design and fabrication of supramolecule based nano-scaled devices. One promising route towards such supramolecular assemblies is their electrochemical preparation. To this end it is important to propose relevant model systems allowing to study the working principles of self-assembly towards these organic molecules based nano-scaled devices. This so-called electrochemical “bottom-up” approach, therefore, requires the involved processes such as self-assembly, electron transfers, etc., to be systematically investigated.

The recent development of local probe techniques as Scanning Tunneling Miscroscopy (STM) in combination with methods such as Cyclic Voltametry (CV) and X-ray Photoelectron Spectroscopy (XPS) has opened a new window to study interface phenomena on solid state surfaces (metals, semiconductors, superconductors, polymers, ionic conductors, insulators) in-situ (in an electrolyte) and ex-situ (in ultrahigh vacuum) at an atomic/molecular level.

At solid/liquid interfaces, a number of processes of interest may take place, e.g. the adsorption/desorption of species from the electrolyte such as anions and organic molecules, and surface reactions such as corrosion/corrosion inhibition, formation/growth of new compounds, etc. Detection of the atomic structure at the solid/liquid interface and investigation of the processes occurring at these interfaces at the atomic/molecular level play, therefore, a crucial role in order to understand the nature of these processes as well as to apply them in technology.

In this framework, three interesting kinds of molecular building block are focused on in this work to examine their self-assembly on a reactive copper substrate, namely, phthalocyanine molecules, porphyrin molecules and viologen species.

The choice of copper serving as substrate for molecular adsorption is also due to many interesting aspects, e.g. the higher reactivity of copper compared to that of other noble metals such as Au, Ag, Pt, and its more negative potential window compared to those metals. These advantages are expected to offer a number of undiscovered astonishing phenomena relating to the electrochemistry and the self-assembly of supramolecular structures on the copper surfaces under non-reactive and/or reactive conditions.

The choice of the first molecular system, i.e. metallophthalocyanine molecules (MPcs), is motivated due to the fact that the metallophthalocyanines and their derivatives have attracted special interest because of their applications in the areas of solar cells [1], gas-sensing devices [2], photovoltaic applications [3], ultrafast optical switches [4], organic field effect transistors [5], pigments and dyes [6], etc. The properties of self-assembled layers of these molecules were in fact already investigated in part under UHV conditions [7-10] and in non-aqueous solutions [11-12]. In turn, there are few reports on adlayer of phthalocyanine molecules in electrochemical environment because of the low solubility of many Pcs in polar solvents [13]. Although, Itaya's group published some reports on zinc-phthalocyanine adlayer structures formed on a Au(111) surface in $HClO_4$ electrolyte by immersing the substrate into a benzen solution containing ZnPc molecules [14] they limited the electrode potential in the positive range. As a result, little information of the adlayer structures of the phthalocyanine in the negative, reductive potential regime is available. One goal of this thesis was, therefore, to investigate the electrochemistry and self-assembly of this zinc phthalocyanine on an iodide modified Cu(100) electrode in acidic solution. The water soluble zinc phthalocyanine molecules were synthesized by Prof.Torres' group (Madrid) [15].

The second class of molecules addressed in this work are porphyrin derivatives. As mentioned above, porphyrin adlayers are applied in a wide range of electronic fields, such as molecular logic devices [16] and molecular sensors [17]. In addition, porphyrins are well-known to play a crucial role in naturally vital processes such as in heme for the transfer and storage of oxygen or in chlorophyll for the photosynthesis of green plants [18]. Furthermore, they can also be used to produce drugs for the photodynamic therapy [19-20]. All these reasons motivated to study these compounds. In fact, the electrochemical properties of adsorbed layers of some porphyrin derivatives have been examined in the past by means of conventional methods such as CV, spectroscopy, etc. [21]. Also, ordered structures of adsorbed porphyrin thin films forming both under UHV conditions [22-26] and in electrochemical environment [27-30] have been investigated. However, this is the first time that the self-assembly of redox-active 5,10,15,20-Tetrakis(4-trimethylamonium-phenyl) porphyrin tetra(p-toluenesulfonate) (abbreviated as $[H_2TTMAPP]^{4+}$) molecules on a reactive copper single crystal electrode is studied and reported. Besides, an additional goal of this work is to examine self-assembled layers of iron porphyrin (FeTMPyP) at the solid/liquid interface in order to replenish former work of our group [31].

The last system of choice in this work are dibenzyl-viologen molecules (DBV). It is evident that these molecules have attracted much attention in the field of surface electrochemistry for the last few decades due to their widespread applications as chromophores, electron transfer mediators, and most recently as gating molecules in model systems for electronic devices that are based on molecular architectures. Similar to the previous two systems, their solution electrochemistry as well as adsorbed structures on metal and HOPG substrates are well documented in the literature [32-34]. However, their electrochemical and structural properties on a Cu(111) oriented substrate is still unknown.

Most recently, bimolecular films have been found to be applied in a variety of fields such as photosynthesis, biofuel cell [35-37], oxygen reduction [38]. These prospective applications motivate more and more attempts of scientists worldwide into research, design and fabrication of biohydrogen molecular devices and biofuel cells based on such bimolecular layers. Motivated by these initial successes, the electrochemical properties and the adsorbate structures investigation of two-component adlayers consisting of porphyrin and viologen molecules are also studied here for the first time.

In this dissertation, the text consists of four parts. The first part provides the readers the motivations for carrying out this work as well as the outline of the thesis in chapter 1 “Introduction and outline”. The second part concerns the background and fundamentals of as follows: Chapter 2 presents a brief overview about the electrochemistry at the solid/liquid interface, the principle of in-situ ECSTM and ex-situ XPS as well as their experimental setups. The structures of the anion modified copper surfaces are shown in detail in Chapter 3. The rest of this part, namely chapter 4 contains an overview about supramolecular chemistry as well as about the organic molecules chosen in this work. The third part describes the results and the discussion of the self-assembly of the organic molecules on various anion modified copper surfaces in three separate chapters. Chapter 5 concentrates on the attempt to self-assemble of the zinc phthalocyanine on an iodide terminated Cu(100) surface under non-reactive conditions using a combination of EC-STM and XPS experiments. The self-assemblies of the free base porphyrin (H_2TTMAPP) and of iron porphyrin (FeTMPyP) are presented extensively and systematically in chapter 6 describing the electrochemistry, the structure of the porphyrin adlayers, the role of the substrate symmetry, the influence of the anion template and the potential induced surface reactions. Chapter 7 deals with the adsorption of the viologen (DBV) on the Cu(111) electrode surface, and chapter 8 relates to the self-assembly of the bimolecular adlayer of H_2TTMAPP and DBV on the copper surfaces. The final part gives the readers a summary and some general conclusions in chapter 9.

Chapter 2

Electrochemistry at the solid/liquid interface and experimental methods

2.1 Electrochemistry at the solid/liquid interface

2.1.1 Introduction

The structure and composition of electrified solid-liquid interfaces as well as their electrical charge distribution is of great fundamental interest in electrochemistry. Many scientifically and technologically relevant processes occur at these interfaces, i.e. corrosion, electro-catalysis, compound formation and galvanic deposition, e.g. the copper damascene process (electroplating). Therefore, an atomic-scale understanding of the interfacial structure is mandatory in order to control the fabrication of new surface structures and materials. In this chapter, the conventional structure models of electrified solid-liquid interfaces are presented. Furthermore, the cyclic voltammetry as one of the most important methods to characterize the solid/liquid interface is described.

2.1.2 Solid/liquid interfaces

An electrical double-layer is formed at the solid/liquid interface of an ideally polarizable electrode surface upon exposing it to an electrolyte solution at which no charge transfer can occur regardless of the potential imposed by an external voltage source. This double layer is composed by a charged metal surface and an interfacial regime in the electrolyte phase containing an excess of ionic particles counterbalancing the charge at the electrode q_e. A positively charged electrode, for instance, attracts a layer of negative ions. The overall interface must be neutral with $q_e + q_s = 0$ where q_s is the excess charge of ions in the nearby solution. The surface charging can be carefully controlled by the applied “Galvani” potential to the electrode [39]. The characteristics of the structure and the interactions within this electrical double layer need to be considered in the interpretation of electroanalytical data. Various models of the electric double layer have been proposed differing in the spatial distribution of the assembled counter-charges in the electrolyte.

2.1.2.1. The Helmholtz model

The earliest model of the electric double layer was introduced by Helmholtz in 1879 [40]. Helmholtz treated the double layer mathematically as a simple capacitor, based on a physical model in which a single layer of ions is adsorbed at the surface. A rigid double layer is formed with one-by-one matching of charges. The arrangement resembles a plate capacitor with distance of $d = a/2$ between the two plates, where a defines the diameter of the solvated anions. Pure electrostatic forces are responsible for the attraction of the ionic particles. The potential drop Ψ across the interface can be deduced by solving the Poisson equation:

$$\frac{d^2\psi}{dx^2} = -\frac{\rho(x)}{\epsilon\epsilon_0} \qquad 2.1$$

in which ρ is the charge density, ε is the dielectric constant of water and ε_0 represents the dielectric constant of vacuum.

The solution of this equation is given by:

$$\frac{d\psi}{dx} = const \qquad 2.2$$

The potential, under the given boundary conditions, decreases linearly within the intermediate region between the metallic surface and the so called “outer Helmholtz” plane (being discussed below). The Helmholtz model, however, does not take into account the thermal motion of ions which tends to dissolve the compact double layer [39].

2.1.2.2. The Gouy-Chapman-Stern-Grahame (GCSG) model

The development of theoretical models of the electrolytic double layer is represented in a detailed review article [41] and a more modern model of the charge density distribution nearby metal surfaces is the so-called "***Gouy-Chapman-Stern-Grahame"*** model. This model is a combination of the Helmholtz and the Gouy-Chapman [42] model, in which the finite size of ions and their thermally activated motion are taken into account. The main difference in the double layer determination is based on the following assumption: (i) Ions in the Stern plane are considered to have lost their hydration shell; (ii) Ions in the diffuse layer retain their hydration shells. As a result, on the electrolyte side the charge can be roughly divided by two planes, namely, the Inner (IHP) and the Outer Helmholtz Plane (OHP), into three regions: the inner Helmholtz layer, the outer Helmholtz layer and the diffuse double layer, as represented in Fig.2.1.

- The inner Helmholtz layer: This layer is based on the assumption that a single layer of specifically adsorbed anions which are desolvated maintain direct chemical contact with the electrode surface, resulting in the inner Helmholtz plane at a distance of r/2, where r equals the diameter of the unsolvated anions. The ionic particles are, thus, directly bound to the metal surface atoms [43]. This phenomenon occurs primarily with anions and is often accompanied by the formation of periodically ordered adsorbate layer [44].

- The outer Helmholtz layer: This layer is formed by solvated ions which interact more weakly and purely electrostatically with the electrode surface through the hydration sphere. The outer Helmholtz plane is hence at a distance of a/2 with a being the radius of a solvated ion.

Under the condition that the potential drop is small the model could be described by the following equation:

$$\frac{d^2\psi}{dx^2} = \chi^2\psi \qquad 2.3$$

Herein, the quantity χ provides the length scale for the screening and $1/\chi$ is associated with the thickness of the ionic countersphere around each ion and is called the Debye length:

$$\chi = \sqrt{\frac{2n_0 z^2 e^2}{\varepsilon\varepsilon_0 kT}} \qquad 2.4$$

with n_0 being the total ion concentration, k is the Boltzmann constant, z is the ion valency and e is the electron charge.

Applying common boundary conditions, i.e. $\psi(0) = \psi_0$ and $\psi(\infty) = 0$, the potential ψ of the system is obtained:

$$\psi(x) = \psi_0.e^{-kx} \qquad (2.5)$$

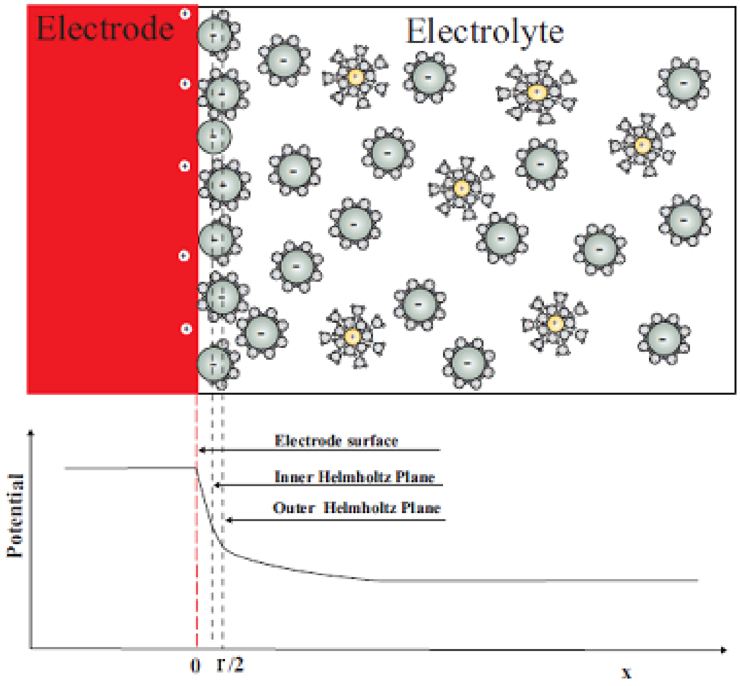

Figure 2.1: The Gouy-Chapman-Stern-Grahame (GCSG) model

As a consequence, the potential decreases exponentially with increasing distance x to the surface. An increase of the salt concentration leads to a steeper drop and thus to a shorter Debye length.

Accordingly, specific adsorption can be observed within the IHP, i.e. the ions loose partially or fully their hydration shell, whereas the OHP contains only solvated ions. In addition, both Helmholtz layers are at fixed distance and their potential drops are linear. In contrast, the drop in the diffuse layer is exponential. The capacitance of the double layer is the total capacitance C of the two compact layers and that of the diffuse layer in series and can be calculated from:

$$\frac{1}{C} = \frac{1}{C_{Hin}} + \frac{1}{C_{Hout}} + \frac{1}{C_{diff}} \tag{2.6}$$

2.1.3 Surface reactions

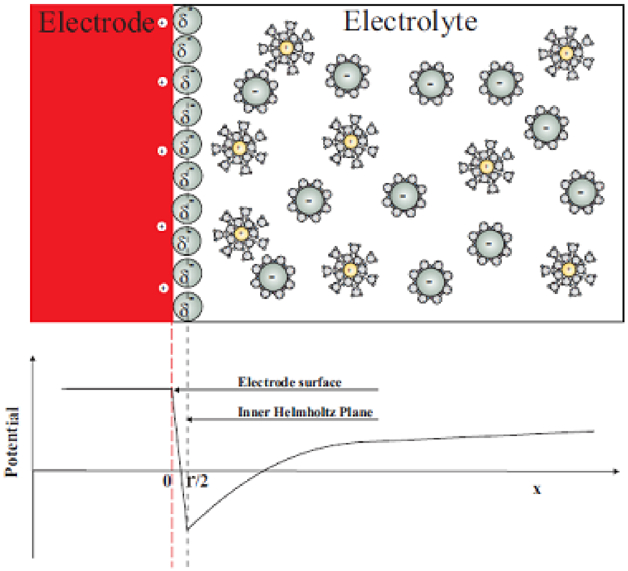

Figure 2.2: Specific adsorption of anions on a metal surface

Besides the intrinsic electrostatic interaction between the charged electrode surface and the ions in the electrolyte as mentioned above via the GCSG-model, chemical interaction between anions such as iodide, sulfate, etc. and the electrode surface must also be taken into account in the electrolyte media. At the solid/liquid interface, these anions may loose their hydration shell and adsorb directly on the electrode surface. This phenomenon is called specific adsorption. In many cases, specific anion adsorption results in the formation of a condensed anion layer. The model describing the specific adsorption of anions on a metal surface is presented in Fig. 2.2.

As illustrated in this model, the potential first decreases linearly in the regime limited by the electrode surface and the IHP that crosses the centers of dehydrated ions, and then re-increases exponentially towards the bulk solution.

The specific anions adsorb strongly on the electrode surface resulting in the formation of a condensed, laterally ordered and immobilized layer which can be visualized by means of microscopies such as electrochemical scanning tunneling microscopy (EC-STM).

Astonishingly, these specifically adsorbed layers can serve as templates for the self-assembly and immobilization of organic molecules on the electrode surfaces, especially, for positively charged organic cations such as porphyrins, phthalocyanines and viologens which will be elucidated in this dissertation. Such a model illustrating adsorption of a positively charged organic molecule on a specifically adsorbed anion layer is proposed in Fig.2.3.

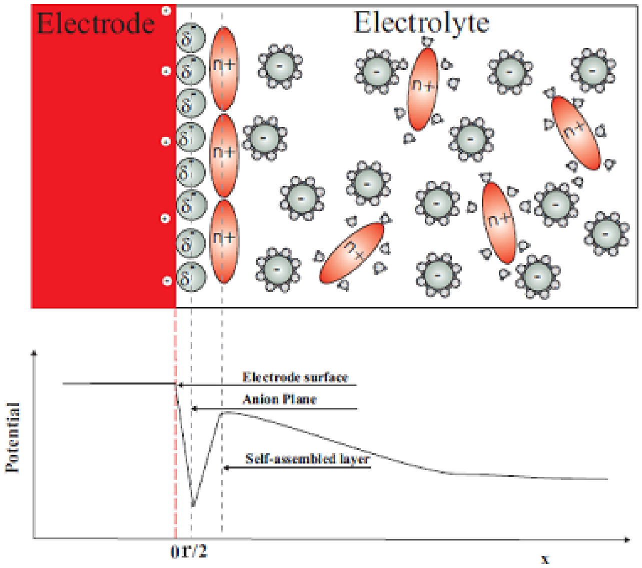

Figure 2.3: Self-assembly of positively charged organic cations on a specifically adsorbed anion layer.

2.1.3.1. *Structure of the electrode surface: The Jellium model*

In this section, we introduce the interfacial structure of the solid electrode surface that is neglected in all models mentioned above.

A simple model illustrating some fundamental properties of the electronic structure of surfaces is the so-called "Jellium model". In this model, the positive charge of the ion cores is spread out uniformly over the whole solid (jellium) while the valence electrons move in the potential produced by this jellium. At the surface, while the positive background charge stops abruptly (so called Jellium edge) the electron density does not. Instead, the electron density oscillates near the surface (Friedel oscillations) before decaying exponentially out of the solid. This phenomenon is described in Fig. 2.4. This contribution of the electron density produces an electrostatic dipole layer at the surface even in vacuum. This dipole creates an attraction for electrons to the surface and leads to a step in the surface potential [45-46] which prevents electrons from leaving the metal through the surface.

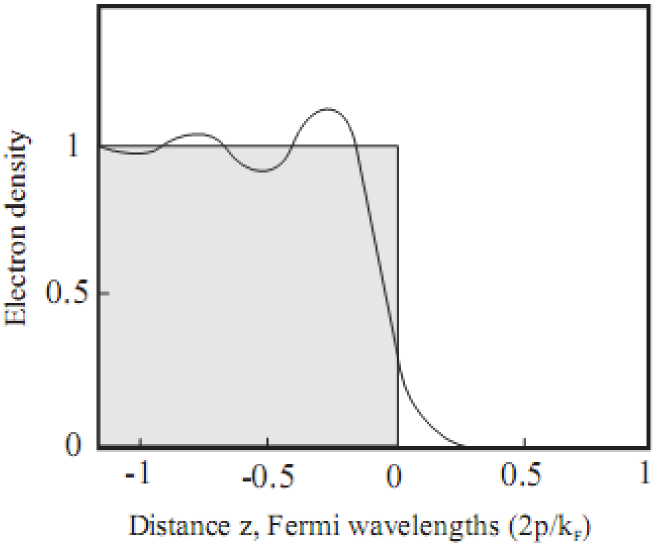

Figure 2.4: Charge density as a function of the distance from the surface in Fermi wavelengths as predicted by the Jellium model [45].

It becomes evident that the electrostatic potential including the surface dipole depends on the roughness of the surface, i.e. its atomic scale structure. Fig. 2.5 shows the so-called “Smoluchowski smoothing” at steps which introduces new dipoles at the surface. Consequently, the work function depends on the crystallographic orientation of the face of the crystal. For instance, the work function of Cu (fcc) is 4.94 eV, 4.59 eV and 4.48 eV for the (111), (100) and (110) surface, respectively [46].

The presence of adsorbates on the electrode surface contributes two different dipolar contributions to the work function. The first contribution arises from the charge transfer between the surface and the adsorbate. Indeed, when an electropositive adsorbate such as an alkali metal forms a chemical bond with a transition metal surface the alkali metal tends to donate charge into the metal causing a decrease of the work function. In contrast, an electronegative adsorbate, such as oxygen, sulfur or halogens, withdraws charge leading to an increase of the work function. The second one is taken into consideration when a molecular adsorbate has an intrinsic dipole. Depending on the relative orientation of the molecular dipole with respect to the surface this contribution either enhances or depresses the work function [45].

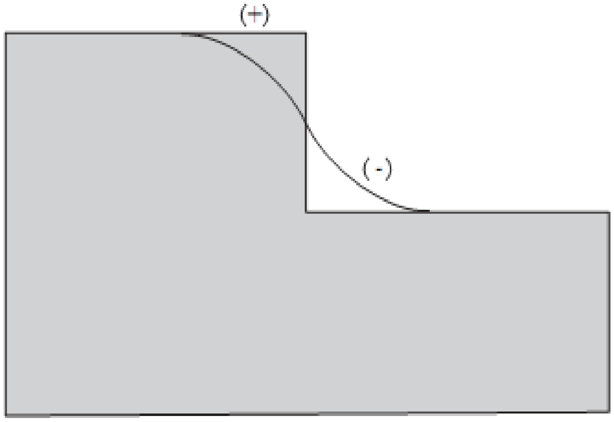

Figure 2.5: Smoluchowski smoothing: The electrons at a step attempt to smooth out the discontinuity of the step [45].

2.1.4 Cyclic voltammetry

It was first reported in 1938 and then theoretically described in 1948 by Randles and Sevcik [47], the cyclic voltammetry (CV), one of the voltammetric methods, which has become the most common technique used for acquiring qualitative and quantitative information about electrochemical reactions. It offers a rapid location of redox potentials of electroactive species. This technique consists of scanning linearly the potential of a stationary working electrode forth and back between two chosen limits, using a triangular potential waveform, at a known sweep rate, υ (Fig. 2.6). In order to obtain a cyclic voltammogram, i.e. the resulting plot of current versus potential, the current at the working electrode is measured during the potential scan. Depending on the desired information, single or multi-cycles can be used. This method is used throughout this dissertation in order to investigate the general electrochemical behavior of the chosen system.

In order to consider the potential drop between electrode and bulk solution a so called three electrode configuration consisting of a working electrode, a counter electrode and a reference electrode is employed. The last one is mandatory to measure potentials which are not affected by the current flowing through the working and counter electrodes. Kinetic as well as thermodynamic data can be obtained by scan rate dependent CV measurement.

A cyclic voltammometry is often the first experiment in an electroanalytical study due to the fact that this method offers a rapid determination of redox potentials of electroactive species and a convenient evaluation of the effect of the solvent upon the redox process. CV can provide significant information on the thermodynamics of redox processes, on the kinetics of heterogeneous electron transfer reactions, as well as on coupled chemical reactions or adsorption processes. Furthermore, this method is not only used for evaluating the interfacial behavior of electroactive compounds such as organic molecules, as well as metal complexes, but is also widely used for the characterization of the adsorption-desorption process of anions on metal surfaces.

2.2. Microscopy at the solid/liquid interface - EC-STM

2.1.1 Introduction

The invention of scanning tunneling microscopy (STM) nicely exemplifies the creation of a new research tool by innovative implementation of scientific and technological knowledge, thereby further advancing fundamental science and technology. The quantum-mechanical phenomenon of electron tunneling had been known for a long time, but the use of this phenomenon for the imaging of a conducting surface with atomic scale was realized only in 1982 when the first scanning tunneling microscope was built by Binnig and Rohrer [48-50]. Only four years after the first successful operation of the STM, Binnig and Rohrer received the Nobel Prize in physics in 1986. At present, the STM is a powerful tool for analyzing metallic and semiconducting surfaces due to the real-space visualization of the surfaces on the atomic scale.

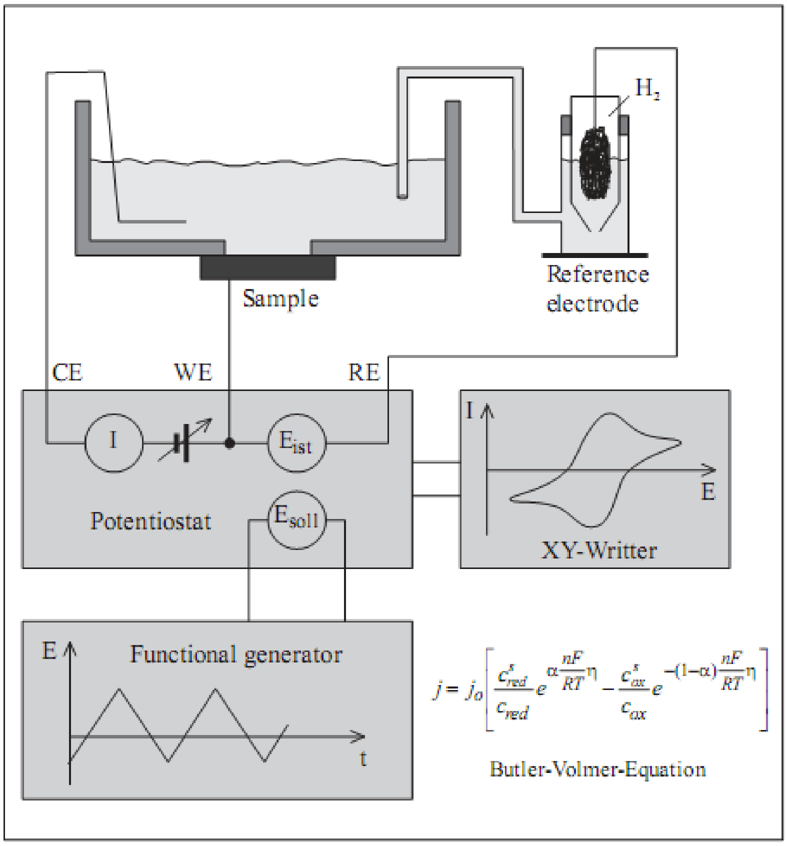

Figure 2.6: Working principle of the three electrode configuration, CE: counter electrode; WE: working electrode; RE: reference electrode [61].

The STM has been first used in an ultra high vacuum environment (UHV) for investigating the surface properties of various inorganic conducting materials. Although much of the early STM work has focused on surfaces in vacuum, the STM, in fact, can also be used to obtain images of surfaces in contact with liquids or air. The first STM working at solid-liquid interfaces has been introduced by Sonnenfeld and Hansma in 1986 [51]. From that time on, the so-called *Electrochemical Scanning Tunneling Microscopy* (EC-STM) has attracted more and more attention. These EC-STMs are able to image directly the electrode surface in solution (in-situ). The capability of offering structural information on the atomic level makes it highly convenient for in-situ studies of time dependent electrochemical processes, such as corrosion, electrodeposition, adsorption, as well as surface modification and passivation [45,52-54].

In the following we will discuss in detail the physical background of the tunneling effect, the working principle of the STM and, in particular, the experimental set-up.

2.2.2 Tunneling effect

As mentioned above, the STM principle works based on the tunneling effect between the tip and the sample surface. Tunneling is a quantum-mechanical phenomenon in which an electron with energy E can penetrate a potential barrier $\Phi > E$. The wave function ψ describing the quantum state of the electron decays exponentially in the classically forbidden region according to:

$$\psi(z) = \psi(0) exp \frac{-z\sqrt{2m(\Phi - E)}}{\hbar} \qquad 2.7$$

where m is the mass of the electron, $\hbar$ is the Dirac constant and $\hbar = 1.05 \times 10^{-34}$Js, Φ is the barrier height in eV and z is the width of the barrier.

In the STM set-up, a metallic tip approaches the sample to a distance z of about one nanometer, so that the wave functions of the electrons in the tip and the sample overlap each other within the vacuum gap, as described in Fig.2.7. Depending on the bias voltage applied, electrons can tunnel from the tip into the sample or vice versa.

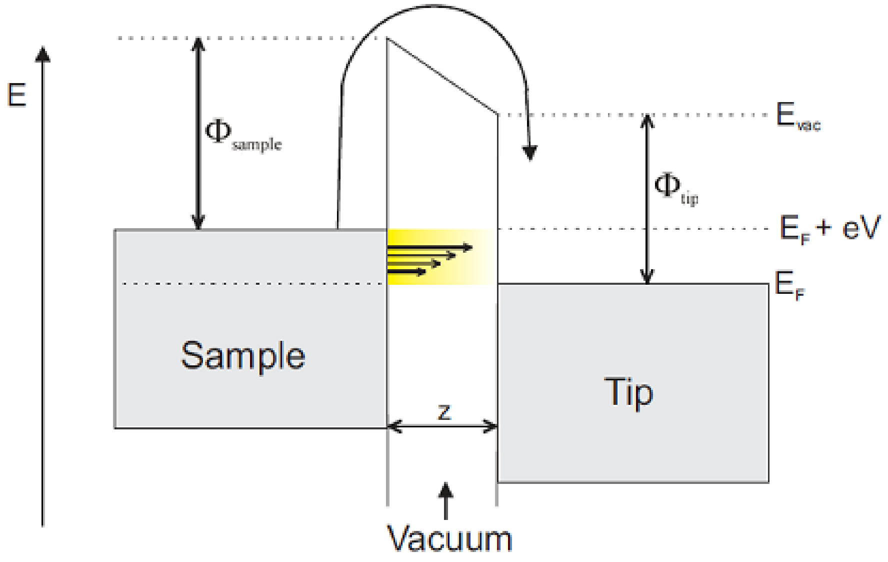

Figure 2.7: Energy level diagram of a tunnel junction.

The tunneling current I_t can be calculated by taking the density of states into account at the Fermi edge of the sample, $\rho(E_F)$, as follows [55]:

$$I_t \infty V\rho(E_F)exp\left[-2\frac{z\sqrt{2m(\Phi-E)}}{\hbar}\right] \infty\, V\rho(E_F)e^{-1.025z\sqrt{\Phi}} \qquad 2.8$$

It becomes evident that the tunneling current is a complex convolution of the electronic properties of the tip as well as the sample.

In recent years, various theories on STM were developed which deal with a realistic surface-tip system in three dimensions [56]. According to the theory proposed by Tersoff and Hamann [57-59] the tunneling current is proportional to the surface local density of states (LDOS) at the Fermi level evaluated at the location of the tip. This theory is based on assumptions such as a small bias, a low temperature and a tip which is represented by an s-wave function. The relation between the tunneling current and the bias voltage V as well 2.9 distance between tip and sample z is given by:

$$I_t \infty Ve^{-kz\sqrt{\Phi}}\rho(\vec{r}_0 E_F)$$

Based on equation 2.9 it could be deduced that the tunneling current decreases exponentially as a function of the separation between tip and sample. This result leads to an extremely highly vertical resolution of STM image, a variation of the distance by 1 Å results in a tunneling current change by one order of magnitude. Similarly, if the current varies within 2%, the distance remains constant to within 0.01%. As to the lateral resolution, about 90% of the tunneling current flows through the gap between the outermost atom of the tip and the closest atom of the surface. Then surface atoms with an atomic separation down to ~ 2 Å can be resolved [60]. The main advantage of the Tersoff and Hamann approach lies in the fact that the electronic properties of the local probe (the tunneling tip) can be eliminated. The tunneling current depends only on the local density of states of the surface without the tip contribution.

2.2.3 Working principle of the STM

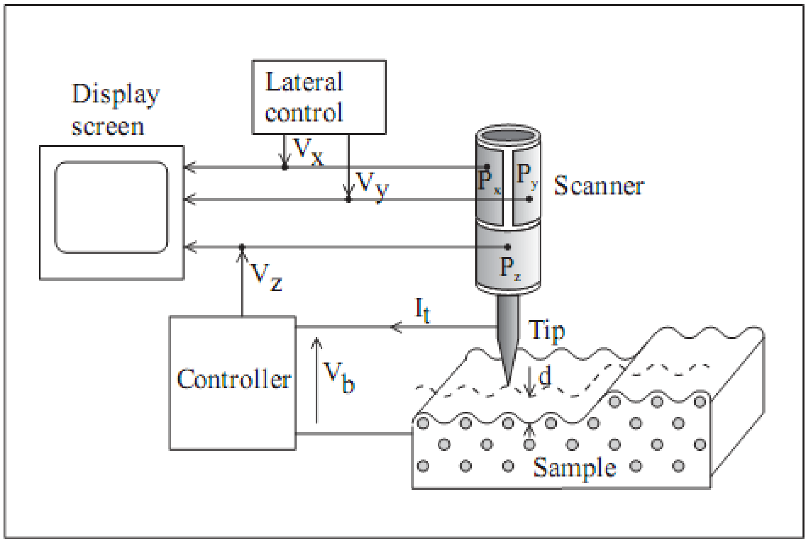

Figure 2.8: Working principle of the Scanning Tunneling Microscopy (STM): V_b: bias voltage; I_t: tunneling current; V_x: lateral controller voltage; V_y: lateral controller voltage; V_z: vertical controller voltage [59].

An atomically sharp metal tip which scans over the conductive surface under investigation is the essential part in the scanning tunneling microscope as illustrated in Fig.2.8. The metal tip is fixed into a scanner - a piezo tube containing three components: P_x, P_y, P_z. A piezoelectric ceramic material is used as electromechanical transducer which converts electric signals V_x, V_y, V_z of 1 mV to 1 kV applied to the P_x, P_y and P_z electrodes with respect to an electrode inside the tube into mechanical motion in the range from fractions of an Å to a few µm. A feedback electronics is used to control the tip-sample separation. The voltage applied to the piezo P_z is governed by the feedback system so that I_t remains constant during scanning the tip with P_x and P_y over the surface. At constant work function ψ, $V_z(V_x, V_y)$ yields the topography of the surface, z(x, y). A computer system is needed to control the tip position, to acquire data, and to convert data into an image. Additionally, further auxiliary components are necessary as a coarse positioning system in order to bring the tip into the tunneling regime, and a vibration isolation system [59-60].

In principle, two operating modes could be used for the STM measurement, namely the constant current mode and the constant height mode [48,60] (see Fig. 2.9).

- ***The constant-current mode (a):*** In this mode, I and V signals are kept constant, x and y are varied by rastering the tip, and the z-signal is measured as a function of x and y. Comparatively large and rough sample areas can be imaged without any damage of the tip or the sample surface resulting from tip crash phenomenon. A disadvantage of this mode is the limited scan rate which must be kept quite slow allowing the feedback system to control the z position of the tunneling tip.

- ***The constant-height mode (b):*** This mode is applied with stipulation that z and V signals are kept constant, x and y are varied by rastering the tip, and I is monitored as a function of x and y. With this mode, a higher scan rates can be applied and, hence, thermal drift effects in high resolution imaging can largely be eliminated. However, scan sizes are limited to flat areas in order to avoid "tip crash" phenomena since the feedback loop is switched off.

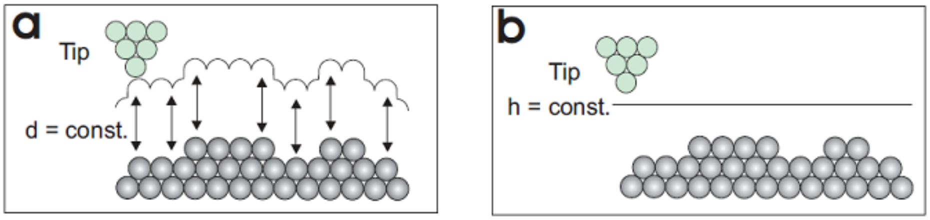

Figure 2.9: STM operation modes. a) Imaging a surface in the constant current mode. The surface contour plot is obtained by the z-signal (voltage that has to be applied for the positioning) upon scanning; b) Imaging the surface in the constant height mode. The tunneling current is recorded.

All STM images shown in this thesis are taken in the constant-current mode.

2.2.4 The STM setup at the solid/liquid interface

The electrochemical tunneling microscopy (EC-STM) combines the STM with a potentiostat and an electrochemical cell, so that it can work in an electrochemical environment. It appears more complicated than an STM working in UHV since the EC-STM must deal with a complex tip-sample-electrolyte system. The potentiodynamic EC-STM presented in this thesis is a home-built system built up by Wilms, Kruft and Bermes [59,61]. This system is developed as a special Besocke type STM instrument [62] in combination with an electrochemical cell and has various advantages over most commercial systems. Technical details about this EC-STM can be found in refs. [59,61,63]. Here only a brief description is presented.

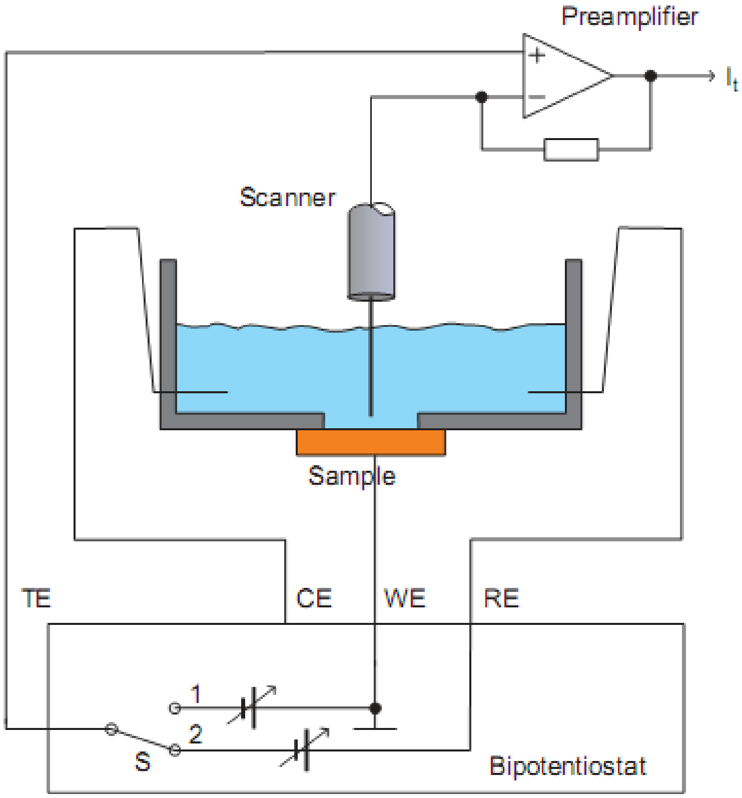

Figure 2.10: Principle of the potential control for potentiostatic and potentiodynamic imaging with the Electrochemical Scanning Tunneling Microscope (EC-STM). TE: tip electrode; CE: counter electrode; WE: working electrode; S: switch; I_t: tunneling current [59].

The working principle of the potentiodynamic EC-STM system is illustrated in Fig.2.10. The three-electrode configuration (WE, CE, RE) controlled by a potentiostat can be used separately to investigate the electrochemical properties of the sample-electrode. In combination with the STM, the tunneling tip has to be considered as a second working electrode resulting in a four-electrode arrangement controlled by the bipotentiostat. Note, the control of the sample potential is independent from the tip potential. The tip potential has to be optimized so that any Faradaic current through the tip is minimal because it is superimposed to the tunneling current and could, hence, disturb the proper tip height control. Such a system enables to measure:

1. Cyclic voltammograms similar to the case of a normal three-electrode arrangement.
2. Potentiostatic STM images when the switch S (Fig.2.10) is in position 1, and the tip potential can be adjusted to a value where the Faradaic current disappears.
3. Potentiodynamic STM images when the switch S is in position 2 and the tip adjusted and held constant versus the reference electrode. Hence, the sample potential is varied while the tip potential remains unaffected.

Such a survey of the complete home-built EC-STM system is shown in Fig.2.11. The most important parts of the EC-STM are the tunneling unit and an electrochemical cell which are placed within an aluminum chamber (1). This aluminum chamber can be filled with a protective Argon gas atmosphere and additionally serves as a shielding against acoustic and electromagnetic noises. In order to damp higher frequencies larger than 100 Hz the STM is placed on a stack of brass plates separated by rubber pieces. The chamber is placed on a heavy granite plate (8) suspended with steel springs (9) from the ceiling. This damping stage has a resonance frequency of less than 1 Hz and effectively protects the STM from outer vibrations in the low frequency regime. The protective gas is purified by using a gas purification system before being introduced into the aluminum chamber. The electrolyte from the electrolyte supply system (6) is first degassed by the purified protective gas and then fed into the electrochemical cell. The hose pump (7) is used to adjust the circulation of the electrolyte through the electrochemical cell. The STM controller (2) is used for governing the STM unit and a computer (4) for controlling the movement of the scanner and displaying the STM images. The operation of the electrochemical cell is controlled by a bipotentiostat (3) and the cyclic voltammograms are recorded by the second computer system (5).

The mechanical setup of the STM (disassembled) (a) and the top view of the electrochemical cell (b) is represented in Fig.2.12. For each measurement, the sample must be prepared according to a process described below (see Sec.2.2.6). Then, the sample is mounted into the electrochemical cell (Fig.2.12b). This cell is then fixed into the STM-base (Fig.2.12a) and filled with the electrolyte under potential control. The tip is installed in the scanner and adjusted to have a convenient length. The STM head, which carries the scanner unit and the preamplifier, is put down onto the three grub screws. After the electrical connections are made, the scanner unit is lowered down by turning the lifting screw thereby setting down the ramped ring with the scanner onto the piezolegs. Scanner and tip are now mechanically decoupled from the scanner head. The STM unit is then isolated within the aluminium chamber and the granite plate is freely suspended from the ceiling. From now on the scanner can be controlled by the STM control unit and the computer in order to approach the tip to the sample. After the tunneling tip reaches the tunneling regime, all the fine movements and the images recording can be controlled by the computer system. The potential applied to the sample is under control and adjusted by the bipotentiostat unit.

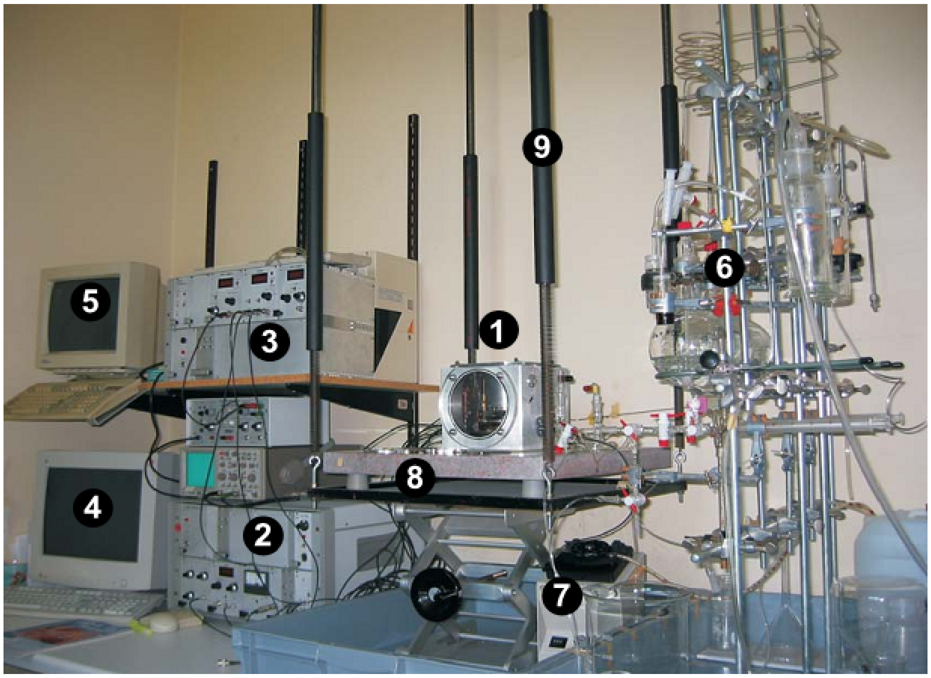

Figure 2.11: Photograph of the home-built EC-STM: (1) aluminum chamber for the STM; (2) STM control unit; (3) bipotentiostat; (4) computer for controlling the STM unit and displaying STM images; (5) computer for displaying the cyclic voltammograms; (6) electrolyte supply and gas purification system; (7) hose pump; (8) heavy granite plate; (9) steel springs connected with the ceiling.

2.2.5 Tunneling tips

The geometry and material of the tunneling tip plays a key role in producing STM images with atomic resolution. A blunt tip will usually deliver poor images. Tunneling tips can be produced by etching or tearing a thin metal wire.

Tips are most commonly made from Tungsten or Platinum/Iridium alloys. In the framework of this thesis tunneling tips have been made from tungsten wire by using an electrochemical etching method.

The process of the tip making is as follows: Firstly, the tunneling tips were electrochemically etched from a 0.25 mm diameter tungsten wire by piercing the W-wire through a thin lamella of 2 M KOH electrolyte suspended by a Pt loop. Then a potential with a amplitude of ±4 V and a frequency of 100 Hz was applied between the wire and the loop electrode for a total of 3 minutes while the electrolyte was exchanged every minute. After that, the amplitude of the alternating voltage was reduced to ±2 V, and the etching process continued until the free end of the tungsten wire fell off. The tip was then carefully rinsed with high purity water. After the tip became dry it was coated by passing it through a drop of hot glue [59,64-65]. Due to its high curvature the very tip remains uncovered.

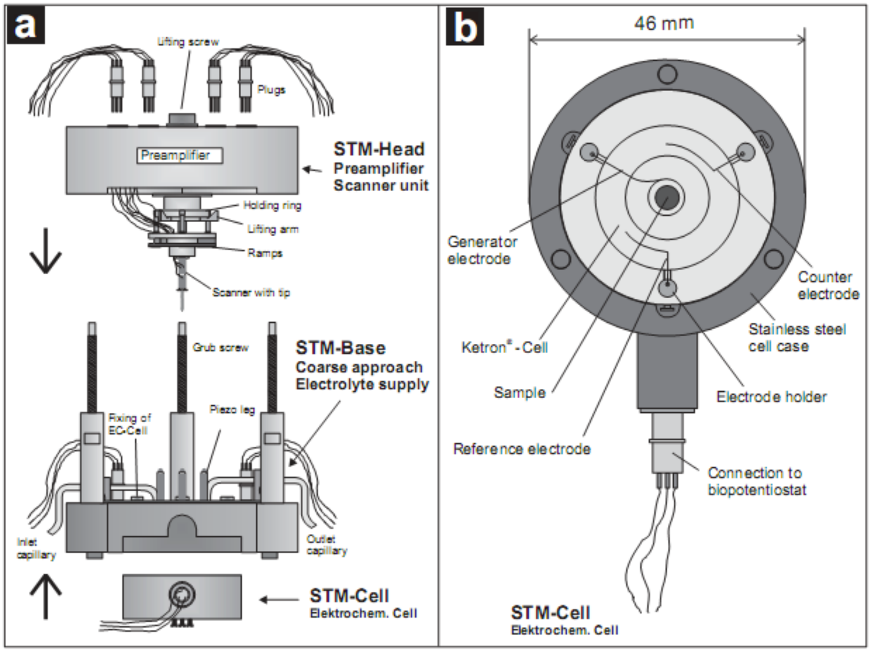

Figure 2.12: a) Sketch of the home-built electrochemical scanning tunneling microscope; b) electrochemical cell [59].

2.2.6 Sample preparation

With the aim to perform useful STM measurements the surfaces have to be reproducibly well prepared and defined. In addition, in order to study the interplay between the structure and reactivity of the surface, many well-defined single crystalline surfaces especially with low indexes have been used, e.g., Au, Ag, Pt, Cu, etc. [64,67]. Depending on the nature of the electrode material, particular preparation recipes are selected. Typical methods for preparing samples for electrochemical measurements are listed as follows [66]:

- ***UHV-EC:*** In this method, the surfaces are cleaned in UHV by cycles of Ar-ion bombardment and high temperature annealing. This method is successfully applied to various metals such as Pt, Au, Pd [67-68], which after cleaning are transferred (air-free) into the electrolyte.
- ***Flame-annealing and quenching method:*** This method was introduced by Clavilier in 1980 in which a Pt single crystal was annealed in a flame and then quenched in pure water. Noble metal surfaces are prepared by this method such as Pt [69], Au [70], Ir [71], Rh, Pd [72] and Ag [73].
- ***Electrochemical etching method:*** In contrast to the noble metals, such reactive metals as Cu. Ni. Fe, Co are easily oxidized in a flame, in air and even in the contact with only trace amounts of oxygen. They can be very well prepared by the electrochemical etching method, i.e. electropolishing.

In the frame of this work, Cu(100) and Cu(111) samples were employed and prepared by the electropolishing procedure which was first proposed by Brisard et al. [74]. The Cu(111) and the Cu(100) sample were cut from a single-crystal rod, oriented by Laue diffraction and first mechanically polished using a diamond paste with different grain sizes down to 0.25 µm. A surface orientation of less than 0.5° off the (100) or (111) plane is required to guarantee a reproducibly smooth surface. Since copper is a quite reactive metal, a thick oxide layer is formed at the surface when this metal is exposed to air. Therefore, in order to remove this native oxide layers, the sample must be electropolished prior to each STM experiment. To this end the single crystal was electropolished in a separate cell for about 40 s in 50% orthophosphoric acid at an anodic potential of 2 V. The surface used is kept parallel to the electrolyte surface and waved gradually in order to obtain a regularly electropolished surface. After electropolishing, the copper surface was rinsed with the supporting electrolyte (HCl or H_2SO_4) to remove the phosphoric acid and was then covered with a drop of purged electrolyte in order to protect the copper surface against oxidation. After that the electrode was mounted into the electrochemical cell which was protected in the aluminum chamber filled with Ar atmosphere. Initial CVs and STM images were recorded under potential control in the pure supporting electrolyte [59,63,64] in order to check the quality of the copper surface.

2.3. Synchrotron X-ray photoelectron spectroscopy

2.3.1 Introduction

X-ray photoelectron spectroscopy (XPS), one of the most frequently used methods for surface analysis and also known as electron spectroscopy for chemical analysis (ESCA), is a quantitative spectroscopic technique exclusively used in UHV in order to measure the elemental composition, as well as the chemical and electronic state of the elements that exist within a material. The XPS information is gained by measuring the kinetic energy and number of electrons that escape from the top 1 to 10 nm in depth of the material and the analytical area is routinely in a range from only 0.5 to 1 mm^2.

In surface electrochemistry, accompanied by the in-situ STM measurements that give a direct visualization, the XPS technique is used as an ex-situ method providing additional information on the chemical composition of the solid/liquid interface after emersion.

In this thesis, the solid/liquid interface analysis system (SoLiAS) installed at the synchrotron facility BESSY in Berlin, which enables to transfer safely the electrochemically processed surface into the XPS analyzer chamber without exposure to air, is employed in order to gain information about the phthalocyanine adlayers on an iodide modified copper surface.

2.3.2 Working principle of XPS

Surface analysis by XPS involves irradiating a solid under UHV condition with monoenergetic soft X-rays and analyzing the emitted electrons by their kinetic energy as described in Fig.2.13. A detailed description of the photoelectron spectroscopy and its applications can be found in [75].

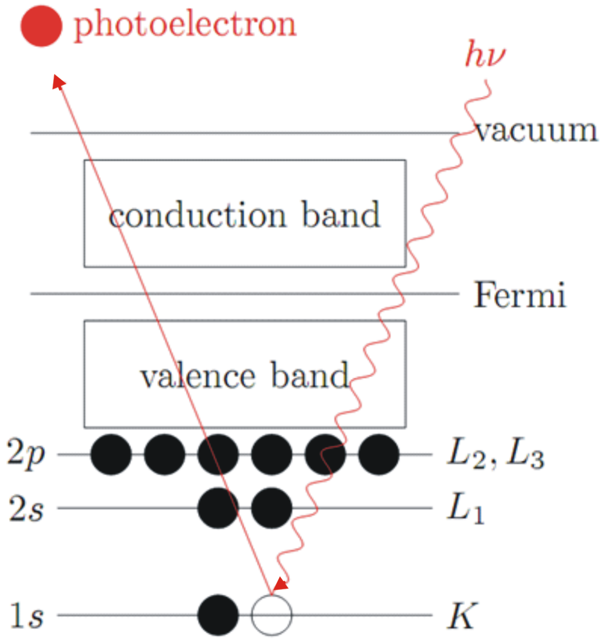

Figure 2.13: General principle of the X-ray photoelectron spectroscopy.

The spectrum obtained is a plot of the number of detected electrons per energy interval versus their kinetic energy. Indeed, individual elements are characterized by defined energy levels and, hence, produce a unique spectrum. As a result, in a mixture of elements, the spectrum is approximately the sum of the peaks of each constituent. Due to their very small mean free path length the detected electrons originate from only the top few atomic layers, making XPS a surface sensitive technique for chemical analysis. On the basis of peak heights, peak areas, peak positions and separations on the energy scale also quantitative data can be obtained.

Using a light source of known X-ray wavelength the electron binding energy (BE) of the emitted electrons can be determined by using the following equation based on the work by Ernest Rutherford (1914):

$$E_{binding} = E_{photon} - (E_{kinetic} + \emptyset) \qquad 2.10$$

where $E_{binding}$ is the binding energy of the electron, E_{photon} is the energy of the X-ray photon used, $E_{kinetic}$ is the kinetic energy of the electron measured by the instrument and ϕ is the work function of the spectrometer.

There are many materials that can be analyzed by using this XPS method such as inorganic compounds, metal alloys, semiconductors, polymers, elements, catalysts, glasses, ceramics, paints, papers, teeth, bones, medical implants and many others.

Generally, the XPS method can be used to measure:

- Elemental composition of the surface (top 1-10 nm usually),
- Elements that contaminate a surface,
- Chemical or electronic state of each element in the surface,
- Uniformity of elemental composition across the top surface (line profiling or mapping),
- Uniformity of elemental composition as a function of ion beam etching (depth profiling).

Therefore, the XPS can be employed to determine:

- The nature and the quantity of those elements that are present within ~10 nm from the sample surface,
- Contaminants, if any, existing in the surface or the bulk of the sample,
- The chemical state of one or more of the elements in the sample,
- The binding energy of one or more electronic states,
- The thickness of one or more thin layers (1-10 nm),
- The density of electron states.

Fig. 2.14 shows the scheme of a typical XPS set-up, including the following main components:

- A source of X-rays (X-ray gun or synchrotron radiation),
- An ultra-high vacuum (UHV) stainless steel chamber with UHV pumps,
- An electron collection lens,
- An electron energy analyzer,
- Magnetic field shielding,
- A vacuum sample introduction chamber,
- Sample holder and manipulators,
- A computer with software for data acquisition, storage, presentation and analysis.

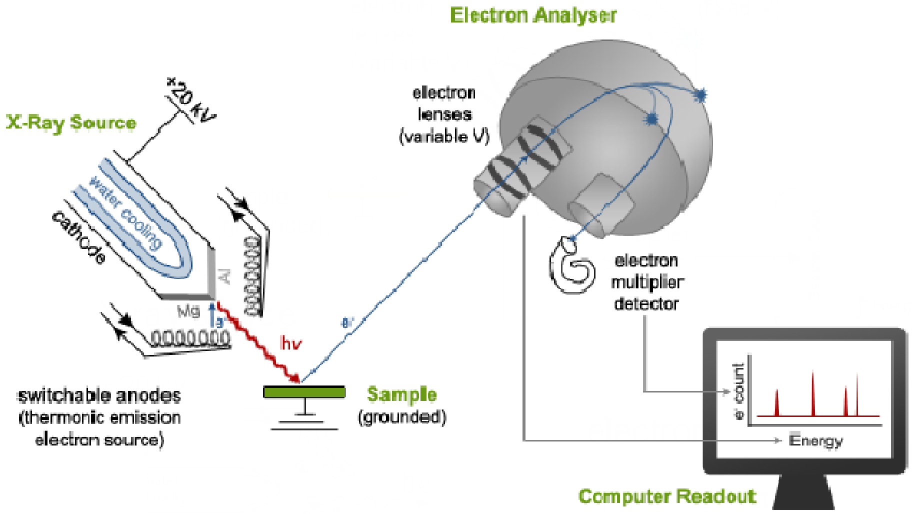

Figure 2.14: Scheme of an X-ray photoemission spectrometer [76].

Quantitative analysis is possible because the photoionization cross sections for core electrons are largely independent of the chemical bond. The intensity I_A of the escaping photoelectrons for a species A is given by:

$$I_A \sim \sigma_A(h\nu)\ D(E_A)\ L_A(\gamma)\ N_A\ \lambda_M(E_A)\ \cos\Theta \qquad (2.11)$$

$\sigma_A(h\nu)$ is the photoionization cross section at the incident photon energy hv,

$D(E_A)$ is the efficiency of the detector at the electron energy E_A,

$L_A(\gamma)$ is the photoelectron emission probability of an atom A at the angle γ of the incident photon with respect to the surface normal.

N_A is the density of atom A in the analyte,

$\lambda_M(E_A)$ is the inelastic mean free path of electrons with energy E_A in the matrix M,

Θ is the angle between the surface normal and the direction to the spectrometer.

Because of the difficulties to determine experimentally most of these parameters, the equation 2.11 can be simplified by disregarding the angular dependence $L_A(\gamma)$ and the mean free path $\lambda_M(E_A)$, and using tabulated atomic sensitivity factors (ASF), e.g. [75,77]. Thus a simple relationship between intensity and the number of emitters can be identified:

$$I_A \sim ASF_A\, N_A \tag{2.12}$$

The ratio of the photoelectron intensities of two components is given by:

$$\frac{I_A}{I_B} \approx \frac{ASF_A . N_A}{ASF_B . N_B} \tag{2.13}$$

Alternatively, the apparent mole fraction of a component is:

$$X_A \approx \frac{\frac{I_A}{ASF_A}}{\sum_i \frac{I_i}{ASF_i}} \tag{2.14}$$

In order to quantify the XP-spectra the intensity is defined as the peak area. Since part of the emitted photoelectron undergoes scattering processes within the solid resulting in electrons with lower kinetic energy, each XP-peak is superimposed on an increasing background. Therefore a subtraction of this background before further analysis of the spectra is essential.

The quantitative accuracy of the XPS method depends on several parameters such as: signal-to-noise ratio, peak intensity, accuracy of relative sensitivity factors, correction for electron transmission function, surface and volume homogeneity, correction for energy dependency of electron mean free path, and degree of sample degradation due to irradiation. Under optimized conditions, the quantitative accuracy of the atom % values calculated from the major XPS peaks is 90-95% of the atom % values of each major peak. If a high level quality control protocol is used, the accuracy can be further improved. Under work conditions, where the surface is a mixture of contamination and the expected material, the accuracy ranges from 80-90% of the value reported in atom % values. The quantitative accuracy for the weaker XPS signals, those having peak intensities 10-20% of the strongest signal, are 60-80% of the true value.

The analysis area depends on the instrument design. The typical radius of the analysis area ranges from 10 to 200 micrometers. The largest size for a monochromatic beam of X-rays is 1–5 mm. Non-monochromatic beams are 10–50 mm in diameter. Spectroscopic image resolution levels of 200 nm or below have been achieved on latest imaging XPS instruments using synchrotron radiation as X-ray source.

XPS can be performed using either a commercially built XPS system, a home built XPS system or a synchrotron based light source combined with an electron analyzer. Commercial XPS instruments in the year 2005 used either a highly focused 20 to 200 micrometer beam of monochromatic aluminium Kα X-ray or a broad 10-30 mm beam of non-monochromatic (polychromatic) magnesium X-rays. A few, special design XPS instruments can analyze volatile liquids or gases, materials at low or high temperatures or materials at roughly 1 torr vacuum, but there are relatively few of these types of XPS systems.

2.3.3 Synchrotron XPS and SoLiAS setup

The development of synchrotron radiation sources has enabled highly monochromatic, high resolution and high intensity studies to be carried out with radiation spanning a much wider and more complete energy range (5 - 5000 eV). SXPS has a continuously variable excitation energy, enabling variation of the cross section and mean free path for the specific measurement. The SoLiAS station is operated on the TGM 7 as well as on the U49/2-PGM2 beamline at BESSY in Berlin [78], providing excitation energies in the range 20-130 and 86-1400 eV, respectively.

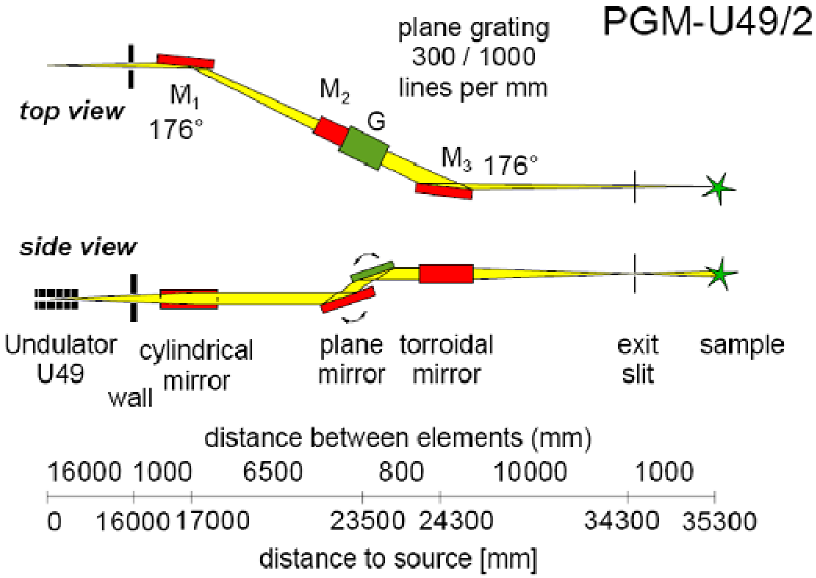

Figure 2.15: Schematic optical layout on beamline PGM-U49/2 (BESSY-Berlin).

The SoLiAS system is a six-chamber system, described in Fig. 2.16, consisting of:

1. EC cell for sample preparation under electrochemical control,

2. Buffer cell for pumping out the remaining moisture and transferring the sample from the electrochemical cell to the vacuum system,

3. Adsorption chamber with evaporators or more sample preparation facilities using molecular beam epitaxy (not applied in these measurements),

4. Analysis chamber including a LEED optics, an XPS electron analyser (SPECS Phoibos 150) and radiation source,

5. UHV preparation like sputtering and annealing the sample,

6. Load lock.

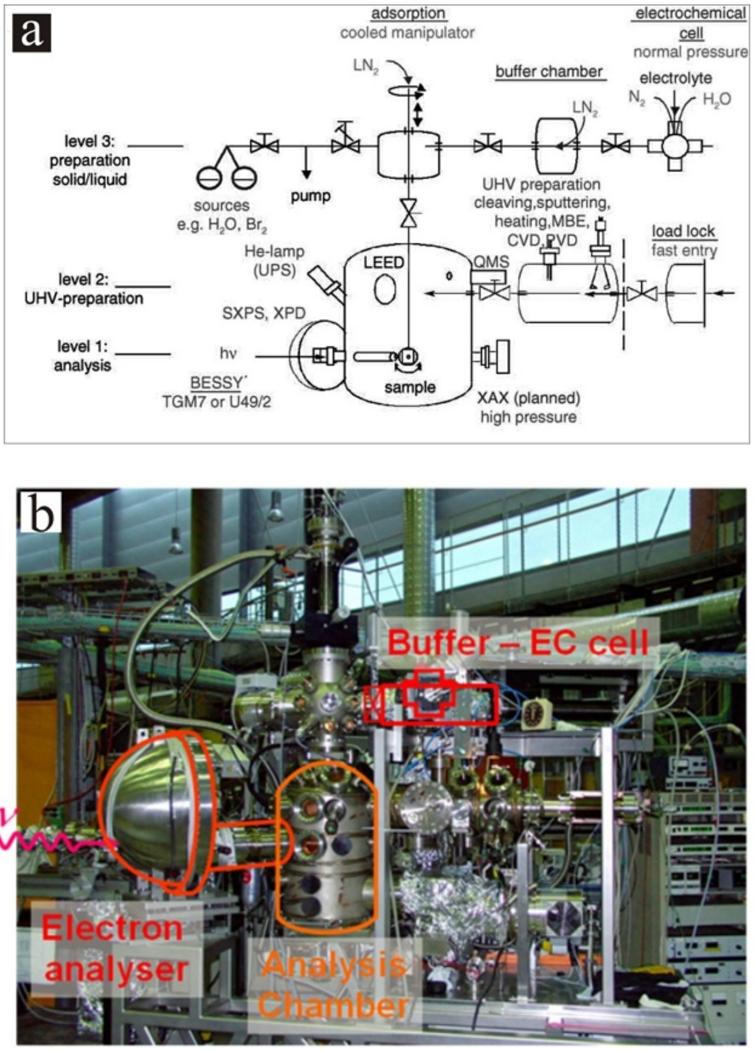

Figure 2.16: The SoLiAS: (a) schematic drawing, (b) photograph.

The buffer chamber enables sample transfer without contact to ambient air. If atomically thin surface layers are to be analyzed with highest surface sensitivity and spectroscopic resolution, very special measures have to be taken in order to avoid contamination by ambient air or ubiquitous hydrocarbons. Therefore it is required to carry out the entire wet processing under normal pressure in a high purity inert gas atmosphere in a system directly attached to the UHV system. The SoLiAS system fulfills these demands. Without contact to ambient air, the sample is transferred via a buffer chamber, which may be vented with high purity inert gas, into the UHV analysis chamber.

Vice versa, the SoLiAS station also permits contamination free transfer of the sample from UHV into the electrochemical cell. All parts of the SoLiAS station, and the electrochemical cell are separated by plate valves from each other and each part is evacuated by its own magnetically levitated turbo pump. The base pressure of the analysis chamber amounts to $1*10^{-10}$ mbar. The structure of the electrochemical cell is further explained below. The actual electrochemical cell is housed in a Teflon holder at the bottom of a three dimensional glass cross with six equivalent openings. Both the Teflon holder and all other attachments are secured with plastic clips. Fig. 2.17a shows the three dimensional glass cross, including the electrochemical cell, the magnetic thrust rod with sample holder and sample for sample transfer into the analysis chamber, and the capillary for drying the sample after emersion. Fig.2.17b describes the electrochemical cell used for the adsorption of molecules before transferring into the UHV chamber.

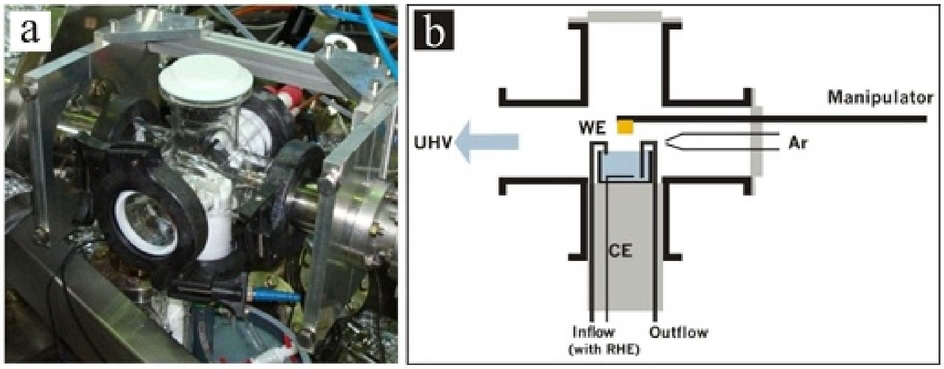

Figure 2.17: Glass cross with electrochemical cell: (a) photograph, (b) schematic drawing

2.3.4 Sample preparation and XPS measurements

Electrochemical processing of the sample to be investigated was performed in the atmospheric pressure inert-gas cell using a classical hanging meniscus configuration followed by a transfer of the electrode into the vacuum via the buffer chamber. After 10 min. of adsorption the sample was emersed out of solution and the solution residue on the surface was blown away with dry argon gas and then transferred to UHV under Ar-atmosphere. Thus, there is no hint of a drying-up residue which should be indicated by a K2p signal from KI in the XP-spectra. Photoelectron spectra were obtained using a Phoibos 150 MCD 9 analyzer (SPECS). All spectra were recorded in normal emission and are referenced to the respective Fermi level of the metallic substrate. Thus, the displayed energy scales in the XPS spectra correspond to binding energies (BE). The total experimental resolution including the energy width of the photon beam and the detector resolution amounts to 100 meV.

Chapter 3

Substrates

3.1. Introduction

In an EC-STM measurement, not only do electrochemical reactions occur on the working electrode, also structural transitions and self-assembly processes of adsorbates are observed. The influence of the 2D structure and nature of the adsorbate structures become evident. To elucidate this aspect, copper single crystals with two different orientations, i.e. Cu(100) and Cu(111), have been used in the framework of this thesis.

3.2. Copper surfaces

Copper, known as an important transition metal, has attracted much attention due to several of its important properties, e.g. it is an excellent electrical conductor, ductile, etc. so that it is widely used both in everyday life and in technology. Indeed, for a long time, it has been used as an electrical conductor (wires), as a building material (roofing, tubing, etc.), and as a component of various alloys [79]. Recently, copper has been considered as one of the key materials of the twenty-first century due to its application as wiring material in the state-of-the-art chip design replacing the former aluminum technology. Damascene Cu electroplating for on-chip metallization, which has been developed in the early 1990s, has been central to IBM's Cu chip interconnection technology [80-81], etc.

On the other hand from the electrochemical point of view, the choice of copper takes advantage of its higher reactivity in comparison with that of noble metals such as Au, Ag, and Pt. The potential window of copper is more negative than that of those metals. These aspects are expected to offer a number of undiscovered interesting phenomena concerning the electrochemistry and the self-assembly of molecular structures on the copper surfaces under reactive conditions.

However, the application of this material at the nanometer scale requires a more sophisticated understanding of the relevant interface properties and processes of those devices containing reactive materials like copper. An atomic scale understanding of corrosion phenomena, corrosion inhibition by organic molecules, oxidation, anodic dissolution and the formation of passivating films on copper is thus of vital interest.

In this thesis, such anion modified copper surfaces serving as substrates for the self-assembly of supramolecular structure were used. It is worthy to note that the presence of an anion adlayer on a copper surface acts as an interface where the adsorption of molecules takes place. Therefore it is the anion adlayer which is supposed to determine the structure of the building-blocks not only by their conformation but also by enhancing the adsorption due to electrostatic attraction.

STM images as well as the crystal lattice of the bare, anion-free Cu(100) and Cu(111) surfaces are presented in Figure 3.1. The nearest neighbor distance (NND) of Cu-Cu is a_{Cu} = 2.56 Å.

3.3. Anion modified copper surfaces

3.3.1. Overview of anion modified metal surfaces

Adsorption of ions on well defined substrate surfaces plays an important role in electrochemistry. It is well-known from various electrochemical processes such as in galvanic deposition, etching, corrosion and electro-catalysis that the presence of specifically adsorbed anions can significantly affect the electrochemical reactivity of the metal electrodes.

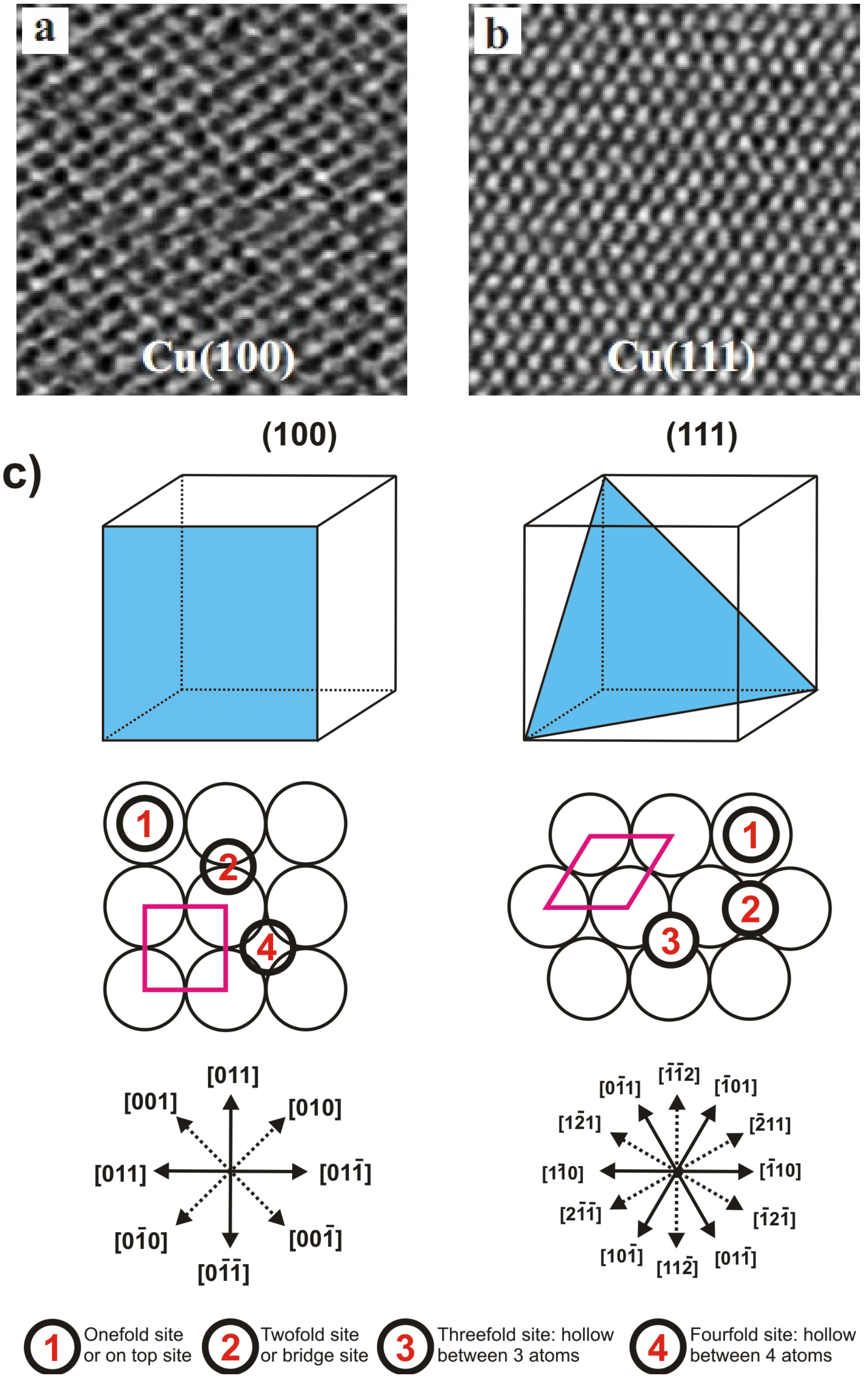

Figure 3.1: STM-images of copper surfaces in diluted sulfuric acid: a) Cu(100) surface, 3.8 nm × 3.8 nm, U_b = 35 mV, I_t = 5 nA, E = 90 mV vs RHE; b) Cu(111) surface, 3.8 nm × 3.8 nm, U_b = 3 mV, I_t = 2.5 nA, E = -300 mV vs RHE; c) (100) and (111) planes of an face-centered cubic (fcc) metal with different sites on the surfaces referring to ref.31.

Once a metal surface is brought into contact with aqueous electrolytes, the tendency towards specific anion adsorption increases in the sequence: $F^- < PF_6^- < BF_4^- < ClO_4^- < Cl^- < Br^- < I^-$ [82]. Anions with strongly bound solvation shells such as F^-, ClO^{-4}, PF^{-6} interact with the electrode surface by pure electrostatic forces and are not specifically adsorbed on the metal surfaces. In contrast, weakly solvated anions such as SO_4^{2-}, Cl^-,Br^-, I^-, can strip a part of their solvation shell and form chemical bonds with the metal surfaces (see following section) [44]. Consequently, these anions can specifically adsorb and can form close-packed, ordered adlayer structures on electrode surfaces.

In part the characterization of the adlayer structures was mainly done by using ex-situ methods such as electron diffraction and photoemission techniques. The invention of the STM and then EC-STM [49,50,52] has revolutionized the field of surface electrochemistry allowing in-situ studies, i.e. in solution, of the interfacial structure. Various ordered structures of halides, pseudohalides and oxoanions have been observed by in-situ studies on single crystal electrode surfaces of the fcc metals Au, Ag, Cu, Pt, Pd, Ni [44,60,64,65,67,84-102]. Especially, the specific adsorption of these anions on the reactive copper surfaces was intensively studied by Wandelt's group [83-88,99-102], Itaya's group [67,89,93] and others [44,96-98]. These adsorbed layers will be presented and discussed in detail in the following sub-sections.

3.3.2. Chloride modified Cu(100) surface

When a Cu(100) surface is in contact with a diluted hydrochloride acid (HCl 10mM) at potentials within the double layer regime of copper, chloride adsorbs spontaneously and forms highly ordered adlayers as described in Fig.3.2. The adlayer lattice is square and commensurate with respect to the substrate lattice. The adlayer can be described by assuming a $(\sqrt{2}\times\sqrt{2})R45^\circ$ or c(2×2) unit cell (Fig.3.2a,b) [97,98,103]. The chloride atoms reside in four-fold hollow sites on the Cu(100) lattice [104]. The surface coverage of the chloride adlayer is 0.5 monolayer (ML) and the nearest neighbor distance is $\sqrt{2}a_{Cu} = 0.362$ nm. The hard-sphere model of this c(2 × 2) structure is presented in Fig.3.2c.

The specific chloride adsorption induces a step faceting resulting in substrate steps which are aligned parallel to the <001> directions. Upon the chloride adsorption/desorption the steps reversibly change their shape from a random orientation and fuzzy appearance on the Cl-free surface to predominantly [010]-

and [001]-oriented steps with strongly reduced mobility of copper atoms at the steps on the Cl-covered surface (Fig.3.2a). As a consequence, typical angles between steps of 90° can be observed in the presence of the chloride. Especially, the deposition or dissolution of copper proceeds by the subsequent addition or removal of primitive $(\sqrt{2} \times \sqrt{2})R45^o$ unit cells along these edges, i.e. along the [010] or the [001] orientation [44]. Step faceting is a result of a copper mass transport in the course of the so-called "electrochemical annealing" that is facilitated in the presence of complexing chloride species.

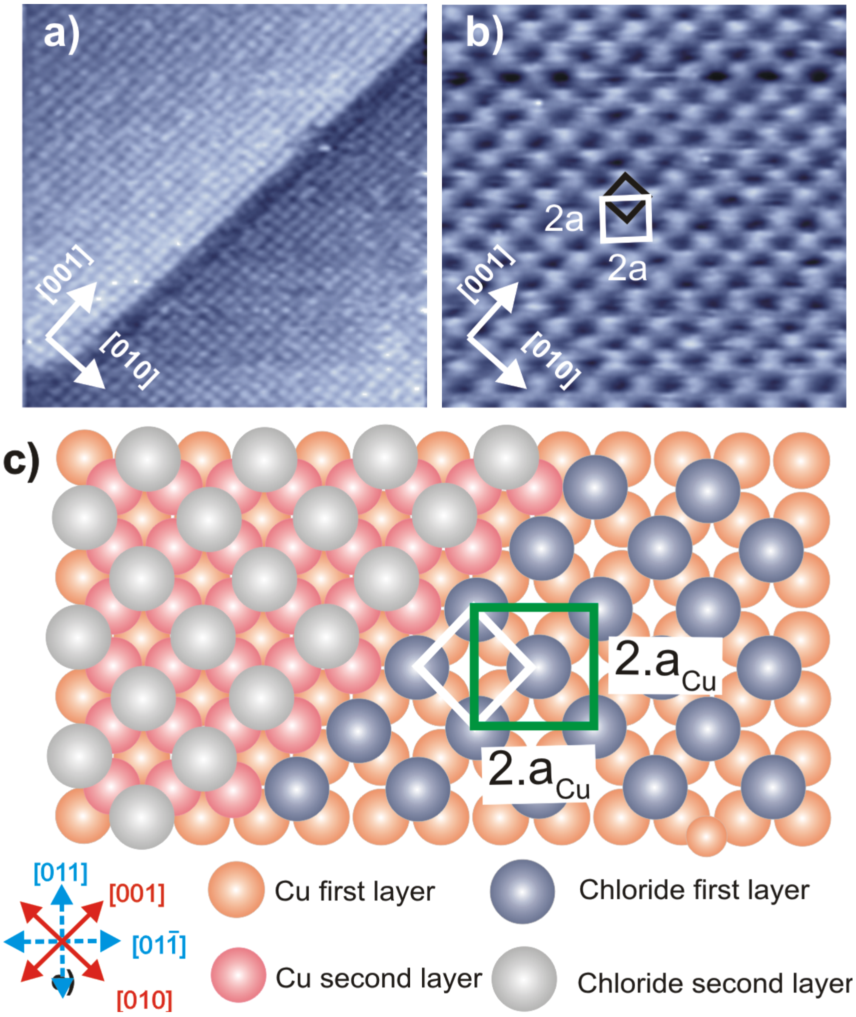

Figure 3.2: STM images of a chloride covered Cu(100) electrode surface: a) typical copper steps preferentially aligned parallel to the close packed Cl rows 9.92 nm x 9.92 nm, U_b = +40 mV, I_t = 5 nA, E = +20 mV; b) c(2 x 2)-Cl structure on the Cu(100), 4.37 nm x 4.37 nm, U_b = +20 mV, I_t = 2.5 nA, E = -10 mV; c) structural model of the c(2 x 2)-Cl adlayes on Cu(100) [105].

3.3.3. Chloride modified Cu(111) surface

Similarly, chloride anions also strongly and specifically adsorb on a Cu(111) surface and form a highly ordered superstructure. Upon adsorption, the chloride adsorbate causes a restructuring of the surface topography resulting in a change of the substrate step directions which enclose slightly distorted angles of 120° (Fig.3.2a). Like for chloride adsorption on the Cu(100) surface, the step edges run along the close-packed rows of the chloride adlayer. The adsorbate structure is impacted by the electrode potential. At negative potentials near the on-set of the hydrogen evolution process, an ideally hexagonal lattice, commensurate to the Cu(111) substrate lattice, is observed. The unit cell was determined as $(\sqrt{3} \times \sqrt{3})R30^o$ with respect to the underlying Cu(111) layer [84,85,96].

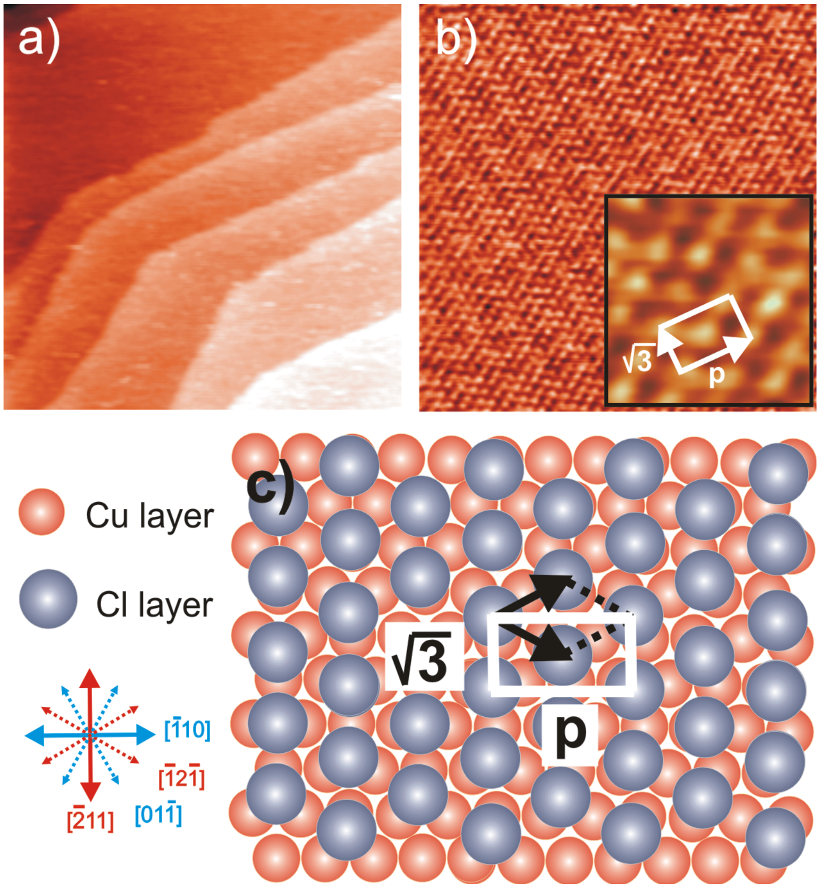

Figure 3.3: Chloride modified Cu(111) surface : a) 70 nm x 70 nm, U_b +220 mV, I_t = 0.2 nA, E = 50 mV; b) c(p ×√3) structure: 14.4 nm × 14.4 nm, 5.58 nm x 5.58 nm, I_t = 2.0 nA, U_b = 75 mV, E = 0.0 mV; c) Hard-sphere model of chloride modified Cu(111).

By contrast, at positive potentials, the chloride structure on Cu(111) is uniaxially compressed as shown in Fig.3.3b. This phase can be described by a centered-rectangular unit cell, $c(p \times \sqrt{3})$, resulting in an additional long-range height modulation [34]. A possible hard-sphere model of this structure is proposed in Fig3.3c.

3.3.4. Iodide modified Cu(100) surface

Immersion of a Cu(100) electrode into an acidic electrolyte containing iodide (5 mM H_2SO_4 + 1 mM KI) leads to a spontaneous specific adsorption of iodide on the copper surface in the potential range between the onset of copper dissolution and the onset of hydrogen evolution. The structure of the iodide adlayer was characterized by EC-STM as shown in Fig. 3.4. Quite similar to the adsorption of chloride on the Cu(100) and on a Cu(111), this specific adsorption also induces a preferential alignment of the copper steps, but with typical enclosed angles that are slightly different from 90° (Fig. 3.4a) [99,100,102].

The structure of the iodide adlayer was found to be strongly dependent on the electrode potential due to so-called *“electro-compression and –decompression”* [99,100,102]. At positive electrode potentials near the onset of the copper dissolution reaction the iodide adlayer is uniaxially incommensurate showing an additional one- dimensional long-range height modulation superimposed on the atomic corrugation as visible in Fig.3.4b,c. The unit cell can be described as c(p × 2)-I with $p > 2a_{Cu}$ which is uniaxially expanded with respect to the commensurate c(2 × 2) structure (Fig.3.4c). This p value increases with the decrease of the electrode potential (expansion). Because of the four-fold symmetry of the Cu(100) substrate, two rotational domains of the $(p \times 2) - I$ can be observed [99,100,102]. This structure was used as substrate for the self-assembly of porphyrin molecules in the framework of this thesis. The surface coverage corresponding to this structure was calculated as 0.4 ML related to the Cu(100) lattice [99,100].

Besides, $(5 \times 2) - I$ (p = 2.5) with four iodide atoms per one unit cell was also observed at electrode potentials just before reaching the CuI formation.

In contrast, at a certain potential close to the onset of the hydrogen evolution reaction a phase transition can be observed which leads to the formation of a

$c(6 \times 2) - I$ phase which remains stable even under massive hydrogen evolution [99]. In addition, a $p(2 \times 2) - I$ phase can also be obtained when a very low iodide concentration of iodide is used [100].

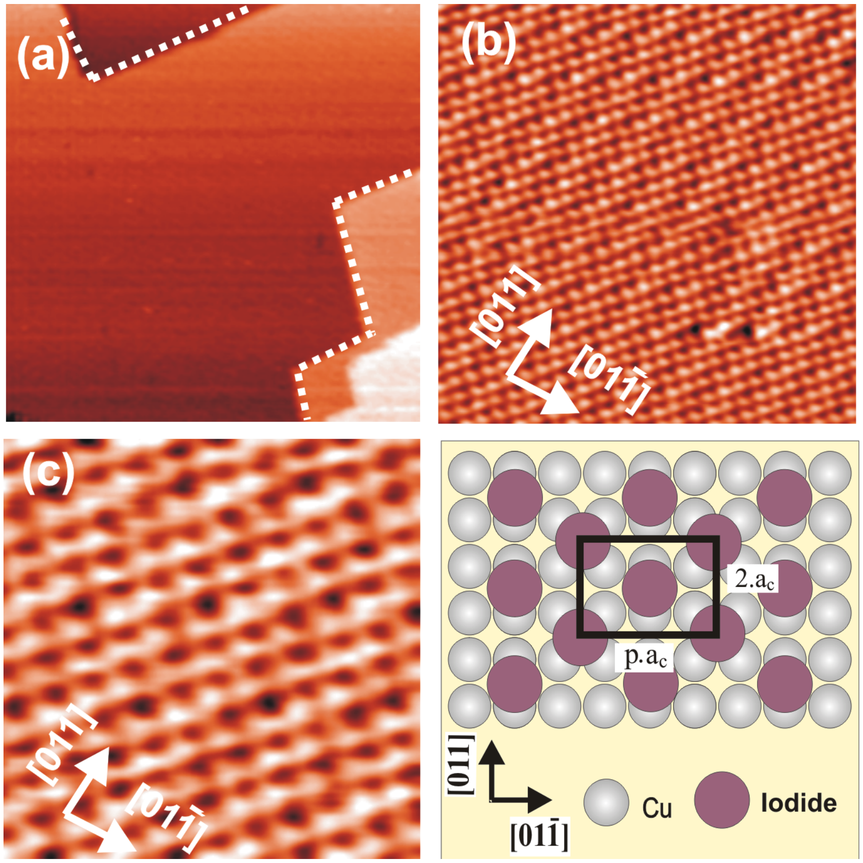

Figure 3.4: Surface morphology and atomic structure of the iodide modified Cu(100) electrode surface, a) large scale iodide terraces showing a step-edge angle of 90° , 47 nm x 47 nm, I_t = 0.25 nA, U_b = 150 mV, E = 0 mV; b-c) 14.4 nm x 14.4 nm and, 5.6 nm x 5.6 nm, I_t = 1 nA, U_b = 70 mV, E = -100 mV; d) Hard-sphere model of c(px2)-I phase on Cu(100).

3.3.5. Bromide modified Cu(111) surface

Similar to chloride, bromide also specifically adsorbs on a Cu(111) surface and forms a highly ordered superstructure causing a restructuring of the surface topography resulting in a change of substrate step directions which enclose slightly distorted angles of 120° (Fig.3.5a). The step edges on the Cu(111) surface run along the close-packed rows of the bromide adlayer. The adsorbate structure is also impacted by the electrode potential. At negative potentials a $(\sqrt{3} \times \sqrt{3})R30^{o}$ with respect to the underlying Cu(111) was imaged [34]. Whereas a $c(p \times \sqrt{3})R30^{o}$ unit cell is observed on the Cu(111) surface when the electrode potential is in the more positive potential regime [34]. Compared to chloride, the potential dependence of compression for the bromide is greater. This can be explained in terms of the lattice constant of the Cu(111) and the diameter of Br. The van der Waals diameter of Br (0.39 nm) is between Cl (0.36 nm) and I (0.43 nm). And, hence, Br may possess the characteristics of both I and Cl in regard to the compression behavior.

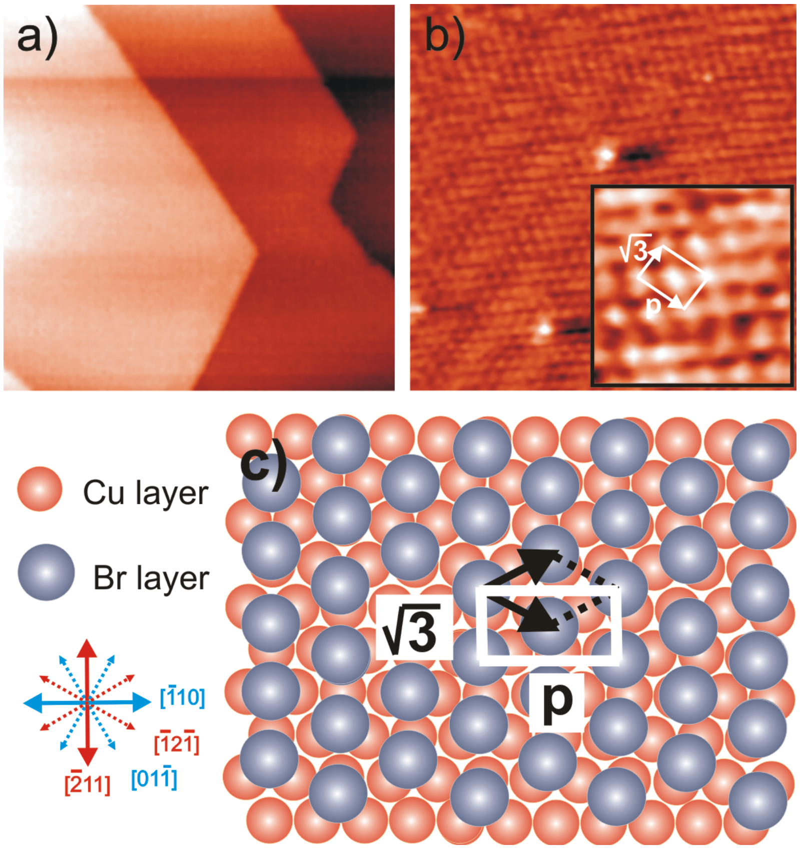

Figure 3.5: Bromide modified Cu(111) surface : a) 64.4 nm x 64.4 nm, U_b = +175 mV, I_t = 0.2 nA, E = 50 mV; b) A c(p ×√3) structure: 13.61 nm × 13.61 nm, I_t = 2.0 nA, U_b = 75 mV, E = 0.0 mV; c) Hard-sphere model of bromide modified Cu(111).

3.3.6. Sulfate modified Cu(111) surface

As other anions, sulfate anions specifically adsorb on Cu(111) and form typical superstructures. In addition, the adsorption and desorption of the sulfate anions on the Cu(111) surface is also well documented to depend strongly on the electrode potential. The sulfate adsorption/desorption and the corresponding adlayer formation/decay processes are kinetically hindered. This means that these processes are slow and can be observed by STM measurements in real time [59,63,86,87]. Within the potential range of the sulfate adsorption, the sulfate anions form a characteristic anisotropic Moiré pattern as seen in Fig.3.6.

The appearance of the long range modulation of the Moiré structure was explained by a sulfate induced reconstruction of the Cu(111) electrode. The expansion of the topmost copper layer leads to a misfit with respect to the second copper layer. As a consequence, the growth of Cu islands and terraces is caused by a mass transport out of the underlying copper. The sulfate layer on reconstructed Cu(111) was proven to have a pseudo $(\sqrt{3} \times \sqrt{7})$ unit cell. The distance between sulfate particles in adjacent rows is 0.71 nm and within the same row 0.47 nm. The two lattice vectors enclose an angle of 36°. A distortion of the reconstructed first copper layer in comparison with the second hexagonal copper layer underneath leads to a slight distortion of the long-range Moiré superstructure. Consequently, there are three rotational domains of the Moiré structure which are rotated by an angle of 120° with respect to each other due to the 3-fold symmetry of the second copper layer. Clearly visible in high resolution STM images are two kinds of STM dots (see Fig.3.6b). The brighter and bigger ones are assigned to the sulfate (or bisulfate) anions. The smaller ones that form characteristic zig-zag rows between the sulfate rows are assigned to co-adsorbed water or hydronium species. The co-adsorption of H_2O molecules stabilizes the sulfate layer [105-106]. A hard-sphere model of this co-adsorption of sulfate and water is presented in Fig.3.6c.

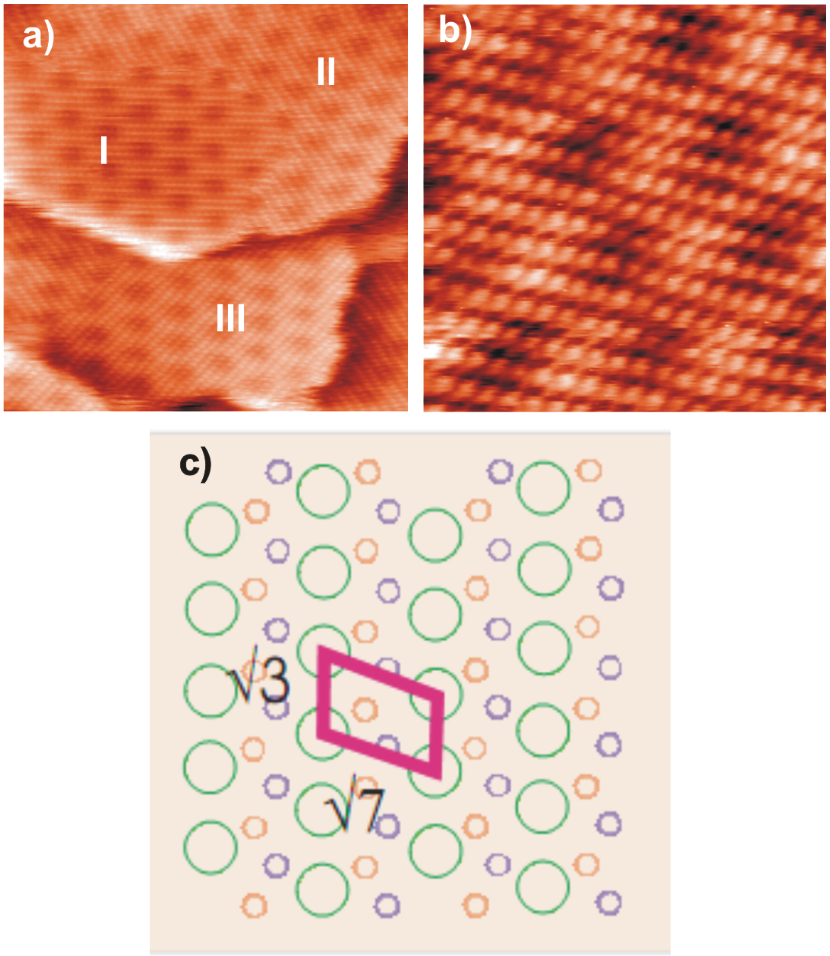

Figure 3.6: Surface morphology and atomic scale structure of sulfate and water modified Cu(111) surface : a) Three rotational domains of sulfate/water coadsorption layer: 40 x 40 nm, I_t = 1 nA, U_b = +50 mV, E = +150 mV; highly ordered array of coadsorbed sulfate and water on Cu(111): 8.4 x 8.4 nm, I_t = 1.2 nA, U_b = +50 mV, E = +60 mV; c) Hard-sphere model with a $\left(\sqrt{3} \times \sqrt{7}\right)$ unit cell of sulfate/water coadsorption on Cu(111).

Chapter 4

Supramolecular chemistry and self-assembly of organic molecules on solid surfaces

4.1. Introduction

As a branch of modern chemistry, supramolecular chemistry has been a major topic in recent decades dealing with design, fabrication and characterization of complex molecular architectures on the nanometer scale [107-108]. While traditional chemistry focuses on the covalent bond, supramolecular chemistry examines the weaker and reversible non-covalent interactions between molecules. These forces include hydrogen bonding, metal coordination, hydrophobic forces, van der Waals forces, π-π interactions and electrostatic effects. Important concepts that have been demonstrated by supramolecular chemistry include molecular self-assembly, folding, molecular recognition, host-guest chemistry, mechanically-interlocked molecular architectures, and dynamic covalent chemistry [109]. The biggest challenge for the electrochemists is to seek such convenient models simulating the natural processes under realistic conditions, e.g. nano-sized devices, machines and actuator [110]. The exploitation of the rules of supramolecular chemistry is the basis for the so called *"bottom-up"* approach that allows one to build up supramolecular surface structures from simpler molecular building blocks via non-covalent weak forces. As a result molecular architectures are obtained which exhibit a significantly higher complexity than the individual molecular building-blocks following Lehn's definition of supramolecular chemistry as the "*chemistry beyond the molecule*" [108,111]. Supramolecular structures are the result not only of additive but also of cooperative interactions, including hydrogen bonding, hydrophobic effects and metal coordination. Their properties differ from the sum of the properties of the individual component [112].

In a new text book about supramolecular chemistry [112], Ariga and Kunitake subdivided supramolecular chemistry in three categories related to the size of the molecular target system:

- The molecular recognition chemistry or the chemistry associated with a molecule recognizing a partner molecule: Molecular recognition as the basis of supramolecular chemistry has been defined as "a process involving both binding and selection of a substrate by a given receptor molecule as well as possibly a specific function". There are two types of receptors: (i) endo-receptors are host molecules that have binding sites inside their molecular structures ("inner surface") and (ii) exo-receptors are host molecules with binding sites on their outer surfaces [112-113].

- The chemistry of molecules built to specific shapes: It is possible to build molecules of medium size which have unique geometric features and provide the key to many tailored supramolecular topologies. For example, fullerenes are like "molecular soccer balls", carbon nanotubes, etc. One can design one-dimensional supramolecular objects, rectangles, squares, three dimensional cages, molecular branching such as dendrimers (molecular tree), molecular rings, etc. [112,1184-115].

- The chemistry of molecular assembly from numerous molecules: Supermolecules can also be programmed from a huge number of components producing a supramolecular self-assembly with a defined shape and structure. For example, supramolecular crystals, micelles, monolayers and Langmuir-Blodgett films on the surface of water, self-assembled monolayers on solid surfaces, etc. [112,113,116-117]. Here the concept of self-assembly is used for the spontaneous assembly of several molecules into a single, highly structured supramolecular aggregate [118]. The intermolecular interactions within supramolecules are non-covalent and quite diversified such as:

- Electrostatic interaction occurs between charged species, and is relatively strong compared to other non-covalent interactions, and non-directional.
- Hydrogen bonding occurs only when the interacting functional groups are properly oriented, and is weak and directional.
- Coordinative bonding occurs between a metal ion and electron-rich atoms, and is of moderate strength and directional.
- The van der Waals interaction is weak, non-directional and less specific than other interactions described above, it acts between all kinds of molecules.
- Hydrophobic “interaction” occurs between hydrophobic molecules in water and is the major driving force for hydrophobic molecules to aggregate.
- π-π interactions between aromatic rings are present when the aromatic rings face each other, and the overlap of π-electrons results in an energetic gain.

The formation of supramolecular architectures may be due to one kind of these interactions or a combination of them. By mastering these interactions, one can control the building of supramolecular systems and create a huge number of supramolecular architectures which have particular forms and specific functions etc. [116]. The development of supramolecular chemistry has opened a wide range of promising application in many fields, especially in nanotechnology [119-121].

The new supramolecular chemistry as mentioned above is, however, mostly applied and explored in solution or in 3D crystals, but not so much yet in two dimensions. Because of the increasing demand to produce surface pattern and devices with nanometer dimensions using the promising “bottom-up” technique, the autonomous ordering and self-assembly of atoms and molecules on atomically well defined surfaces is receiving more and more attention. That is the reason why the self-assembly of supramolecules on solid surfaces has been intensively studied only over the past few years. In addition, the invention of the scanning probe techniques has facilitated the studies because of their ability to visualize molecules in real space [119,122].

The self-assembly of supramolecular entities on solid surfaces can be in fact divided into two groups as follows:

- Self-assembly of molecules on solid surfaces in ultrahigh vacuum (UHV) based on interactions between molecules (intermolecular interactions) and interactions between the molecule and the substrate (adsorbate-substrate interactions).
- Self-assembly of molecules on solid surfaces at the solid/liquid interface where intermolecular, molecules-substrate and molecules-solvent interactions are taken into accounts.

It becomes evident that the molecular self-assembly process at the solid/liquid interface is quite complex and is a result of a delicate balance among all these interactions [22] and, hence it can be restricted to the monolayer regime or may extend to multilayers. The concept of self-assembled monolayers (SAMs) was discovered in the case of chemisorption of thiolates on gold [114]. However, it is discernible nowadays that self-assembled monolayers can be formed in a wide range of systems with different supramolecules on different solid surfaces.

In the framework of this thesis the self-assembly of organic molecules at the solid/electrolyte interface employing phthalocyanine, porphyrin and viologen molecules, respectively, as building-blocks was examined showing highly ordered self-assembled monolayers, sub-monolayers and disordered phases. This self-assembling process can be controlled by changing the adsorbate-substrate interactions, i.e. by easily changing the electrode potential in the case of electrostatic interaction, etc.

4.2. Phthalocyanine molecules

Phthalocyanine (Pc) is an intensely blue-green coloured macrocyclic compound that is widely used in dyeing [6,123-124]. The story of phthalocyanines began in 1928 at the Grangemouth plant of Scottish Dye Ltd. during the industrial preparation of phthalimide from phthalic anhydride. As described by McKeawn in his excellent review on phthalocyanine anhydride synthesis, the glass-lined reaction vessel containing phthalic anhydride had cracked, exposing the outer steel casing to the reaction resulting in the formation of a blue-green material.

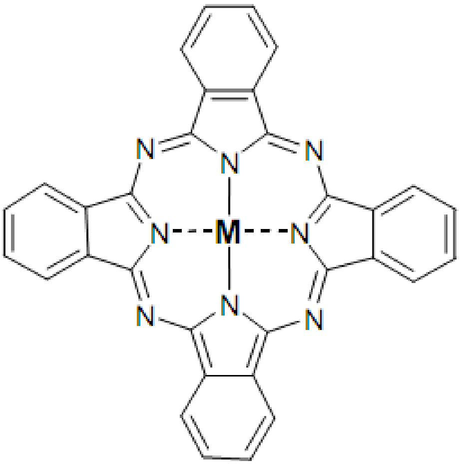

Figure 4.1: Chemical structure of unsubstituted metallophthalocyanine (MPc).

The simplest molecule of this group is unsubstituted phthalocyanine whose chemical structure is illustrated in Fig.4.1. This molecule is a beautifully symmetrical 18 π-electron aromatic macrocycle. Like the porphyrins (see section 4.3), the Pc macrocycle can be host to over seventy different metal ions in its central cavity in order to form corresponding metallophthalocyanine compounds. Since its discovery, the Pc and its derivatives have been extensively used as colorants (dyes or pigments) [6,123-124], in solar cells [1], in gas-sensing devices [2], in photovoltaic applications [3], as ultrafast optical switches [4], in organic field effect transistors [5], and recently in laser cancer therapy [124-125].

Recently, design and fabrication of phthalocyanine based nano-sized devices are receiving more and more attentions. One of the solutions is to fabricate highly ordered phthalocyanine patterns with nanometer dimensions on well-defined surfaces [126-128]. The technique of choice is the self-assembly of these supramolecules on metal surfaces. The ordered phthalocyanine layers can be produced from the vapor phase in ultrahigh vacuum [7-10,126-127]. However, there are few reports on the adlayer of phthalocyanine molecules in electrochemical environment because of the low solubility of many Pcs in polar solvents [13,128].

In this thesis, we focus on the self-assembly of a new phthalocyanine synthesized by the group of Prof. Torres (Madrid), namely 2,3,9,10,16,17,23,24-Octa(3-(N'-methyl)-pyridyloxy)-5,28:14,19-diimino-7,12:21,26-dinitrilotetra benzo (c,h,m,r)(1,6,11,16) tetra azacycloeicosinato (2-)-N29,N30,N31,N32 zinc(II)-iodide, abbreviated in the following as [ZnPcPyMe]$^{+4}$, due to its high solubility in water (Fig.4.2). The iodide modified Cu(100) surface serves as template for this adsorption.

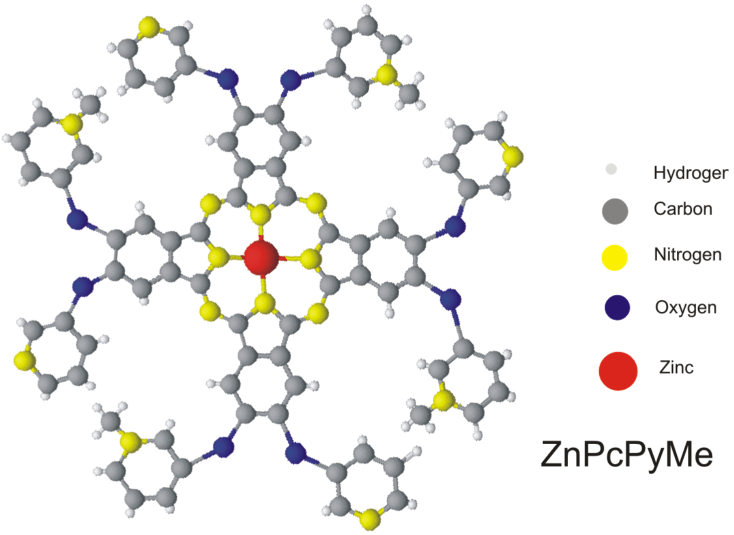

Figure 4.2: Chemical structure of the [ZnPcPyMe]$^{4+}$ molecule.

In aqueous and/or non-aqueous solutions, this phthalocyanine is known to undergo four reversible redox processes in order to form corresponding reduced and/or oxidized forms. From the electrochemical point of view, it is expected to observe, using STM measurements, different phases related to the various redox states.

Additionally, from UHV studies it was known that all phthalocyanines lie flat on the bare metal surface due to their large planar π system so that the π bonding to the surface can be maximized [22]. For an electrochemical environment one can expect that phthalocyanines might interact electrostatically with the charged electrode surface. A significant difference to the situation in UHV arises from the fact that the electrode surface may already be modified by the presence of the pure supporting electrolyte in terms of a specific anion adsorption. Hence, phthalocyanine is expected to interact with the specifically adsorbed anion layer and not with the bare metal surface.

4.3. Porphyrin molecules

Porphyrin molecules are cyclic molecules in which the parent macrocycle consists of four weakly aromatic pyrrole rings bridged by methene groups [129-130]. The simplest molecule of this group is porphine whose chemical structure is shown in Fig. 4.3. This figure also shows the numbering system for the porphyrin nucleus which was proposed by Hans Fischer and developed by the International Union of Pure and Applied Chemistry (IUPAC) and the International Union of Biochemistry (IUB) [130].

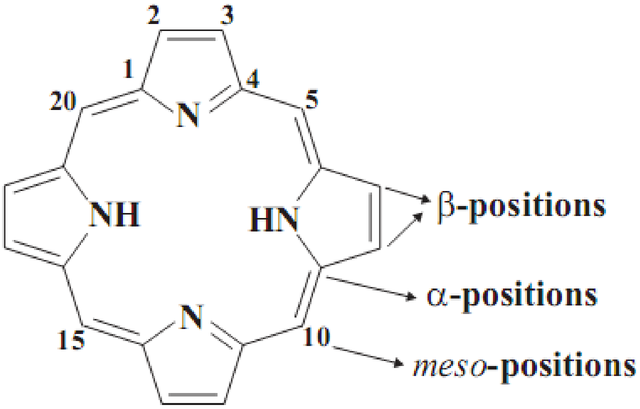

Figure 4.3: Porphine and nomenclature of porphyrin.

Most metals can be inserted into the central cavity of the porphyrin macrocycle producing metalloporphyrins. Porphyrins (both free base porphyrins and metalloporphyrins) are applied in many potential fields such as photodynamic therapy [28], as electrocatalysts for the reduction of inorganic and organic nitrocompounds [131-132], or as chemical sensors and molecular logic devices [16-17].

Similar to phthalocyanine molecules, in order to make use of the relevant properties, the fabrication of highly ordered porphyrin patterns with nanometer dimensions on well-defined surfaces is of interests. The molecules of choice in this thesis are a redox-active 5,10,15,20-Tetrakis(4-trimethylammoniophenyl) porphyrin tetra(p-toluenesulfonate) and 5,10,15,20-Tetrakis-(N-methyl-4-pyridyl)-porphyrin-Fe(III) pentatosylat), abbreviated as H_2TTMAPP and FeTMPyP whose chemical models are described in Fig.4.4. These porphyrins were supplied by Frontier Scientific as well as Sigma Aldrich and are of reagent grade, water soluble and halide free. They were used without further purification. In solution these porphyrins remain as cations.

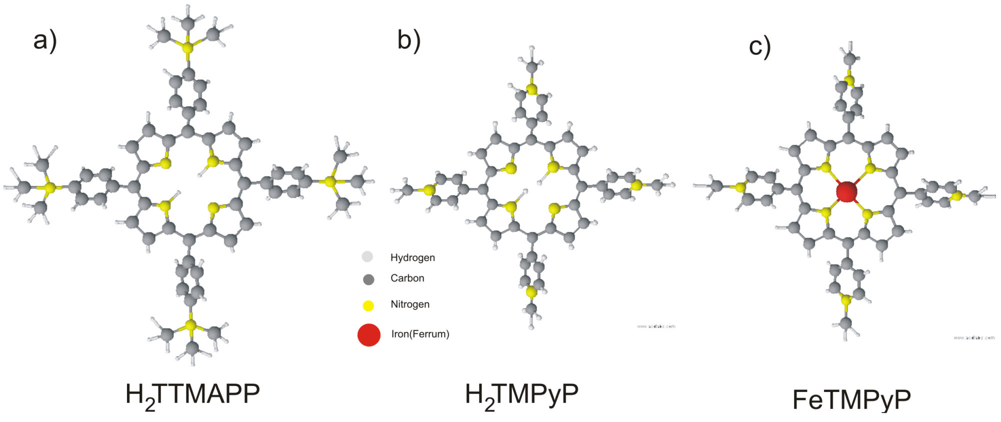

H_2TTMAPP H_2TMPyP FeTMPyP

Figure 4.4: Chemical model of (a) H_2TTMAPP; (b) H_2TMPyP and (c) FeTMPyP molecules.

The self-assembled layer of H_2TTMAPP on reactive copper surface is studied for the first time in electrochemical environment, whereas ordering of FeTMPyP leads to a different conclusion compared to a former report [60]. Results obtained on different anionic substrates will show the influence of the negatively charged substrates on the self-assembly process. Furthermore, the self-assembly processes of these molecules, occurring under the electrochemical conditions, are strongly impacted by the electrode potential which governs the electrostatic interactions between the positively charged porphyrin cations and the negatively charged anion modified copper substrates. The electrode potential induced self-assembled phase transition will also be examined in this contribution.

4.4. Viologen molecules

Viologen molecules are certainly among the most intensively studied molecular building-blocks in supramolecular chemistry. A sketchy overview of the viologens is drawn out as follows: The common name of “viologen” derives from Michaelis who noted the violet colour formed when 1,1’-dibenzyl-4,4’-bipyridinium underwent a one electron reduction to form a radical cation (as dimer). Then, the term “viologen” has been used widely to mean a compound or salt of anion X- and 4,4’-bipyridine to form 1,1’-disubstituted-4,4’-bipyridine (Fig. 4.1), regardless of its redox-state. The bipyridine group has one nitrogen atom per ring. The two pyridine rings are not always coplanar but are skewed with an inter-plane angle (dihedral angle) of certain degrees depending on their redox-state [33].

Because of the two nitrogen atoms, viologens have three redox-states: dication, radical cation and uncharged molecules. All three common viologen redox-states can be converted into each other in an electrochemical environment by two single electron transfer reactions. The bipyridinium dication is the most stable of the three common redox forms, and is the usual starting material for a study.

In fact, the solution and surface electrochemistry of viologens is well documented in the literature [32-33,133-136]. In this thesis, we continue examining the surface redox chemistry and the related phase behavior of an adsorbed viologen by using a combination of CV and STM measurements. The viologen of choice is 1,1’-dibenzyl-4,4’-bipyridinium molecule, abbreviated as DBV.

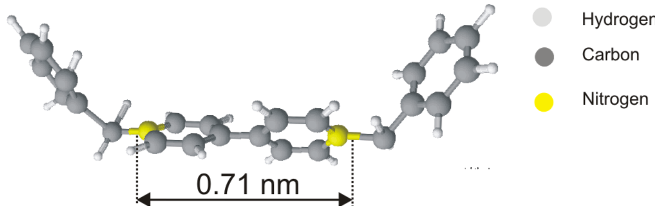

Figure 4.5: The chemical structure of DBV molecule.

The chemical model of DBV molecules is displayed in Fig.4.5. The core of the molecules consist of a 4,4'-bipyridinium group with an intramolecular distance of 0.71 nm between the nitrogen atoms, and the extra methylene group separates the phenyl groups from the central bipyridinium unit, forming two benzyl groups as outer ligands. Due to the methylene groups as connectors, the outer chain of DBV molecules can bend as shown in Fig.4.5, and the total length of isolated DBV molecules is about 1.55 nmm.

The quantum chemical optimization of the molecular viologen structures of the redox-states in the gas phase, done by Kirchner and Kossmann [137,138], shows that the DBV^{2+} exhibits a pronounced non-zero interplanar dihedral-angle between the two pyridinium rings of $\Phi(DBV^{2+}) = 40.11$. The same is observed after the reduction of the isolated DBV^{2+} to the corresponding radical mono-cation with a resulting dihedral angle $\Phi(DBV^{\bullet+}) = -5.41$ (Fig.4.6). For the uncharged DBV^0 molecule the dihedral angle is close to zero with $\Phi(DBV^0) = -0.11$.

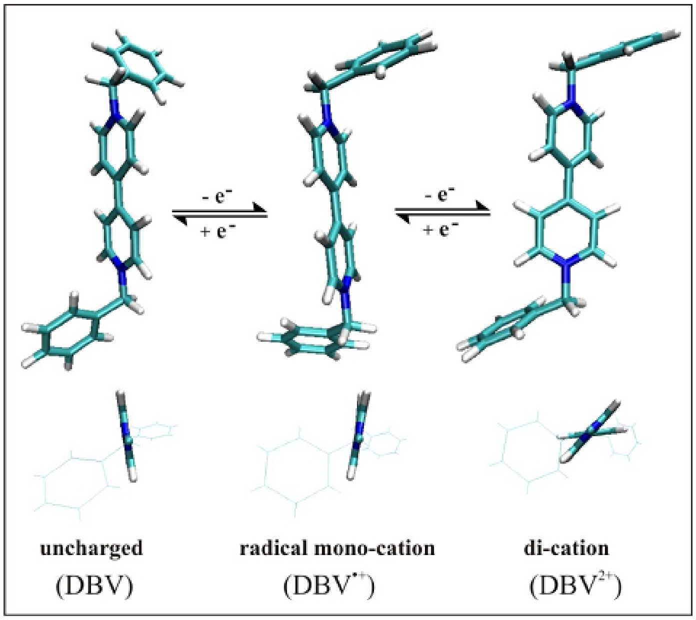

Figure 4.6: DFT based structure optimization of the isolated DBV^{2+}, $DBV^{\bullet+}$ and the uncharged DBV^0 molecules according to ref.44.

The different redox-states of the DBV molecule are expected to result in phase transitions on the chloride modified Cu(111) surface, similar to those taking place on Cl/Cu(100) [138-140].

Chapter 5

Self assembly of phthalocyanine molecules on an I/Cu(100) electrode: In-situ STM and ex-situ XPS studies

5.1. Introduction

It is well known that all phthalocyanine derivatives (Pcs) are insoluble in aqueous solutions. Hence, it is impossible to get information on their electrochemistry and adsorption in this environment. Most studies regarding electrochemistry of the phthalocyanines were therefore carried out in non-aqueous solutions [11-12]. It is found that these molecules are in principle reducible at their ligands and/or central metals in several reduction steps in order to form the corresponding reduced species. Likewise, self-assembly of the phthalocyanines was well studied and documented in the literature mostly in UHV environment [7-10]. However, there are only few reports on ordering of the phthalocyanine molecules in electrochemical environment because of the low solubility of many Pcs in polar solvents [13,128]. Although, Itaya’s group has published some reports on zinc-phthalocyanine self-assembled structures formed on an Au(111) surface in $HClO_4$ electrolyte by immersing the substrate into a benzen solution containing ZnPc molecules [14], but they just restricted the electrode potential to the positive range. Therefore, information about the adlayer structures of the phthalocyanine in the regime of reduction potentials is still lacking.

In order to improve the solubility of phthalocyanine derivatives, the soluble phthalocyanine has been successfully synthesized, termed as 2,3,9,10,16,17,23,24-Octa(3-(N'-methyl)-pyridyloxy)-5,28:14,19-diimino-7,12:21,26-dinitrilotetrabenzo(c,h,m,r) (1,6,11,16) tetraazacycloeicosinato (2-)-N29,N30,N31,N32 zinc(II) (abbreviated as $[ZnPcPyMe]^{4+}$) by the group of Prof. Torres in Madrid. Therefore, for the first time the molecular electrochemistry and self-assembly can be investigated in acidic solution environment.

In this contribution, ex-situ XPS is employed to determine the adsorption of the molecules on the electrode surface via the nitrogen signal. But also in-situ STM as a structural sensitive local probe technique is used to provide direct images of the adsorbed phthalocyanine films on the surface.

It was proven in the literature [141-142] that the dissolution of the central metal atoms out of the central phthalocyanine cavity can take place once the metal phthalocyanine complexes are dissolved in acidic solvents resulting in the formation of the respective metal-free complexes. Metal removal of $[ZnPcPyMe]^{4+}$ molecules in the sulfuric acid media used here, therefore, also occurs in order to form the corresponding $[H_2PcPyMe]^{4+}$ molecules. In order to prove this, a measurement of the Zn-2p signal is carried out by employing the XPS measurement. As a consequence the present CVs and STM measurements refer to the $[H_2PcPyMe]^{4+}$ molecules instead of the $[ZnPcPyMe]^{4+}$ precursor.

As mentioned in section 4.2, in solution these molecules are reduced by four single- electron transfer steps in order to form the respective reduced products owing to the doubly degenerated e_g symmetry in the π-ring system. In case of $[H_2PcPyMe]^{4+}$ used, due to the electron withdrawing by eight N-methyl-pyridyl substituents on four peripheral benzene rings, the π-electron system of the $[H_2PcPyMe]^{4+}$ ring is delocalized leading to a lowering of the energy levels for the LUMO of pyrrolic macrocycles. The $[H_2PcPyMe]^{4+}$ molecules, therefore, are easy to reduce in acidic media in order to form the corresponding cationic radicals. Hence, within the potential window of copper (from -450 mV to +300 mV vs RHE) at least the first reduction step of free base phthalocyanine, i.e. $[H_2PcPyMe]^{4+}$, to the corresponding reduced products are expected to be observe by both CVs and STM measurements.

The aim of this chapter is, therefore, to study the metal core dissolution in acidic solution, the electrochemical behavior and the adsorption of $[H_2PcPyMe]^{4+}$ molecules on an iodide modified Cu(100) electrode surface under non-reactive and/or reactive conditions.

5.2. Molecular adsorption determination by XPS spectra

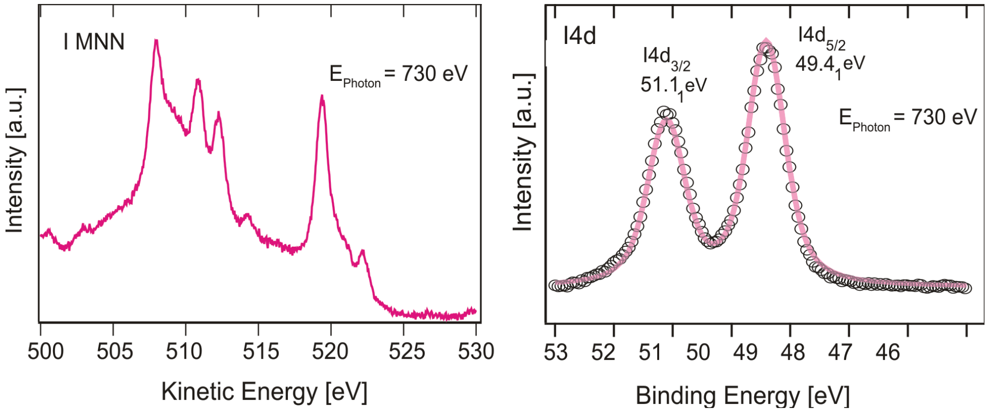

Figure 5.1: a) The I MNN Auger signal of chemisorbed iodide on Cu(100). b) The I4d XPS spectrum of the same sample. Both spectra are recorded with E_{Photon} = 730 eV. The emersion out of the electrolyte has been performed at E = –150 mV vs. RHE.

We have combined the EC-STM studies with SXPS (Synchrotron Photoelectron Spectroscopy) in order to investigate the adsorption of $[ZnPcPyMe]^{4+}$ molecules on a chemisorbed iodide monolayer on Cu(100). Prior to the adsorption of the phthalocyanine, the sample was cycled in 1 mM KI/50 mM H_2SO_4 electrolyte until a steady state CV has been obtained. The electrolyte has been exchanged under potential control at –150 mV vs. RHE by the phthalocyanine containing solution (0.5 mM $[ZnPcPyMe]^{4+}$/1 mM KI/50 mM H_2SO_4). After 10 min. of adsorption at –150 mV the sample was emerged out of solution and the solution residue on the surface was blown away with dry argon gas and then transferred to UHV under Ar-atmosphere. Thus, there is no hint of a drying-up residue which should be indicated by a K2p signal in the XP-spectra.

Photon energies of 245 eV, 730 eV and 1200 eV have been used for the systematic variation of the excitation and the related escape depth of the photoelectrons. The following XPS analysis relies on the assumption that the chemical composition of the interface does not alter upon emersion and transfer to the UHV except the evaporation of water.

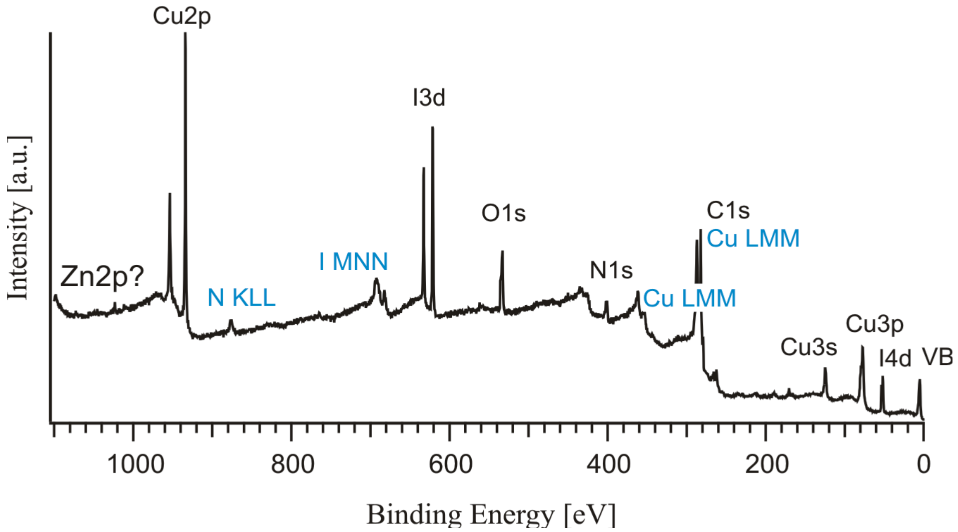

Figure 5.2: Survey spectra of the sample at E_{Photon} = 1200 eV.

The samples have been prepared analogously to the EC-STM experiments. The underlying monolayer of chemisorbed iodide has been identified by the I4d signal and the IMNN Auger signal (Fig.5.1). The Auger signal has been acquired in the XPS detection mode, hence the derivative of this signal does not need to be presented. These signals conform to the data of chemisorbed iodide that are reported by Huemann et al. [54].

Fig.5.2 shows the survey spectrum obtained at photon energies of 1200 eV. These spectra show the typical signals of copper, carbon (note, that in the spectra obtained at 1200 eV the C1s signal is superimposed by the CuLMM Auger signal.), oxygen and nitrogen. Astonishingly there are sulphur signals obvious, but neither an adequate Zn2p ($E_B(Zn2p_{3/2})$ = 1022 eV nor a Zn3p ($E_B(Zn3p_{3/2})$ = 89 eV [143] signal.

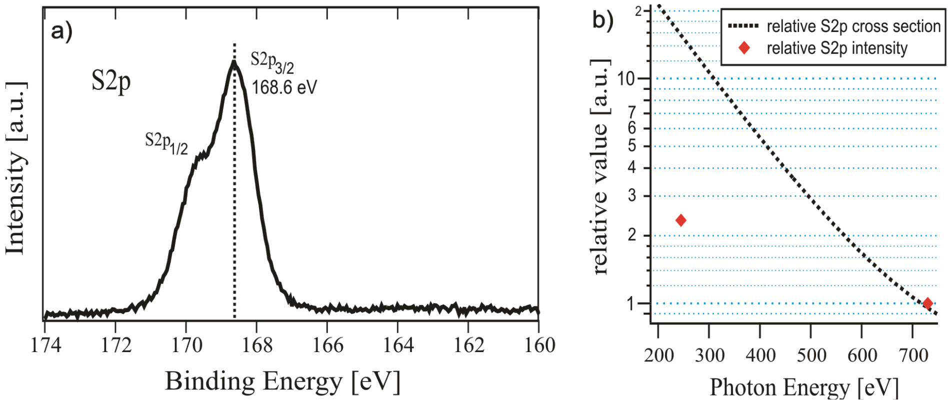

Figure 5.3: a) The S2p detail spectrum. E_{Photon} = 730 eV. The binding energy indicates the presence of coadsorbed sulfate ions. The spectrum has been measured after approximately one minute of irradiation, hence the signal does not show a considerable decomposition of sulphate. b) The S2p signal intensity measured at E_{Photon} = 245 eV and E_{Photon} = 730 eV and atomic photoionization cross section. The values have been normalized to the values at E_{Photon} = 730 eV.

The sulphur signal showing up in Fig.5.3a appears at a binding energy of 168,6 eV ($S2p_{3/2}$) indicating the adsorption of sulphate ions [143]. Thus, the signal can be assigned to the coadsorption of sulphate anions from the electrolyte (50 mM sulphuric acid) within the positively charged phthalocyanine layer. An adsorption of the sulphate anions on the topmost layer can be ruled out due to a comparison of the integrated signal intensities and the atomic photoionization cross sections [144]. The integration is done, after Tougaard background subtraction from 160 eV to 173 eV covering the whole S2p spectrum, because sulphate tends to decompose to reduced species (e.g. sulphite) during an electron beam exposure or the photoelectron flux [145-146] based on synchrotron irradiation. Fig5.3.b shows the photoionization cross section of the S2p signal and its intensity measured with photon energies of 730 eV and 245 eV (red dots). Both the cross sections and the signal intensities are normalized to their values at 730 eV. If the sulphate anions adsorb on the topmost layer an increase of the signal intensity by factor 16 should be observed between the excitation energies 730 eV and 245 eV, but we observe only an increase by the factor 2,3. At an excitation energy of 245 eV the S2p photoelectrons have a kinetic energy around 75 eV, therefore the signal is very surface sensitive, signals arising from a position deeper than the topmost layer are highly damped. Hence, it is plausible that the coadsorbed sulphate anions are located within the organic layer. The coadsorption of the sulphate may be necessary for electroneutrality. Consequently, the O1s signal in Fig.5.2 (detail spectrum not shown here) originates from the ligand related oxygen atoms, the sulphate or its decomposition products and, probably, a water residue from the electrolyte.

The N1s detailed spectrum (Fig.5.4a) can be split up into four contributions and shows also some features which are not in agreement with a zinc phthalocyanine. The $[ZnPcPyMe]^{4+}$ which has been used in this study contains several pyridinium groups which are necessary for the water solubility of the phthalocyanine. We assign the signal contribution at 401,8 eV to the pyridinium groups. This assignment is in agreement with our work on viologens (4,4'-bipyridinium salts) [147]. Nilson et al. [148] have published XPS measurements of the zinc phthalocyanine which is deposited on InSb(001) in vacuum. They found only a single signal at 399,1 eV which shows a slight broadening with increasing coverage. In contrast, beside the contribution of the pyridinium groups, our spectrum shows three contributions at 400,8 eV, 400,2 eV and 399,1 eV. The latter one coincides with the contribution referred to by Nilson et al., but we assign it to a new unknown species which is formed due to beam damage after some time of irradiation as shown in Fig.5.4b. A similar phenomenon has also been observed in our previous work on viologens [147]. The signal at 400,2 eV is related to the aza-bridging nitrogens according to the work of Alfredsson et al. [149]. They have evaporated H_2Pc on a conducting glass substrate in UHV. We suppose a protonation of all pyrrolic nitrogen atoms or a degeneration caused by mesomerism that leads to a uniform signal. Consequently, we assign the signal at 400,8 eV to the pyrrolic nitrogen atoms, this binding represents also the mean value of the binding energies that Alfredsson et al. have reported for the distinguishable pyrrolic nitrogen atoms.

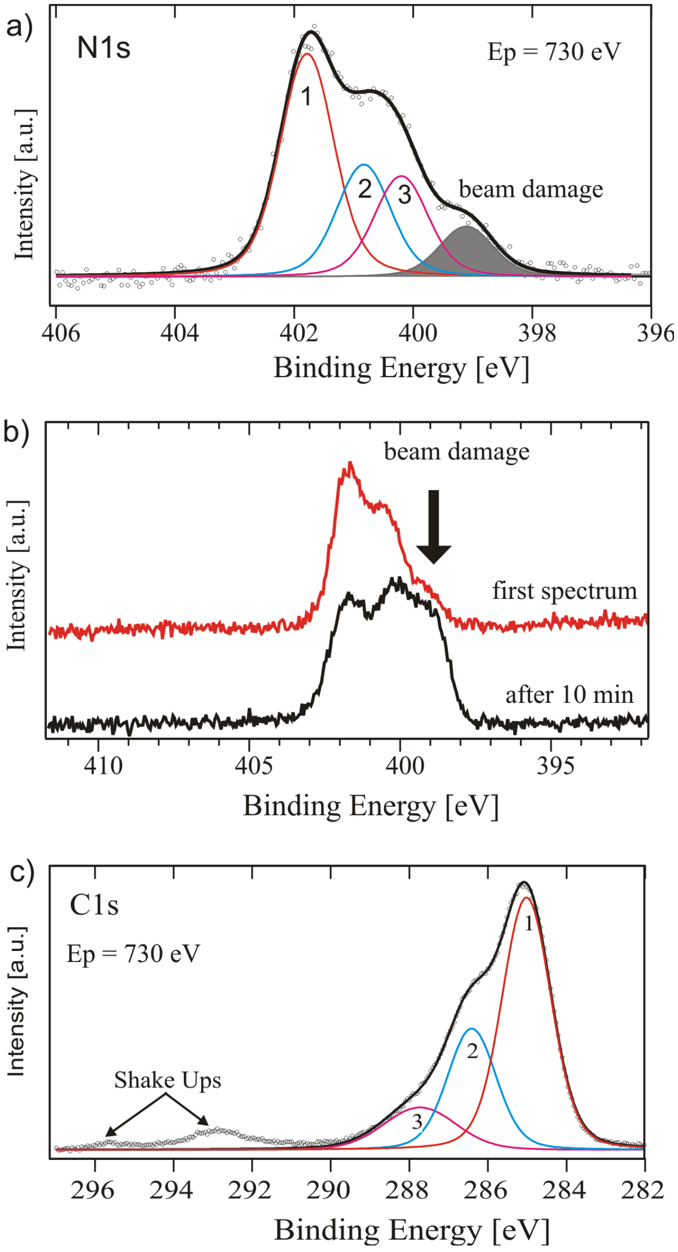

Figure 5.4: a) The N1s detail spectrum measured at E_{Photon} = 730 eV. The signal is split up into four contributions: **1**-E_B = 401,8 eV pyridinium groups, **2**-E_B = 400,8 eV pyrrolic nitrogen atoms, **3**-E_B = 400,2 eV aza-bridging nitrogen atoms. b) The amount of beam damage which causes a contribution at around 399 eV after 10 minutes of irradiation. c) The C1s detail spectrum measured at E_{Photon} = 730 eV. The positions of shake-up signals are marked by arrows. Due to several chemically not identical carbon atoms and the superposition with shake-up signals latter are not considered in the deconvolution.

As the N1s spectrum also the C1s spectrum (Fig.5.4c) can consists of contributions of different chemically inequivalent carbon atoms. The maximum at around 285 eV shows that there are contributions of benzene like carbon atoms. The shoulder at higher binding energies is caused by carbon atoms bonded to nitrogen or oxygen atoms. The analysis of the C1s spectrum is furthermore complicated by superpositions of shake-up process signals which are also described by Alfredsson for the simpler H_2Pc.

The XPS data indicate a replacement of zinc by hydrogen atoms in the acidic solution, because there is no zinc signal observable and a zinc replacement is also indicated by the contributions of the N1s spectrum. A coadsorption of sulphate ions within the organic layer has been observed and is possibly necessary in order to conserve electroneutrality.

5.3. Metal replacement mechanism in acidic environment

The most astonishing result is the absence of any zinc signals. Mass spectrometry (ESI+, data not shown here) of pure ZnPcPyMe has shown that it contains zinc, thus, we can exclude an *a-priori*-zinc-free phthalocyanine. The absence of the zinc in the adsorbed phthalocyanine layer can be explained by a replacement of the zinc by hydrogen atoms from the acidic electrolyte (pH value 1~2). This result is in complete agreement with literatures [141-142]. Caugrey et al. [141] have studied the stability of metalloetioporphyrin toward acids. They listed the relative rates of metal ion replacement in sulfuric-acetic acid solution and in hydrochloric-acetic acid solution as follows: Ni(II) < Co(II) ≅ Cu(II) << Zn(II). Furthermore, the solvolysis reaction of zinc porphyrin upon acid catalysis was reported by Hambright and his co-workers [142]. Consequently, the kinetics of dissociation of zinc porphyrin in acid solution was described by the following equation:

$$ZnP + 4H^{+} + 4X^{-} \rightarrow H_4P^{2+} + Zn^{2+} + 4X^{-}. \qquad (5.1)$$

And, at a constant acid concentration, the rates of Zn(II) displacement by hydrogen atoms were found to be in the relative order as follows [147].

$$\begin{array}{ccccc} \mathrm{HI} & \mathrm{H_2SO_4} & \mathrm{HNO_3} & \mathrm{HBr} & \mathrm{HCl} \\ < & < & < & < & \\ 1 & 8 & 85 & 186 & 675 \end{array} \qquad (5.2)$$

As a result, the ZnPcPyMe molecular precursors are converted into the corresponding free base H_2PcPyMe molecules in the course of dissociation. This means the molecules adsorbing on an iodide modified Cu(100) electrode surface in all presented measurements are metal free H_2PcPyMe instead of the Zn(II) complex.

In brief, XPS measurements provided precise information to confirm the metal replacement mechanism, taking place in acidic solutions. Thus, in the following sections, CVs and STM measurements actually refer to H_2PcPyMe molecules.

5.4. Electrochemistry of free base phthalocyanine ($[H_2PcPyMe]^{4+}$)

5.4.1. CVs of HOPG in $[H_2PcPyMe]^{4+}$ containing acidic solution

In the present work for the first time, the solution redox behavior of $[H_2PcPyMe]^{4+}$ complex is investigated by mean of cyclic voltammetry in sulfuric acid medium using a Cu(100) substrate as the working electrode.

In principle, the redox processes of metallophthalocyanines can occur at the ligand and the metal center [150-151]. The phthalocyanine ring can undergo successive one-electron reduction or oxidation to yield anionic or cationic radicals, respectively. Regarding the redox active metals, metal oxidation or reduction occurs at potentials between those corresponding to ligand reduction or oxidation. While ligand related reduction, i.e. $[MPc(-2)]^0 + e^- \leftrightarrows [MPc(-3)]^-$, is associated with the position of the LUMO, ligand related oxidation, i.e. $[MPc(-2)]^0 \leftrightarrows [M(II)Pc(-3)]^- + e^-$, is associated with the position of the HOMO [152]. With respect to $[H_2PcPyMe]^{4+}$ molecules, after zinc metal replacement, the redox processes can only involve the peripherical N-methyl-pyridyloxy groups, and the phthalocyanine ring itself. Because the redox processes influencing the peripherical pyridyl substituents take place at potentials lower than the cathodic limit of the narrow copper potential window, they are not considered in the following [30]. The redox processes, therefore, are just affected by the central phthalocyanine core involving maximum four single electron reduction steps in total and can be subdivided into several transfer steps.

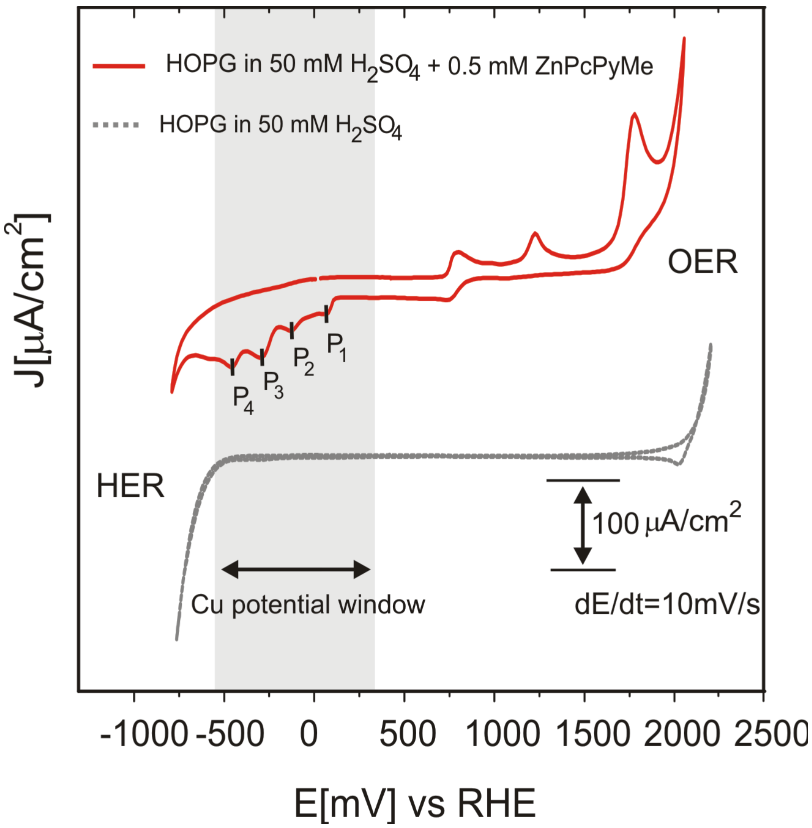

Figure 5.5: Cyclic voltammograms of HOPG exposed to pure supporting electrolyte (black curve) and phthalocyanine containing electrolyte (red curve); the grey regime indicates the respective copper potential window; dE/dt = 10 mV/s.

In order to identify more precisely the phthalocyanine related redox processes without influence of the copper dissolution reaction, an HOPG electrode was employed to measure such complementary voltammograms. It is pointed out that HOPG is an inert electrode surface with no specific anion adsorption on it. Therefore, any influence of anion ad- and/or de-sorption processes on the phthalocyanine-related electron transfer steps does not need to be taken into consideration on the HOPG electrode. The voltammetric curve of the HOPG in pure supporting electrolyte given in the black CV in Fig.5.5 exposes a much larger potential window for HOPG compared to that of copper.

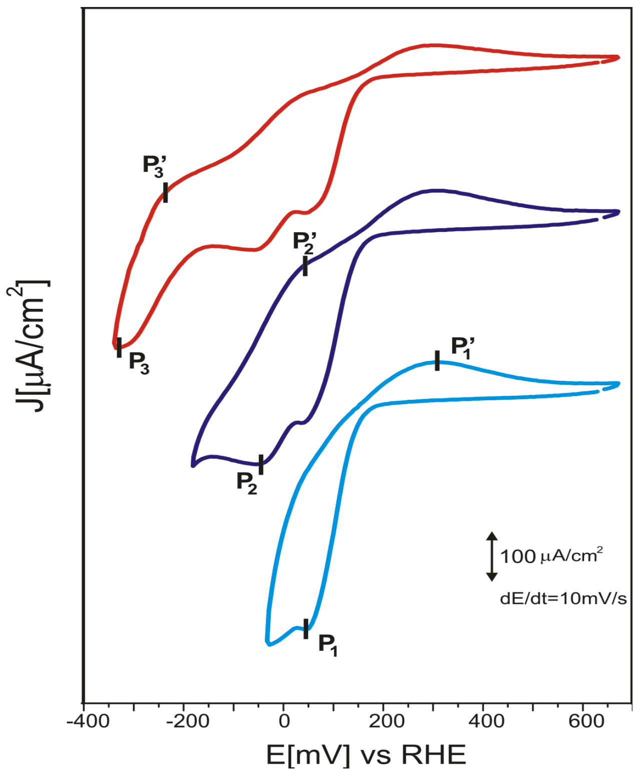

Figure 5.6: Scanning potential dependence of redox peaks of H_2PcPyMe on an HOPG electrode with the first three reversible redox processes being indicated, respectively; scan rate: dE/dt = 10 mV/s.

Several cathodic and anodic current peaks emerge in the red CV when the supporting electrolyte is replaced by the working one containing phthalocyanine molecules (50 mM H_2SO_4 + 1mM KI + 0,5 mM ZnPcPyMe). Our attention is directed to the reduction processes which take place due to the electron exchange between adsorbates and the underlying layer. Four reduction peaks labeled from P_1 to P_4 with their corresponding potentials at E = +89 mV, -98 mV, -260 mV, and -429 mV, respectively, are observed and are ascribed to four single electron transfer steps in total [11,146]. Herein, a (quasi) reversible pair of peaks P_1/P_1' with P_1' situated at E = +315 mV has been assigned to the diffusion controlled first one-electron transfer process. All further phthalocyanine reduction processes represented by peaks P_2-P_4 (red CV in Fig.5.5, Fig.5.6 and Fig.5.7) are in turn attributed to the next electron transfer processes. The potential dependent appearance of peaks is depicted in Fig.5.6 in which the intensities of peaks are equal, indicating that each pair of curves presents a reversible process concerning only a one electron transfer. This hypothesis is in good agreement with former reports [13].

5.4.2. CVs of copper in $[H_2PcPyMe]^{4+}$ containing acidic solution

Fig.5.7 describes cyclic voltammograms of a Cu(100) electrode in pure electrolyte and electrolyte containing $H_2PcPyMe$ molecules. A featureless CV is observed in case of pure electrolyte in contact with the Cu(100) electrode surface (black CV), whereas a drastic deviation appears in the CV of the Cu(100) either in iodide or in a mixture of iodide and the molecule containing electrolytes, respectively (blue and red CVs). The electrochemical behavior of the iodide adlayer and CuI film formation on the copper electrodes (the blue curve) were well documented in the literature, for detail see ref. [51-53] and papers cited therein.

Focusing on the CVs of a Cu(100) electrode in electrolyte containing mixed iodide and $H_2PcPyMe$ molecules as described by the red CV (Fig.5.7), it should be noted that individual reduction peaks are ill-defined compared to the corresponding HOPG CVs. For instance, peak P_1' disappears due to the exponential current of the copper dissolution peak (around +300 mV) and/or 3D-CuI formation [53], whereas peak P_1 coincidentally arises with the CuI dissolution peak. In addition, the second wave is located at somewhat more negative potential than in the HOPG curve. Furthermore, while peak P_3 is observed as a broad ill-defined curve, peak P_4 is located within the HER in both cases of the used electrolytes. Apparently, the oxidation peaks are too broad to determine their position precisely, or in other words they are nearly disappeared in the reverse (i.e. anodic) scanning. The molecule-anion interaction is proposed to cause the difference in the electrochemical behavior between the HOPG and the copper electrode. In addition, the pH concentration used (≈ 1) also drastically impacts on peak intensities, namely the curve amplitudes become smaller as the pH decreases [13]. Lever et al. reported on voltammetric studies of tetrasulphonated phthalocyanines (MTsPc) in aqueous solutions. They pointed out that the voltammetric peaks are as a function of the pH as follows: the lower the pH concentration is the less defined the peaks are. Especially, when the pH is lower than 4, some curves become too broad or even disappear [13].

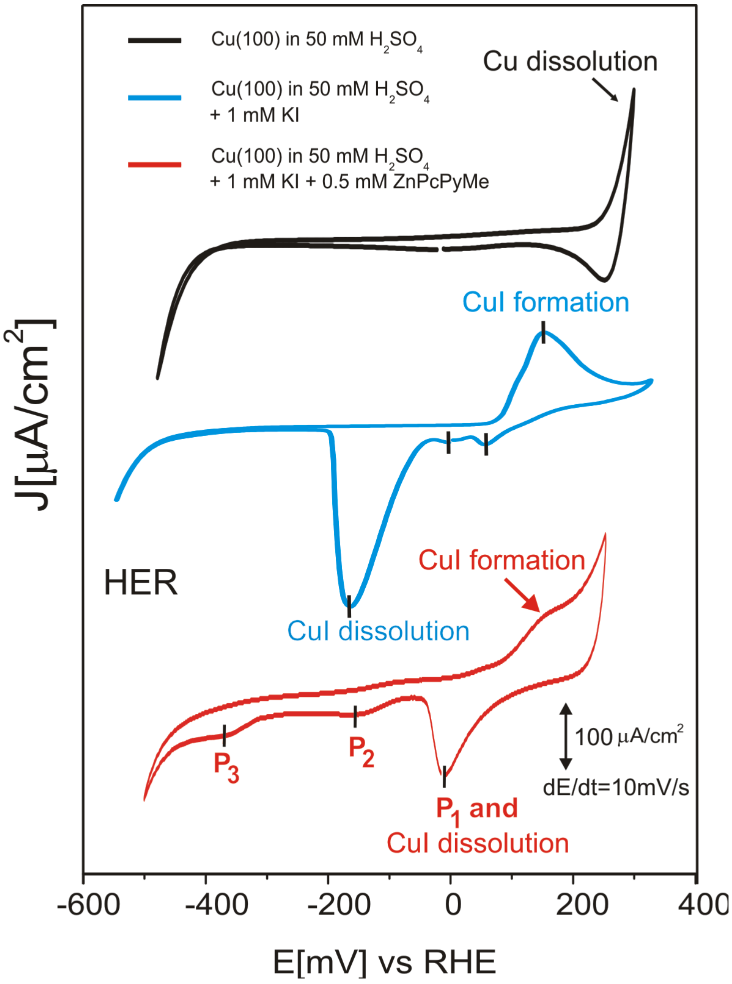

Figure 5.7: Black curve: CV of Cu(100) in pure supporting electrolyte (50 mM H_2SO_4); Green curve: CV of Cu(100) in $[H_2PcPyMe]^{4+}$ containing electrolyte (50 mM H_2SO_4 + 0.5 mM $[H_2PcPyMe]^{4+}$); Red curve: CV of Cu(100) in electrolyte containing a mixture of iodide and phthalocyanine (50 mM H_2SO_4 + 1 mM KI + 0.5 mM $[H_2PcPyMe]^{4+}$); dE/dt = 10 mV/s.

On the basis of these results, it can be assumed that phthalocyanine molecules react once the copper electrode is brought into contact with the electrolyte containing phthalocyanine. As a consequence, the molecules are always in a reduced state within the potential window of the copper where most of the STM experiments on Cu(100) were carried out.

5.4.3. Discussion

According to the simple Hueckel-Theory, the lowest unoccupied molecular orbital (LUMO) of phthalocyanine has a doubly degenerate e_g symmetry and can therefore accept up to four electrons of the π-ring system in the electroreduction processes [154-155]. The electrochemical behavior of the phthalocyanine depends, on the one hand, on side groups or central metals [152,156] and, on the other hand, on the kind of solvent [157-158] and pH [13]. In order to study the influence of the solvent on the electrochemistry, A.B.P. Lever and his coworkers investigated the electrochemical behavior of some metallophthalocyanines in different solvents such as dimethylformamide (DMF), dimethylsulfoside (DMSO) and pyridine. It was found that this property depends on the donicity number (DN) of the solvents [157]. In addition, the pH dependent redox processes were also studied by Zagal et al. [159] and Brown et al. [160]. Furthermore, substitution of nucleophilic and/or eletrophilic side groups on tetrapyrrolic macrocycles may induce significant changes of the energy required for transfer electrons. Giraudeau et al. [128,153] examined the effect of electron-withdrawing substituents on the reduction processes of the phthalocyanine molecules in the dimethylformamide (DMF) medium. The results showed that in case of cyano (CN) substituents, they decreased the average electron density on the total conjugated system resulting in a lowering of the energy levels of the LUMO of pyrrolic macrocycles. The electron affinity of the macrocycles, therefore, increases from a thermodynamics point of view and thus, leads to an easier reduction [161-162]. Koca and his co-workers [152] reported on the electrochemical behavior of various metal-phthalocyanines in dichloromethane (DCM) solvent. Their studies show that copper-, zinc- and, lead-phthalocyanines give ligand-based, diffusion controlled, multi-electron and reversible and/or quasi-reversible redox processes, whereas a cobalt-phthalocyanine complex gives both metal- and ligand-based, diffusion controlled, multi-electron and reversible and/or quasi-reversible reduction one.

In case of $[H_2PcPyMe]^{4+}$ used here, due to the electron withdrawing, eight N-methyl-pyridyl substituents on four peripheral benzene rings, the π-electron system of the phthalocyanine ring is delocalized leading to a lowering of the energy levels with respect to the LUMO of pyrrolic macrocycles similar to the CN substituents [128,153]. The phthalocyanine molecules, therefore, are easy to reduce in acidic media in order to form the corresponding anion radicals expressed by cathodic peaks in the potential window of HOPG and Cu(100) as well. This is supported by a remarkable upward deviation of the reduction potentials compared to that in case of unsubstituted molecules or/and with higher pH solvents used [13,152]. As a consequence, the $[H_2PcPyMe]^{4+}$ visibly undergoes four single electron transfer steps in order to yield the tri-, di-, mono-cation and the neutral species, respectively, as follows:

$$[H_2PcPyMe]^{4+} + e^- \leftrightarrow [H_2PcPyMe]^{3+} \quad (5.3)$$

$$[H_2PcPyMe]^{3+} + e^- \leftrightarrow [H_2PcPyMe]^{2+} \quad (5.4)$$

$$[H_2PcPyMe]^{2+} + e^- \leftrightarrow [H_2PcPyMe]^{1+} \quad (5.5)$$

$$[H_2PcPyMe]^{1+} + e^- \leftrightarrow [H_2PcPyMe]^{0} \quad 5.6)$$

As a consequence of these processes, structural phase transitions within the self-assembled layer of $H_2PcPyMe$ are expected to be observed in the potential window of copper due to the change in charge state and the concomitant modification of the adsorbate-template interactions. A detailed discussion of this matter will be given in the next section.

In the following, the adsorption of $H_2PcPyMe$ molecules on an iodide modified Cu(100) surface is studied with EC-STM.

5.5. Structural determination

5.5.1. Highly ordered self-assembled $[H_2PcPyMe]^{4+}$ adlayer

For the molecular adsorption, the pure supporting electrolyte (50 mM H_2SO_4) is replaced by electrolyte containing a mixture of iodide and phthalocyanine molecules at potential values within the double layer regime of the copper electrode, e.g. E = -50mV, leading instantaneously to the adsorption of the $[H_2PcPyMe]^{4+}$ molecules on the $c(p \times 2) - I/Cu(100)$ surface and the formation of a highly ordered monolayer as shown in Fig.5.8.

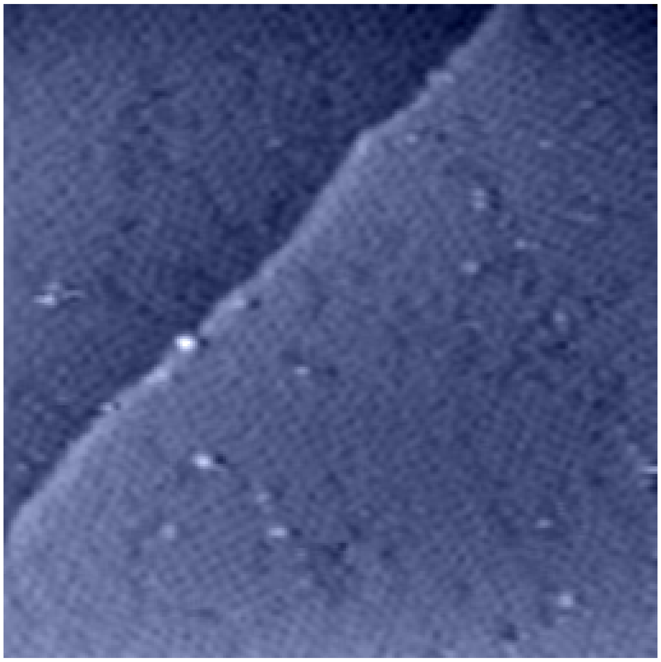

Figure 5.8: Laterally ordered 2D layer of $[H_2PcPyMe]^{4+}$ molecules on an iodide modified Cu(100) electrode; 88.62 nm x 88.62 nm, I_t = 0.15 nA, U_b = 480 mV, E = -100 mV.

As depicted in Fig.5.9a the $[H_2PcPyMe]^{4+}$ adlayer occurs in several rotational domains denoted as I and II enclosing an angle of 56 ± 2° with respect to each other. The molecular arrangement within the self-assembled layer is revealed in detail in Fig.5.9b,c. As a result, molecules are arranged in rows (dashed white lines) and all molecules within one row are rotated with respect to the row direction by an angle of 45 ± 2°. There are two pronounced phases observed, namely the square phase (Fig.5.9b) and the rhombic phase (Fig.5.9c). While a square shaped structure is observed in the former phase, a rhomb liked pattern is imaged for the latter. Individual molecules can be recognized as a black hole surrounded either by four bright square features or by four rectangular ones which are attributed to the pyridyl groups with flat-lying orientation. Possible models illustrating the arrangement of the $[H_2PcPyMe]^{4+}$ molecules on the iodide modified Cu(100) electrode surface are also proposed in the second half of Fig.5.9b and c. A reasonable interpretation for this observation is based on the difference in the electron density between the central cores and the ligands. It is likely that the electron density at the central cores of the $[H_2PcPyMe]^{4+}$ is lower than that at the ligands resulting in the formation of the visible dark holes compared to the bright contrasts of the ligands.

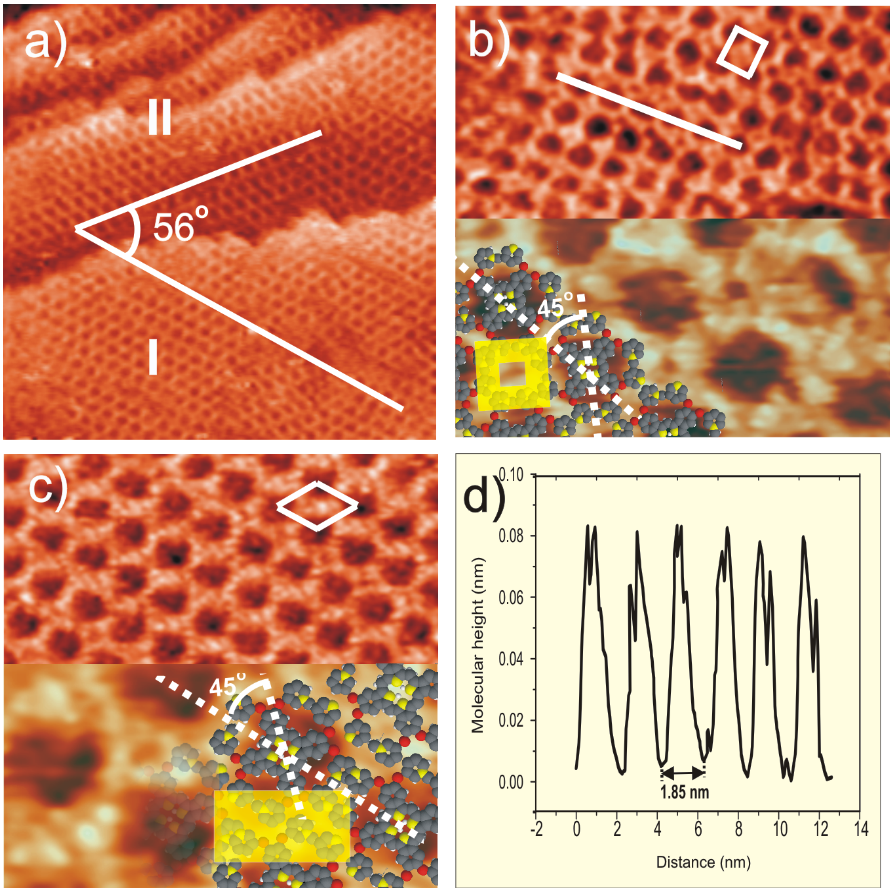

Figure 5.9: Surface morphology and atomic structure of Cu(100) in the presence of phthalocyanine molecules; a) Co-existence of rotational domains: 57.6 nm x 57.6 nm, I_t = 0.15 nA, U_b = 370 mV, E = -100 mV, b) Upper part : typical square lattice STM image of phase A: 24.8 nm x 12.4 nm, I_t = 0.2 nA, U_b = 370 mV, E = -100 mV; Lower part: molecular resolution of phase A with the proposed molecular model: 7.82 nm x 13.91 nm, I_t = 0.2 nA, U_b = 370 mV, E = -100 mV. Yellow square indicates the square like shape observed. c) Upper part: typical rhombic pattern STM image of phase B: 19.5 nm x 9.9 nm, I_t = 0.15, U_b = 360 mV nA, E = -100 mV; Lower part: molecular resolution of phase A with the proposed molecular model: .82 nm x 13.91 nm, I_t = 0.15 nA, U_b = 360 mV, E = -100 mV. Yellow rectangle indicates the square like shape observed d) Line profile recorded along the white line shows an intermolecular distance of 1.85 ± 0.1 mm.

The ordering of the $[H_2PcPyMe]^{4+}$ on the I/Cu(100) substrate is governed by a combination of intermolecular van der Waals interactions and hydrogen bonding [163] originating from the substituted functional pyridyl groups. The hydrogen bonding, based on the interaction between hydrogen atoms locating at the methyl groups and nitrogen atoms on the pyridyl groups of adjacent molecules, play a crucial role for the ordering of molecular networks. This has been affirmed for the role of substituted groups in the self-assembly of molecular adlayers [164]. The intermolecular distance measured by the line profile in Fig.5.9d is about 1.85 ± 0.1 nm.

A detailed structural correlation between the $[H_2PcPyMe]^{4+}$ adlayer and the iodide lattice underneath could be achieved by a careful adjustment of the tunneling conditions [138,140]. Two STM images of 14.4 nm^2 for phase A were successively recorded at the same surface area using different tunneling conditions as shown in Fig.5.10. Under moderate tunneling conditions, i.e. at low tunneling current and high bias voltage, the $[H_2PcPyMe]^{4+}$ film is imaged with high submolecular resolution (Fig.5.10a). In turn, the underlying iodide lattice becomes clearly visible by applying more drastic tunneling conditions, i.e. low bias voltage and high tunneling current. In this case, the tunneling tip penetrates into the organic adlayer which leads to the local removal of the phthalocyanine molecules during scanning (Fig.5.10b). This experiment suggests that an interaction between the phthalocyanine adlayer and the iodide lattice is weaker than the chemisorptive Cu-I interaction that can not be broken by the tunneling tip [139]. From these results, a direct correlation between the organic overlayer and the iodide lattice underneath can be obtained. Consequently, the molecular rows do not run parallel to the [011] commensurate orientation of the iodide interlayer which is aligned along the close-packed atom rows of the Cu(100) substrate. This clearly excludes a template effect of the substrate surface, but rather hints to a molecular self-assembly. Interestingly, the angle between close-packed molecular row and the [011] substrate direction of about 28° is one half compared to the angle between rotational domains indicating that these two rotational domains (I and II) are two mirror domains. Taking the four-fold symmetry of the (quasi) square substrate lattice into account, two more rotational $[H_2PcPyMe]^{4+}$ domains rotated by 90° are expected. Consequently, the $H_2PcPyMe$ molecules self-organize into four possible rotational domains on the iodide pre-adsorbed Cu(100) surface (plus translational domains within them) [31].

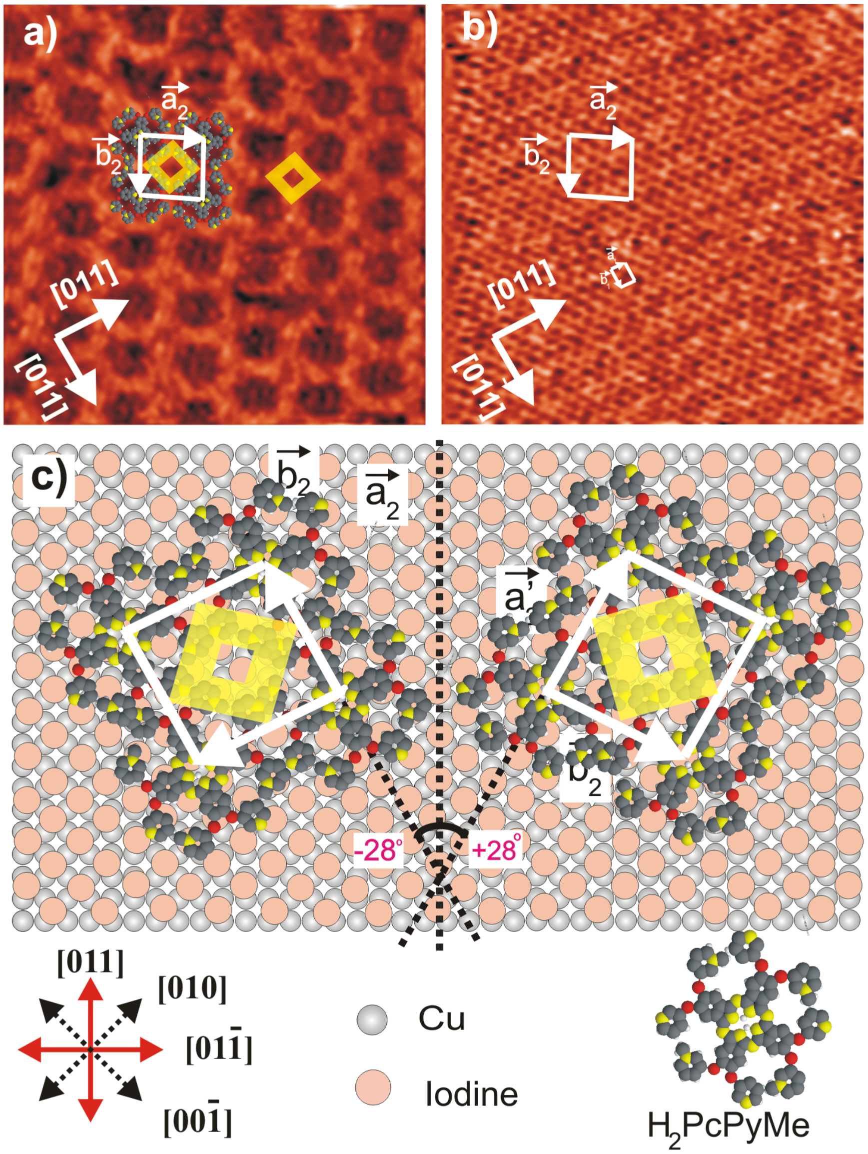

Figure 5.10: Structural correlation of phase A between the $[H_2PcPyMe]^{4+}$ layer and the underlying iodide lattice by a systematic variation of the tunneling conditions, a) 14.4 nm x 14.4 nm, I_t = 0.3 nA, U_b = 353 mV, E = -110 mV; b) 14.4 nm x 14.4 nm, I_t = 1.8 nA, U_b = 25 mV, E = -100 mV; c) Tentative structure model of the $[H_2PcPyMe]^{4+}$ quasi-square phase on I/Cu(100) with two mirror domains.

On the basis of a graphical superposition of the two STM images in Fig.5.10a and b of phase A, a unit cell of the $[H_2PcPyMe]^{4+}$ adlayer can be described either by a $\begin{vmatrix} 3 & 3/2 \\ -3/2 & 3 \end{vmatrix}$ transformation matrix or by a $(\sqrt{45/4} \times \sqrt{45/4})R28°$ unit cell in Wood-notation with respect to the $c(p \times 2)$-I lattice and contains one molecule. The lattice constants are also determined with $|\vec{a}_2| = |\vec{b}_2| = 1.81$ nm enclosing an angle of $91 \pm 2°$ for the case of $c(p \times 2)$-I phase with p=2.5. Based on this result, a tentative structure model of the phthalocyanine adlayer on the I/Cu(100) substrate is proposed in Fig.5.10c. The molecular surface coverage is also calculated to be about 0.048 ML related to the iodide underneath, or 3.04×10^{13} molecules/cm^2.

Similarly, Fig.5.11 presents such a correlation of phase B between the $[H_2PcPyMe]^{4+}$ molecular overlayer (Fig.5.11a) and the underlying iodide lattice (Fig.5.11b) at a molecular level. On the basis of the c(p x 2)-I phase serving as internal calibration lattice we could calculate the unit cell containing two $[H_2PcPyPMe]^{4+}$ molecules either by a $\begin{vmatrix} 4 & 0 \\ 1/2 & 9/2 \end{vmatrix}$ transformation matrix or by a $(3\sqrt{2} \times 3\sqrt{2})R28^o$unit mesh with lattice constants of $|\vec{a}_2| = 2.05$ nm and $|\vec{b}_2| = 2.89$ nm, respectively. The surface coverage for the phase B is about 3.37×10^{13} molecules/cm^2 indicating that the phase B is about 10% more condensed than phase A. A possible structural model for the phase B is also proposed in Fig.5.11c describing a rhombic pattern derived from a contraction of the square lattice in phase A along the [011] direction resulting in the formation of the corresponding rectangular shaped protrusions (yellow rectangle) as observed by STM images (Fig. 5.9b and Fig.5.11a). Obviously, such a change of the molecular position adsorbing on the iodide lattice leads to the observed modification of the phthalocyanine adsorbed structure.

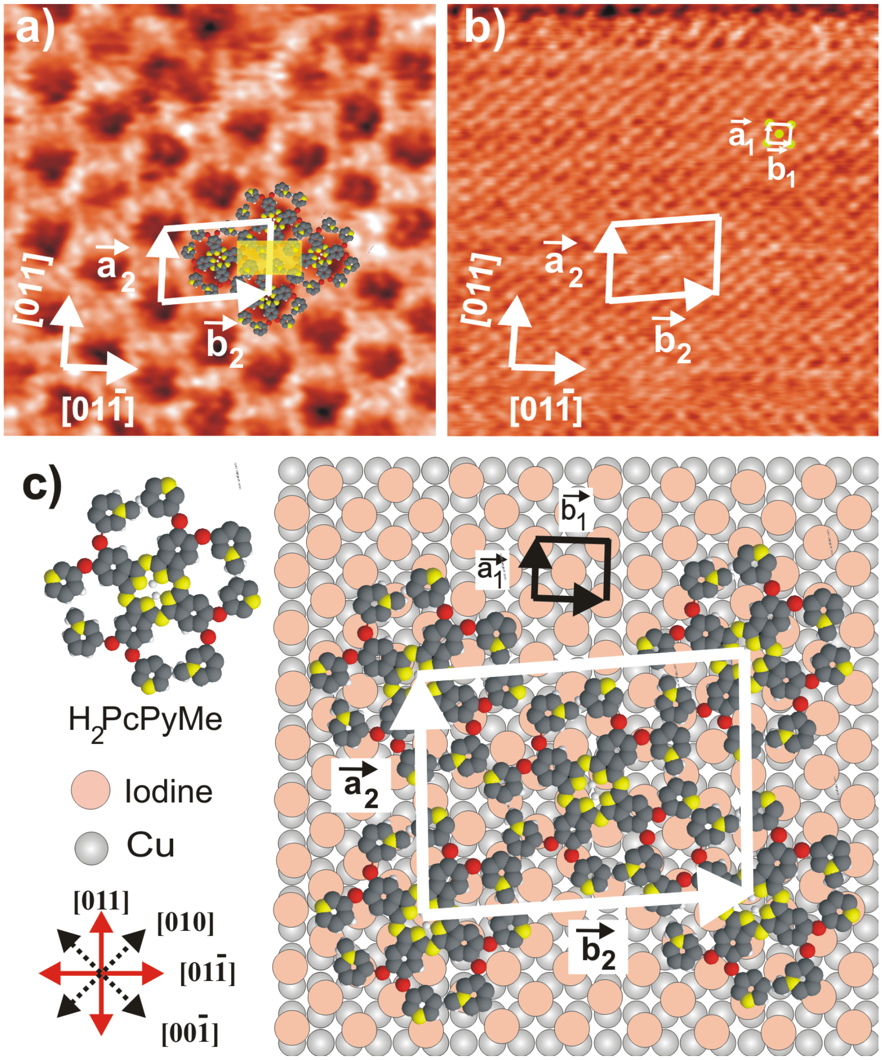

Figure 5.11: High resolution STM images describing the relation between the $[H_2PcPyMe]^{4+}$ molecular overlayer and the iodide lattice underneath in phase B, a) 14.4 nm x 14.4 nm, U_{bias} = 400 mV, I_t = 0.15 nA, E = -100 mV; b) 14.4 nm x 14.4 nm, U_{bias} = 25 mV, I_t = 1.8 nA, E = -100 mV; c) possible sphere model of the molecular adsorption for phase B.

In order to explain the occurrence of two different phase A and B the following hypothesis is proposed for discussion (see Fig.5.12). It is well known that the c(p x 2)-I structure forming on the Cu(100) electrode surface reveals a wave-like modulation [154,167-168] with a wave-length 2p times as long as the Cu-Cu distance (see Fig.3.4 in chapter 3). Assuming that ten nearest molecules numbered from 1 to 10 populate positions as depicted in Fig.5.12, namely molecules 1 and 2 are located at the crest of the waves H1 and H2, while the lower wave valleys (L1,L2) are assigned to the locations of molecules 3 and 4. This order is successively repeated with respect to molecules 5-6 resulting in the formation of the observed square phase (phase A). However, instead of lying at the expected positions i.e. at the wave bases L2 and L3 as describing by diffuse molecular markers, molecules 7 and 8 are shifted perpendicularly with respect to the molecular rows by half a molecular distance resulting in their locations on the crest of waves (H3 and H4) as depicted in Fig.5.12. This reordering is repeated by the molecules 9 and 10 etc. Consequently, the square phase (phase A marked by blue unit cell) is distorted into a rhombic structure (phase B denoted by yellow unit cell). In brief, molecules in a close packed row forming the phase A are arranged in the order: H-L-H (or L-H-L), whereas the phase B formation obeys a H-H-H (or L-L-L) ordering.

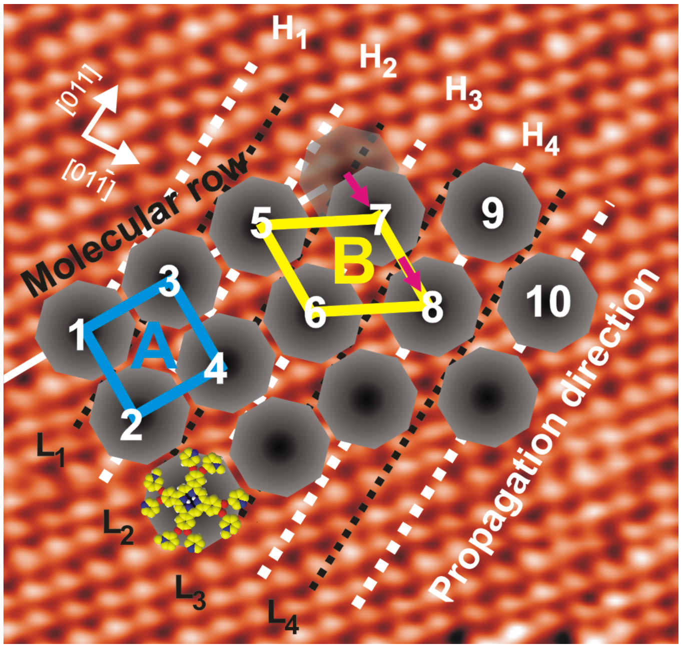

Figure 5.12: Illustrative model for the formation of the respective phase A and phase B. While the square phase (phase A) is formed with an order of L-H-L (or H-L-H), the rhombic phase (phase B) originates from H-H-H (or L-L-L) ordering.

5.5.2. Co-adsorption of sulfate anions

As mentioned above, co-adsorption of sulfate anions within the phthalocyanine adlayer is suggested by XPS results via the S2p signal and suggested by the conservation of electroneutrality. Interestingly, this phenomenon is clearly observed at an atomic level by the EC-STM results. Indeed, the sulfate anions are observed surrounding the phthalocyanine molecules marked by white arrows in Fig.5.13. This assignment is supported by the fact that the iodide underlayer is basically uncharged, hence, the topmost cationic molecular adlayer, which holds an excess of charge in the side groups, seeks for charge neutrality by capturing anions from the working electrolyte. As a result, the SO_4^{2-} anions are fixed between the molecular propeller-blades rather than at the free areas on the surface. In addition, there is no SO_4^{2-} anion adsorption on-top of the phthalocanine molecules. This is supported by the high resolution STM images which are almost smooth and show no bright dots on the molecules. This observation is also consistent with the XPS results suggesting that the coadsorbed sulfate anions are located within the organic adlayer.

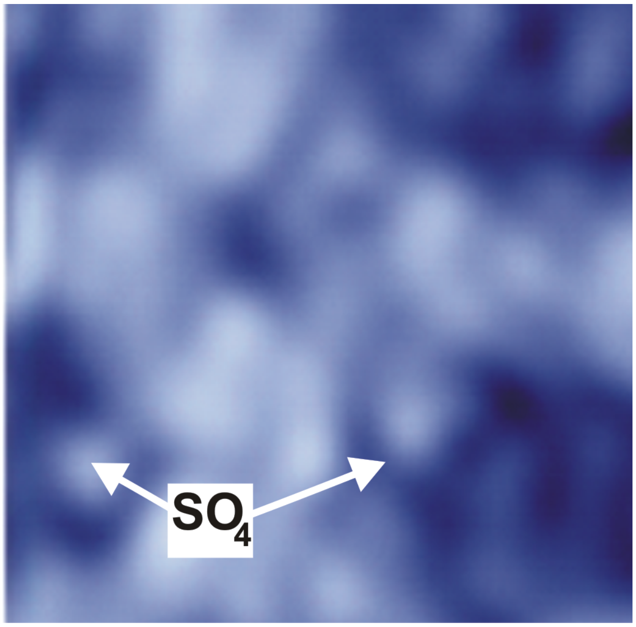

Figure 5.13: Co-adsorption of $[H_2PcPyMe]^{4+}$ molecules and SO_2^{-4} anions (bright dots) on an iodide modified Cu(100) electrode surface in order to neutralize the adsorbate layer charge; 2.75 x 2.75 nm, I_t = 1.8 nA, U_b = 25 mV, E = -100 mV.

4.5.3. Charge induced adsorption probability

We also investigated the adsorption ability of another kind of phthalocyanine, namely an uncharged molecule (abbreviated as ZnPcPy, its chemical structure is shown in Fig.4.2 but without the outer CH_3 groups) for comparison with that of $[H_2PcPyMe]^{4+}$ molecules. The aim of this section is, therefore, to study the influence of the molecular charge on the molecular adsorption characteristics. The same preparation process is applied for the CVs and the STM investigations. In this section, only STM results are used to compare the adsorption possibility of $[H_2PcPyMe]^{4+}$ versus H_2PcPy molecules. In the center the Zn central metal has been replaced by hydrogen atoms in the course of dissolution, as discussed in section 5.4.3.

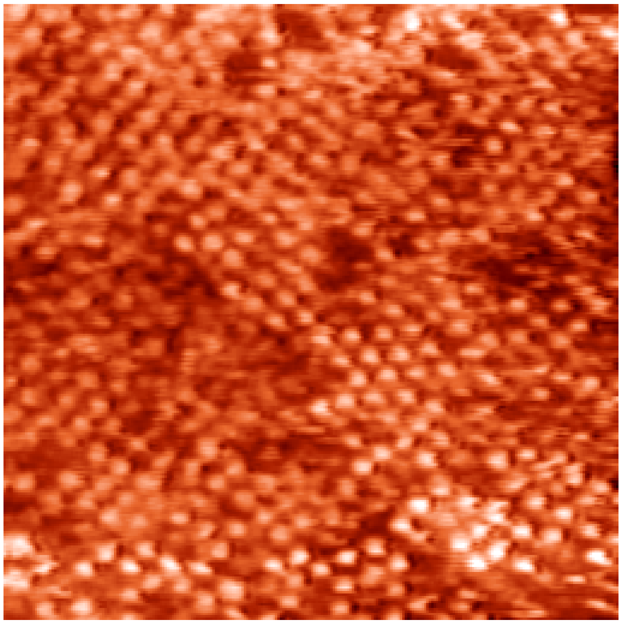

Figure 5.14: Large scale STM image showing a relatively mobile adlayer of H_2PcPy molecule on an iodide modified Cu(100) due to weak interactions between the adsorbates and the underlying iodide lattice; 57.62 x 57.62 nm, I_t = 0.15 nA, U_b = 510 mV, E = -40 mV.

Figure 5.14 presents a typical STM image of H_2PcPy molecular self-assembly on an iodide modified Cu(100) electrode surface. The top layer is observed as a disordered layer even after several hours exposure indicating a weak interaction between the adsorbate and the underlying lattice. It can be seen that the H_2PcPy molecules are laterally not well ordered on the surface. The molecules are only weakly physisorbed because the iodide layer is well known as an uncharged layer, hence, electrostatic interaction between the first adlayer and the iodide underneath does not play a dominant role. As a result, only the hydrogen bonding and van der Waals interactions assumed to govern the molecular adsorption process are not strong enough to stabilize 2D self-assembled ordering.

In order to demonstrate the role of electrostatic interactions in lateral ordering of the molecular adlayer, a chloride layer is employed instead as the template for H_2PcPy adsorption. Chloride anions are well known to form a negatively charged c(2 x 2) superstructure on the Cu(100) electrode surface facilitating the adsorption of organic cations. Therefore, H_2PcPy adsorption was also carried out in 10 mM HCl solution.

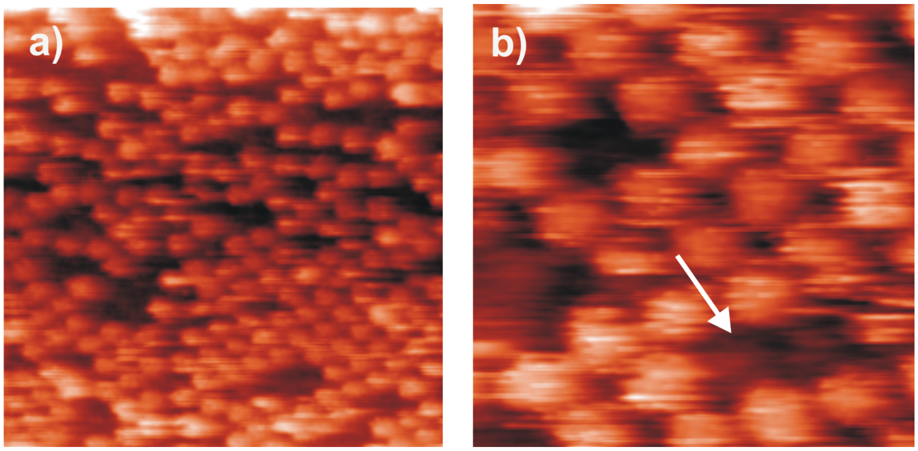

Figure 5.15: Typical medium and high resolution STM images showing an H_2PcPy layer on a chloride terminated Cu(100):a) 43.21 x 43.21 nm, I_t = 0.1 nA, U_b = 360 mV, E = 0 mV; b) 14.4 x 14.4 nm , I_t = 0.1 nA, U_b = 280 mV, E = 0 mV.

Typical large scale and high resolution STM images for the adsorption of H_2PcPy molecules on a chloride terminated Cu(100) electrode surface are displayed in Fig.5.15. It can be seen that the H_2PcPy adsorbates are still rather mobile and only moderately ordered regardless of the negative charge excess on the template. However, the adsorbed molecules are arranged in small domains surrounded by random arrangements (Fig.5.15a). A close view into the ordered domains show a square lattice with individual molecules appearing in sphere shape as observed in Fig.5.15b. Obviously, destabilization hinders a direct visualization by the STM. Consequently, instead of a flat lying and propeller shaped appearance the H_2PcPy molecules appear as round and noisy dots. Also defects appear on the surface marked by white arrows due to a displacement of mobile molecules during scanning.

On the basis of the observed results, it can be concluded on the important role of electrostatic forces for the adsorption of the organic molecules on halides modified copper substrate. The positively charged molecules are found to give much better ordered structures in the STM measurement than the uncharged molecules.

5.6. Summary

Adsorption of H_2PcPyMe molecules on an iodide modified Cu(100) electrode in an electrochemical environment has been studied by a combination of CV, in-situ STM and ex-situ XPS measurements.

The XPS measurements provide complementary information resulting in some interesting conclusions as follows:

- In acidic environment the metal cores of the phthalocyanine complexes are replaced by hydrogen atoms in order to form the corresponding *metal free* molecules as concluded from the absence of the Zn2p signals in the XPS spectra.
- The appearance of S2p signals indicates co-adsorption of sulfate anions within the phthalocyanine adlayer due to neutralization of the positively charged $[H_2PcPyMe]^{4+}$ adsorbates.

The CV results with HOPG and Cu(100) show a series of reduction peaks indicating that the H_2PcPyMe molecules undergo four successive single-electron reduction steps in acidic medium yielding organic tri-, di-, and mono- anions as well as neutral molecules, respectively. These reduction processes involve the phthalocyanine ligands only, and not the eight substituted groups and the central metal.

The main part of this chapter focuses on STM images showing a highly ordered adlayer of $[H_2PcPyMe]^{4+}$ molecules on the iodide modified Cu(100) electrode surface sub-divided into two distinct phases, namely, a square phase (phase A) and a rhombic phase (phase B). Molecular rows in the ordered layer are not oriented along the commensurate direction of the iodide layer underneath, i.e. the [011] direction which runs parallel to the close-packed atom rows of the Cu(100) substrate. This clearly excludes a template effect of the substrate surface, but rather hints to a molecular self-assembly. And, co-adsorption of sulfate anions within the phthalocyanine adlayer is for the first time demonstrated by XPS data as well as EC- STM observation.

Moreover, the influence of electrostatics, i.e. between the positively charged molecular lobes of the molecules and the anion layer on the halide pre-covered Cu(100) electrode surface is also investigated. The STM results elucidate that while the positively charged molecules ($[H_2PcPyMe]^{4+}$) form stable ordered structures due to a combination of van der Waals, hydrogen bonding and, in particular, electrostatic interactions between the phthalocyanine molecules and the iodide anion layer, the uncharged molecules are weakly bound and rather disordered on the measured surface.

Chapter 6

Self-assembly of Porphyrin on a copper surface

6.1. Introduction

The aim of this chapter is to characterize the redox chemistry and the structural features of the adlayer of a porphyrin derivative ($[H_2TTMAPP]^{4+}$) on a copper electrode surface. The electrochemical properties as well as the self-assembly of simple porphyrins were in fact well studied and documented in the literature for both UHV [23-25,165-166)] and electrochemical environment [27,28,30,167-169]. However, the structural characterization of this porphyrin derivative is for the first time done in electrochemical media using our home-built STM probe. In this molecule, the four extra trimethylamonium-phenyl groups (see Fig.4.4a) are expected to lead to the formation of different structures compared to TMPyP (see Fig. 4.4b) due to additional intermolecular side-group and substrate/side-group interactions.

The self-assembly process of supramolecules on a well defined metal surface at the solid/liquid interface is well known to be affected by a number of factors. It is, therefore, necessary to understand in detail the influence of the individual parameters on the lateral order subsequently allowing a precise control of the supramolecular self-assembly of new porphyrin derivatives not only on the measured surface but also on other metal substrates. In this chapter, the following factors that may have impact on the self-assembly have been studied:

- The substrate symmetry: The crystalline surface orientation is known to significantly impact on the molecular self-organization due to the difference in contact to the surface. Therefore, for comparison Cu(100) and Cu(111) surface orientations are used.
- The nature of the preadsorbed anions: Due to the differences in charge density and adsorbate structure on the copper electrodes, the anionic buffer layers are expected to govern the molecular ordering on the surface. In this framework, three halogens, i.e. chloride, iodide and bromide, as well as sulfate anion, were employed for the investigations. While chloride anions are known to form a negatively charged layer, less charged layers are obtained with iodide and bromide anions [104].
- The electrode potential: This factor is expected to govern the anionic layer de/readsorption processes and any electron transfer induced molecular phase transitions.
- The metal center of the porphyrin complexes: Redox reactions involving the central metal atom taking place in aqueous solutions are expected to influence phase transition of the ordered layer. In this work an iron porphyrin derivative was used.

On the basis of a combination of cyclic voltammetry and in-situ STM measurements, the following issues will be discussed in detail:

- Firstly, cyclic voltammetry with HOPG and copper electrodes in pure and molecules containing electrolytes will be compared in order to gain information of the electrochemical properties of the respective system. In fact, all eight systems resulting from the Cl, Br, I and SO_4^{2-} anions modified Cu(100) and Cu(111) electrode surfaces have been investigated by mean of CV measurements. The HOPG was employed as working electrode in order to investigate the electrochemical characteristics of the porphyrin. HOPG offers the advantage of a very broad potential window of -500 mV to 2200 mV vs. RHE, which helps to assign the redox processes taking place within the narrow potential window of the copper electrodes [170]. Moreover, no anion preadsorption occurs on HOPG, which provides insight into the influence of the anion buffer layers present on the copper electrodes.

- Secondly, STM results are presented in order to clarify the influence of parameters like anion pre-adsorbate, substrate symmetry, etc. as well as the electrode potential on the self-assembly process of $[H_2TTMAPP]^{4+}$ molecules on the anion modified Cu(111) and Cu(100) electrodes.

6.2. Electrochemistry of metal free porphyrin ($[H_2TTMAPP]^{4+}$)

6.2.1. CVs of HOPG in $[H_2TTMAPP]^{4+}$ containing acidic solution

The voltammetric curve of HOPG, at first in the pure electrolyte (10 mM HCl), is depicted in Fig.6.1 (dashed grey curve) showing the broad potential window without the appearance of any cathodic and anodic peaks, demonstrating that the HOPG surface is not affected by the presence of the halide anions, namely the chloride anions in this case. The CV is considerably altered as soon as the supporting electrolyte is substituted by the working electrolyte containing the $[H_2TTMAPP]^{4+}$ molecules (solid black curve in Fig.6.1) including several anodic and cathodic current peaks.

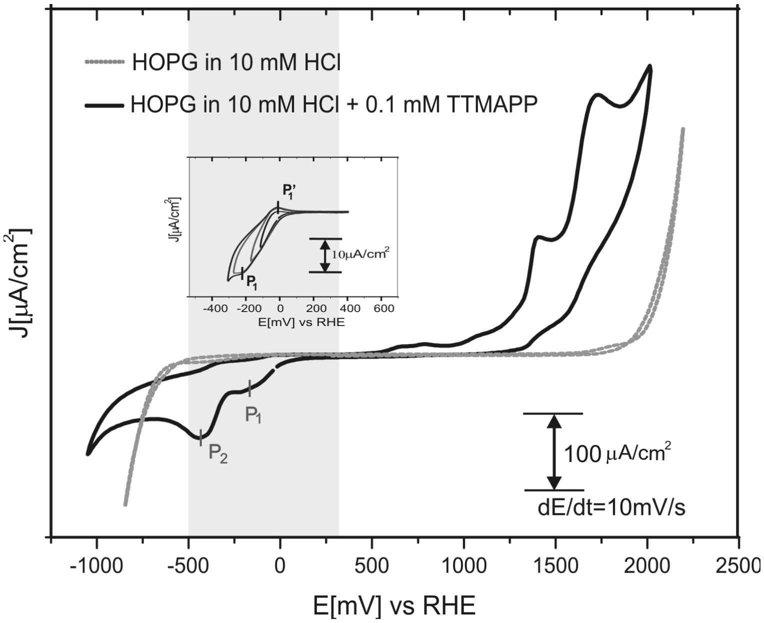

Figure 6.1: Voltammetric curves of a HOPG electrode in pure 10 mM HCl electrolyte (dashed grey curve) and in 10 mM HCl + 0.1 mM $H_2TTMAPP$ solution (solid black curve); inset figure indicates the reversible reduction-reoxidation pair of peaks relating to the first two-electron transfer step; scan rate dE/dt = 10 mV/s.

The first observation is, that both the cathodic and anodic limits of the CV are shifted to more negative potentials, i.e. the hydrogen evolution reaction (HER) is retarded by the presence of the molecules, while the oxygen evolution reaction (OER) starts already at less positive potentials. Next we concentrate on the redox processes only which fall into the potential window of copper, i.e. the range between -500 mV and +300 mV as indicated in Fig.6.2. The first porphyrin redox process represented by a (quasi) reversible pair of peaks with P_1 = -210 mV and P'_1 = -30 mV vs RHE (see Fig.6.3) is assigned to the diffusion controlled first two-electron transfer process, namely reduction (P_1) and reoxidation (P_1'). The further reduction process underlying peak P_2 has no obvious reoxidation counterpart because this is considered to appear within the potential range from +700 to +2000 mV, in agreement with the ref.171-175 and papers cited thesein, indicating that this reduction process is irreversible. This behavior is likely to derive from the influence of anion adsorption, however, the precise interpretation for this process is still subject for controversy.

It is well known that all redox processes detectable within the potential window of HOPG affect the inner ring system of the porphyrin molecules only, those affecting the outer ligands are outside this potential range [172]. This is even more true for the CVs with copper surfaces as becomes obvious from Fig.6.2. Compared to the previously studied $[H_2TMPyP]^{4+}$ the reduction peaks P_1 and P_2 are shifted by about 370 mV to more negative potentials [30], indicating the higher stability of the $[H_2TTMAPP]^{4+}$ ring against reduction.

6.2.2. CVs of copper in $[H_2TTMAPP]^{4+}$ containing acidic solution

Cyclic voltammograms of both copper surfaces in pure supporting electrolyte (dashed black curves) as well as in porphyrin containing solutions (red and green curves) are presented in Fig.6.2. The potential window of the copper in the blank electrolytes is limited by two peaks, namely the copper dissolution reaction (CDR) setting the anodic limit and the hydrogen evolution reaction (HER) determining the cathodic limit:

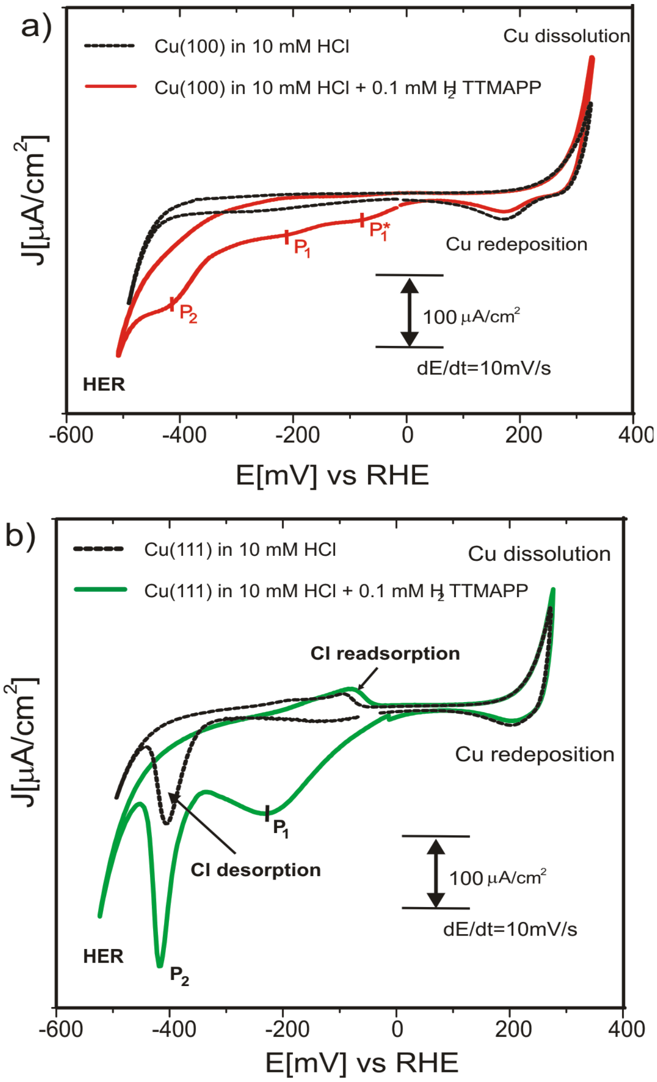

Figure 6.2: Typical CVs of (a) Cu(100) and (b) Cu(111) electrode surface in 10 mV HCl (dash black curve) and in 10 mM HCl + 0.1 mM $[H_2TTMAPP]^{4+}$(solid red and solid green curves), dE/dt = 10 mV/s.

Fig.6.3 illustrates the appearance of peaks depending on the potentials (CV 1 and 2) as well as on electrode nature. While the oxidation curve $P_1^{'}$ is observed in the CV of HOPG (CV1 in Fig.6.3), it is completely absent in the reverse scan of the CVs of the copper electrodes (CV3 and 4). These observed phenomena have to be assigned to the presence or non-presence of specifically adsorbed anions, i.e. their adsorption/desorption. In addition, in the presence of the molecules the copper re-deposition features are still persistent (similar to the CVs in porphyrin free electrolyte) in the cathodic direction scan. This observation means that dissolved copper cations are not coordinated into the free base $[H_2TTMAPP]^{4+}$ molecules in order to form the corresponding metal complexes, i.e. $[CuTTMAPP]^{4+}$ molecules, in the copper dissolution regime, as, in turn, was observed with H_2TMPyP [30].

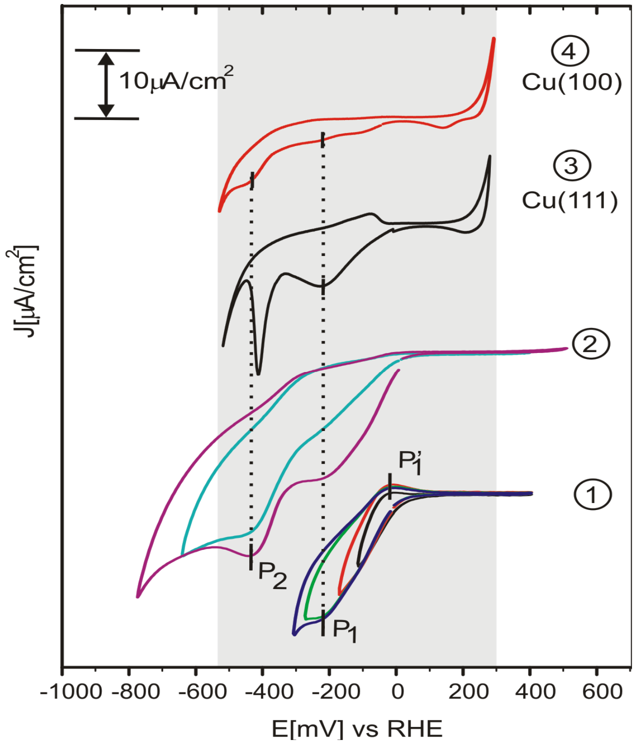

Figure 6.3: Potential dependent reduction peaks in the CV of HOPG (CV 1 and 2) and of copper (CV 3 and 4) in the $[H_2TTMAPP]^{4+}$ containing electrolyte.

6.2.3. Discussion

In this section, redox processes involving “solution” as well as “surface limited” reactions that are observed in the above CVs will be discussed in detail in order to answer the question: How does the redox mechanism of $[H_2TTMAPP]^{4+}$ take place in acidic media?

Most molecules of the porphyrin family either are insoluble or have only limited solubility in aqueous solutions. Many interesting processes, therefore, which might be investigated, are obscured due to aggregation and precipitation phenomena [190]. Nevertheless, some porphyrin derivatives have been modified to have a high solubility owing to the substitution with polar peripheral groups. Among these molecules, the 5,10,15,20-Tetrakis (4-trimethylamonium-phenyl) porphyrin tetra(p-toluenesulfonate) is well known to be water soluble in solution within the pH range from 0 to 14 due to four positively charged trimethylammonio-phenyl substitutients [15]. Therefore, this species has become relevant with respect to kinetic investigations in aqueous solution which are of considerable interest in a variety of disciplines. In the following, its electrochemical properties are discussed and interpreted in detail.

After dissolution in acidic solution, $[H_2TTMAPP]^{4+}$ molecules are believed to undergo an acid/base reaction forming the respective porphyrin diacid that remains stable in the potential range from 0 mV to 1000 mV vs RHE instead of the monocationic $[H_3TTMAPP(0)]^{5+}$ species [171-172] according to:

$$[H_2TTMAPP(0)]^{4+} + 2H^+ \overset{K_1}{\Leftrightarrow} [H_4TTMAPP(0)]^{6+} \qquad (6.1)$$

The dissociation constant taking e.q. 6.1 into account is either 2.2 ± 0.2 determined by Hambright and coworkes. [172] or 4.01 proposed by Wilson et al. [174].

Regarding reduction processes of this porphyrin derivative, it could be seen that $[H_2TTMAPP]^{4+}$ molecules undergo several distinguishable reduction processes in acidic media denoted by P_1 and P_2 in the CV curves (Fig.6.1-6.3), respectively, which are known to involve 6 electrons in total. The first reversible two-electron reduction step is described by the following sequence [192]:

$$[H_2TTMAPP(0)]^{4+} + 2e^- + 2H^+ \leftrightarrow [H_4TTMAPP(-II)]^{4+} \qquad (6.2)$$

$$[H_4TTMAPP(0)]^{6+} + 2e^- \leftrightarrow [H_4TTMAPP(-II)]^{4+} \qquad (6.3)$$

The electron transfer number (n) of the corresponding redox process was in fact determined to be 1.7 by Lever et al. [21] according to Faraday's rule:

$$\Gamma = Q/(n.F) \qquad (6.4)$$

where Γ is the surface coverage (mol), Q is the surface charge (C) and F is the Faraday constant (96487 $C.mol^{-1}$). On the basis of this result we can conclude that the first redox wave is a two-electron transfer process. Obviously, the first reduction step just takes place on the porphyrin core rather than the positively charged trimethylamonium- phenyl groups. Reduction reactions caused by these redox-active groups are suggested to take place more negatively than the HER on HOPG as well as copper electrodes, and, thus, these reactions can be neglected in the course of this thesis. Nevertheless, these reduction products may be protonated via an acid/base equilibrium in order to form the corresponding $[H_5TTMAPP(-II)]^{5+}$ species with K_2 of 0.96 [174] according to:

$$[H_4TTMAPP(\text{-II})]^{4+} + H^+ \overset{K_2}{\Leftrightarrow} [H_5TTMAPP(\text{-II})]^{5+} \qquad (6.5)$$

As a result, beyond the first two-electron transfer step, both reduction products, $[H_5TTMAPP(-II)]^{5+}$ and $[H_4TTMAPP(-II)]^{4+}$, respectively, are in the working electrolyte. These reduction modes are suggested to remain stable within the potential regime from -420 mV to -210 mV vs RHE, i.e. within the intermediate potential between P_1 and P_2 (Figs. 6.1; 6.2 and 6.3) [171,176].

This assumption is in accord with former studies [21,174,177]. Wilson et al. [174] investigated the electrochemical behavior of $[H_2TMPyP]^{4+}$ in acidic solution. They found that the overall reduction process involves the addition of six electrons and is sub-separated into either three distinct two-electron steps or one two-electron and one four-electron steps depending on the pH.

However, a significant difference between $[H_2TTMAPP]^{4+}$ and $[H_2TMPyP]^{4+}$ are the reduction potentials. The first reduction of the $[H_2TTMAPP]^{4+}$ molecules apparently initiated at P_1 = -210 mV vs RHE is negatively shifted by 370 mV compared to that of the $[H_2TMPyP]^{4+}$ molecules [30]. Perhaps, the observed deviation can be attributed to the impact of the functional groups [171,176]. The substitution of the four methyl pyridyl groups by the four highly polarized trimethylamonium ones on the porphine core causes this modification. The trimethylamonium $(CH_3)_3N^+$ group is well known to be also a strong polar group [178] that interferes with the electron density of the π ring system. While the polar effects of the methyl (CH_3) substituents on the TMPyP molecules are close to zero, the influence of the $(CH_3)_3N^+$ groups in the $[H_2TTMAPP]^{4+}$ is appreciable [179]. Consequently, the $(CH_3)_3N^+$ groups tend to prevent electrons at the porphine ring from the delocalization resulting in the alteration of the electrochemical behavior. Furthermore, owing to the strong polarity of the $(CH_3)_3N^+$ groups, the positive charge density on the side-groups is increased, resulting in an enhancement of electrostatic interactions between the molecules and the chloride layer underneath. The adsorption strength of the $[H_2TTMAPP]^{4+}$ molecules on the chloride modified copper electrodes is, hence, much large than that of $[H_2TMPyP]^{4+}$ reported by Hai et al. [31].

The reduced product continues either being further reduced at more negative potentials or being re-oxidized in the reverse (i.e. anodic) scan. Redox processes take place completely or partially depending on the nature of the electrode. Indeed, CVs of HOPG in a working electrolyte containing porphyrin molecules showed a combination of reversible and irreversible pairs of peaks, which relate to several electron transfer steps as reported by Hai et al. [30] and Phan et al. [171].

At potentials negative than the cathodic peak P_1 the $[H_2TTMAPP]^{4+}$ molecules undergo further successive reduction steps. Regarding these steps, one can observe either two further two-electron reduction steps or one four electron transfer step depending on the pH used [174]. In the present case, only one cathodic peak is visible in the narrow potential range of copper as well as in the broad potential regime of HOPG. On the basis of this observation one can draw the conclusion that the final reduction step relates to one four-electron transfer process, i.e. the $[H_5TTMAPP(\text{-II})]^{5+}$ and $[H_4TTMAPP(\text{-II})]^{4+}$ species are directly reduced to the (-VI) oxidation state with four additional electrons, according to either:

$$[H_4TTMAPP(\text{-II})]^{4+} + 4e^- + 4H^+ \rightarrow [H_8TTMAPP(\text{-VI})]^{4+} \qquad (6.6)$$

or

$$[H_5TTMAPP(\text{-II})]^{5+} + 4e^- + 3H^+ \rightarrow [H_8TTMAPP(\text{-VI})]^{4+} \qquad (6.7)$$

However, this final step could from the electrochemical point of view be a combination of two overlapping reduction processes in which the individual reduction consists of only two-electron transfer step [30]. These reduction processes are illustrated as following sequences:

$$H_4TTMAPP(\text{-II})]^{4+} + 2e^- + 2H^+ \rightarrow [H_6TTMAPP(\text{-IV})]^{4+} \qquad (6.8)$$

$$[H_5TTMAPP(\text{-II})]^{5+} + 2e^- + 2H^+ \rightarrow [H_7TTMAPP(\text{-IV})]^{5+} \qquad (6.9)$$

and:

$$[H_6TTMAPP(\text{-II})]^{4+} + 2e^- + 2H^+ \rightarrow [H_8TTMAPP(\text{-IV})]^{4+} \qquad (6.10)$$

$$[H_7TTMAPP(\text{-II})]^{5+} + 2e^- + H^+ \rightarrow [H_8TTMAPP(\text{-IV})]^{4+} \qquad (6.11)$$

The sequence of reduction steps of $[H_2TTMAPP]^{4+}$ molecules is illustrated in Fig.6.4 according to ref.190. The red cycles describe structural changes within the molecular core due to the two-electron transfer processes as well as the resulting protonation steps.

Astonishingly, the copper porphyrin complex, i.e. $[CuTTMAPP]^{4+}$ molecules, has not been formed in the copper dissolution regime due to Cu(II) incorporation into the free base $[H_2TTMAPP]^{4+}$. In this regime, the copper electrode may serve as the source of Cu^{2+} species for Cu incorporation in acidic solution. However, the Cu re-deposition peak emerging in the cathodic scan persists indicating that the Cu(II) cations are re-deposited on the copper electrode surface rather than participating in an incorporation reaction.

In summary, based on the resulting CVs with HOPG as well as the copper electrodes several significant conclusions can be drawn:

- The free base porphyrin and its diacid form, i.e. $[H_2TTMAPP(0)]^{4}$ and $[H_4TTMAPP(0)]^{6+}$, remain stable in the potential regime from +1000 mV downward to +0 mV vs RHE where the diacid species is formed via the acid/base equilibrium.
- The $[H_2TTMAPP]^{4+}$ molecules undergo one two-electron and one four-electron transfer step within the potential window of HOPG and the copper electrodes. While the former is considered as a reversible process, the latter is irreversible.
- Copper incorporation into the free base $[H_2TTMAPP]^{4+}$ species is not accomplished in the copper dissolution regime where the copper substrates may serve as sources for Cu^{2+} ions.

6.3. Structural determination

The aims of this section is to determine structures of $[H_2TTMAPP]^{4+}$ molecules on the halide modified copper electrodes in aqueous solutions. It is well known that ordering of other porphyrin derivatives has been investigated in both UHV and electrochemical environment. For instance, adsorption of $[H_2TMPyP]^{4+}$ molecules on either bare metal electrodes or on halides terminated metal surfaces studied in aqueous media under non-reactive condition [27-29,180-181] as well as reactive condition [31] has been reported. In addition, other porphyrins were also studied in UHV [168,182-285] and in electrochemical solution [27,28,30,167-169]. However, structural characterization of adsorbed $[H_2TTMAPP]^{4+}$ molecules has not been investigated till now though its electrochemical behavior was examined [21]. It is for the first time, that the adsorption of the $[H_2TTMAPP]^{4+}$ molecules on halide modified copper electrode surfaces is performed and discussed under both non-reactive and reactive conditions.

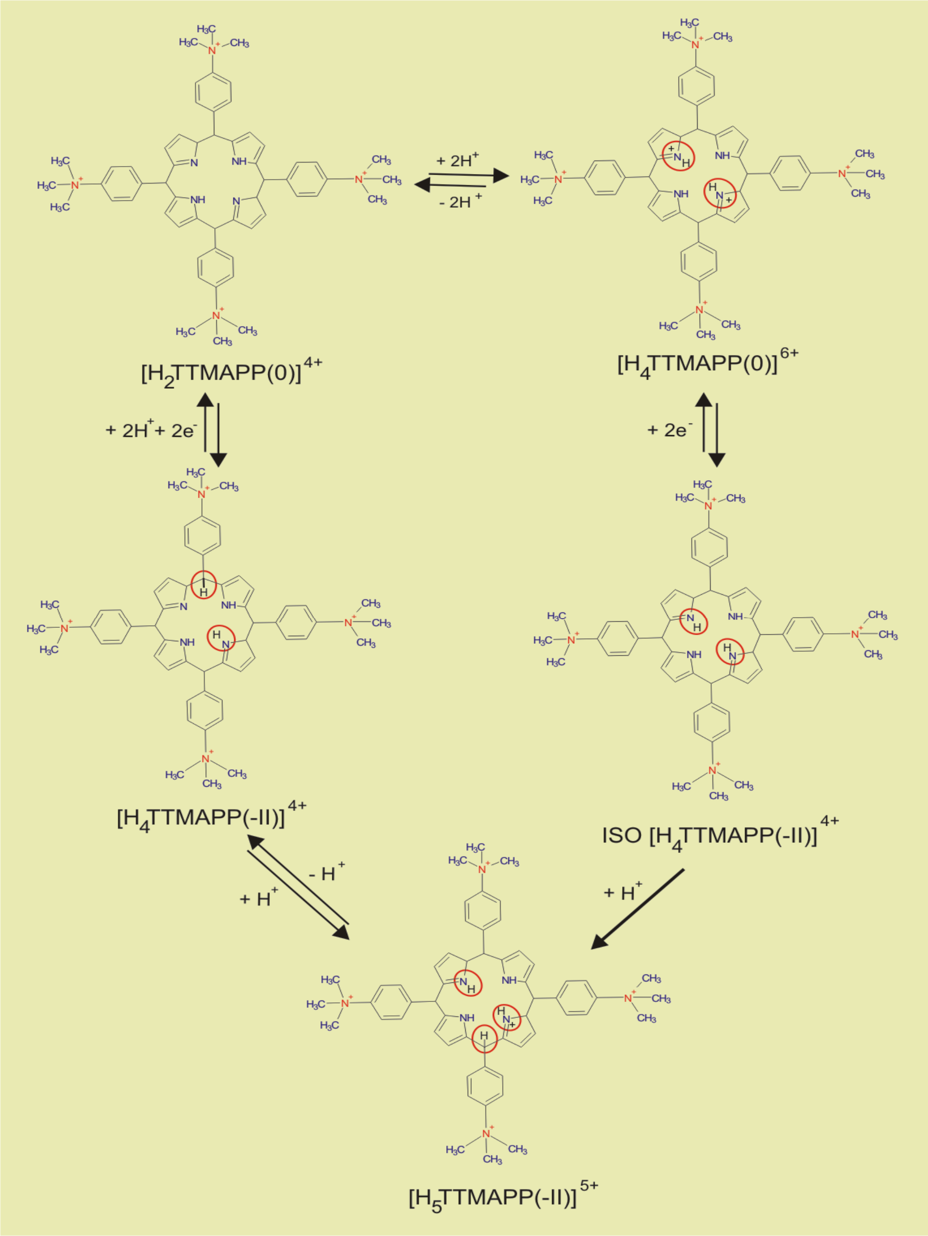

Figure 6.4: Sketch illustrating reactants and products of the first reduction step of $[H_2TTMAPP]^{4+}$ molecules from ref. 174.

6.3.1. Self-assembly of $[H_2TTMAPP]^{4+}$ molecules on a chloride modified Cu(111) electrode

All experiments performed in this section were carried out under non-reactive condition, i.e. in the potential regime more positive than peak P_1 (Fig.6.1), where the free base porphyrin ($[H_2TTMAPP(0)]^{4+}$) is stable.

As mentioned in subsection 3.3.2, chloride anions form a $c(p \times \sqrt{3})$ superstructure on the Cu(111) electrode surface when the Cu(111) electrode is brought into contact with chloride containing solution. This layer remains stable and acts as a template when the pure supporting electrolyte (10 mM HCl) is replaced by the same electrolyte containing the $[H_2TTMAPP]^{4+}$ molecules.

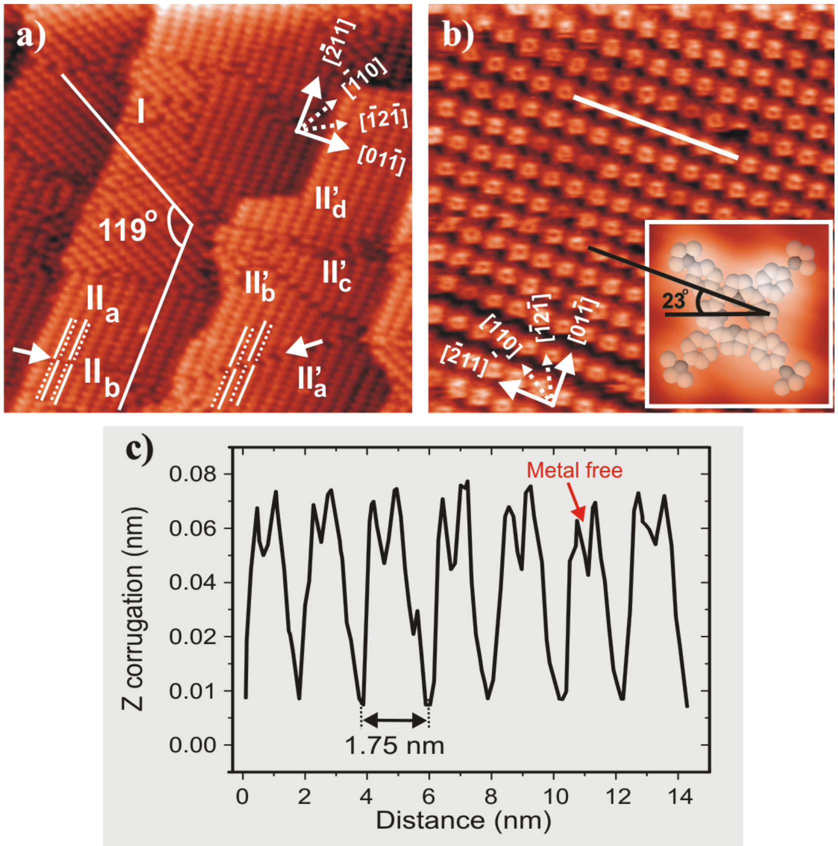

Figure.6.5: Atomic structure and surface morphology of the $c(p \times \sqrt{3})$Cl precovered Cu(111) surface in the presence of $[H_2TTMAPP]^{4+}$ molecules; a) 61.46 nm x 61.46 nm, I_t = 0.1 nA, U_b = 346 mV, E = +50 mV; b) 28.81nm x 28.81 nm, I_t = 0.2 nA, U_b = 230 mV, E = +20 mV, c) Line profile recorded along the white line in Fig.6.5b yielding the intermolecular distance of 1.75 nm.

A typical large scale STM image measured soon after the electrolyte replacement showing the surface structure of the $[H_2TTMAPP]^{4+}$ adlayer on top of $c\left(p \times \sqrt{3}\right)$-Cl/Cu(111) surface is displayed in Fig.6.5. It is seen that the molecules are self-assembled into an ordered layer of molecular rows covering the atomically flat terraces. Furthermore, two domains rotated by 119° (denoted by I and II) are discernible, which clearly manifests the influence of the substrate symmetry on the molecular self-organization. The deviation of the rotation angles from 120^{o} is assigned to a slight drift during scanning and a measuring artifact because the same deviation is also found for the substrate step-edges which are still clearly visible. Thus, again the presence of the molecules on the surface has no impact on the typical structure of the chloride precovered substrate. Furthermore, within individual rotational domains, there are also translational domains visible in Fig.6.5a, termed as $II_{a,b}$ and $II'_{a\text{-}d}$, respectively. It becomes evident, that the orientation of a close-packed molecular row runs parallel to a step-edge, corresponding to the close-packed rows of the chloride underneath [85,104,186]. And, hence, the $[H_2TTMAPP]^{4+}$ molecular rows are orientated parallel to the highly symmetric directions of the chloride lattice. Alternatively, they are aligned parallel to the $\langle\bar{2}11\rangle$ directions of the Cu(111) substrate.

A medium scale STM image (Fig.6.5b) illustrates the molecular arrangement within each domain and accentuates that $[H_2TTMAPP]^{4+}$ molecules are arranged in rows. All molecular symmetry axes are not coincident to the direction of molecular rows but rather rotated by an angle of 23° with respect to the molecular rows as depicted in the inset of Fig.6.5b. Each molecule is recognized by its square-like shape enclosing a hole in its center indicating the flat-lying arrangement of the molecules on the surface. This conformation is reminiscent of chemical structure of the $[H_2TTMAPP]^{4+}$ molecules illustrated in Fig.4.4 and consistent with maximum electrostatic interactions between the molecules and the substrate. On the basis of line profile measurements the intermolecular distance is calculated to be 1.75 ± 0.1 nm as shown in Fig.6.5c. The small minimum at the top of each peak supports the notion that the molecules are metal-free.

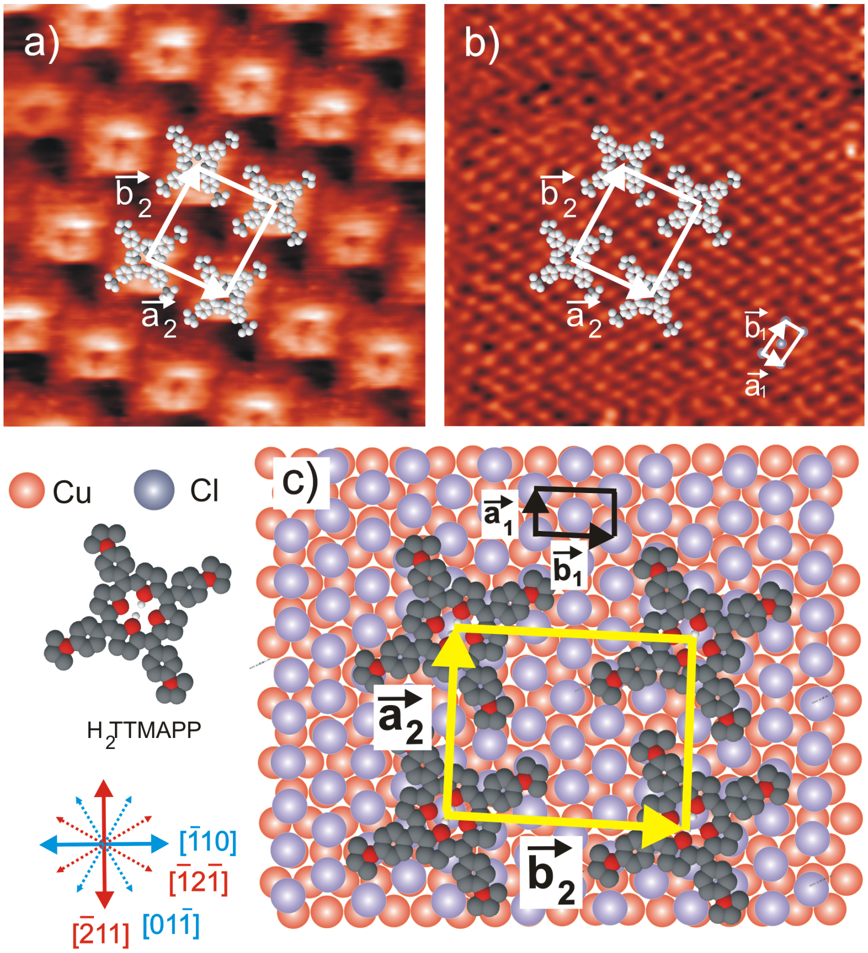

Figure 6.6: Relation between the $[H_2TTMAPP]^{4+}$ overlayer and the anionic chloride layer underneath on Cu(111): a) $H_2TTMAPP$ overlayer: 8.51 nm x 8.51 nm, I_t = 0.25 nA, U_b = 222 mV, E = +20 mV; b) Underlying chloride lattice: 8.51 nm x 8.51 nm, I_t = 4.5 nA, U_b = 15 mV, E = +20 mV; c) Tentative structure model of the $[H_2TTMAPP]^{4+}$ adlayer.

Furthermore, the structural relation between the molecular structure and the chloride underneath is also investigated here. Such a series of the STM images recorded at the same surface area under different tunneling conditions is presented in Fig.6.6 (see also section 6.3.3). Under moderate tunneling conditions (high bias voltage and low tunneling current), the covering porphyrin adlayer is imaged with sub-molecular resolution (Fig.6.6a). Contrarily, under more drastic tunneling conditions (low bias voltage and high tunneling current) the tunneling tip penetrates into the porphyrin film which is locally removed upon scanning so that the underlying chloride lattice becomes clearly visible. As a result, the molecular rows adsorbed on the chloride modified Cu(111) electrode run parallel to the close-packed chloride atomic rows, corresponding to the $\langle\bar{2}11\rangle$ directions of the Cu(111) substrate [207]. The unit cell $(\vec{a}_2, \vec{b}_2)$ as depicted in Fig.6.6a and b with $|\vec{a}_2| = 1.75$ nm and $|\vec{b}_2| = 2.03$ nm, enclosing an angle of 90°, contains one molecule and corresponds to a (3 x 4)-superstructure with respect to the $c(p \times \sqrt{3})$Cl underlayer. With respect to the (1×1)-Cu(111) lattice, the unit cell of the $[H_2TTMAPP]^{4+}$ adlayer can be described as a $(3p \times 4\sqrt{3})$ superstructure. A possible structure model is also proposed in Fig.6.6c. Taking the substrate symmetry into account, there are three rotational domains coexisting on the electrode surface. The surface coverage per domain was also calculated and is 0.042 ML with respect to the chloride lattice underneath, or 2.8 x 10^{13} molecules/cm^2.

6.3.2. Lateral ordering of $[H_2TTMAPP]^{4+}$ adlayer on Cl/Cu(100)

Changing the substrate symmetry, i.e. using a four-fold symmetric $c(2 \times 2)$Cl precovered Cu(100) surface as the template, it is expected to induce some differences in the molecular pattern of the adsorbed porphyrin layer.

Preparation and measurement procedures for the adsorption of $[H_2TTMAPP]^{4+}$ molecules on a chloride modified Cu(100) electrode surface are the same as those carried out on Cl/Cu(111). Fig.6.7 shows the surface morphological and atomic structure of the $c(2 \times 2)$Cl precovered Cu(100) surface in the presence of $[H_2TTMAPP]^{4+}$ cations at an electrode potential of E = +20 mV vs RHE. First of all the straight step-edges running in orthogonal directions like in Fig.6.7a prove the persistence of the $c(2 \times 2)$Cl layer underneath the organic molecules. Moreover, the whole $c(2 \times 2)$Cl/Cu(100) surface is spontaneously covered by the porphyrin molecules, forming several domains denoted as D_1 and D_2, respectively, which are rotated by an angle of 45 ± 1° with respect to each other (Fig.6.7a). From a closer view into domain D_1 (Fig.6.7b), it is clear that the direction of the close-packed molecular rows forms an angle of 22 ± 1° with respect to the steps. The molecular rows, hence, neither run parallel to any high symmetry axes of the chloride lattice underneath nor to the close-packed atom rows of the Cu(100) substrate. The two rotational domains (termed D_1 and D_2) are two mirror domains with the mirror plane being aligned along the [010] substrate direction. Fig.6.7c displays the self-assembled structure of the $[H_2TTMAPP]^{4+}$ molecules on the molecular level. The molecules are arranged in rows with an intermolecular distance of about 1.95 ± 0.1 nm as measured by the line-profile in Fig.6.7d. All molecules in a row are rotated by an angle of 19 ± 1° with respect to the direction of the row (see inset in Fig.6.7c). This value is somewhat different from published results for the adsorption of $[H_2TMPyP]^{4+}$ on Cl/Cu(100) [208] and on I/Cu(100)

[182], which exhibit an angle of 17 ± 1°. The most plausible explanation for this difference is the higher steric demand of the longer ligands of $[H_2TTMAPP]^{4+}$ compared to $[H_2TMPyP]^{4+}$. Each molecule looks like a four-fold propeller with a hole in its center (see Fig.6.8a and profile in Fig.6.8d). This indicates again that the molecules are metal-free and are lying flat on the Cl/Cu(100) surface due to their large planar π-system [187]. Only occasionally some distorted molecules are also observed within the molecular adlayer on the Cl/Cu(100) surface indicated by white arrow in Fig.6.7c.

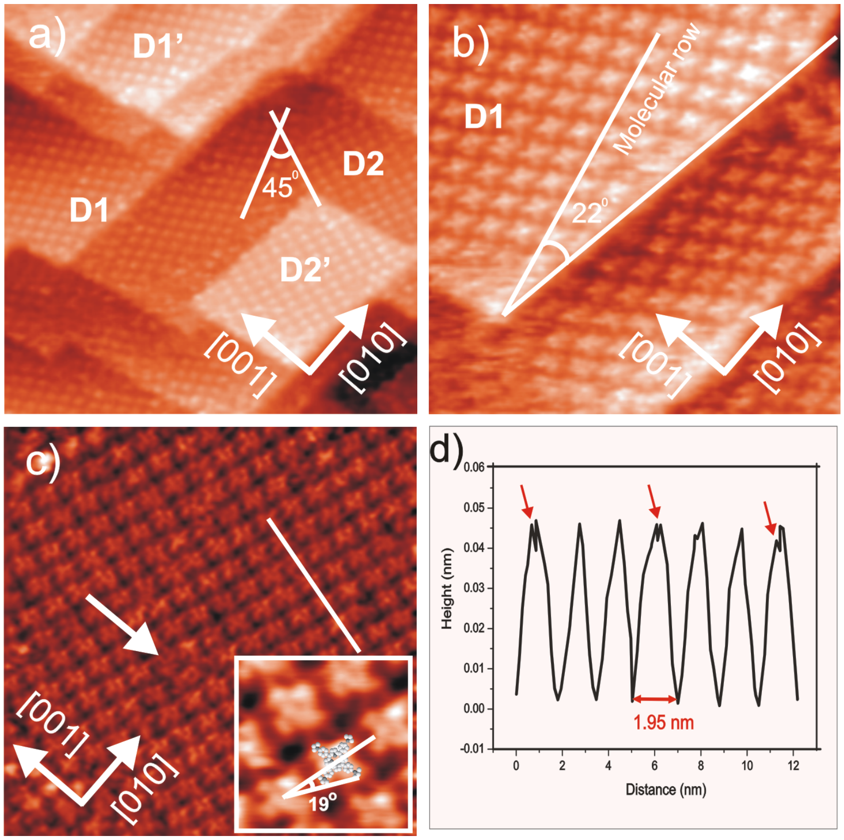

Figure 6.7: STM images of a $[H_2TTMAPP]^{4+}$ layer on a chloride modified Cu(100) surface; a) 80.47 nm x 80.47 nm with two rotational domains D1 and D2; b) Alignment of $[H_2TTMAPP]^{4+}$ molecules at the step-edges within domain D1; 24.42 nm x 24.42 nm, I_t = 0.1 nA, U_b = 168 mV, E = +20 mV; c) Molecular arrangement, 28.81 nm x 28.81 nm, I_t = 0.15 nA, U_b = +150 mV, E = +19 mV; inset: molecular rotation of 19^o vs row direction. The white arrows describe the crystallographic directions [001] and [010] of the Cu(100) substrate; d) Line profile recorded along the white line in Fig.5c indicating the intermolecular distance of 1.95 nm.

As mentioned above, the close-packed molecular rows do not run along any high symmetry direction of the underlying chloride lattice. By reason of surface symmetry, therefore, there are two co-existing mirror domains with respect to each close-packed direction of the chloride mesh underneath, in agreement with the experimental observation described in Fig.6.7. Consequently, by taking the quadratic symmetry of the chloride lattice into account, the adsorbed porphyrin structure is self-arranged into four rotational domains in total on such a chloride pre-terminated Cu(100) electrode surface.

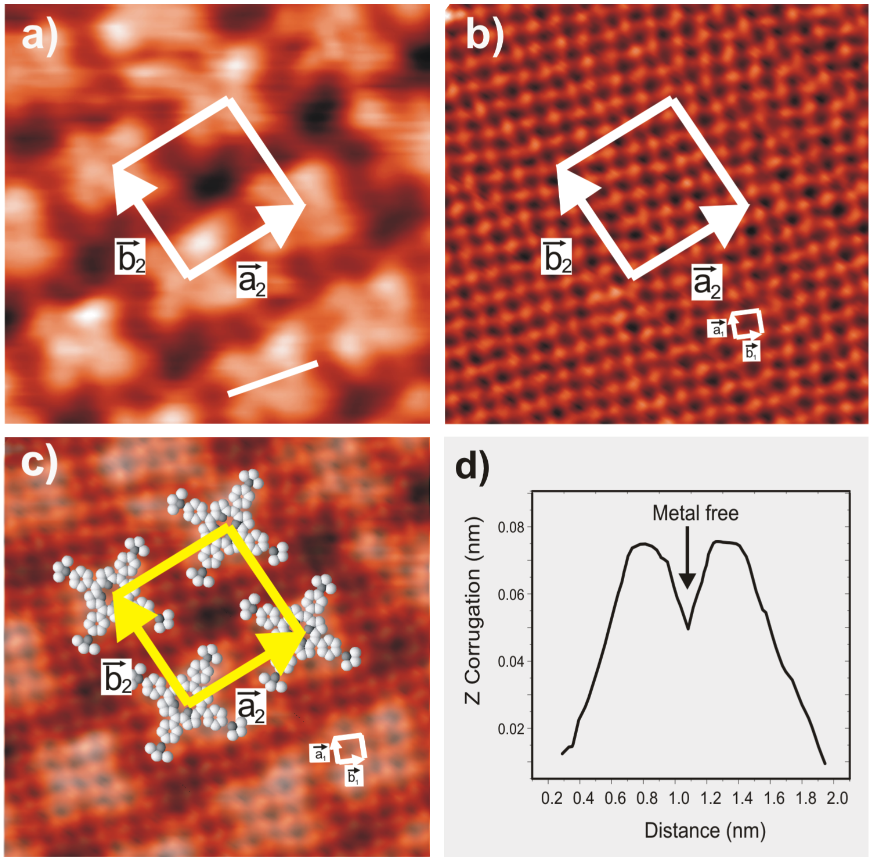

Figure 6.8: Structural relation between the $[H_2TTMAPP]^{4+}$ adlayer and the chloride lattice underneath, a) 6.9 nm x 6.9 nm, I_t = 0.15 nA, U_b = 247 mV, E = -20 mV; b) 6.1 nm x 6.1 nm, I_t = 2.5 nA, U_b = 10 mV, E = -20 mV; c) Superposition of panels a and b; ($\vec{a}_1, \vec{b}_1$) and ($\vec{a}_2, \vec{b}_2$) indicate the chloride and the porphyrin unit cells, respectively, d) Line profile cross one molecule along the white line in Fig.6.8a; the central minimum indicates the metal-free molecular core (see also line profile if Fig.6.7d).

The structural relationship of the porphyrin adlayer and the chloride lattice underneath could again be obtained by a careful adjustment of the tunneling conditions. The two 6.9 nm x 6.9 nm STM images displayed in Fig.6.8a and b were consecutively recorded at the same surface area.

Under "moderate" tunneling conditions with high bias voltage and low tunneling current (U_{bias} = 247 mV, I_t = 0.15 nA), i.e. a large tip-surface distance, the covering porphyrin adlayer is imaged as shown in Fig.6.8a (see also section 6.3.3). By contrast, under more "drastic" tunneling conditions with low bias voltage and high tunneling current (U_{bias} = 10 mV, I_t = 2.5 nA) the tunneling tip penetrates into the porphyrin film which is locally removed upon scanning so that the underlying chloride lattice becomes clearly visible (Fig.6.8b). First of all these experiments prove that the interaction between the porphyrin film and the underlying chloride lattice is weaker than the chemisorptive Cu-Cl bond which persists even under the drastic tunneling conditions. Secondly, the molecular rows run parallel neither to the close-packed anion rows corresponding to the [001] direction of the chloride under-layer nor to the close-packed atom rows of the Cu(100) electrode. Fig.6.8c is the graphical superposition of the two successively taken STM images of Fig.6.8a and b showing the relative position of the adsorbed film and the underlying chloride lattice. As a result, the direction of the molecular rows are rotated by an angle of 23 ± 1° with respect to the [001] direction of the chloride lattice, inferring that the angle of the direction of porphyrin rows and the [011] direction of the copper lattice is 22 ± 1° (as depicted in the hard-sphere structure model in fig.6.9). The unit cell of the porphyrin adlayer contains one molecule as shown in Fig.6.8c and can be described either by a $\begin{pmatrix} 5 & 2 \\ -2 & 5 \end{pmatrix}$ transformation matrix or by a $\left(\sqrt{29} \times \sqrt{29}\right)R23^o$ unit cell with respect to the $c(2 \times 2)$Cl lattice which serves as the internal calibration lattice. Consequently, the lattice constants of the molecular mesh are calculated to be $|\vec{a}_2| = |\vec{b}_2|$ = 1.95 nm in agreement with the line profile in Fig.6.6, enclosing an angle of 91 ± 2°. Alternatively, the unit-cell of the $[H_2TTMAPP]^{4+}$ adlayer can be transformed into the Cu(100)-(1 × 1) lattice by a $\left(\sqrt{58} \times \sqrt{58}\right)R22^o$ unit-mesh in Wood-notation or a $\begin{pmatrix} 7 & 3 \\ -3 & 7 \end{pmatrix}$ transformation matrix. A possible model describing two mirror domains on a chloride modified Cu(100) electrode surface is depicted in Fig.6.9. On the basis of this model the surface coverage per domain of the porphyrin adlayer is calculated to be 0.0345 ML relative to the density of the chloride layer, or 2.63 x 10^{13} molecules/cm^2.

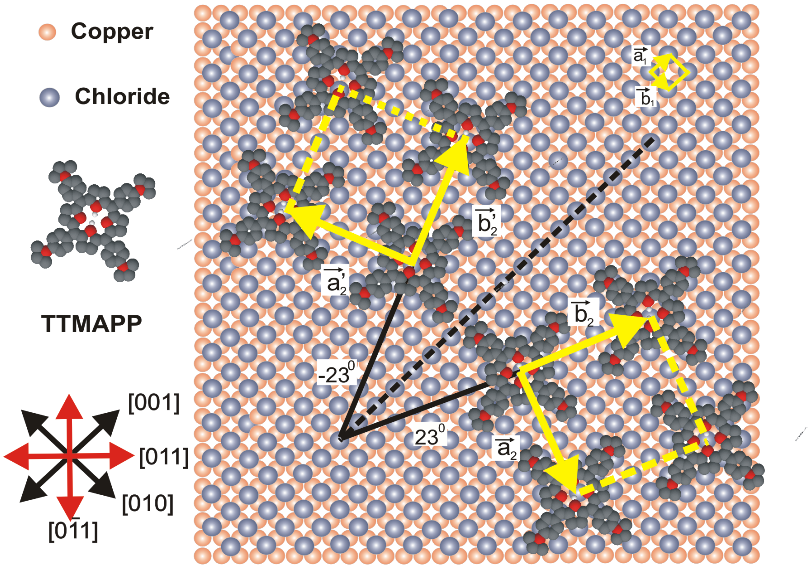

Figure 6.9: Structure model of mirror domains of $[H_2TTMAPP]^{4+}$ molecules on a chloride modified Cu(100) electrode with a rotational angle of 46° between them.

6.3.3. Tunneling conditions dependent supramolecular features

The structural characterization of supramolecules in self-assembled layers observed by the microscopic probe is sensitive to the tunneling conditions, and, hence, one can enhance these features by a careful variation of the tunneling conditions. In this particular sense, such a typical STM experiment regarding the tip-sample separation variation will be carried out, namely, by reducing the tip-sample separation by lowering the bias voltage or increasing the tunneling current. Thereby, the tunneling tip acts as a brush sweeping the organic molecular layer away and leaving the chloride lattice behind. Fig.6.10 illustrates a direct visualization of the tip induced molecular desorption on a chloride modified Cu(111) electrode surface. The step indicates the same surface area measured. While characteristic features of the $[H_2TTMAPP]^{4+}$ adlayer are visible in Fig.6.10a, the lateral ordering of the $[H_2TTMAPP]^{4+}$ molecules decays when the tunneling conditions come close to the “drastic”, i.e. high tunneling current and low bias voltage (Fig.6.10b). Thereby, the tip comes close to the surface and the ordered adlayer is completely removed resulting in the observation of the chloride lattice underneath as presented in Fig.6.10c and its inset.

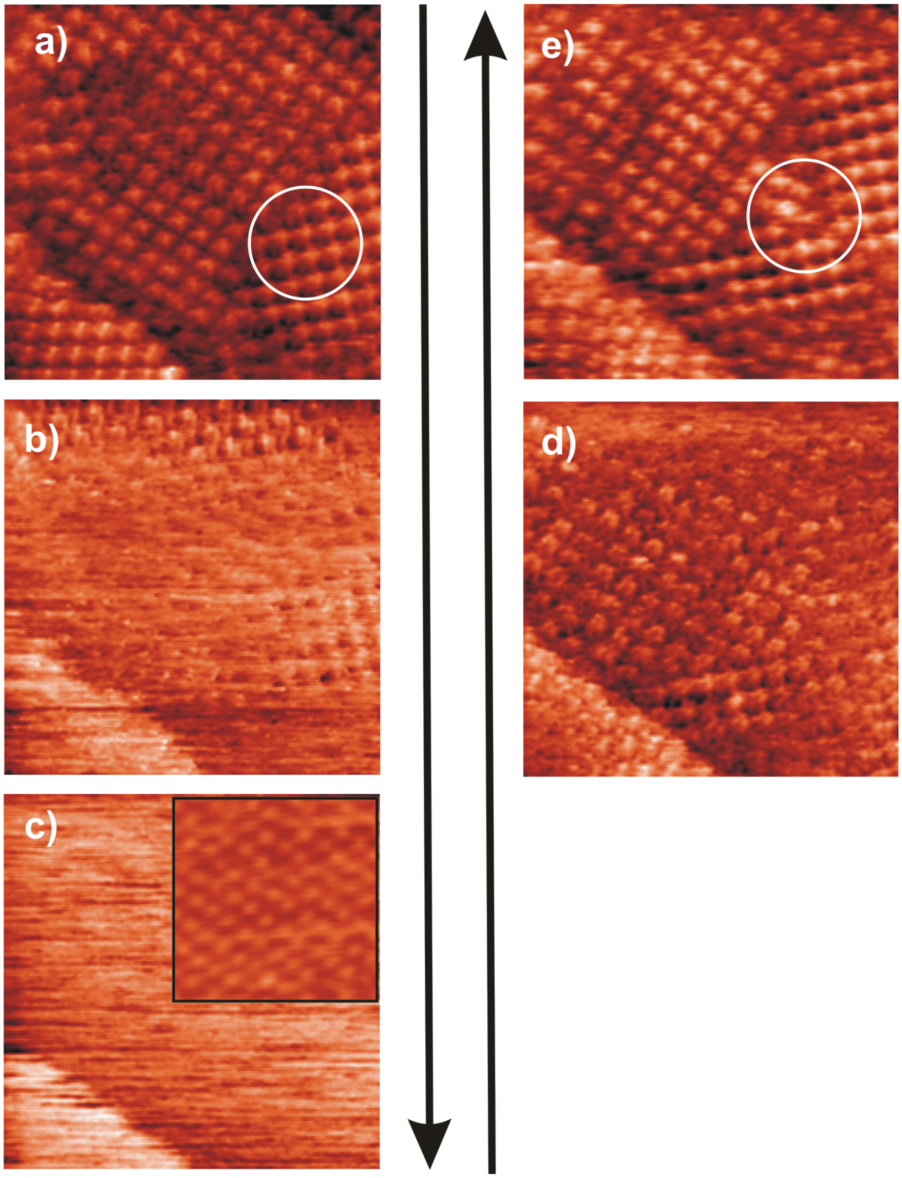

Figure 6.10: Series of STM images illustrating the reversible tip induced removal of the $[H_2TTMAPP]^{4+}$ adlayer on Cl/Cu(111): 30.73 nm x 30.73 nm, E = +10 mV; a) I_t = 0.1 nA, U_b = 285 mV; b) I_t = 0.6 nA, U_b = 285 mV; c) I_t = 1.2 nA, U_b = 128 mV; d) I_t = 0.3 nA, U_b = 224 mV; e) I_t = 0.1 nA, U_b = 318 mV.

The inset in Fig.6.10c shows a high resolution STM image demonstrating the quasi three-fold symmetric arrangement of chloride anions on the Cu(111) electrode surface or the so-called c(p x $\sqrt{3}$)-Cl superstructure mentioned in sub section 3.3.2. Retraction of the tunneling tip by applying “moderate” tunneling conditions (low tunneling current and high bias voltage) results in a restoration of the $[H_2TTMAPP]^{4+}$ ordered adlayer on top of the chloride template (Fig.6.10.d-e). This indicates that the tip induced removal/restoration of the organic film covering the Cl/Cu(111) electrode is a reversible process. Obviously, after resetting the moderate tunneling conditions the $[H_2TTMAPP]^{4+}$ molecules reform a new self-assembled layer on the Cl/Cu(111). The two rotational domains observed before the removal (Fig.6.10a) are restored (Fig.6.10e) though small modifications have been accomplished at the domain boundary indicated by white cycle. This means that the chloride layer underneath remains unaffected by this treatment due to the fact that the chloride-copper interaction is much stronger than the interaction between the organic molecules and the chloride lattice [140].

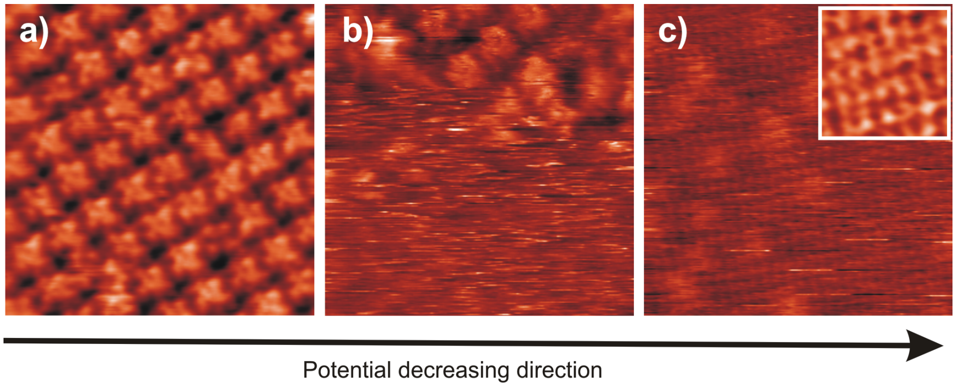

Figure 6.11: Series of STM images illustrating the tip induced removal of the $[H_2TTMAPP]^{4+}$ adlayer on Cl/Cu(100): 14.4 nm x 14.4 nm, E = -20 mV; a) I_t = 0.15 nA, U_b = 247 mV; b) I_t = 0.4 nA, U_b = 100 mV; c) I_t = 1.4 nA, U_b = 30 mV.

The same experiment is also done with the $[H_2TTMAPP]^{4+}$ adlayer on the chloride terminated Cu(100) electrode surface. In order to investigate the tip induced removal/restoration phenomenon a typical series of STM images observed at the same surface area but different tunneling conditions is shown in Fig.6.11. A full monolayer of $[H_2TTMAPP]^{4+}$ molecules is observed in the course of an experiment with “moderate” tunneling conditions as shown in Fig.6.11a with a characteristic square-like structure. Once the tunneling tip is brought close to the sample surface the $[H_2TTMAPP]^{4+}$ adlayer is swept away (Fig.6.11b) leaving the c(2 x 2)-Cl superstructure behind as seen in Fig.6.11c and the inset. Similarly, the $[H_2TTMAPP]^{4+}$ molecules re-assemble right after the tip is retracted from the sample surface like shown in Fig.6.10 for Cu(111), but not shown here again. Similar removal experiments of organic adsorbates from an anion terminated electrode surface have been reported in the literature [27,140,180].

6.3.4. Influence of electrode potentials on lateral ordering of $[H_2TTMAPP]^{4+}$

This section describes the lateral ordering of $[H_2TTMAPP]^{4+}$ molecules in the chloride de/readsorption and the copper dissolution regimes where the "underlying surface" is directly affected by the electrode potentials. While in the former the molecules are forced to undergo an order/disorder phase transition, in the later the adlayer is dissolved via corrosion of the copper surface.

6.3.4.1. Potential induced phase transition

As mentioned above porphyrin molecules undergo two separate reduction steps labeled as P_1 and P_2 (Fig.6.1 and Fig.6.3), respectively, in the potential window of the Cu(111) electrode which is expected to affect the ordering of the molecular overlayer. In order to prove this assumption the STM is employed to study changes of the lateral ordering upon shifting the electrode potential downwards through the corresponding reduction peaks. Fig.6.12 shows a series of STM images successively recorded at the same area while the working potential is adjusted from the right to the left side of the peak P_1 in Fig.6.3 and vice versa. The resulting STM images show an order/disorder phase transition taking place on the measured surface when the potential passed over the first reduction feature. While a full monolayer of the porphyrin molecules is observed at a potential of E = +10 mV (Fig.6.12a), the surface coverage of $[H_2TTMAPP]^{4+}$ adlayer is reduced due to the fact that $[H_2TTMAPP]^{4+}$ molecules desorb from the surface (Fig.6.12b) as the working potential approaches the reduction peak P_1, i.e. E = -170 mV vs RHE. Disordering of the lateral structure dominantly takes place at the step edges as well as at the domain boundaries where the intermolecular interaction and interaction between adsorbate and underlying chloride lattice are limited owing to lattice mismatching.

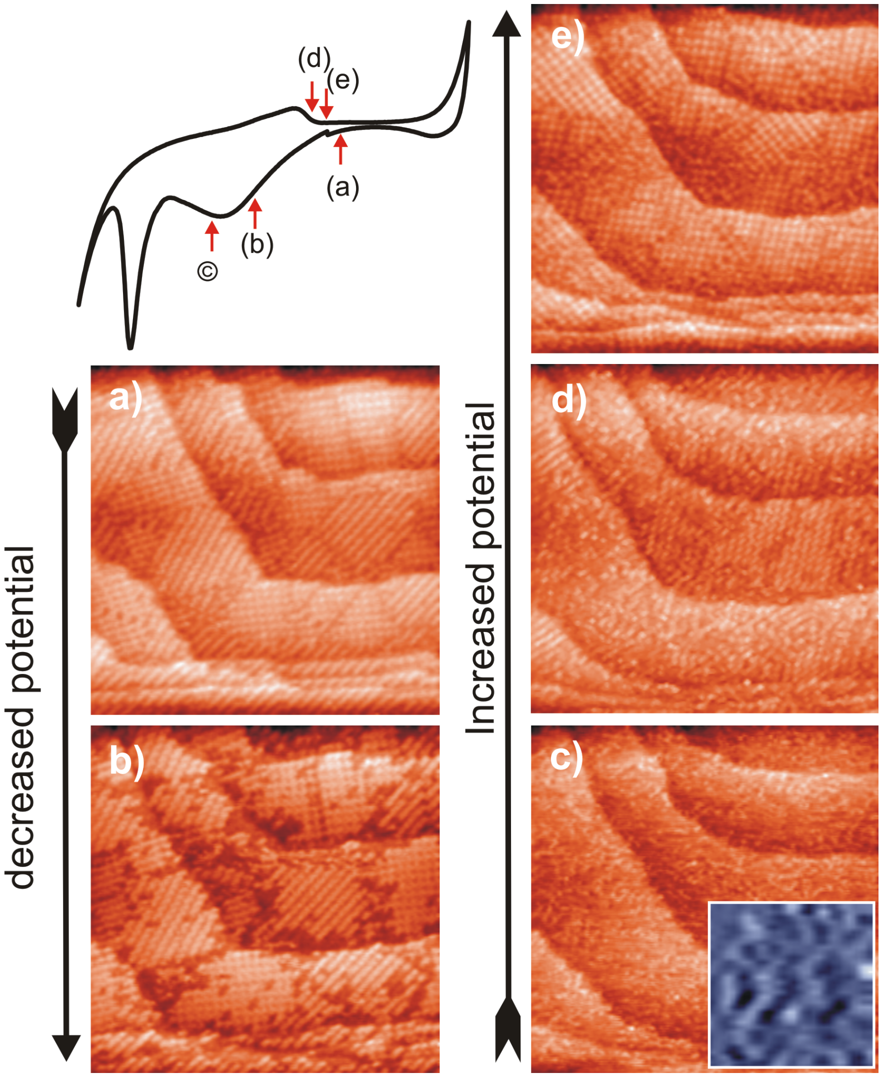

Figure 6.12: Surface reaction induced order/disorder phase transition of molecular adlayer on a chloride modified Cu(111) electrode surface, STM series: 76.82 nm x 76.82 nm; a) I_t = 0.1 nA, U_b = +274 mV, E = +10 mV; b) I_t = 0.1 nA, U_b = +275 mV, E = -170 mV; c) I_t = 0.1 nA, U_b = +276 mV, E = -240 mV;d) I_t = 0.1 nA, U_b = +298 mV, E = -45 mV; e) I_t = 0.1 nA, U_b = +386 mV, E = -35 mV.

The lateral ordering disappears completely from the surface when the electrode potential reaches E = -240 mV as seen in Fig.6.12c indicating that the ordered adlayer decays due to the fact that some $[H_2TTMAPP]^{4+}$ adsorbates escape from the surface and are transported back into the “bulk” solution leaving a disordered adlayer behind (inset in Fig.6.12c and see also coadsorption of H_2TTMAPP and DBV molecules in chapter 8). This phase transition within the porphyrin film appears plausible due to the fact that the delicate balance between the substrate-adsorbate and the adsorbate-adsorbate interactions is modified by the first electron transfer process that reduces the free base molecules $[H_2TTMAPP]^{4+}$ to the corresponding reduction products, i.e. the $[H_4TTMAPP(-II)]^{4+}$ species according to eq.6.1 (see section 6.2.3). As mentioned in the previous section, the first redox reaction of the $[H_2TTMAPP]^{4+}$ molecules is a quasi-reversible process with the re-oxidation peak at E = -30 mV. The oxidized product, i.e. the free base $[H_2TTMAPP]^{4+}$ species, are, therefore, expected to re-adsorb on the surface in order to restore the lateral ordering after sweeping the potential back into positive direction. Fig.6.12 d-e shows a restoration of the ordered adlayer of porphyrin molecules controlled by the electrode potential. While a partial lateral ordering is observed when the potential is held at E = -45 mV (Fig.6.12d) a full rearrangement of the ordered adlayer becomes stable, enclosing several distinguishable rotational domains as depicted in Fig.6.12e, when the applied potential is E = -10 mV. It was found that in both scan directions (cathodic and anodic sweeping) the structural surface phase transitions of the adsorbed porphyrin species are slower than the porphyrin redox-chemistry of solution species and, hence, revealing a significant potential hysteresis between the potential resulting in visible change in the STM images and that of the CV measurement.

In the case of a Cu(100) electrode, the order/disorder phase transition of $[H_2TTMAPP]^{4+}$ is similarly observed. For the observation of this phase transition a series of STM images was again recorded at the same surface area but decreasing the electrode potentials as illustrated in Fig.6.13. A highly ordered layer of $[H_2TTMAPP]^{4+}$ molecules with several mirror domains remains visibly stable at E = -25 mV vs RHE. However, when the working potential approaches the peak P_1 as mentioned above the $[H_2TTMAPP]^{4+}$ molecules start to leave from the surface, dominantly from places at domain boundaries (Fig.6.13b). The desorption process is accelerated at more negative potentials and, hence, the lateral ordering becomes almost completely destroyed (Fig.6.13c). A disordered film covering the electrode surface is observed at E = -260 mV (see Fig.6.13d and inset) indicating that the lateral ordering breaks down on the surface, the electrostatic adsorbate-substrate interactions weaken and, hence, the $[H_2TTMAPP]^{4+}$ molecules are no longer stabilized ontop of the electrode surface.

The phase transition is in fact quasi reversible, similar to the case of the Cu(111) electrode surface (as shown in Fig.6.12).

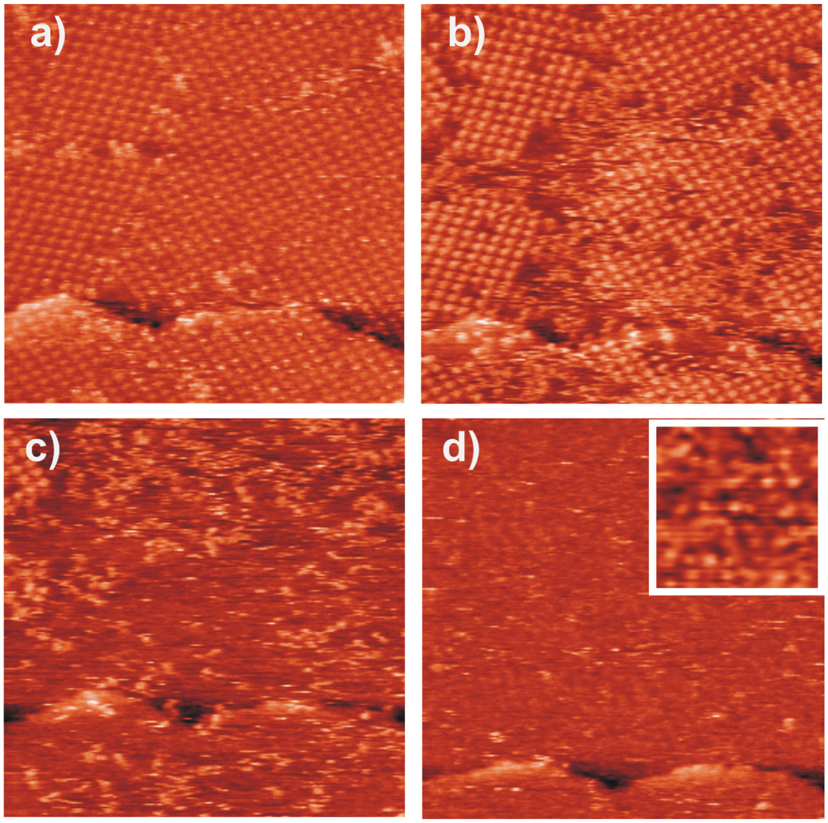

Figure 6.13: Surface reaction induced ordered/disordered phase transition of molecular adlayer on a chloride modified Cu(100) electrode surface, STM series: 57.62 nm x 57.62 nm, I_t = 0.1 nA; a) U_b = +235 mV, E = -25 mV; b) U_b = +246 mV, E = -160 mV; c) U_b = +246 mV, E = -230 mV;d) U_b = +246 mV, E = -260 mV, high resolution inset showing a disordered layer.

6.3.4.2. Potential induced copper dissolution reaction

Copper corrosion is observed as the working potential is moved positively through E = +90 mV vs RHE. In both cases of halide anions [98,211] and, in addition, molecules [30,104] modified copper surfaces, the corrosion mechanism is preferentially taking place at steps. For instance, the preferential corrosive direction is perpendicular to the step-edges in the case of Cu(100). In this section, the copper dissolution is studied for the first time on a Cu(111) surface in the presence of $[H_2TTMAPP]^{4+}$ organic molecules as the covering adlayer. In order to observe this process, a series of STM images is recorded at the same surface area but under different tunneling conditions as shown in Fig.6.14. Fig.6.14a shows a typical morphology of the $[H_2TTMAPP]^{4+}$ layer adsorbed on the Cu(111) electrode surface with three rotational domains and step directions rotated by 120° with respect to each other. In addition, six terraces labeled from 1 to 6, respectively, are inspected in order to investigate the dynamics of the corrosion process. As a result, as soon as the potential is increased to approach the corrosion regime as indicated in the inserted CV the step-edges predominantly change as follows: the upper terraces are the ones where the copper corrosion takes place predominantly. Moreover, the orientations, in which the corrosion process strongly proceeds, run parallel to the $\langle\bar{2}11\rangle$ directions (marked by white arrows in Fig.6.14b). Thus, the copper atoms are dissolved gradually resulting in a gradual decay of the upper terraces (Fig.6.14b÷d). Consequently, once the potential is increased by a step from E = +110 mV to E = +140 mV, terraces 4, 5 and 6 are removed successively out of the imaged area and, coincidently, terraces 1 and 2 are more and more enlarged (Fig.6.14e÷g). A drastic dissolution happens as indicated by a disordered and cloudy appearance on the whole surface if the working potential is slightly positively shifted (Fig.6.14h). Upon a negative re-adjustment of the potential, the corrosion intensity is visibly decreased manifesting itself by re-deposition of copper. Copper atoms redeposit at the step/edge resulting in a restoration of the chloride structure and the readsorption of organic molecules.

Astonishingly, the free copper cations released from the surface have not substituted the hydrogen atoms in the central porphyrin ring in order to form the corresponding $[CuTTMAPP]^{4+}$ species in a so called “metallization” reaction, which was observed in the case of adsorbed $[H_2TMPyP]^{4+}$ molecules [30]. Recalling the CV of the Cu(111) electrode in $[H_2TTMAPP]^{4+}$ containing electrolyte (Fig.6.2), two cathodic peaks describing the stepwise reduction from respective Cu^{2+} and Cu^{+} cations to neutral Cu atoms in the negative scanning direction are still persistent indicating that the dissolved copper ions are not consumed by insertion into the porphyrin core. The stronger impact of the $(CH_3)_3N^+$ groups in $[H_2TTMAPP]^{4+}$ on the electron density than that of the methyl groups in $[H_2TMPyP]^{4+}$ is assumed to enhance the bonding energy between the porphine ring and the hydrogen atoms. Consequently, free copper cations are not incorporated into the porphyrin molecules, but rather are re-deposited on the electrode surface via the following reactions:

$$Cu^{2+} + e^- \leftrightarrow Cu^+ + e^- \leftrightarrow Cu^0 \qquad (6.12)$$

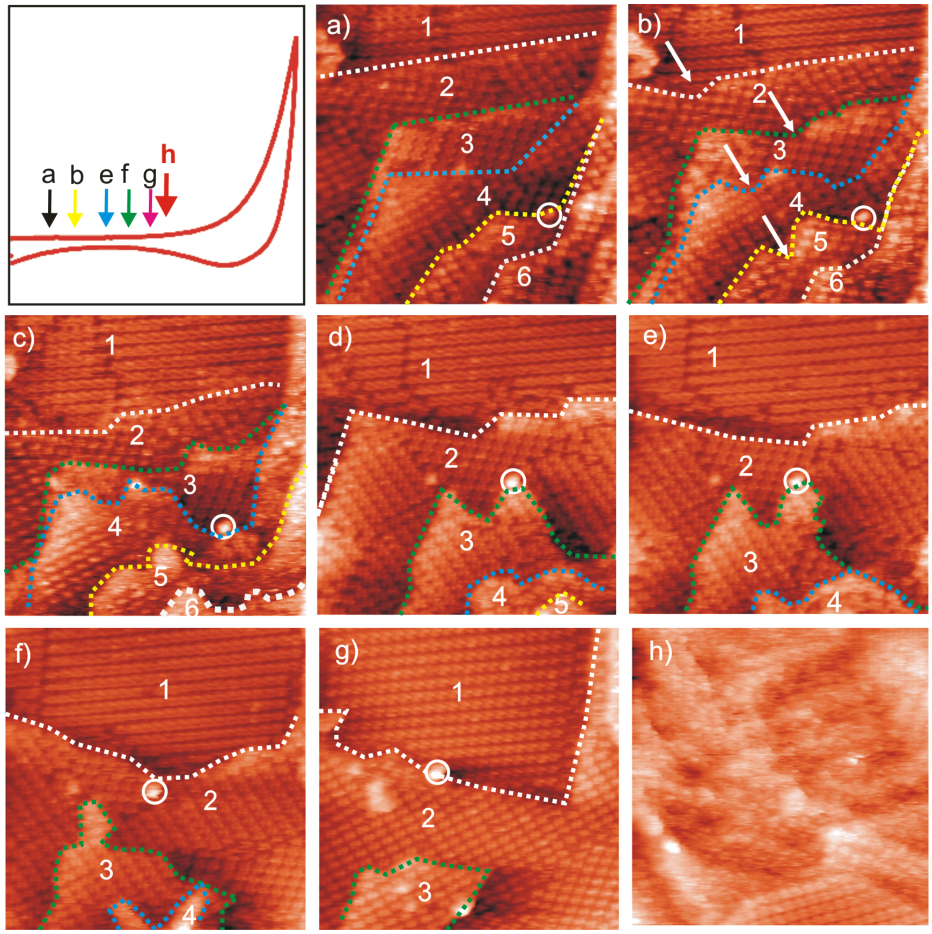

Figure 6.14: Copper dissolution in the presence of $[H_2TTMAPP]^{4+}$ on the Cu(111)/Cl, STM series: 43.21 nm x 43.21 nm, I_t = 0.1 nA, U_b = +275 mV; a) E = +70 mV; b) E = +90 mV; c-d) E = +105 mV; e) E = +110 mV; f) E = +125 mV; g) E = +140 mV; h) E = 143 mV. The feature indicated with white circle serves as marker for the same scanning area; the dashed lines describe the step deviations from the previous image.

6.3.4.3. Potential induced domain ripening

Before the onset of copper dissolution also a potential induced domain ripening is observed as marked by white ellipses in Fig.6.15. In the first stage observed at E = +45 mV, the molecular rows within the marked ellipse are aligned parallel to domain I which is oriented parallel to the $[\bar{2}11]$ direction (indicated by the dash white line in Fig.6.15a). By adjusting of working potential in positive direction, molecular rearrangement takes place, namely the molecular rows start to gradually rearrange their orientation by running now parallel along domain II, i.e. they tend to align parallel to the $[1\bar{2}1]$ direction denoted by the dashed arrows in Fig.6.15b. Finally, all molecular rows within the ellipse are re-aligned parallel to the domain II when the potential reaches E = +75 mV (Fig.6.15c). This indicates the competition between domains at domain boundaries in order to create a more stable state with less mismatch at domain boundaries.

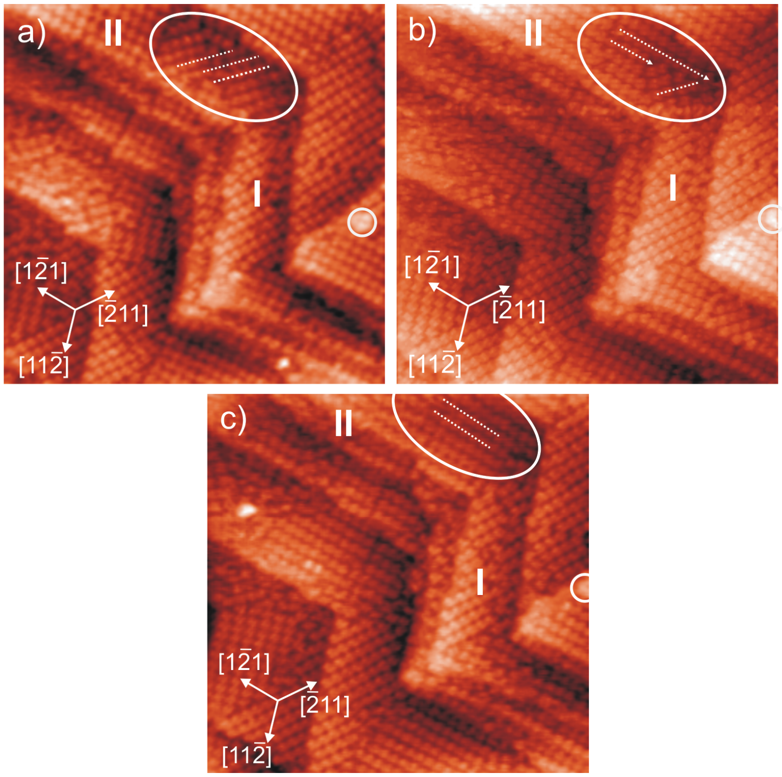

Figure 6.15: Domain reconstruction of $[H_2TTMAPP]^{4+}$ molecules at domain boundaries; STM series: 61.46 nm x 61.46 nm, I_t = 0.15 nA, U_b = +334 mV; a) E = +45 mV; b) E = +60 mV; c) E = +75 mV. White ellipses serve as markers for the same location; the dashed lines describe the molecular rows and their transition upon scanning.

6.3.6. Discussion

The adsorption of $[H_2TTMAPP]^{4+}$ molecules on a chloride modified copper electrode has been investigated by a combination of CVs and EC-STM. Unlike in former publications, the adsorption of the $[H_2TTMAPP]^{4+}$ molecules has been investigated in the whole potential window of Cu(111), i.e. under non-reactive conditions and at reactive conditions. Observations on the molecular adsorption, potential dependent phase conformations and transitions as well as the copper corrosion mechanism in the presence of molecules are presented depending on the working potential.

At non-reactive conditions, i.e. the measured potentials are more positive than E= -30 mV (P_1' peak), free base porphyrin molecules ($[H_2TTMAPP(0)]^{4+}$) strongly adsorb on both chloride modified Cu(111) and Cu(100) electrode surfaces and form a quasi-square lattice as seen in Fig.6.5 and Fig.6.7. Individual molecules are recognized as propeller like shapes with four bright lobes at the corners. These pronounced lobes are assigned to the four positively charged trimethylamonium phenyl groups attached to the porphyrin core whereas a visible vacancy hole is also observed in the molecular center. On the basis of the obtained STM results the $[H_2TTMAPP]^{4+}$ molecules are found to lie flat on the chloride template. In fact, flat orientations of porphyrin derivatives in the non-reactive potential regime were also reported in the literature [27-29,180-181] due to a combination of the large π-system of the porphyrin ring and the four positively charged groups at the corners. Therefore, in order to maximize the van der Waals as well as the electrostatic interactions an arrangement of the porphyrin rings parallel to the substrate is completely plausible.

The formation of lateral ordering of free base porphyrin molecules on Cu(111) and Cu(100) is from the electrochemical point of view governed by a delicate balance between molecule-substrate and molecule-molecule interactions. In terms of intermolecular interactions, in combination with the van der Waals interactions, electrostatic repulsion between the attached positively charge trimethlyamonium-phenyl groups is considered to play an important role in the self-organization of the $[H_2TTMAPP]^{4+}$ molecules. As a result, a typical rotation angle between the molecular axes and the direction of the molecular rows balancing the electrostatic repulsive forces is discernible. In contrast, the molecule-substrate interaction is considered to be responsible for surface diffusion or surface mobility which plays a key role for the molecular lateral ordering. In part, the adsorption of other porphyrin derivatives on metal surface has been investigated with iodide layers serving as the template [27-29]. Typically, the adsorbed layer of iodide anions on copper substrates is hydrophobic and uncharged [104]. Therefore, only the van der Waals type interactions are expected to play a role for the adsorption. In contrast to iodide, a chloride layer remains negatively charged upon adsorption [94]. Thus, the molecule-substrate interaction is controlled not only by the van der Waals interactions but also by the electrostatic interactions between the positively charged porphyrin ring and the specifically adsorbed chloride anion interlayer. However, the molecular arrangement of the self-assembled layer on a chloride terminated Cu(111) differs from that on the Cu(100) electrode surface evidently resulting from a modification of the delicate balance between the molecule-substrate and the molecule-molecule interactions.

The lateral ordering of $[H_2TTMAPP(0)]^{4+}$ on a chloride modified Cu(111) substrate is governed by the underlying chloride lattice, namely, the molecular rows are highly oriented along the chloride anion rows underneath even at step-edges (Fig.6.5), which coincide with highly symmetric directions of the Cu(111) substrate, i.e. the $\langle \bar{2}11 \rangle$ direction, as depicted in Fig.6.6. Obviously, the molecular close packed rows run parallel to the commensurate direction of the chloride lattice, hence, resulting in the formation of three equivalent rotational adsorbate domains on top. In contrast, the molecular rows of the $[H_2TTMAPP(0)]^{4+}$ adlayer on the Cl/Cu(100) electrode surface are parallel neither to the close packed atomic row of the underlying chloride anions nor to the high symmetry axes of the Cu(100) substrate. This clearly excludes a template effect of the Cu(100) substrate surface, but rather hints to a pure molecular self-assembly. Furthermore, the rotation angle between the symmetry axis of an individual molecule and the direction of the molecular row on the Cl/Cu(111) of 23° (Fig.6.6) is bigger than that of 19° on the Cl/Cu(100) substrate.

Obviously, the difference of surface orientation, i.e. (111) vs (100), is from the structural point of view, responsible for a non-equivalence of the molecule-substrate and the molecule-molecule electrostatic interactions taking place on the Cu(111) compared to that on the Cu(100). This is proven by the difference in domain orientations, the molecular row alignment and the self-rotational angle of individual molecules and, hence, a higher molecular density on the Cu(111) than on the Cu(100) surface.

In the present chapter, also the $[H_2TTMAPP(0)]^{4+}/Cl/Cu(111)$ as well as the $[H_2TTMAPP(0)]^{4+}/Cl/Cu(100)$ staking sequence have been investigated by a systematic alteration of the tunneling conditions (Fig.6.6, Fig.6.8, Fog.6.10, and 6.11) in order to elucidate the crucial role of the underlying anion lattice for the adsorption of organic molecules. Applying moderate tunneling conditions, i.e. high bias voltage and low tunneling current, the porphyrin adlayer on top is observed whereas under more drastic tunneling conditions, i.e. low bias voltage and high tunneling current, the organic layer is swept away leaving the chloride layer behind. In this particular sense, the tunneling tip acts as a potential controlled tool sweeping the organic molecular overlayer away. This is in accord with former reports [27,140] which used this approach in order to prove the existence either of an iodide layer underneath a porphyrin overlayer on Au(111) [27] or of a chloride layer under viologen films on Cu(100) [140].

Based on the electrochemical and microscopic results it could be proven that the electrode potential has visible influence on surface structure. By inducing the first reduction step by a two-electron transfer a phase transition is taking place from an ordered packing to a corresponding disordered phase (Fig.6.12 and 6.13). The ordered phase (phase I) is formed by strong adsorption of free base porphyrin molecules, i.e. the $[H_2TTMAPP(0)]^{4+}$ species. In contrast, the amorphous phase is built up by reduced species ($[H_4TTMAPP(-II)]^{4+}$), formed according to eq.6.2 and/or eq.6.3 in subsection 6.2.1. Consequently, the lateral ordering observed at non-reactive conditions is converted into a disordered phase as seen at Fig.6.12c and 6.13c when the first reduction takes place. On the basis of the observed STM results it can be concluded that the change in the lateral ordering of the porphyrin adlayer appears due to a modification in the delicate balance between the substrate-adsorbate and the adsorbate-adsorbate interactions caused by the electron transfer processes. Obviously, the positive charge on the reduced species, i.e. $[H_4TTMAPP\ (-II)]^{4+}$, is lower than on the free base $[H_6TTMAPP\ (0)]^{4+}$. Therefore, the electrostatic interaction to the chloride interlayer is considerably reduced when the $[H_2TTMAPP]^{4+}$ molecules undergo the first reduction step resulting in an increased mobility of the reduced species on the electrode surface.

Our results may be compared to the adsorption of $[H_2TMPyP]^{4+}$ molecules on chloride modified Cu(100) [30] and Cu(111) [31] surfaces under reactive conditions. It has been found that in both cases of copper electrodes used, the reduced species of the H_2TMPyP molecules adsorb more strongly than that of the present molecules. Indeed, while a somehow ordered structure was observed in case of the Cu(100) surface, an ill-ordered double layer of the $[H_2TMPyP]^{4+}$ was visible on the Cu(111) substrate. This hints to the impact of the side groups on the polarization as well as the delocalization of the π-system in porphine rings which result in a reduction of the adsorbate-substrate interactions and the immobilization of the reduced states of the present $[H_6TTMAPP (0)]^{4+}$ molecules.

A further reduction of the reduced species relating to the last four-electron transfer step results in the formation of the corresponding reduction products. However, potentials, where this step is taking place, are close to the chloride desorption regime (Fig.6.2). The CV observations show that the chloride desorption occurs before this second reduction step of the $[H_2TTMAPP]^{4+}$ molecules. Consequently, for the further reduced molecules, i.e. $[H_8TTMAPP(-VI)]^{4+}$, ordered structures are not observed by STM measurement due to the chloride desorption. In addition, while the CV of Cu(111) in pure HCl electrolyte shows a sharp and less intensive peak P_2 corresponding to the chloride desorption at E_d = -395 mV, this peak appears more negative by about 20 mV when the Cu(111) electrode is in contact with the $[H_2TTMAPP]^{4+}$ containing electrolyte (Fig.6.2b). From the electrochemical point of view, the chloride desorption process is hindered in the presence of the molecular overlayer, i.e. $[H_4TTMAPP(-II)]^{4+}$ and $[H_8TTMAPP(-VI)]^{4+}$, on the Cu(111) surface. The $[H_8TTMAPP(-VI)]^{4+}$ is believed to be of low solubility and, hence, accumulates on top of the chloride terminated Cu(111) electrode surface [31]. In order to circumvent the influence of the de/adsorption processes of the anions, bromide or iodide anions were mostly employed because they do not desorb within the potential window of copper [83,169]. The preadsorbed bromide layer on the Cu(111) surface has been found to be stable in the whole potential window of copper with a $(\sqrt{3} \times \sqrt{3})R30$ superstructure [104,188]. The adsorption of the $[H_2TTMAPP]^{4+}$ molecules on a bromide modified Cu(111) electrode as well as the charge transfer induced phase transition will be discussed in the following sections.

Concerning the copper dissolution phenomenon, a copper incorporation into the adsorbed porphyrin molecules which was shown to take place with $[H_2TMPyP]^{4+}$ molecules [30] was not observed here. This is interpreted to be due to the presence of the four highly polarized trimethylamonium groups, i.e. $(CH_3)_3N^+$ [171]. Compared to $[H_2TMPyP]^{4+}$, the ligands are larger in the present case. Moreover, trimethylamonium $(CH_3)_3N^+$ is well known to be a strong polar group. While the polar effects of the methyl (CH_3) substituents on the $[H_2TMPyP]^{4+}$ molecules are close to zero, the influence of the $(CH_3)_3N^+$ groups in the $[H_2TTMAPP]^{4+}$ is accountable [179]. Consequently, the $(CH_3)_3N^+$ groups tend to prevent electrons in the porphine ring from delocalization, resulting in the alteration of the electrochemical behavior as observed.

6.4. Anion template effect

6.4.1. Introduction

The aim of this section is to examine the influence of different anion templates on the formation and ordering of $[H_2TTMAPP]^{4+}$ molecular adlayers due to differences in the electrostatic characteristics. It is well understood that, in contrast to chloride anions which remain negatively charged after adsorption, iodide and bromide anion adlayers on copper electrode surfaces are largely uncharged [138]. The delicate interaction between the positively charged organic molecules and the underlying anion template is, therefore, changed resulting in a plausible alteration of the lateral ordering on top.

Besides, as mentioned in sub-section 3.3.6, sulfate anions strongly adsorb on a Cu(111) surface and form an incommensurate superstructure in which both the sulfate anions and water molecules are co-adsorbed. And, hence, an additional goal is to investigate the influence of more complex anion layers on the ordering of the $[H_2TTMAPP]^{4+}$ adlayer.

6.4.2. $[H_2TTMAPP]^{4+}$ on Br/Cu(111)

Figure 6.16 describes typical CVs of a Cu(111) in pure supporting HBr electrolyte (dashed grey curve) and in electrolyte containing $[H_2TTMAPP]^{4+}$ molecules (solid black curve). Similar to the CVs of the Cu(111) in pure chloride solution (10 mM HCl) presented in sub-section 6.2.2, this CVs is also limited by two typical reactions, i.e. (i) the reductive hydrogen evolution reaction (HER) in the negative limit and (ii) the oxidative copper dissolution reaction (CDR) in the positive limit. Bromide desorption/readsorption peaks also appearing in the potential window of the Cu(111) are in agreement with Itaya et al [109]. The CV of the Cu(111) surface in the $[H_2TTMAPP]^{4+}$ containing electrolyte shows modifications occurring at potentials close to the HER. This observation is consistent with CV results obtained using a mixture of $[H_2TTMAPP]^{4+}$ and chloride anions as the working electrolyte mentioned in the previous sections. Consequently, the $[H_2TTMAPP]^{4+}$ molecules also undergo several reduction steps to form the corresponding reductive species once the Cu(111) surface is brought into contact with the $[H_2TTMAPP]^{4+}$ containing bromide electrolyte. For detail see section 6.2.3 - discussion.

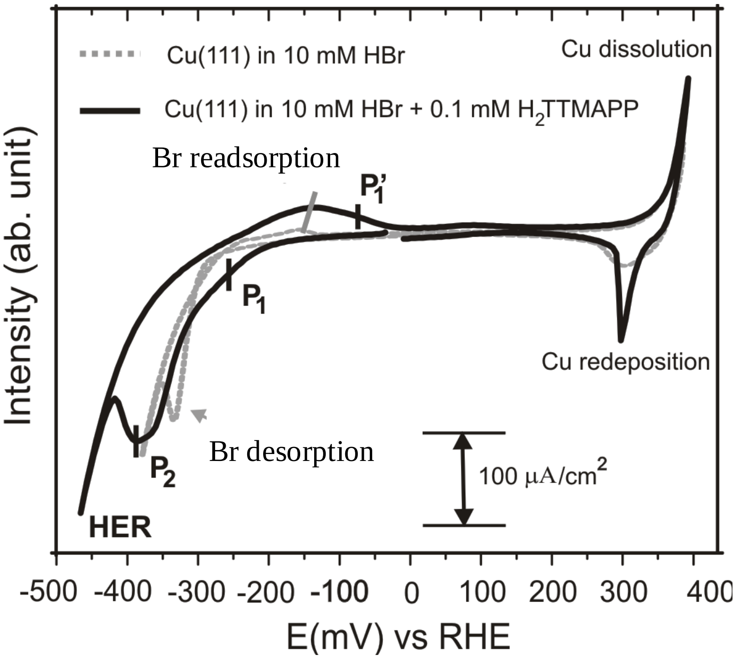

Figure 6.16: Cyclic voltammogams of Cu(111) in pure 10 mM HBr (dashed grey curve) and in electrolyte containing $[H_2TTMAPP]^{4+}$ molecules (solid back curve).

For the adsorption of the $[H_2TTMAPP]^{4+}$ molecules the same procedure as described in section 6.3.1 is applied. Thereafter, the bromide covered Cu(111) surface is imaged first by STM in order to confirm the presence of this anion layer on the measured surface. The bromide anions are known to form also an ordered $c(p \times \sqrt{3})$ on the Cu(111). In addition, the step-edges are observed to run parallel to the close-packed rows of the bromide anions, i.e. to run preferentially along the $\langle\bar{2}11\rangle$ directions of the Cu(111) substrate [188].

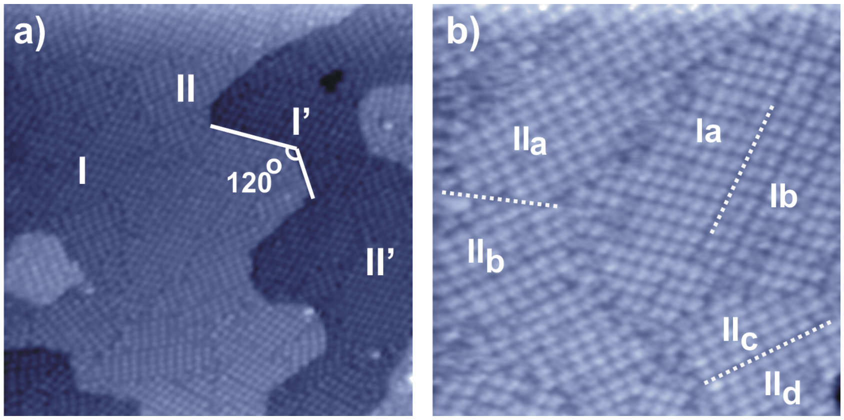

Figure 6.17: (a) Large scale STM image showing a full monolayer of $[H_2TTMAPP]^{4+}$ molecules adsorbed on a bromide modified Cu(111): 78.6 nm x 78.6 nm, I_t = 0.1 nA, U_b = 280 mV, E = +20 mV; (b) Medium scale STM image consisting of two rotational domains as well as translational domains: 35.4 x 35.4 nm, I_t = 0.1 nA, U_b = 280 mV, E = +20 mV.

By changing the pure HBr electrolyte for an electrolyte containing the $[H_2TTMAPP]^{4+}$ molecules within the double layer regime, the $[H_2TTMAPP]^{4+}$ molecules spontaneously adsorb on the Br/Cu(111) template and form a laterally ordered monolayer as described in Fig.6.17a. Step-edges crossing each other by an angle of 120° indicate that the bromide layer remains stable on the Cu(111) surface. Additionally, two rotational molecular domains enclosing an angle of 120 ± 2° reflecting the substrate symmetry of the underlying Cu(111), are also observed. This indicates that the molecular rows of each domain are aligned parallel to the close packed bromide rows underneath which run along the $\langle\bar{2}11\rangle$ directions of the Cu(111) substrate [104,188]. A closer view into a higher resolution STM image, represented in Fig.6.17b, shows that in company with detailed rotational domains denoted I and II, respectively, there are several co-existing translational domains as well. Focussing on domain boundaries, two different kinds of domain boundaries are distinguished. Namely, the first kind of boundaries runs parallel to the molecular rows within domains indicated by dash white lines, e.g. those between sub-domains Ia and Ib, IIc and IId. The distance between two nearest molecular rows of these domain boundaries seems to be slightly large than that within individual domains. The second kind of translational domain boundaries is considered to be aligned along √3 directions of the molecular rows, e.g. the boundary between IIa and IIb, and, hence, run parallel to the close packed Cu atom rows of the Cu(111) substrate underneath.

Figure 6.18a shows a detailed structure of the $[H_2TTMAPP]^{4+}$ adlayer with partly submolecular resolution. Similar to the case of the Cl/Cu(111) template, molecules within each domain arrange in rows. Individual molecules are recognized as a rectangle instead of a square shape as indicated in fig.6.18a which rotate by an angle of 12 ± 1°with respect to the molecular rows. A plausible interpretation is due to an electronic effect. Indeed, the STM images display the electronic charge density of molecules and, thus, a delicate change of the electronic charge density can result in a modification of the molecular shape as seen in this case.

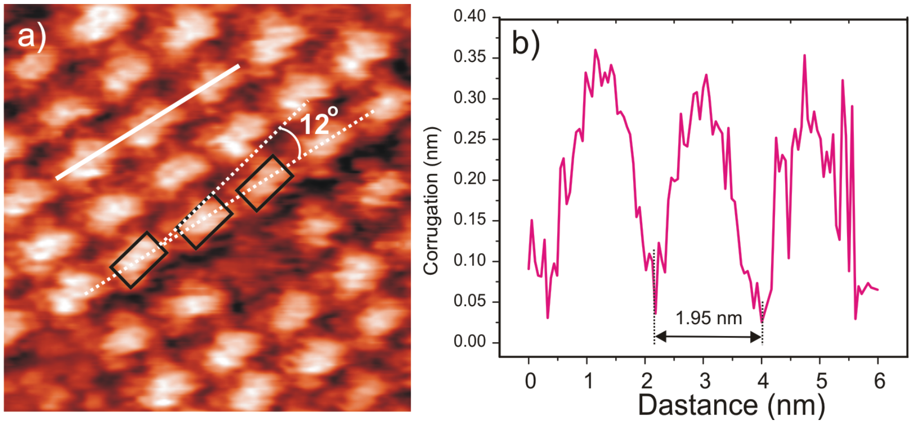

Figure 6.18: a) High resolution STM image of an $[H_2TTMAPP]^{4+}$ adlayer on a bromide terminated Cu(111) in which each molecule is recognized with a rectangular shape: 15.36 x 15.36 nm, I_t = 0.1 nA, U_{bias} = 222 mV, E = -50 mV; b) Line profile recorded along the white line in Fig.6.18a indicates an intermolecular distance of 1.95 ± 0.1 nm.

6.4.3 $[H_2TTMAPP]^{4+}$ on I/Cu(111)

For the adsorption of $[H_2TTMAPP]^{4+}$ molecules on the I/Cu(111) template, the experimental procedure is the same as in the Br/Cu(111) case, i.e. the pure electrolyte was replaced by one containing both the iodide and the $[H_2TTMAPP]^{4+}$ molecules at a potential within the double layer regime. Note, in case of the iodide anions serving as template the measured potential is always kept lower than +100 mV vs RHE in order to avoid the formation of a 3D CuI film due to copper dissolution [54,104,169].

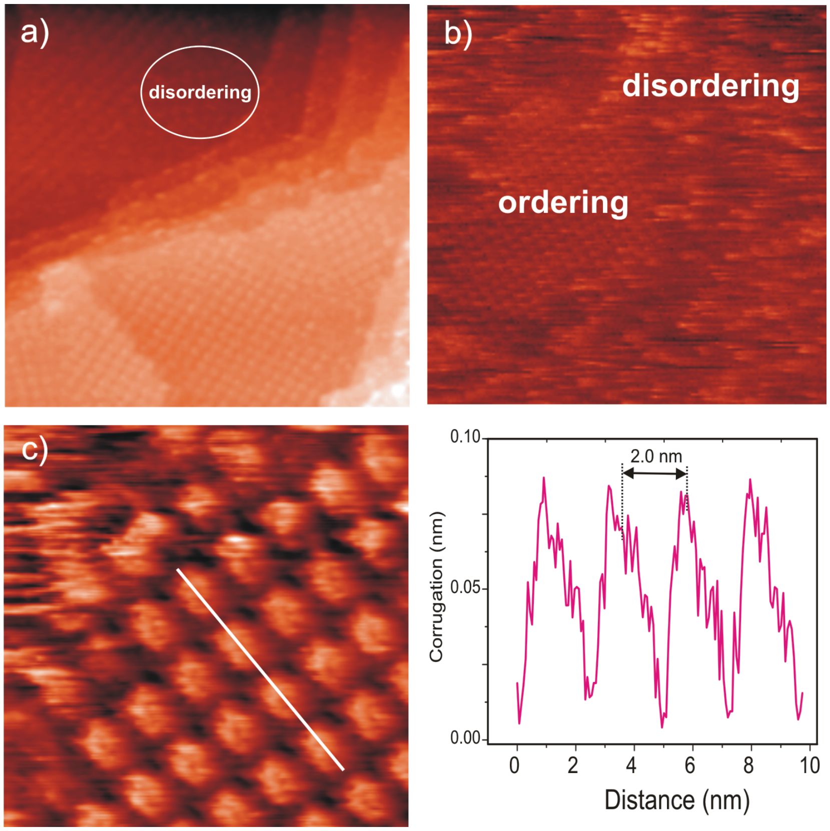

Figure 6.19: a) Large scale STM image showing a sub-monolayer of $[H_2TTMAPP]^{4+}$ molecules adsorbed on an iodide modified Cu(111) surface: 64.24 nm x 64.24 nm, I_t = 0.1 nA, U_{bias} = 200 mV, E = -20 mV; (b) Medium scale STM image consisting of two distinguishably ordered and disordered domains : 60.4 x 60.4 nm, I_t = 0.2 nA, U_{bias} = 280 mV, E = -20 mV; c) High resolution STM image showing rectangularly shaped adsorbed $[H_2TTMAPP]^{4+}$ species on the I/Cu(111) surface: 14.4 x 14.4 nm, I_t = 0.1 nA, U_{bias} = 200 mV, E = -20 mV; d) Line profile recorded along the white line in Fig.c indicates the intermolecular distance to be 2.0 ± 0.1 nm.

Fig.6.19 describes the surface morphology of the $[H_2TTMAPP]^{4+}$ adlayer on an iodide modified Cu(111) surface right after the electrolyte exchange took place. It can be seen that lateral ordering occurs only partly and, hence, results in the formation of disordered sub-areas as marked by white cycles (Fig.6.19a). In an attempt to achieve full ordering of the $[H_2TTMAPP]^{4+}$ adlayer the system was kept stable for hours within the double layer regime of the Cu(111) substrate. However, the ordering process of the $[H_2TTMAPP]^{4+}$ film came to a standstill, i.e. one can not observe a full ordered monolayer of the $[H_2TTMAPP]^{4+}$ molecules on the I/Cu(111) template under the conditions which did lead to complete ordering on the other two halide layers, i.e. chloride and bromide. This indicates the interactions with the substrate are only of the weak van der Waals type between the positively charged $[H_2TTMAPP]^{4+}$ molecules and the uncharged iodide layer underneath. A high resolution STM image of an ordered patch of the $[H_2TTMAPP]^{4+}$ molecules is shown in Fig.6.19c. Individual molecules are realized as a rectangle (marked in black) and form close packed molecular rows (dash-white line). This observation is similar to the case of the $[H_2TTMAPP]^{4+}$ overlayer on the Br/Cu(111) template mentioned in section 6.4.2.

6.4.4. $[H_2TTMAPP]^{4+}$ on SO_4^{2-}/Cu(111)

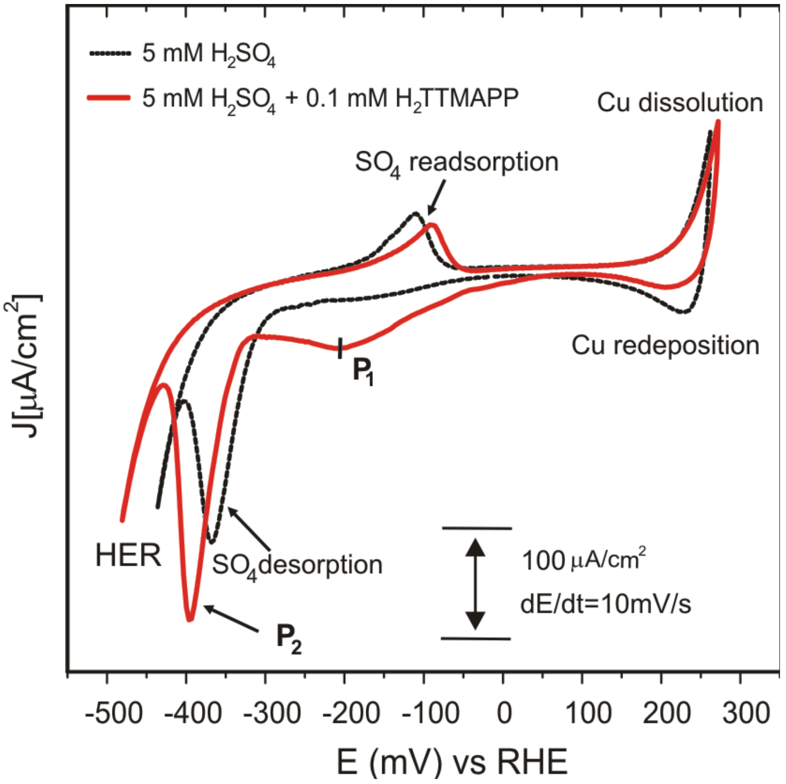

Figure 6.20: Typical cyclic voltammograms of Cu(111) in 5 mM H_2SO_4 (dash black curve) and in 5 mM H_2SO_4 + 0.1 mM $[H_2TTMAPP]^{4+}$ (red curve), dE/dt = 10 mV/s.

Finally, a more complex anion layer is employed as the template for the adsorption of the $[H_2TTMAPP]^{4+}$ molecules. On a Cu(111) substrate sulfate anions strongly adsorb and form a commensurate long-range Moiré superstructure. In addition, water molecules are considered to co-adsorb with the sulfate anions forming “zig-zag” rows between the sulfate anions [186]. For details see section 3.3.6 as well as ref.205 and papers cited therein. On the basis of this more complex template, the electrochemical behavior and structural properties of the $[H_2TTMAPP]^{4+}$ molecules on a sulfate modified Cu(111) electrode surface are expected to be different from those found on the Cl/Cu(111), Br/Cu(111) and I/Cu(111) templates.

Fig.6.20 shows representative steady state CVs of Cu(111) in the absence (dashed black curve) and the presence (red curve) of $[H_2TTMAPP]^{4+}$ molecules in solution. Similar to CVs in other anion containing electrolytes, the potential window of the Cu(111) electrode in the pure supporting electrolyte (5 mM H_2SO_4) is limited by two chemical reactions: (i) the reductive hydrogen evolution reaction at the cathodic limit and, (ii) the oxidative copper dissolution reaction at the anodic limit. Besides these two typical current peaks, also sulfate desorption/readsorption peaks are observed in this CV denoted by $P_{SO4\text{-}de}$ and $P_{SO4\text{-}read}$. The same CV was obtained by Broekmann et al. [85,186] and recently Hai et al. [30]. A drastic change in the CV curve is observed after replacing the pure supporting electrolyte by one containing $[H_2TTMAPP]^{4+}$ cations. The derivations are on the one hand the appearance of two new cathodic peaks P1 and P2 and on the other hand a shift of the sulfate readsorption peak toward positive potential. These changes have to be assigned to the presence of the $[H_2TTMAPP]^{4+}$ molecules and the reduction processes discussed in detail in section 6.2.3.

For the adsorption the $[H_2TTMAPP]^{4+}$ containing electrolyte is directly introduced into the cell at potentials where the sulfate anions have already adsorbed on the Cu(111) surface.

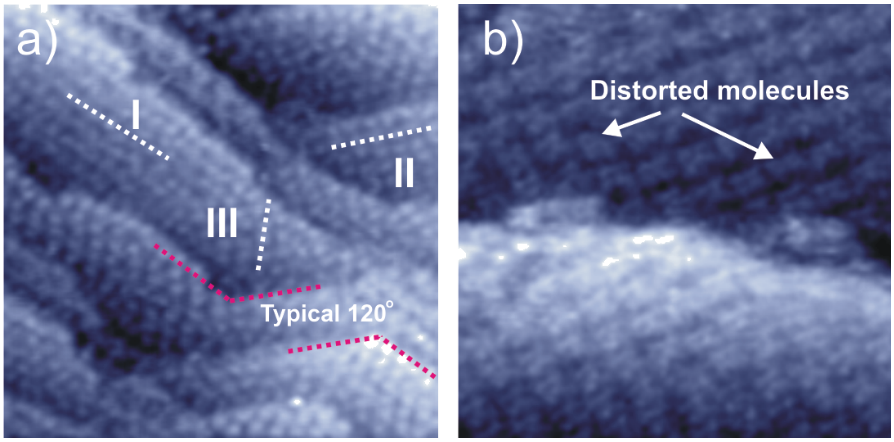

Figure 6.21: (a) Typical large scale STM image of an $[H_2TMPyP]^{4+}$ adlayer on a sulfate modified Cu(111) surface including three rotational domains rotated by an angle of 120° : 61.64 nm x 61.64 nm, I_t = 0.1 nA, U_b = 208 mV, E = +30 mV; (b) High resolution STM image showing a square shaped lattice in which each molecule could be recognized as a square; there are also some distorted molecules indicated by white arrows: 22.14 nm x 22.14 nm, I_t = 0.15 nA, U_b = 276 mV, E = +30 mV.

Fig. 6.21 shows typical large scale and medium level STM images, recorded at “moderate” tunneling conditions (I_t = 0.1 nA, U_{bias} = 208 mV), in which the step directions enclose angles of 120° reflecting the symmetry of the Cu(111) substrate. There are several rotational domains co-existing on the imaged area as marked by I, II and III, respectively (Fig.6.21a). The higher resolution STM image in Fig.6.21b provides the arrangement of the molecules as well as their orientation. Similar to the previous cases, molecules within one domain arrange in rows and individual molecules are rotated by an angle of 17 ± 1° with respect to the direction of the molecular row (indicated by white dotted lines in Fig.6.22a). However, molecules appear in different shapes and sizes on the same terrace. Indeed, some molecules are visibly smaller and distorted (marked by white arrows in Fig.6.21b and circles in Fig.6.22a) than others with the normal square shape. A reasonable explanation for this difference of the molecular sizes and shapes is the assumption that molecules are located at non-equivalent adsorption sites on the underlying periodic Moiré sulfate structure. Therefore, molecules can be flatly located at either the valleys, the slopes or the hill sites of the Moiré structure. Furthermore, different orientations of the molecular plane with respect to the electrode surface, which may lead to the different molecular appearance difference, is a further plausible reason. Those $[H_2TTMAPP]^{4+}$ molecules that are not flat-lying but tilted on the Moiré structure may appear differently in the STM images. This phenomenon was also observed in the case of SO_4/Cu(111) serving as the template for the adsorption of $[H_2TMPyP]^{4+}$ molecules [31].

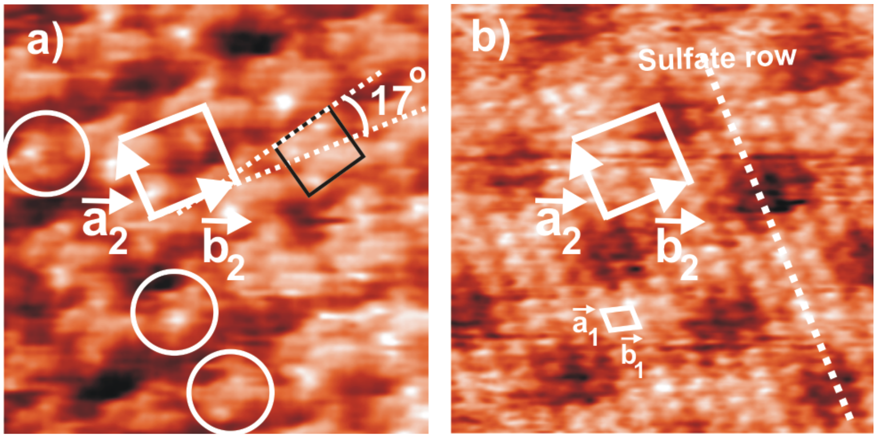

Figure 6.22: Structural relation between $[H_2TTMAPP]^{4+}$ adlayer and a sulfate lattice underneath, a) 10.7 nm x 10.7 nm, $I_t = 0.15$ nA, $U_b = 275$ mV, E = +30 mV; b) 10.7 nm x 10.7 nm, $I_t = 0.8$ nA, $U_b = 106$ mV, E = +30 mV; c) Superposition of panel a and b with unit cell containing 1 molecule.

High resolution STM images describing the correlation between the $[H_2TTMAPP]^{4+}$ adlayer and the underlying Moiré sulfate lattice are shown in Fig.6.22. These figures are recorded at the same surface area but again under different tunneling conditions. Under “soft” tunneling conditions (low tunneling current and high bias voltage) the tunneling tip is far from the measured electrode surface and, hence, one can image the topmost molecular adlayer as represented in Fig.6.22a. In contrast, with “hard” tunneling conditions (high tunneling current and low bias voltage) the tunneling tip-sample separation is shortened. Consequently, the tunneling tip sweeps the $[H_2TTMAPP]^{4+}$ molecules away leaving the Moiré sulfate lattice behind (Fig.6.22b). Based on this graphical correlation it can be seen that the close packed rows of the $[H_2TTMAPP]^{4+}$ molecules run parallel to sulfate close packed rows underneath. By symmetry reason, three rotational domains of the $[H_2TTMAPP]^{4+}$ adlayer are expected reflecting the substrate symmetry of Cu(111). It is evident that the structural formation of the $[H_2TTMAPP]^{4+}$ layer is “templated” by the SO_4^{2-} lattice underneath resulting in the formation of the three symmetric rotational domains. The sulfate anions adsorb on Cu(111) forming a quasi $(\sqrt{3}\times\sqrt{7})$ superstructure [85,186]. The unit cell of this lattice $(\vec{a}_1,\vec{b}_1)$ is depicted in Fig.6.21b with $|\vec{a}_1|$ = 0.47 ± 0.01 nm and $|\vec{b}_1|$ = 0.70 ± 0.01 nm [186]. Using this $(\sqrt{3}\times\sqrt{7})$ superstructure as an internal calibration lattice one can describe the $[H_2TTMAPP]^{4+}$ unit cell $(\vec{a}_2,\vec{b}_2)$, shown in Fig.6.22a, by a transformation matrix as follows:

$$(\sqrt{3}\times\sqrt{7})SO_4^{2-} - \begin{vmatrix}4 & 0\\ 1 & 3\end{vmatrix} - [H_2TTMAPP]^{4+}$$

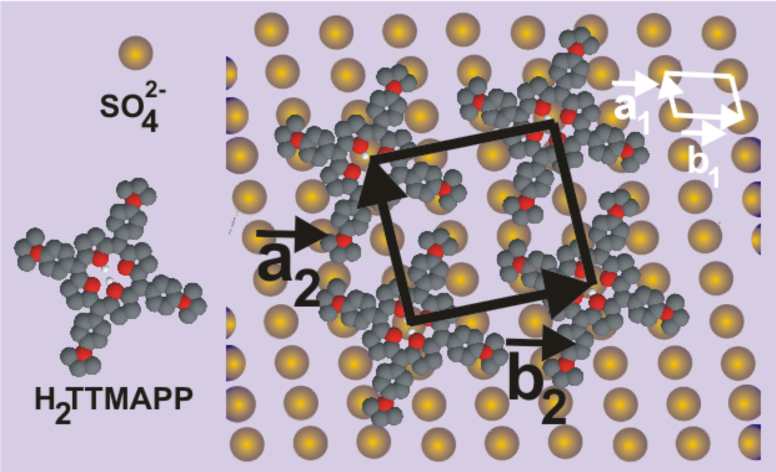

Figure 6.23: Structural model of $[H_2TTMAPP]^{4+}$ molecules adsorbed on a sulfate modified Cu(111) electrode surface.

A possible model describing the adsorption of $[H_2TTMAPP]^{4+}$ species on a sulfate modified Cu(111) electrode surface is proposed in Fig.6.23. On the basis of the internal calibration lattice $(\vec{a}_1,\vec{b}_1)$ one can calculate the lattice vectors building up a unit cell of the $[H_2TTMAPP]^{4+}$ adlayer to be $|\vec{a}_2|$ = 1.88 ± 0.01 nm and $|\vec{b}_2|$ = 2.16 ± 0.1 nm enclosing an angle of 92°. The molecular coverage per domain is about 0.083 ML with respect to the sulfate lattice or 2.46 x 10^{13} molecules/cm^2.

As mentioned above and from other reports [85-87,105,106,186] it becomes evident that sulfate adsorption and desorption are reversible and can be observed by both the CV and the STM measurements. The reversible pair of peaks is pronounced in both cases of absence and presence of $[H_2TTMAPP]^{4+}$

molecules and the presence or absence of the SO_4^{2-} layer plays a dominant role in the formation of the $[H_2TTMAPP]^{4+}$ adlayer.

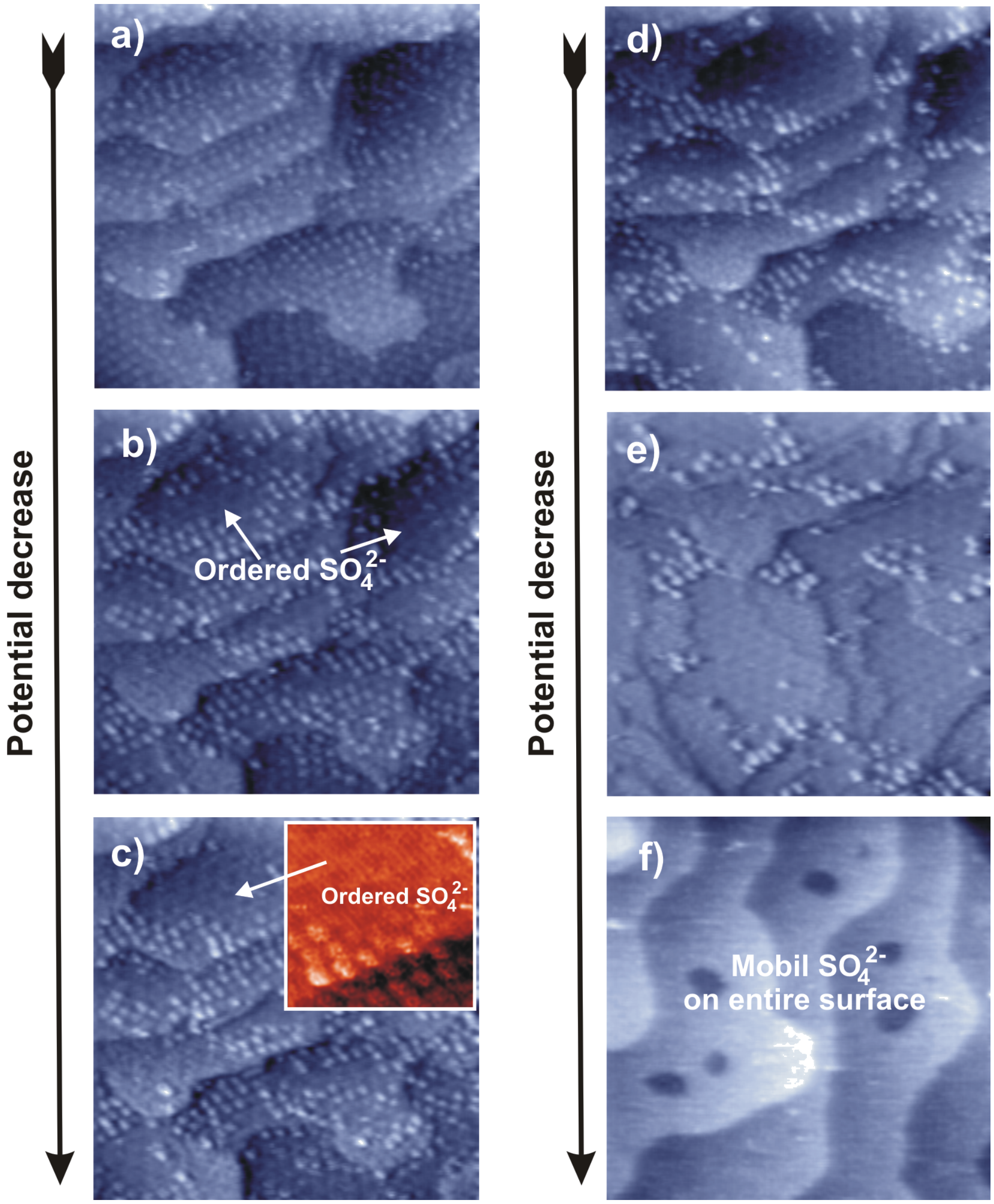

Figure 6.24: Potential induced co-desorption of $[H_2TMPyP]^{4+}$ and sulfate layer, 57.62 nm × 57.62 nm, U_b = 215 mV, I_t = 0.1nA, a) E = -180 mV; b) E = -190 mV; c) E = -200 mV; d) E = -215 mV; e) E = -230 mV; f) E = -250mV vs RHE.

The series of STM images recorded at the same surface area but at different electrode potentials shows the co-desorption process of both the sulfate anions and the $[H_2TTMAPP]^{4+}$ molecules. In Fig.6.24a the $[H_2TTMAPP]^{4+}$ molecules are recognized as bright dots covering the whole SO_4^{2-}/Cu(111) template at E = -180mV. By decreasing the electrode potential the $[H_2TTMAPP]^{4+}$ molecules start to desorb from the surface (indicated by white arrows in Fig.6.24b). The co-desorption process is accelerated upon applying more negative potentials as seen in Fig.6.24c to e and completed at E = -250 mV (Fig.6.24f). The typical disoriented step-edges are observed for the Cu(111) surface right after the co-desorption process and even the positively charged $[H_2TTMAPP]^{4+}$ molecules are no longer adsorbed on the bare Cu(111) substrate. This is in complete agreement with results from Hai et al. [30,187] on the adsorption of $[H_2TMPyP]^{4+}$ molecules on I/Cu(100) and SO_4^{2-}/Cu(111). However, in the present case the desorption of the $[H_2TTMAPP]^{4+}$ molecules is due to the first reduction process of the molecules as mentioned in the previous sections. Indeed, the first reduction of the molecules occurs at a potential around E = -210 mV resulting in the phase transition from an ordered pattern to a disordered phase in which the reduced species, i.e. $[H_4TTMAPP(\text{-II})]^{4+}$, are forced to desorb from the surface even though the sulfate layer is still present on the Cu(111) surface as shown in the inset of Fig.6.24c. The influence of the sulfate desorption on the $[H_2TTMAPP]^{4+}$ layer is, therefore, unclear. The whole desorption is, thus, a sequence of processes as follows: (i) firstly, the $[H_2TTMAPP]^{4+}$ molecules desorb from the ordered SO_4^{2-}/Cu(111) surface due to their first reduction step and (ii) secondly, desorption of the ordered SO_4^{2-} layer underneath occurs leaving the adsorbate free Cu(111) surface behind as observed in Fig.6.24f.

In the reverse scan, the SO_4^{2-} anions are forced to readsorb forming again the laterally ordered SO_4^{2-} Moire structure, thereby enabling $[H_2TTMAPP]^{4+}$ readsorption as shown in Fig.6.25.

At E = -245 mV the typical Cu(111) surface with disoriented step-edges is observed (Fig.6.25a). At this potential it is not possible to image any porphyrin molecules located on the surface under whatever tunneling conditions. The Moiré structure is restored gradually by changing the electrode potential positively as marked by white arrows in Fig.6.25b. As a consequence, together with the Moiré structure $[H_2TTMAPP]^{4+}$ molecules start to readsorb on top of areas where SO_4^{2-} anions are immobilized rather than on the Moiré free copper surface (Fig.6.25b). After the electrode potential reaches E = -70 mV the whole surface is again covered by the SO_4^{2-} anions. However, there are some areas which are still free of molecules indicated by a white arrow in Fig.6.25c. This observation reveals that the $[H_2TTMAPP]^{4+}$ molecules readsorb only after the re-formation of the sulfate/water Moiré layer.

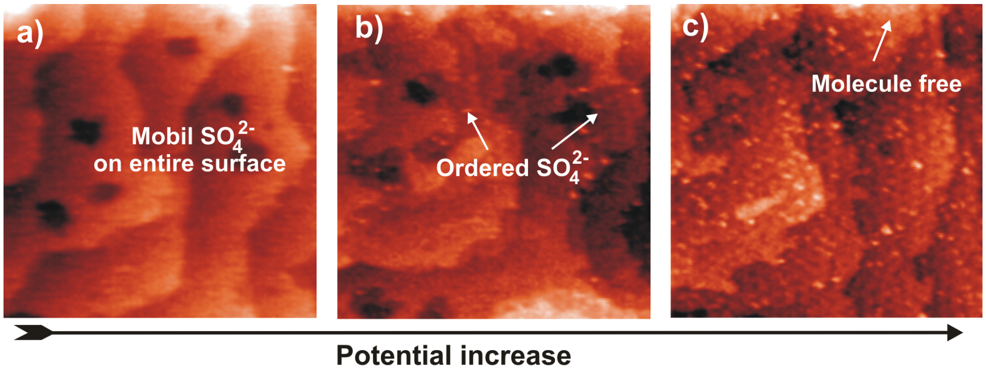

Figure 6.25: Potential induced coadsorption of $[H_2TTMAPP]^{4+}$ and SO_4^{2-} anions on a Cu(111) surface: 57.62 nm × 57.62 nm, U_b = 215 mV, I_t = 0.1nA, a) E = -245 mV; b) E = -167 mV; c) E = -70 mV vs RHE.

6.4.5. Discussion

With the four anion templates chosen, i.e. the chloride, bromide, iodide and sulfate modified Cu(111) surface, for the adsorption of $[H_2TTMAPP]^{4+}$ molecules it becomes evident one more time the predominant role of the anion layer underneath for the immobilization and the formation of an ordered adlayer of positively charged organic cations on metal surfaces such as porphyrins. Although all four anions facilitate the formation of ordered layers of organic porphyrin molecules, the structure of the lateral ordering is strongly impacted by the nature of the pre-adsorbed anion.

Indeed, it is well documented that bromide and iodide layers forming on a Cu(111) electrode surface are almost uncharged, resulting in the fact that the interaction between the positively charged porphyrin cations and these layers is of weak van der Waals type. This leaves the porphyrin cations on the Br/Cu(111) or I/Cu(111) template quite mobile. The $[H_2TTMAPP]^{4+}$ molecules adlayer forming on these substrates is also less condensed (for the case of the Br/Cu(111) template) or results only in a sub-monolayer of individual patches on I/Cu(111). Evidently, the adsorption of the $[H_2TTMAPP]^{4+}$ molecules on the bromide and/or the iodide modified Cu(111) electrodes is much weaker than that of its derivative, namely $[H_2TMPyP]^{4+}$, on the same templates [187]. Hai et al. found that the

$[H_2TMPyP]^{4+}$ molecules strongly adsorb on the iodide modified Cu(111) forming a commensurate monolayer. This observation was in agreement with former reports which investigated the self-assembly of $[H_2TMPyP]^{4+}$ molecules on I/Au(111), I/Ag(111) and I/Pt(111) [27,28,180,181]. Compared to $[H_2TMPyP]^{4+}$ the $[H_2TTMAPP]^{4+}$ molecule reveals a significant modification, namely the trimethylamonium-phenyl side-group $[(CH_3)_3N\text{-}C_6H_5]^+$ substituents instead of the N-methyl-4-pyridyl side-groups $[CH_3\text{-}NC_5H_5]^+$. Due to this substitution not only the electrochemical behavior but also adsorption strength of the $[H_2TTMAPP]^{4+}$ molecules is discernibly changed. A reasonable interpretation of this difference is based on the different distribution of the electron density on the molecular entities as a whole.

Contrarily, chloride and sulfate layers are known to remain negatively charged after adsorbing on Cu(111) substrate. As a result, $[H_2TTMAPP]^{4+}$ molecules adsorb stronger on these templates due to the electrostatic interaction between the positively charged $[H_2TTMAPP]^{4+}$ molecules and negatively charged chloride or sulfate anion layer underneath resulting in the formation of close-packed highly ordered layers of the $[H_2TTMAPP]^{4+}$ molecules. In the case of the SO_4^{2-}/Cu(111) template, unlike the porphyrin adlayer on Cl/Cu(111) or I/Cu(100) where the porphyrin molecules reveal a flat lying orientation on the electrode surface, the orientation of the $[H_2TTMAPP]^{4+}$ molecules is different due to the Moiré structure underneath. While some molecules are lying flat on the surface indicated by their square shaped structure some others may be inclined to the surface expressed by smaller and asymmetric shapes as indicated by white arrows in Fig.6.21b.

Especially, with a chloride modified copper electrode serving as the template the driving forces for adsorption of positively charged $[H_2TTMAPP]^{4+}$ cations are mainly based on electrostatic interaction. This force results in a formation of a highly ordered $[H_2TTMAPP]^{4+}$ adlayer which was shown and discussed in detail in section 6.3.1. In this case, while the $[H_2TTMAPP]^{4+}$ molecules form on both Cu(111) and Cu(100) substrates a square lattice on the short range, the orientation of the $[H_2TTMAPP]^{4+}$ adlayer as a whole is governed by the symmetry of the underlying anion lattice on the long range. These observations one more time underline the important role of the underlying anionic layer in the lateral ordering on top.

On the basis of the observed STM images and the CVs one can undoubtedly conclude that the underlying anionic layers play a crucial role for the self-assembly of positively charged organic molecules. By changing either the anionic layer or the potential of the working electrode influences the delicate interaction between the adsorbate layer and the anionic lattice underneath and leads to a modification of structural properties of the molecular overlayer, e.g. conformation, orientation, phase transition. In both cases the different surface charge densities result in a different balance between the adsorbate-adsorbate and the adsorbate-substrate interactions and, hence, a different self-assembled structure on the surface.

6.5. Iron-porphyrin adsorbed on a chloride modified Cu(100) electrode

6.5.1. Introduction

It is well documented that iron porphyrin has attracted much interest of chemists for many years because of its central roles in a variety of important biological processes [216]. Especially, thin films of this molecule adsorbed on electrode surfaces were employed as catalyst for the dioxygen reduction [190-192] or for the electrochemical generation of free nitric oxide (NO) from nitrite (NO_2^-) [193]. It is known that the electrochemistry of this molecule is quite complicated due to the fact that the iron porphyrin could exist in several redox states depending on the pH of the electrolyte and the nature of the counter anions as well. However, the electrochemical characterization and, particularly, the surface structure properties of this molecule are still lacking. The goal of this section is therefore to gain additional understanding of the electrochemistry and the structure of iron porphyrin monolayers on a reactive copper surface in solution.

6.5.2. Electrochemical characterization of iron porphyrin

In the present work, a water-soluble iron porphyrin, 5,10,15,20-Tetrakis-(N-methyl-4-pyridyl)-porphyrin-Fe(III) pentatosylate (abbreviated as $[Fe^{III}TMPyP]^{5+}$, omitting the counterion) is employed in order to study its electrochemistry in hydrochloric acid media.

The electrochemistry of this molecule was reported for the first time by Neri and Wilson, who found a reversible, one-electron reduction in acidic solutions at a Au minigrid electrode and two electrochemical waves in more alkaline solutions due to the reduction of a dimeric iron porphyrin species [194]. The pH dependence of the monomer-dimer and the acid dissociation equilibria were then examined by Pasternack et al. [195], who concluded that there are several forms of the iron porphyrin when being in an aqueous electrolyte. Using spectroscopic measurements during pH titrations, two observed pK_a values were assigned to involve monomeric porphyrin species. The first pK_a value of 4.7 was related to the following equilibrium:

$$[\mathrm{Fe^{III}TMPyP(H_2O)}]^{5+} + \mathrm{H_2O} \leftrightarrows [\mathrm{Fe^{III}TMPyP(H_2O)\,(OH)}]^{4+} + \mathrm{H^+} \tag{6.12}$$

And the second pK_a value of 6.5 was attributed to the equilibrium:

$$[\mathrm{Fe^{III}TMPyP(H_2O)\,(OH)}]^{4+} \leftrightarrows [\mathrm{Fe^{III}TMPyP(H_2O)_2}]^{3+} + \mathrm{H^+} \tag{6.13}$$

Moreover, a monomer-dimer equilibrium was also reported [195-197] according to:

$$2[\mathrm{Fe^{III}TMPyP(OH)_2}]^{3+} \leftrightarrows [[\mathrm{Fe^{III}TMPyP(OH)}]_2\mathrm{O}]^{6+} + \mathrm{H_2O} \tag{6.14}$$

Electrochemical measurements conducted with a glassy carbon electrode or with an Au minigrid over the pH range of 0-14 in aqueous solutions were later carried out by Forshey et al. [198]. These experiments indicated that four ferric species (three monomeric and one dimeric) and two ferrous species (both monomeric) are adequate to interpret the electrochemical results between pH 1 and 13 [198].

In this thesis, exemplarily, HOPG and Cu(100) are employed as electrodes for the examination of the redox processes taking place in acidic medium with iron porphyrin molecules.

Typical CVs of HOPG in pure supporting electrolyte (dashed black curve) and in electrolyte containing $[\mathrm{FeTMPyP}]^{5+}$ species (red curve) are presented in Fig.6.26. As mentioned in section 6.1.1, the CV of HOPG in pure electrolyte is featureless and limited by two characteristic reactions, namely, the reductive hydrogen evolution reaction at the negative limit and the oxidative oxygen evolution reaction (OER) at the positive limit (for detail see also Fig.6.1).

In contrast, in the $[FeTMPyP]^{5+}$ containing electrolyte the CV of the HOPG exhibits a pronounced change in shape manifested by additional cathodic and anodic peak pairs. On the basis of the observed CV result and previous reports [198-201], the pair of reversible peaks with P_1 at E = +240 mV and P_1' at E = +320 mV vs RHE can be assigned to one electron transfer step resulting in a reduction/oxidation of the central iron from $[Fe^{III}TMPyP]^{5+}$ to $[Fe^{II}TMPyP]^{4+}$ and vice verse. This reversible process is described by:

$$[Fe^{III}TMPyP]^{5+} + e^{-} \leftrightarrows [Fe^{II}TMPyP]^{4+} \qquad (6.15)$$

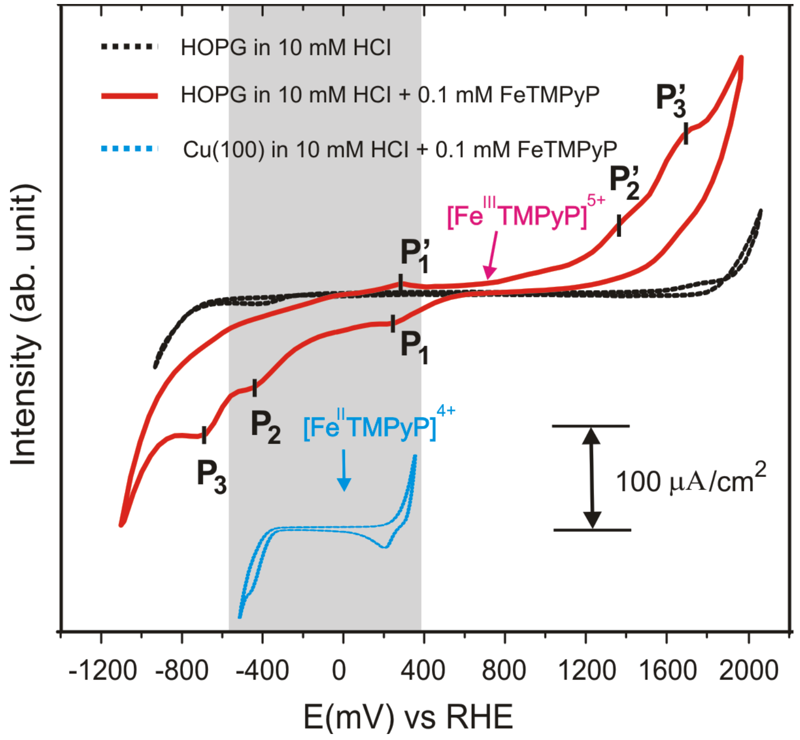

Figure 6.26: Cyclic voltammogram of HOPG in pure supporting 10 mM HCl solution (dotted black curve) and in solution containing FeTMPyP molecules (red curve) enclosing a set of redox peak pairs. The dashed blue curve is the CV of Cu(100) in solution containing FeTMPyP molecules.

This assumption is in good agreement with the former reports [198-201]. Forshey at al. [198] found that in acidic solution the $[Fe^{III}TMPyP]^{5+}$ species undergoes a one-electron reduction in order to form the corresponding $[Fe^{II}TMPyP]^{4+}$ at E = 0.18V vs NHE at a highly polished glassy carbon electrode. Both the oxidized and reduced form of iron porphyrin remained stable as evidenced by the reproducibility of the respective spectral feature when the redox states were cycled and characterized spectro-electrochemically by using an Au minigrid electrode [199]. This was also found by Chen et al. [200], who reported on the electrochemistry of the same molecule in phosphate buffer solution (PBS) on a glassy carbon working electrode with the first reduction potential at E = -0.18 V vs Ag/AgCl, which was somewhat similar to that reported by Forshey et al. [198]. Recently, this was one more time confirmed in a paper by Rama et al. [201] in which the first reduction potential value was found to be about E = +0.15 mV using chemiluminescence. In addition, he and his co-workers also found that on the one hand the $[Fe^{III}TMPyP]^{5+}$ species in aqueous buffer solutions of pH 6-11 exists as the hydroxylated form, HO-Fe^{III}TMPyP which undergoes a one-electron oxidation to form a stable oxo-iron(IV) porphyrin for which the electrochemical reaction is described as follows [201-202].

$$[(HO)Fe^{III}TMPyP]^{4+} \rightarrow [O{=}Fe^{IV}TMPyP]^{4+} + e^{-} + H^{+} \qquad (6.16)$$

and on the other hand the oxo-ferryl porphyrin can be formed in aqueous solution by reduction of the $[Fe^{III}TMPyP]^{5+}$ by dithionite to the $[Fe^{II}TMPyP]^{4+}$, auto-oxidation of which follows rapidly in the presence of molecular oxygen [201]. The formation process of oxo-ferryl porphyrin from its ferrous form in non-aqueous solvent has also been reported previously [203]. Indeed, the ferrous species formed via equation 6.15 serve as initial source for the electrochemical formation of the oxo-ferryl porphyrin according to the following equation [201].

$$[Fe^{II}TMPyP]^{4+} + O_2 \rightarrow [O_2\text{-}Fe^{II}TMPyP]^{4+} \rightarrow [H^{+}O = Fe^{IV}TMPyP]^{4+} \qquad (6.17)$$

At more negative potentials close to the HER, further reduction peaks P_2 and P_3 are detected on HOPG at E_2 = -455 mV and E_3 = -680 mV, respectively. It seems likely that these waves are further reduction steps related to the π-conjugated ring system of the porphyrin ligand used. This hypothesis is supported by Val Caemelbecke et al. [205], who reported that there were three additional reduction steps including six electrons in total after the initial Fe(III)/Fe(II) reduction process in the CV of $[(TMPyP)FeCl]^{4+}(Cl)^{4-}$ in non-aqueous DMF medium in which the first and the second reduction potentials are E = 0 mV and E = -740 mV vs SCE, respectively. It becomes evident that the second reduction potential with E = -740 mV vs SCE or alternatively E = -500 mV vs SHE is rather consistent with our present observation.

Here, the CV of this iron porphyrin is for the first time recorded on a Cu(100) surface in chloride containing electrolyte. Fig.6.27 shows typical CVs of the Cu(100) electrode in the supporting electrolyte (10 mM HCl) given by the dotted black curve and in the $[Fe^{III}TMPyP]^{5+}$ molecules containing electrolyte (10 mM HCl + 0.1 mM FeTMPyP) presented by the blue curve. The CV of the Cu(100) in pure supporting electrolyte, like in section 6.1.1, is characterized only by the reductive hydrogen evolution reaction at the cathodic limit and the oxidative copper dissolution reaction at the anodic limit. After replacing the supporting electrolyte by the $[Fe^{III}TMPyP]^{5+}$ molecules containing electrolyte there are some characteristic deviations within the potential window of the Cu(100) observed. The assignment of the features to peak P1 and P2 results on a comparison to the CV with HOPG as shown in Fig.6.26.

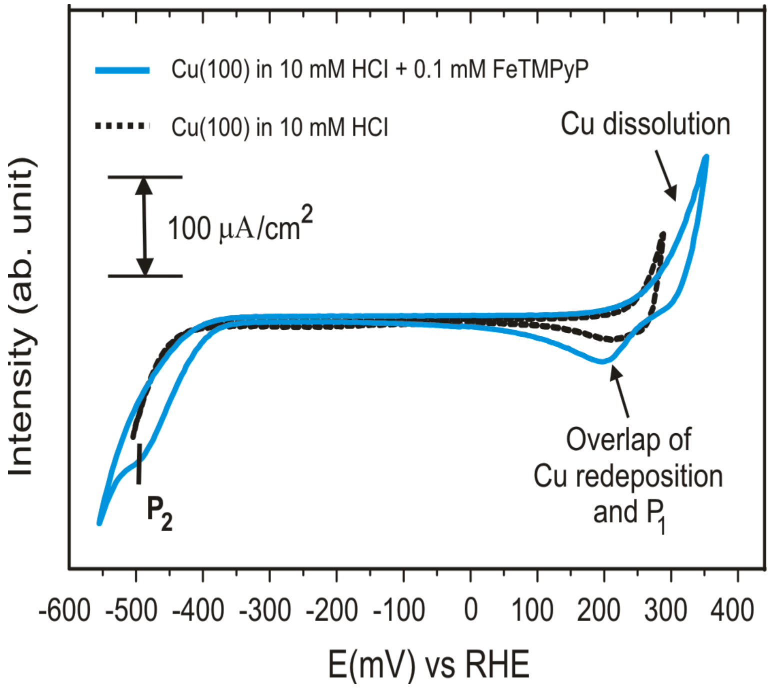

Figure 6.27: CVs of Cu(100) in pure supporting electrolyte (10 mM HCl) described by the dotted black curve and in electrolyte containing FeTMPyP molecules (10 mM HCl + 0.1 mM FeTMPyP) by the blue curve.

6.5.3. Structural determination

In this section, a chloride modified Cu(100) was employed as the template for the self-assembly of the 5,10,15,20-Tetrakis-(N-methyl-4-pyridyl)-porphyrin-

Fe(III) ($[Fe^{III}TMPyP]^{5+}$) purchased from the company Porphyrin Systems. For the molecular adsorption the same routine is carried out as with the metal free porphyrin mentioned above. Namely, the pure supporting electrolyte (10 mM HCl) is replaced at a potential value of E = -50 mV vs RHE by an electrolyte containing the $[Fe^{III}TMPyP]^{5+}$ species. As a result, the whole electrode surface is covered by a highly ordered monolayer of the reduced products, i.e. the $[Fe^{II}TMPyP]^{4+}$ molecules.

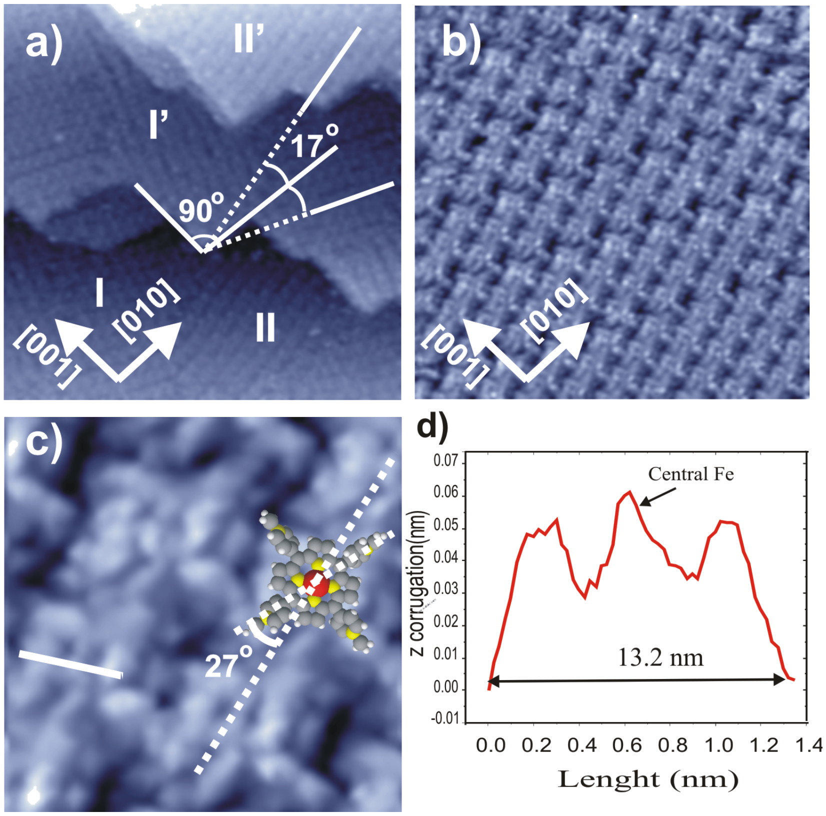

Figure 6.28: (a) Typical large scale STM image of an $[Fe^{II}TMPyP]^{4+}$ adlayer on a chloride modified Cu(100) surface with two mirror domains enclosing an angle of 34° between each other: 36.1 nm x 36.1 nm, I_t = 0.2 nA, U_b = 240 mV, E = -30 mV; b) Medium scale STM image showing a square lattice of molecules: 14.4 nm x 14.4 nm, I_t = 0.2 nA, U_b = 240 mV, E = -30 mV; c) High resolution STM image in which each molecule can be recognized as a propeller like shape including a central protrusion, and each $[Fe^{II}TMPyP]^{4+}$ molecules is rotated by an angle of 27° between the molecular symmetry axis and the direction of the close-packed molecular row: 3.7 nm x 3.7 nm, I_t = 0.2 nA, U_b = 240 mV, E = -30 mV ; d) Line profile measured along the white line in Fig.6.28 indicating the central metal atom.

A typical large-scale STM image showing steps and co-existing rotational domains marked by I and II is presented in Fig.6.28a. The molecules are arranged in rows rotated by an angle of 17° with respect to the step directions. Interestingly, two rotational domains (I and II) rotate by an angle of 34 ± 1° which is twice as big as the angle between the step direction and the molecular rows, indicating that these domains are mirror domains. It was mentioned in section 3.3.2 that the step directions in case of chloride pre-covered Cu(100) electrode surface are aligned along the close packed chloride rows which run parallel to the ⟨001⟩ directions of the Cu(100) underneath. Consequently, the ⟨001⟩ directions are mirror axes of the mirror domains. By symmetry reason, there are four mirror domains in total co-existing on the chloride terminated Cu(100) substrate. The step angle of 90° (Fig.6.28a) is characteristic for the chloride precovered Cu(100) surface which remains stable in the presence of the $[Fe^{II}TMPyP]^{4+}$ species indicating that $[Fe^{II}TMPyP]^{4+}$ adsorption has no impact on the underlying chloride lattice. A typical higher resolution STM image showing the self-arrangement of the $[Fe^{II}TMPyP]^{4+}$ molecules in the domain II, which was acquired in an area of 14.4 nm^2, is presented in Fig.6.28b. Obviously, the molecules are organized in rows forming a quasi-square lattice on the chloride template. The individual molecule is recognized as a square shaped entity and arranged in the same orientation. One mirror axis of the molecules is rotated by an angle of 27° with respect to the molecular row orientations (Fig.6.28c). Astonishingly, the molecular centre appears as protrusion instead of a hollow as observed in the case of metal free base porphyrin adsorption [30,204]. This is illustrated by the line profile in Fig.6.28d recorded along the white line in Fig.6.28c. These bright lobes are assigned to the central iron atom in the porphyrin molecule (see molecular model in the inset figure). This observation is in agreement with previous reports which investigated the adsorption of iron phthalocyanine molecules (FePcs) on gold [205] and HOPG [206] in UHV environment. Ahlund et al. [206] found that the FePc adsorbed on the bare HOPG substrate forming a quasi-square lattice in which the individual molecule appears with a propeller shape enclosing a pronounced protrusion in the centre. Recently, Manandhar et al. also succeeded in studying FePc based thin films on a bare Ag(111) substrate and made the same observation. A reasonable interpretation for the observed protrusions is based on the electron configuration of the central iron atom. Indeed, with metal atoms containing 3d orbitals the states close to the highest occupied (HOMO) and the lowest unoccupied (LUMO) molecule levels are dominated by the 3d orbitals [11,207]. By changing the metal in a metal-porphyrin or metal-phthalocyanine system the corresponding variation in the d orbital participation near the Fermi surface should induce a profound change in the STM images. In particular, for the iron metal the Fe 3d is partially occupied and only 0.4 eV from the energy level of the HOMO [208] resulting in a significant contribution to the ligand HOMO of iron porphyrin. This also becomes evident in case of cobalt containing porphyrin and/or phthalocyanine molecules [11,209]. In contrast, a central depression is imaged with Ni, Cu and Zn atoms within these molecules [11,14,210] due to the fact that the d orbitals of these metals are quite far from the ligand HOMO [211]. In summary, the bright protrusions observed at the centers of the $[Fe^{II}TMPyP]^{4+}$ molecules in the STM images have been interpreted as the tunneling from the partially filled d orbital of Fe.

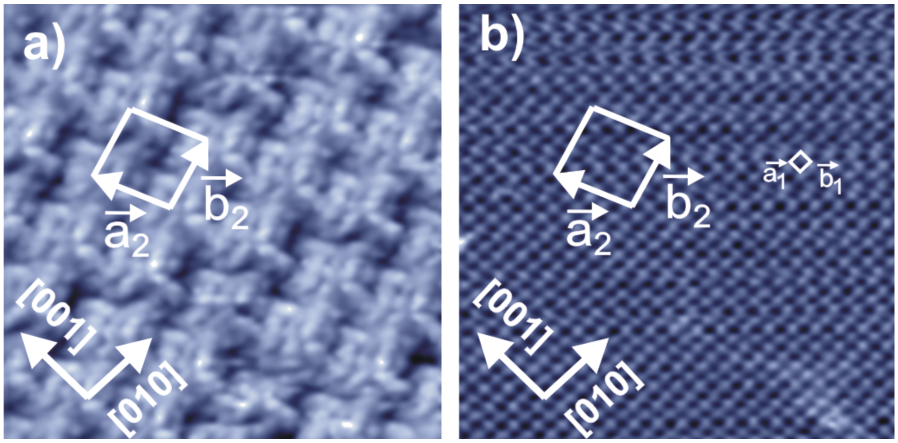

Figure 6.29: Structural relation between an $[Fe^{II}TMPyP]^{4+}$ adlayer and the chloride lattice underneath, a) 7.1 nm x 7.1 nm, I_t = 0.2 nA, U_b = 240 mV, E = -30 mV; b) 7.1 nm x 7.1 nm, I_t = 5 nA, U_b = 40 mV, E = -30 mV.

A graphical correlation between the $[Fe^{II}TMPyP]^{4+}$ adlayer and the underlying chloride lattice is presented in Fig.6.29 which are recorded at the same surface area but under different tunneling conditions. Under *"moderate tunneling conditions",* i.e. low tunneling current and high bias voltage, the tunneling tip is far from the measured surface and, hence, the $[Fe^{II}TMPyP]^{4+}$ adlayer is imaged as shown in Fig.6.29a. The individual molecule can be recognized as a propeller like shape enclosing a protrusion in its center. Contrarily, the tunneling tip acts as a brush sweeping the $[Fe^{II}TMPyP]^{4+}$ molecules away leaving the $c(2 \times 2)$ chloride lattice behind when *"drastic tunneling conditions"* (high tunneling current and low bias voltage) are applied between tip and sample (Fig.6.29b).

On the basis of the superposition of panel a and b, a unit cell $(\vec{a}_{2,}\vec{b}_2)$ containing one $[Fe^{II}TMPyP]^{4+}$ molecule can be described by a $\begin{vmatrix}4 & -1\\ 1 & 4\end{vmatrix}$ transformation matrix with respect to the underlying chloride lattice with $|\vec{a}_2|$ = $|\vec{b}_2|$ = 1.53 ± 0.01 nm enclosing an angle of 93° between each other.

A possible tentative model describing this correlation is proposed in Fig.6.30 in which two mirror domains are rotated with respect each other by an angle of 32° that is somewhat smaller than that (34°) measured on the real STM image possibly due to drift and measuring error. Based on this model, the surface coverage per domain is calculated to be 0.059 ML with respect to the c(2 x 2)-Cl underlying lattice or 4.27 x 10^{13} molecules/cm^2.

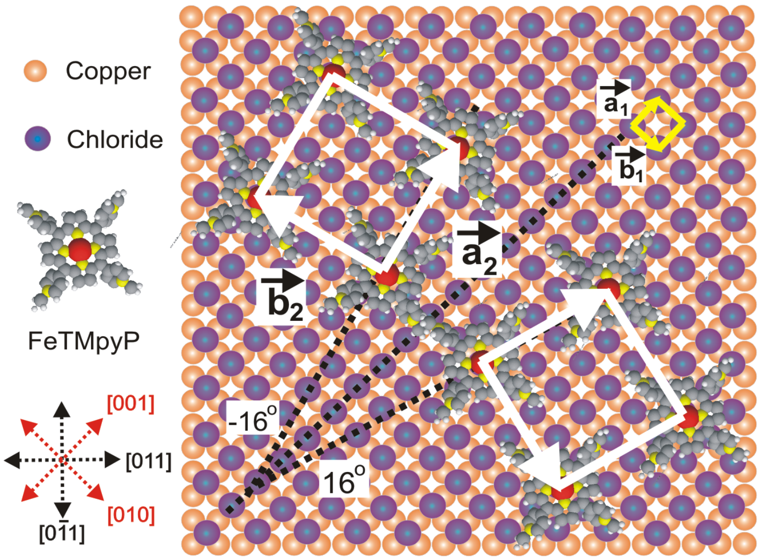

Figure 6.30: Possible tentative model of an $[Fe^{II}TMPyP]^{4+}$ adlayer on a chloride terminated Cu(100), consisting of two mirror domains enclosing an angle of 32°.

6.5.4. Summary

A combination of cyclic voltammetry and electrochemical scanning tunneling microscopy was employed to investigate the electrochemical behavior and the structural charactericstics of $[H_2TTMAPP]^{4+}$ molecules on an anion modified Cu(100) and Cu(111) electrode surface, respectively:

- In the potential window of HOPG and the copper electrodes, $[H_2TTMAPP]^{4+}$ molecules undergo two successive reduction steps involving six electrons in total in order to form the corresponding reduced species, namely $[H_4TTMAPP(\text{-II})]^{4+}$ and $[H_8TTMAPP(\text{VI})]^{4+}$, respectively.
- The ground state, i.e. $[H_2TTMAPP]^{4+}$, molecules strongly adsorb and form a laterally ordered monolayer on both chloride modified Cu(111) and Cu(100) surfaces. In case of the Cl/Cu(111) template, the molecular rows run parallel to the close packed chloride atoms underneath or, alternatively, parallel to the $\langle\bar{2}11\rangle$ directions of the underlying Cu(111) substrate, while this is not the case for the Cl/Cu(111) surface. This impacts on the surface coverage of the $[H_2TTMAPP]^{4+}$ self-assembled layer, namely 2.63 x 10^{13} molecules/cm^2 and 2.8 x 10^{13} molecules/cm^2 on the Cl/C(100) and Cl/Cu(111), respectively.

- The influence of the electrode potential on an order/disorder phase transition is also examined. While the $[H_2TTMAPP]^{4+}$ molecules form an ordered layer on the surface, the reduced species, i.e. $[H_4TTMAPP(\text{-II})]^{4+}$ molecules desorb from the surface leaving a disordered layer behind.

- The Influence of the anion layer on the adsorption of $[H_2TTMAPP]^{4+}$ molecules is systematically investigated in the following sequence: A full self-assembled layer is observed on both chloride and sulfate modified copper surfaces, whereas ordering on a bromide precovered Cu(111) is restricted and more so in the case of the iodide modified Cu(111) surface due to the lack of strong electrostatic interactions.

Furthermore, the self-assembly of iron porphyrin ($[Fe^{III}TMPyP]^{5+}$) molecules on a chloride modified Cu(100) electrode surface was studied. The electrochemical investigation shows that the $[Fe^{III}TMPyP]^{5+}$ molecule undergoes two reduction processes in the narrow potential window of copper (from -450 mv to +300 mV vs RHE). The first reduction step relates to a one-electron step and is assigned to the reduction from $[Fe^{III}TMPyP]^{5+}$ to the corresponding $[Fe^{II}TMPyP]^{4+}$. The ligand related reduction is attributed to the further observed reduction steps.

A highly ordered layer of the $[Fe^{II}TMPyP]^{4+}$ species including four rotational domains is observed on the Cl/Cu(100) with sub-molecular resolution. Based on the STM images, a correlation of the $[Fe^{II}TMPyP]^{4+}$ adlayer and the underlying chloride lattice is proposed. Accordingly, a unit cell containing one $[Fe^{II}TMPyP]^{4+}$ molecule can be described by a $\begin{vmatrix} 4 & -1 \\ 1 & 4 \end{vmatrix}$ transformation matrix with respect to the underlying chloride lattice with $|\vec{a}_2| = |\vec{b}_2| = 1.53 \pm 0.01$ nm enclosing an angle of 93° between each other. A possible tentative model describing this correlation is proposed with the surface coverage per domain of 4.27×10^{13} molecules/cm^2.

Chapter 7

DBV adlayer on a chloride modified Cu(111)

7.1. Introduction

Self-assembly of viologen molecules either on bare or on a halide modified metal substrate has been investigated in electrochemical environments [138-140,212-213]. The lateral ordering of some viologen derivatives such as 2,2'-bipyridine (2,2'-BP) on a bare Au(111) and 4,4'-bipyridine (4,4'-BP) on a bare Cu(111) was reported by Wandlowski et al. [213] and Diao et al. [212]. Especially, adsorption of Dibenzyl-viologen derivatives on a halide modified Cu(100) has been successfully investigated by our group [138-140,214-216]. The viologen molecules are well known to have three reversible redox states, i.e. the dicationic V^{2+}, the radical monocationic $V^{\bullet+}$ and the uncharged V^0 and, hence, their adsorbed structure can be modified in a reversible manner. However, due to the narrow potential window of copper, it is only possible to observe the first redox step from the dicatonic V^{2+} to the corresponding radical monocationic $V^{\bullet+}$ species. Observation of the second reduction by STM is hindered because of the massive hydrogen evolution reaction taking place on copper within the same potential regime. Indeed, Pham et al. [138-139] reported about the formation of a highly ordered “cavitand” phase which formed spontaneously on a c(2 x 2) chloride precovered Cu(100) surface in an HCl acidic electrolyte containing Dibenzyl viologen (DBV) molecules under non-reactive conditions, i.e. at potentials positive of the first molecular reduction reaction. The cavitand phase is replaced by a corresponding “stacked” pattern once the first reduction occurs. Contrarily, Diao et al. found that on a bare Cu(111) surface the dicationic $BiPy^{2+}$ and the radical monocationic $BiPy^{\bullet+}$ of a 4,4′-bipyridine (BiPy) formed the “array” and the “alternative stripe” phases, respectively [212]. However, investigation on structure formation and phase transitions of DBV molecules on the chloride modified Cu(111) electrode surface have still not been published.

The goal of this chapter is, therefore, to investigate the dication DBV^{2+} and radical monocation $DBV^{\bullet+}$ based structure formation on Cl/Cu(111) as well as possible reversible phase transitions. The lateral ordering of the Dibenzyl-viologen derivative on a $c(p \times \sqrt{3})$-Cl/Cu(111) is expected to be different from that forming on the c(2 x 2)-Cl/Cu(100) surface and on the bare (1 x1)-Cu templates due to differences in electrostatic interactions.

7.2. Electrochemical features

The electrochemical characterization of the system Cu(111) in viologen containing hydrochloric acid solution was done by cyclic voltammetry [217-218]. Representative steady-state CVs of Cu(111) in pure electrolyte (dashed black curve) and in electrolyte containing viologen species (red curve) are presented in Fig.7.1. As usual the potential window of Cu(111) in blank electrolyte (10 mM HCl) is limited by the oxidative copper dissolution reaction (CDR) at the anodic limit and the reductive hydrogen revolution reaction (HRE) at the cathodic limit. At intermediate potentials a pair of peaks due to chloride de/adsorption is observed [85,171,176]. In comparison with the CV in the pure supporting electrolyte two characteristic deviations appear in the electrochemical behavior of the Cu(111) surface in the viologen containing electrolyte (10 mM HCl + 0.1 mM DBV^{2+}) [219].

The first difference from the CV in blank electrolyte is related to a considerable shift (70 mV) of the HER towards lower potentials This is attributed to an inhibiting effect of the viologen film on the HER, and indicates that the molecules are still present on the electrode surface in the HER potential regime.

This effect was also reported by Pham et al. [138,139] and Safarowsky et al. [140] when Cu(100) was serving as the working electrode.

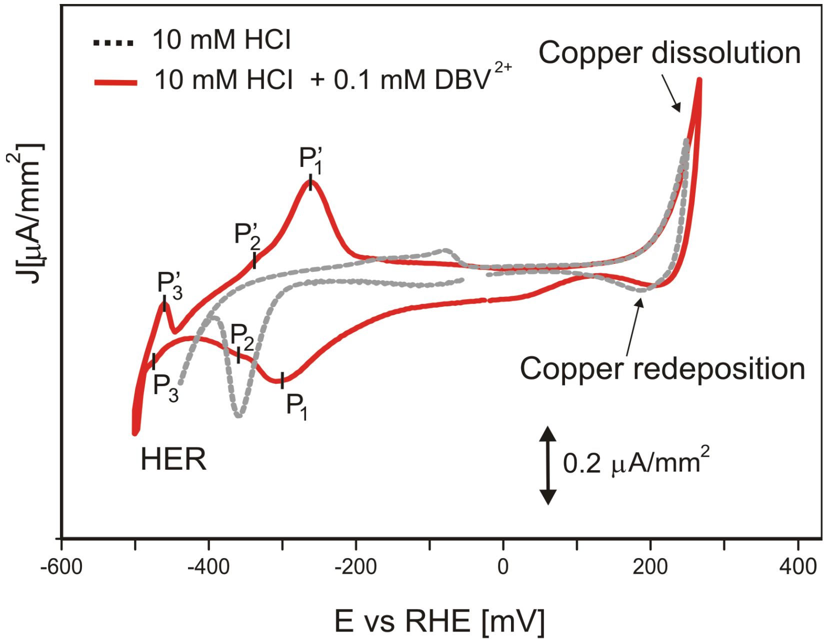

Figure 7.1: Cyclic voltammograms of Cu(111) in pure 10 mM HCl (dash black curve) and in viologen molecules containing electrolyte (red curve), Scan rate dE/dt = 10 mV/s.

The second deviation from the CV in pure supporting electrolyte concerns the appearance of three peak pairs at potentials close to the HER regime. These additional current waves have to be assigned to both viologen related redox processes as well as an order/disorder phase transition due to chloride adsorption/desoprtion [219]. It is well known that the viologen dication (V^{2+}) undergoes two separate one-electron transfer steps in electrochemical environment in order to form the respective viologen radical mono-cation ($V^{\bullet+}$) and the uncharged species (V^0). While the uncharged viologens can accumulate at the electrode surface due to their hydrophobic properties [113] the dication and radical cation species are soluble in aqueous solutions.

Based on the above CV results as well as previous studies [138-140,214-216] the three quasi-reversible pairs of peaks $P_1/P_1^{'}$, $P_2/P_2^{'}$, $P_3/P_3^{'}$, respectively, observed at potentials close to the HER regime in Fig.7.1 are assigned to the reduction of dicationic DBV^{2+} to the corresponding radical mono-cations $DBV^{\bullet+}$, an order/disorder phase transition due to chloride desorption/adsorption and finally the precipitation/dissolution of an adsorbed film of neutral viologen molecules, respectively. For details see the reviews given in ref. 138-140 and the papers cited therein.

Compared to electrochemical features of the Cu(100) electrode [138-140,214-216] in the same working electrolyte the peaks derive from the superposition between “solution” processes and “surface limited” reactions as follows:

The reduction/oxidation of preadsorbed viologen and/or viologen species in solution is described by:

$$DBV^{2+} + e^{-} <==> DBV^{\bullet+} \tag{7.1}$$

This reduced species may form dimers- and/or polymers depending on whether the process occurs in solution or on the surface:

$$2(or\ n)DBV^{\bullet+} <==> [DBV_2]^{2+}(or\ [DBV_n]^{n+}) \tag{7.2}$$

The further reduction of the radical mono-cations to the fully uncharged viologen species (DBV^0, labeled by P_3) is not considered here since this process is believed to occur out of the copper potential window or to lie within the regime of massive hydrogen evolution.

In the following the STM images obtained under non-reactive conditions, i.e. the molecules are adsorbed at a potential where they remain their dicationic character in the adsorbed state, show a new structural motif of DBV molecules on the chloride modified Cu(111) electrode surface and structural changes are presented and discussed. These changes are governed by either the first electron transfer process or by chloride desorption/adsorption manifesting themselves by the peak systems $P_1/P_1^{'}$ and $P_2/P_2^{'}$ in the CV.

7.3. Structural characterization by in-situ STM

7.3.1. Herring-bone phase

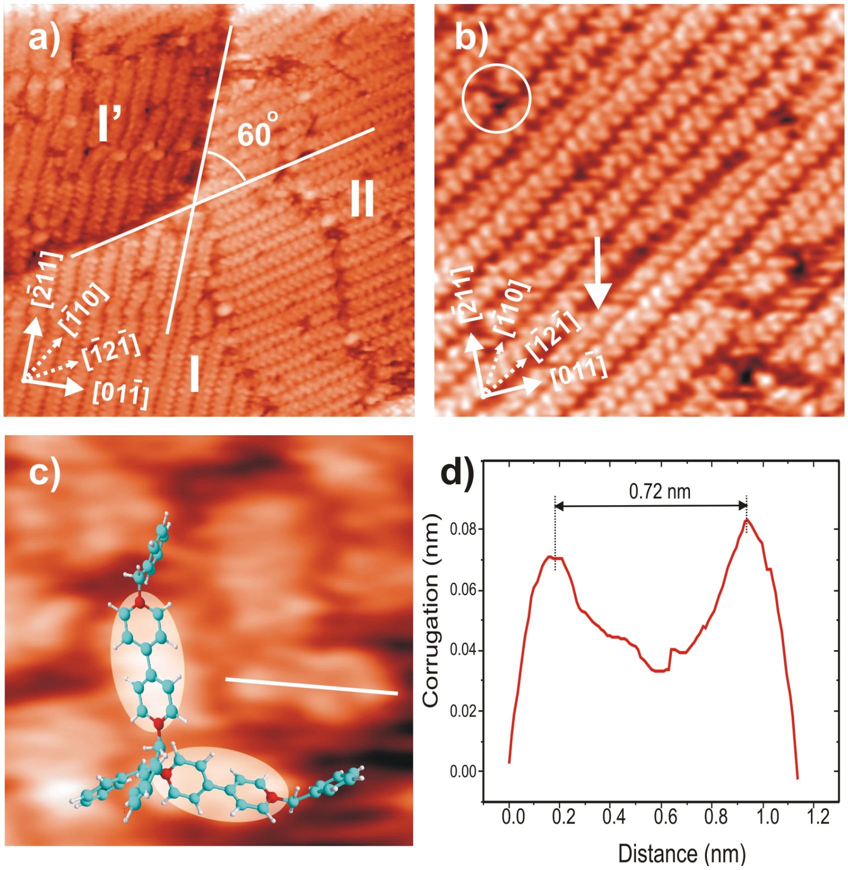

Figure 7.2: Typical STM images of surface morphology and high resolution of the DBV^{2+} related herring-bone phase: a) Surface morphology of the herring-bone phase with a characteristic substrate step angle of 120° and two existing rotational domains: 46.67 x 46.67 nm, U_{bias} = 141 mV, I_t = 0.3 nA, E_w = -180 mV; b-c) Medium scale (30.73 x 30.73 nm) and high resolution (3.2 x 3.2 nm) STM images of herring-bone phase describing two individual DBV^{2+} molecules in each structural element: U_{bias} = 386 mV, I_t = 0.1 nA, E_w = +10 mV; d) Line profile recorded along the white line in Figure 3.c indicates the length of the building blocks of about 7.2 nm in high agreement with the N-N distance within the DBV^{2+} molecule [139].

On the basis of previous in-situ STM studies [171,176] it is known that chloride anions specifically adsorb on Cu(111) forming a well-ordered $c(p \times \sqrt{3})$

superstructure, which remains stable in the potential range between the copper dissolution reaction and about 300 mV close to the onset of the HER. For details see refs. 171,176 and the papers cited therein. This threefold symmetric chloride adlayer, in which steps are aligned parallel to the close-packed chloride rows, is a suitable template for the adsorption of positively charged organic molecules. In contrast to the larger halides, e.g. bromide and iodide the chloride anions remain to a large extent negatively charged upon adsorption [94].

Exposing the $c(p \times \sqrt{3})Cl$ terminated Cu(111) surface to an electrolyte containing DBV^{2+} species within the double layer regime results in the instantaneous formation of a highly ordered DBV^{2+} film. Figure 7.2 shows representative STM images describing the surface morphology and molecular structure of the highly ordered DBV^{2+} adlayer. The typical angle of 120° between substrate steps characteristic for the adsorption of the $c(p \times \sqrt{3})Cl$ layer on the Cu(111) electrode is still persistent showing that the surface morphology is not considerably impacted by the presence of the DBV^{2+} overlayer. From the achieved STM results, one can determine that the DBV^{2+} adlayer occurs in two distinguishable domains denoted as I and II in Fig.7.2a rotated by an angle of 120 ± 2° with respect to each other. In a close-up of the molecular arrangement, it becomes clear that the DBV^{2+} molecules are arranged parallel to step-edges. In comparison with the direction of the close packed chloride rows adsorbed on the Cu(111) surface [85,171,176] one comes to the conclusion that the molecules are stacked along the underlying close-packed rows of chloride via strong electrostatic interactions. On the molecular level, the adsorbed phase is totally different from the well-known "cavitand" phase forming on a chloride modified Cu(100) surface [138-140]. Under the same measuring conditions, i.e. under non-reactive conditions at more positive potentials, a square shaped DBV^{2+} structure is observed on the chloride pre-covered Cu(100) electrode surface, while a new pattern is, for the first time, observed when the DBV^{2+} species is in contact with the Cl/Cu(111) template. Each unit appears to consist of two clearly discernible rod-shaped subunits that meet each other by an angle of 120 ± 2° building up a "***herring-bone"*** shaped self-assembly (Fig.7.2b and c). Additionally, the medium STM image in Fig.7.2b shows that the observed adlayer is composed of zig-zag rows with some defects marked by a white cycle and arrow. It is most likely that each sub-unit consists of two individual DBV^{2+} molecules in which the closer benzyl group tails are overlapping each other in order to form such “heavy boundaries”. In contrast, the dark ditches between molecular rows forming “light boundaries” are assigned to the remaining benzyl lobes as illustrated by the space filling molecular model in Fig.7.2c. Our assumption becomes more evident due to the line profile measurement which is recorded along the white line in Fig.7.2c. As a result, the building block distance is about 0.72 ± 0.01 nm (Fig.7.2.d). This value is in complete agreement with the N-N distance of 0.71 nm within the DBV^{2+} molecule [139].

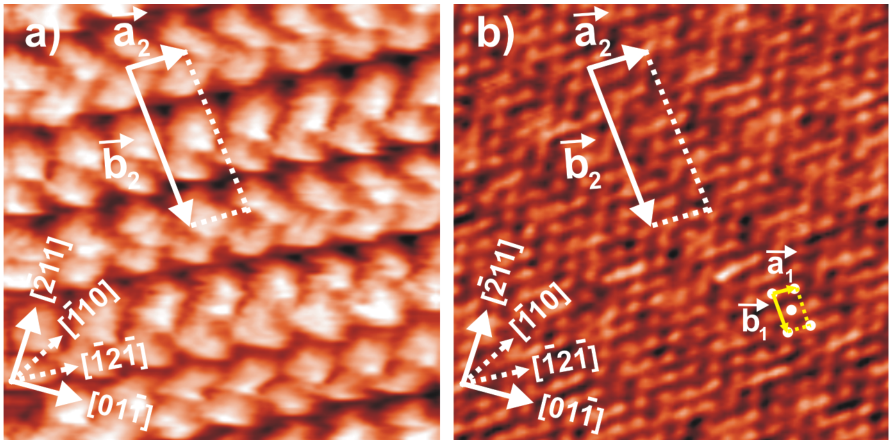

Figure 7.3: Structural correlation between ordered DBV^{2+} herring-bone phase and the anionic chloride lattice underneath: a) 8.5 x 8.5 nm, U_b = 220 mV, I_t = 0.1 nA, E = -10 mV; b) 8.5 x 8.5 nm, U_b = 30 mV, I_t = 5.0 nA, E = -10 mV.

A structural correlation between the DBV^{2+} adlayer and the underlying chloride lattice could be obtained by a careful variation of the tunneling conditions [138-140]. While under soft tunneling conditions (high bias voltage and low tunneling current) the characteristic features of the DBV^{2+} adlayer are observed (Fig.7.3a), the chloride lattice underneath becomes visible after drastic tunneling conditions are applied, i.e. low bias voltage and high tunneling current (Fig.7.3b), which leads to a removal of the viologen overlayer. By comparison of Fig.7.3a and Fig.7.3b it becomes evident that the rod-shaped subunits and their herring-bone arrangement are aligned parallel to the underlying close packed chloride rows, i.e. the $\langle\bar{2}11\rangle$ directions of the Cu(111) substrate.

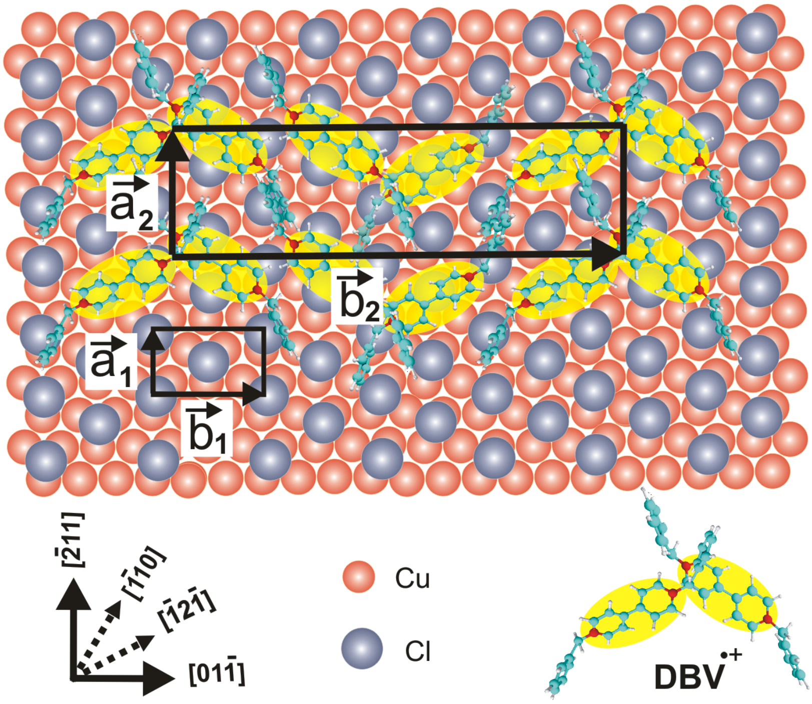

Figure 7.4: Possible model for the adsorption of the DBV^{2+} molecules on the chloride modified Cu(111) electrode surface.

The graphical superposition of panels a and b gives a precise determination of the DBV^{2+} unit cell with respect to the c(p x √3)-Cl phase underneath serving as internal calibration lattice. Therefrom, a DBV^{2+} unit cell containing four molecules could be described by a (2 x 2p) mesh with respect to the $c(p \times \sqrt{3})Cl$ lattice underneath. The lattice constants are estimated to be $|\vec{a}_2| = 0.83 \pm 0.1\,\text{nm}$ and $|\vec{b}_2| = 3.32 \pm 0.1\,\text{nm}$, respectively, enclosing an angle of 88°. Alternatively, the unit-cell of the DBV^{2+} adlayer can be directly related to the copper substrate (1 x 1) mesh assuming a $(4p \times 2\sqrt{3})$ coincidence mesh. A structural model is proposed in Fig.7.4 for the adsorbed phase of the DBV^{2+} on the chloride pre-covered Cu(111) substrate. Taking the substrate symmetry into account, there are three co-existing rotational domains on the copper surface. The surface coverage per domain was also calculated to be $\Theta = 0.25$ ML with respect to the underlying chloride lattice, or 14.49 x 10^{13} molecules/cm^2.

Adsorption of other viologen derivatives on a bare Cu(111) electrode has, in fact, been examined in part. Diao et al. [212] found that the 4,4′-Bipyridine (BiPy) strongly adsorbs on the bare Cu(111) electrode and forms, potential dependent, two distinct ordered phases due to the oxidation state difference. In the potential range from -250 mV to ca. 200 mV vs RHE, where the dication $BiPyH_2^{2+}$ remains stable, a well-defined molecular array was consistently observed with an angle of 60° (or 120°) between molecular rows. In contrast, by changing the electrode potentials downward into the more negative regime passing the reduction peak at ca. -360 mV a stacked phase formed by the radical monocation $BiPyH_2^{\bullet+}$ species was observed and completely replaced the former phase. The staking phase of the $BiPyH_2^{\bullet+}$ was composed of alternating rows of type I and II which were aligned parallel to the <121> and <110> directions of the underlying Cu(111) lattice [212] stressing the predominant role of the underlying template lattice with respect to the adsorption and the phase formation of the organic molecular adlayer.

7.3.2. Stacked pattern

After passing the first reduction peak P_1 as illustrated in Fig.7.1 the dicationic viologen (DBV^{2+}) molecules are reduced to the corresponding radical monocation ($DBV^{\bullet+}$) resulting in a phase transition in order to form the so called “stacking phase”.

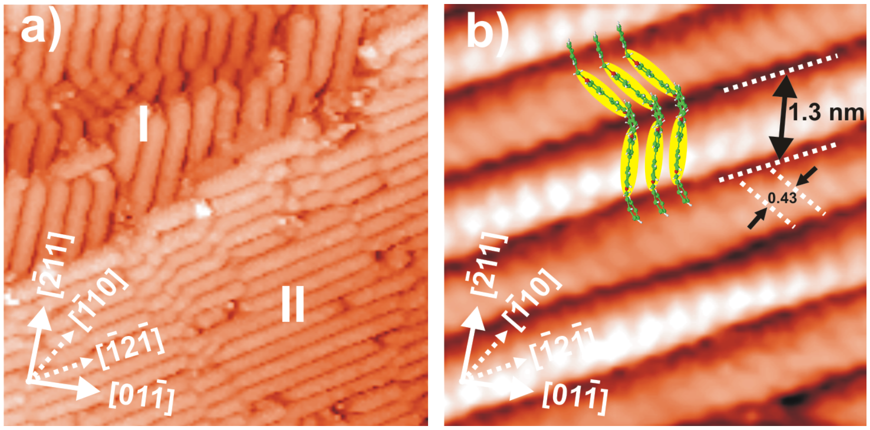

Figure 7.5: (a) Typical STM image showing two rotational domains of the $DBV^{\bullet+}$ alternating stripe pattern, 30.6 nm x 30.6 nm, U_{bias} = 386 mV, I_t = 0.1 nA, E = +10 mV; (b) Highly resolved STM image of the $DBV^{\bullet+}$ alternating stripe pattern, 5.06 nm x 5.06 nm, U_{bias} = 298 mV, I_t = 0.1 nA, E = -286 mV.

Fig.7.5 presents typical meso- and molecular-scale images of the stacking phase of DBV$^{\bullet+}$ molecules on a chloride terminated Cu(111) electrode surface as found in the present work. The stacked rows are aligned parallel to the close-packed chloride rows underneath that run along the $\langle\bar{2}11\rangle$ directions of the Cu(111) substrate (see ref.85 and papers cited therein) as shown in Fig.7.5a. A higher resolution STM image reveals further details of the internal molecular structure, i.e. orientation and packing arrangement within the ordered adlayer. From a close-up of the molecular organization one can assign the elongated dishes in a row to the DBV$^{\bullet+}$ molecules arranged in the same orientation, whereas neighboring rows exhibit on opposite orientation (Fig.7.5b). The intermolecular distances in the same row as well as between adjacent stripes are measured to be ca. 0.43 ± 0.01 nm and 1.3 ± 0.1 nm, respectively [219]. The measured intermolecular distance of 0.43 nm is close to the typical stacking distance of heterocyclic aromatic molecules [220] and has also been observed in the case of a 2.2'-bipyridine phase on a Au(111) [213] and on the Cu(111) [212] surface, respectively, indicating that the driving force of the stack formation is the strong π-π interaction between the viologen radical monocations originating from both the neighboring reduced bipyridinium moieties and the neighboring benzyl groups within the 1D stripes.

Furthermore, such additional π-π interactions between adjacent DBV$^{\bullet+}$ molecules are considered to appear on the surface with the stipulation that the benzyl groups take up a trans-conformation [138] as shown in Fig.7.5b and in the structural model in Fig.7.6. Applying different tunneling conditions as mentioned above the structural correlation between the DBV$^{\bullet+}$ adlayer and the underlying chloride lattice becomes visible. On the basis of a superposition of both lattices the unit cell containing two DBV$^{\bullet+}$ molecules can be expressed by a (1 x 4) coincidence mesh with respect to the c(p x $\sqrt{3}$)-Cl lattice with the lattice constants of $|\vec{a}_2|$ = 0.43 ± 0.01 nm and $|\vec{b}_2|$= 3.32 ± 0.1 nm, respectively.

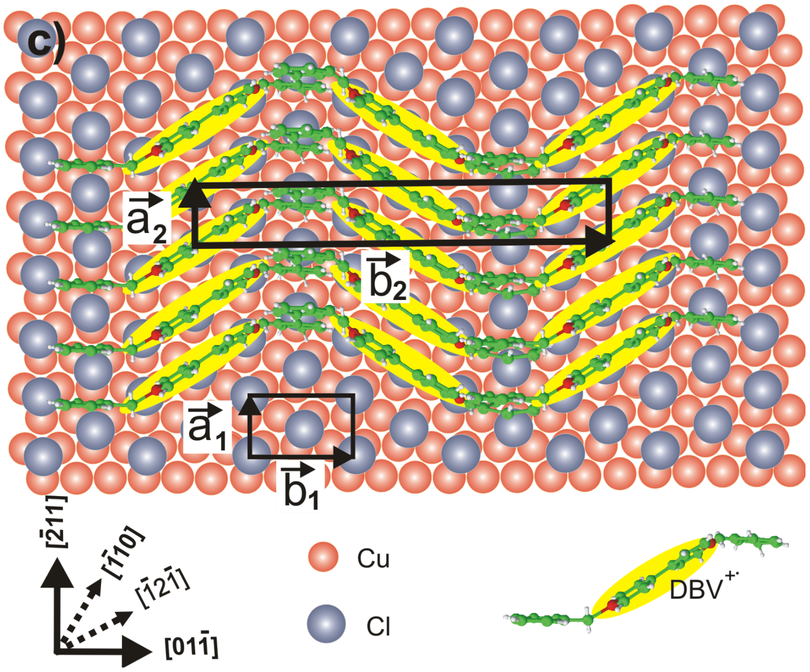

Figure 7.6: Possible model of the alternating stripe pattern on a c(p x $\sqrt{3}$)-Cl modified Cu(111) electrode surface.

For the stacked phase a possible structural model is proposed in Figure 7.6. In this model, both the DBV$^{\bullet+}$ molecules and the stripe propagation directions are aligned along the $\langle\bar{2}11\rangle$ directions resulting in a characteristic angle between them of 60°. While the bright and elongated protrusions are attributed to the bipyridinium cores arranged in a face to face orientation, the dark ditches in between are assigned to the benzyl groups [219]. The DBV$^{\bullet+}$ molecules are considered to be located on the top-sites of three chloride atoms and, hence, the intermolecular distance within a stripe in this model is equal to the atomic Cl-Cl distance, i.e. 0.43 ± 0.01 nm [219], which is consistent with our observation. Taking the substrate symmetry into account, there are three rotational domains co-existent on the copper surface. From the proposed structural model, the DBV$^{\bullet+}$ surface coverage per domain is calculated to be $\Theta = 0.25$ ML with respect to the c(p x $\sqrt{3}$)-Cl serving as the template or 14.30 x 10^{13} molecules/cm^2.

By comparing with the stripe formation on the chloride modified Cu(100) electrode surface one can realize that a significant difference of the radical monocations ($DBV^{\bullet+}$) adsorption on the three-fold symmetric chloride precovered Cu(111) or bare Cu(111) surface is observed, namely the occurrence of stripes with alternating molecular orientation instead of one orientation [212].

7.3.3. Electron transfer induced phase transition

In the present case, the viologen dication based adsorbed structure remains stable in the potential range more positive than -240 mV vs RHE but decays below this potential giving rise a surface phase transition [139,220]. The herring-bone phase disintegrates gradually when the measured potential approaches peak P_1 (cathodic potential sweep) as observed in the red CV in Fig.7.1, where the viologen dication species (DBV^{2+}) are reduced to the corresponding radical monocations ($DBV^{\bullet+}$). Figure 7.7 shows the decay of the herring-bone structure and the simultaneous growth of the new stacked phase (Fig.7.7b and 7.7c) within the potential regime from E = -240 mV to E = -285 mV, in which the step angle of 120° is used as a positional marker. The phase transition process starts preferentially at point defects and domain boundaries as marked by the white arrows in Fig.7.7b. At the final state of the phase transition process, a full stripe pattern including two rotational domains is observed right after the potential reaches the value of E = -285 mV (Fig.7.7d). This proofs the leading role of the underlying chloride lattice for the adsorption of both the viologen dication and the radical monocation species. Additionally, the characteristic angle of 120° between substrate steps remains unaffected by this phase transition process and rules out a chloride desorption/adsorption but rather hints to an electron transfer process (reduction) as the origin of the phase transition. The chloride desorption/readsorption related phase transition will be discussed in the following sub-section.

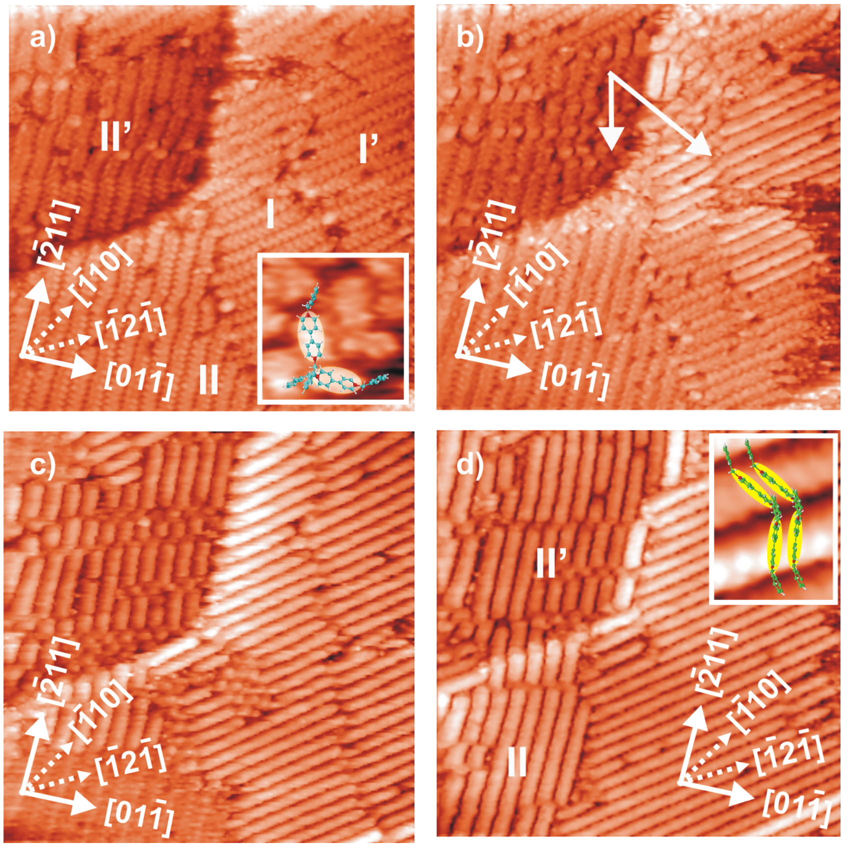

Figure 7.7: Series of STM images recorded under the same tunneling conditions (46.67 x 46.67 nm, U_b = 386 mV, I_t = 0.1 nA) showing the phase transition dynamics from the herring-bone phase to the corresponding alternating stacking pattern. Decay of the herring-bone phase and growth of the stacking phase start preferentially at defect points and step edges: a) E = -230 mV; b) E = -260 mV; c) E = -270 mV; d) E = -285 mV.

Indicated by the peak pair P1/P1’ in the CV of Fig.7.1 the phase transition from the DBV^{2+} herring-bone phase to the alternating stripe pattern is a quasi-reversible process. The DBV^{2+} related herring-bone phase is, therefore, expected to be gradually restored when the working potential is swept back towards the positive potential regime. In order to elucidate that a series of STM images is recorded at the same surface area but for increasing working potential as shown in Fig.7.8. As a result, the alternating stripe phase starts to disintegrate and the herring-bone phase is concurrently re-growing (Fig.7.8 b-e). Similar to the transformation from the DBV^{2+} herring-bone phase to the DBV$^{\bullet+}$ stripe pattern, step-edges and defect points act as activation centers for this phase transition process. Comparing Fig.7.8a and Fig.7.8f it becomes evident that two rotational domains of the DBV^{2+} herring-bone phase are formed after completion of the transition phase (Fig.7.8f) oriented parallel to the two mirror domains of the alternating stripe pattern (Fig.7.8a) aligned along the substrate steps. This observation again affirms the dominant role of electrostatic interactions between the molecular adlayer and the underlying chloride lattice for the lateral ordering.

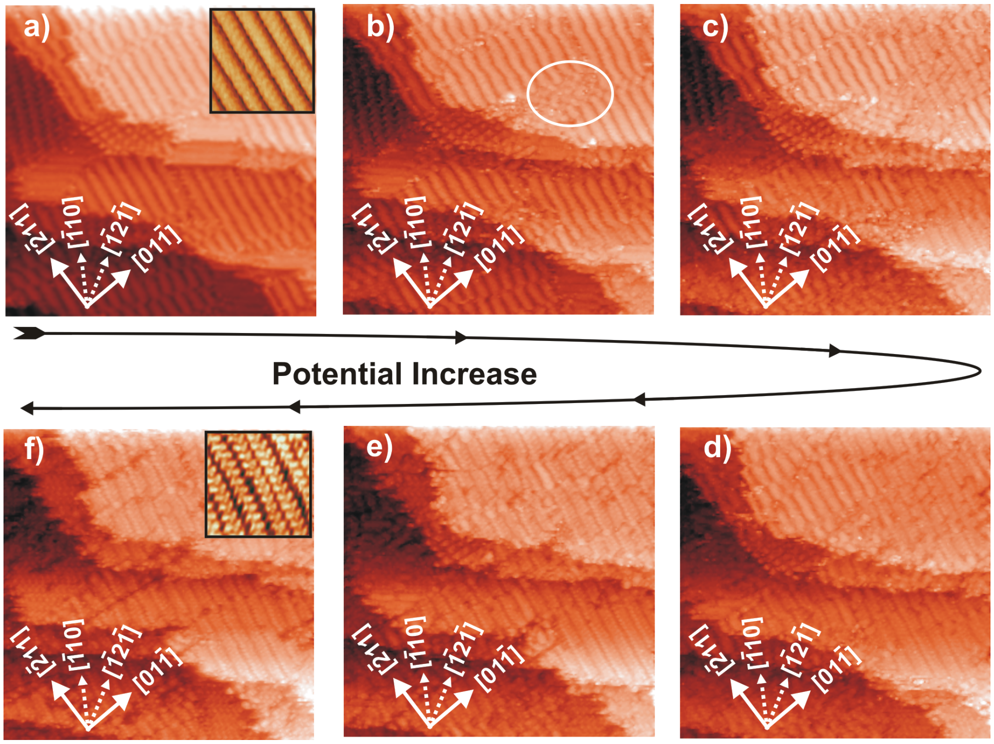

Figure 7.8: Series of STM images showing the disintegration of the alternating stack pattern and restoration of the corresponding herring-bone phase on Cu(111) upon sweeping back toward positive potentials, 46.67 x 46.67 nm, I_t = 0.1 nA; a) U_b = 240 mV, E = -300 mV; b) U_b = 240 mV, E = 290 mV; c) U_b = 200 mV, E = -270 mV; d) U_b = 200 mV, E = -240 mV; e) U_b = 233 mV, E = -200 mV; f) U_b = 233 mV, E = -165 mV.

7.3.4. Dimer phase co-existence

Astonishingly, a dimer phase appears in company with the stripe pattern upon transformation from the herring-bone phase into the stacked phase (Fig.7.9). Such a dimer phase was observed to occur on the Cu(100) surface only with the stipulation that the DBV^{2+} viologen species were adsorbed under reactive condition, i.e. the DBV^{2+} solution was added into the cell in the potential regime from -120 mV to -250 mV [221], where adsorption and reduction occur simultaneously. By contrast in the present context, this dimer phase is observed even when the DBV^{2+} species are in the electrolyte under non-reactive condition, i.e. in the double layer regime of the Cu(111) electrode where the DBV^{2+} molecules have not been reduced to the radical monocations yet [219]. Typical STM images of the coexistence of dimer and stripe phase describing the surface morphology and the molecular structure are shown in Fig.7.9a.

The rows of the dimer phase are also aligned along the step-edges that are oriented parallel to the $\langle\bar{2}11\rangle$ directions as observed in Fig.7.9a. A higher resolution STM image reveals further details of the internal molecular structure, orientation, and packing arrangement in the ordered dimer adlayer (Fig.7.9b and Fig.7.9c). Individual bright spots are recognized as a dimer configuration with an intermolecular spacing of ca. 0.44 ± 0.01 nm as concluded by the line profile measurement depicted in Fig.7.9d. This intermolecular distance completely matches the typical π-stacking assemblies of aromatic systems [212]. Additionally, the dimers are rotated by an angle of 60° (or 120°) with respect to the direction of molecular rows indicating that the orientations of the dimer rows as well as the molecules in each row are always parallel to the $\langle\bar{2}11\rangle$ directions (Fig.7.9c). The basic cause for the dimer formation is the general tendency of the radical mono-cations to dimerize and polymerize right after the viologen dications are reduced according to eq.7.1 and 7.2.

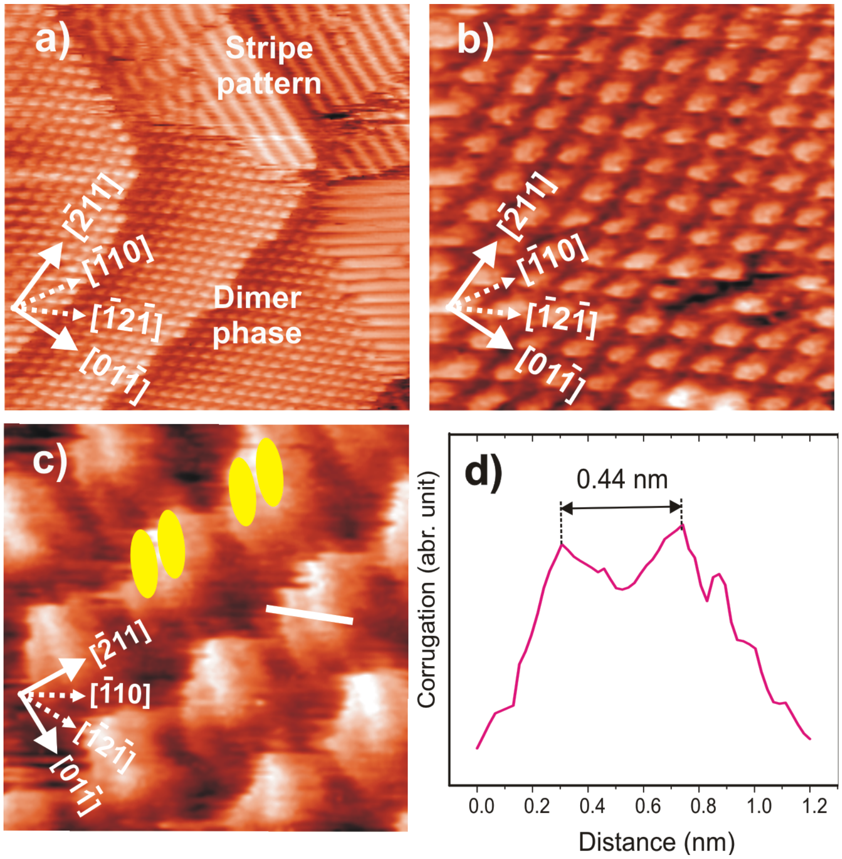

Figure 7.9: STM images of dimer phase and alternating stacked pattern co-existing on the surface: a) 46.67 x 46.67 nm, U_b= 175 mV, I_t = 0.2 nA, E = -310 mV; highly resolved STM images of the dimer phase: b) 15.65 x 15.65 nm, U_b = 175 mV, I_t = 0.2 nA, E = -310 mV; d) 5.63 x 5.63 nm, U_b = 355 mV, I_t = 0.1 nA, E = -295 mV; e) Line profile recorded along the white line in panel c indicates a 0.44 nm intermolecular distance.

7.3.5. Chloride desorption/readsorption phase transition

Finally, also chloride desorption/adsorption taking place when the working potential reaches the potential regime containing peaks P_2, P_2’ in the red CV in Fig.7.1 causes an order/disorder phase transition, which was reported by Pham et al. [138-139] and Phan et al. [219]. Also, this process is a quasi-reversible one as described in Fig.7.10. Chloride desorption preferentially starts at step-edges and point defects where the activation energy for the desorption process is less than within intact areas (Fig.7.10b). Sweeping the potential towards more negative values causes the ordered layer to be gradually replaced by a disordered one as observed in Fig.7.10c and, finally, the disordered phase is visible on the entire surface when the potential reaches E = -370 mV (Fig.7.10d). In the present case, however, it appears, that after dissolution of the ordered phase the radical monocation $DBV^{\bullet+}$ species seem to remain on the Cu(111) surface instead of desorbing concomitant with the chloride anions [30]. Hai et al. [30] found that porphyrin molecules co-desorbed from the Cu(111) surface along with the chloride anions. It is most likely that the interaction between the radical $DBV^{\bullet+}$ species and the bare Cu(111) substrate is stronger than that between the porphyrin species and the bare Cu(111) substrate and, hence, constraining the reduced viologen molecules to the bare surface. This consideration is in agreement with the former studies which examined the adsorption of either 2,2'-bipyridine on a bare Au(111) [213] or 4,4'-bipyridine on a bare Cu(111) [212] electrodes in $HClO_4$ acidic environment. In addition, incomplete desorption of chloride due to hindrance by the disordered viologen layer on top is also considered as another plausible reason for the absence of an ordered layer.

In the reverse scan, a restoration of the alternating stripe pattern is progressively visible (Fig.7.10e). A full stacked stripe pattern with three rotational domains denoted by I, II and II is again imaged once the working potential is passing E = -240 mV (Fig.7.10f). It becomes evident that while the orientations of the domains II and III run parallel to the step-edges, the domain I is rotated characteristically by an angle of 120° with respect to the rest, resulting in a stripe alignment parallel to the underlying close packed chloride rows or, alternatively, parallel to the $\langle\bar{2}11\rangle$ directions of the Cu(111) substrate. Obviously, the chloride anions in the "bulk" solution penetrate through the disordered layer of the viologen monocation and restore its $c(p \times \sqrt{3})Cl$ structure on the bare Cu(111) surface.

It becomes evident that the viologen/chloride/Cu(111) stacking leads to a reciprocal effect between the chloride underlayer and the viologen adlayer. Not only does the chloride desorption influences the ordered layer of the viologen molecules but also the presence of the viologen radical monocations on top has an influence on the chloride desorption/adsorption process. Recalling the electrochemical features of the Cu(111) surface in pure electrolyte (dashed black curve in Fig.7.1) and in DBV^{2+} containing electrolyte (red curve), we found that the HER in the presence of the DBV$^{\bullet+}$ adlayer is shifted negatively by 70 mV as compared to that in the pure supporting electrolyte. On the basis of the STM images, it is evident that the chloride desorption in the blank electrolyte has finished at E = -320 mV vs RHE, whereas this phenomenon has just started at a potential of E = -320 mV (Fig.7.10b) in the case of the presence of the DBV$^{\bullet+}$ overlayer. Hence, it is obvious that the DBV$^{\bullet+}$/Cl stacking still persists after the potential has passed the value of E = -320 mV due to the blocking of preferred desorption sites, i.e. step-edges and point defects, by the organic adlayer. As a result, the more perfect the ordered film the later the chloride desorption takes place.

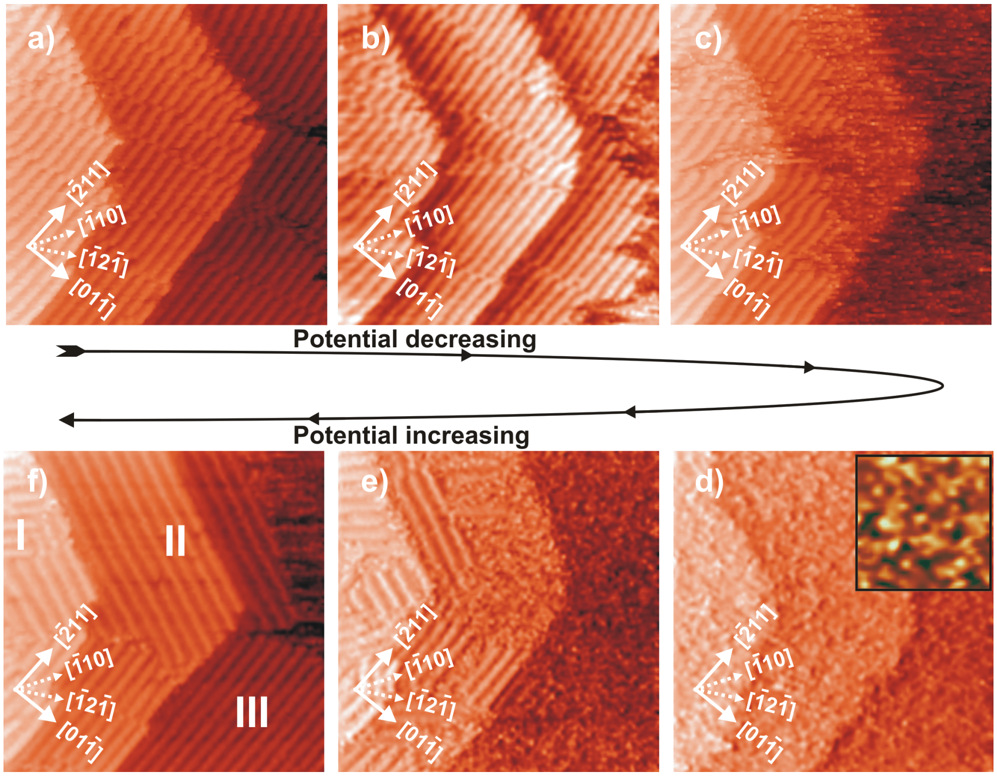

Figure 7.10: Series of STM images showing the decay and restoration of the alternating stripe pattern due to the chloride desorption/adsorption taking place in the potential regime where P_2/P_2' appear in the red CV: 46.67 x 46.67 nm, U_b = 158 mV, I_t = 0.2 nA; a) E = -260 mV; b) E = -320 mV; c) E = -340 mV; d) E = -370 mV; e) E = -290 mV; f) E = -240 mV.

7.4. Summary

Adsorption and self-assembly of DBV^{2+} on a chloride modified Cu(111) electrode under non-reactive have been investigated by means of cyclic voltammetry and in-situ scanning tunneling microscopy.

From the CV measurements, we can observe three distinct redox peak pairs close to the hydrogen evolution reaction on Cu(111) labeled by P_1/P'_1, P_2/P'_2 and P_3/P'_3, respectively. On the basis of the electrochemical findings, it can be concluded that within the potential window of the Cu(111) electrode the DBV^{2+} molecules are reduced in two steps from the dicationic state DBV^{2+} to the corresponding radical mono-cationic $DBV^{\bullet+}$ and the uncharged DBV^0 species (not further discussed here). Compared to the standard potential of $E^0(DBV^{2+}/ DBV^{\bullet+})$ = -330 mV and $E^0(DBV^{\bullet+}/DBV^0)$ = -548 mV vs RHE [33] it become evident that the cathodic peak P_1 is assigned to the first reduction from the dicationic DBV^{2+} to the corresponding radical cationic $DBV^{\bullet+}$ species, whereas the second reduction forming the uncharged DBV^0 molecules is considered to take place in the HER regime where the peak P_3 emerges. The peak pair P2/P2' is attributed to the chloride desorption/readsorption processes taking place on the Cu(111) surface, with a concomitant order/disorder transition of the organic overlayer.

Moreover, the STM experiments support the assignments suggested by the CV data. Indeed, adsorption at non-reactive potentials leads to the formation of a highly condensed and ordered herring-bone phase consisting of pairs of DBV^{2+} molecules in each structural element of the DBV^{2+} adlayer. A tentative structure model for this phase is proposed, which is in good agreement with the obtained high resolution STM images.

In contrast, an alternating stacking pattern of the reduced $DBV^{\bullet+}$ monocation radicals is observed upon passing the first reduction peak P_1 in the red CV in Fig.7.1. Based on a correlation between the adlayer structure and the underlying chloride lattice, it can safely be concluded that the structural motifs of the herring-bone and the stacking phase are predominantly governed by an enhanced electrostatic interaction between the adsorbate species and the negatively charged chloride lattice underneath. The phase transition from the DBV^{2+} related herring-bone phase to the alternating stripe pattern is a quasi-reversible process occurring via nucleation and growth.

An order/disorder phase transition at negative potentials caused by chloride desorption/adsorption, which manifests itself by the P_2/P_2' peaks in the CV, was also studied in this chapter. An amorphous phase is imaged on the chloride-free surface formed by the radical cationic $DBV^{\bullet+}$ species due to persistent interaction between these species and the bare Cu(111) surface. The STM images show that the chloride desorption process takes place from the Cu(111) in the presence of the radical cationic viologen species at more negative potentials than in the pure electrolyte. This hints to an inhibition caused by the ordered stripe film on top. This process is also reversible and, thus, after sweeping the potential back toward the positive regime the chloride anions penetrate through the amorphous layer in order to restore the $c\left(p \times \sqrt{3}\right)$ chloride superstructure underneath. Thereby, the highly ordered stacked $DBV^{\bullet+}$ phase is restored on the freshly reorganized chloride lattice.

Chapter 8

Bimolecular porphyrin/viologen adlayer on copper surfaces

8.1. Introduction

The scope of this chapter is to investigate the competitive adsorption of two positively charged organic molecules, namely porphyrin ($[H_2TTMAPP]^{4+}$) and dibenzyl-viologen (DBV^{2+}) on a Cu(100) and a Cu(111) surface, respectively, by the traditional cyclic voltammetry method in combination with in-situ STM as a structural sensitive local probe technique.

As mentioned in the previous sections, in electrochemical environment $[H_2TTMAPP(0)]^{4+}$ molecules undergo several redox reactions involving 6 electrons in total [171,176]. The first reduction step happening at E = -195 mV vs RHE considered as a reversible process is related to 2 electrons, whereas the other reductions involving 4 electrons in total are irreversible. In turn, there are three redox-states counted for DBV^{2+} molecules, i.e. the dicationic DBV^{2+}, the radical mono-cationic $DBV^{\bullet+}$ and the uncharged DBV^{0}, transforming into each other via two reversible electron transfer steps [33,219]. In the potential window of copper (from -450 mV to +300 mV), the first two reductions of both the $[H_2TTMAPP(0)]^{4+}$ and the DBV^{2+} take place. The further reduction reactions are considered to occur within the HER of the copper substrate. Due to the massive hydrogen evolution reaction, the STM can not detect the adsorption of these species.

From the electrochemical point of view, we expect to image phase transitions occurring within the bimolecular adlayer as well as to visualize directly the competitive adsorption probability of these molecules in different redox states.

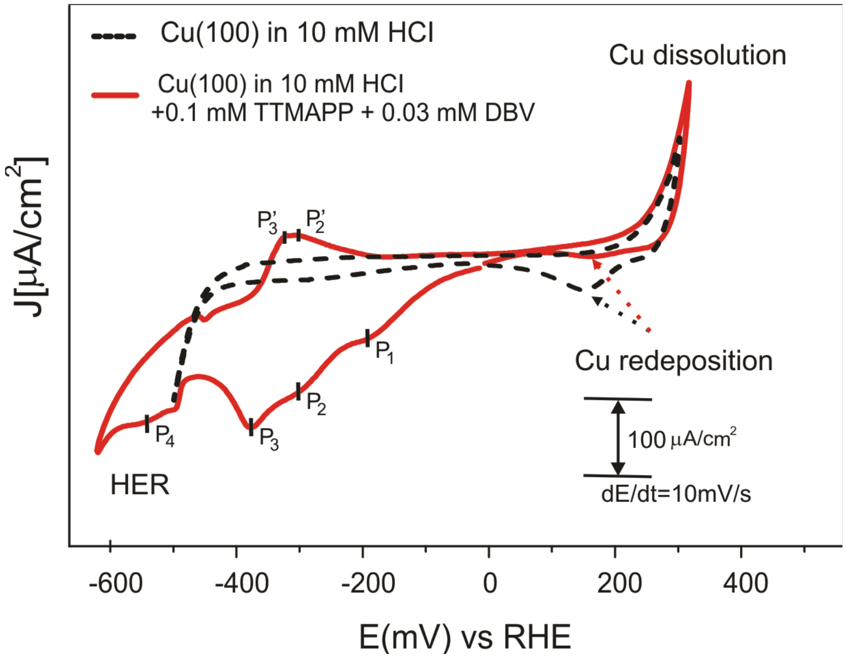

Figure 8.1: Cyclic voltammogram of a Cu(100) electrode in pure hydrochloric acid (dotted black curve) and in an electrolyte containing a mixture of $[H_2TTMAPP]^{4+}$ and DBV^{2+} (red curve).

8.2. Bimolecular adlayer on a chloride terminated Cu(100)

8.2.1. Electrochemical features

Figure 8.1 displays representative steady-state cyclic voltammograms of a Cu(100) surface in both the pure supporting (dotted black curve) and the mixed molecules containing electrolyte (red curve). A featureless CV curve between the cathodic hydrogen evolution reaction (HER) and the anodic copper dissolution reaction (CDR) is characteristic for the Cu(100) in pure hydrochloric acid. The only cathodic peak (actually an unresolved double-peak) at +130 mV is assigned to the redeposition of dissolved copper cations from solution according to: $Cu^{2+} \rightarrow Cu^{+} \rightarrow Cu^{o}$ [222]. In comparison with this CV, a drastic change is observed in the CV of the Cu(100) brought into contact with the solution containing both molecular species indicated by the red curve. The most striking deviation from the CV of the pure supporting electrolyte, in fact, is seen in the cathodic potential regime where several characteristic features arise at P_1= -193 mV, P_2 = -301 mV, P_3 = -405 mV and P_4 = -540 mV vs RHE, respectively, and a considerable shift of the HER [223]. Moreover, while the copper dissolution reactions are seen to take place at the same onset potential, the HER is shifted to more negative potentials by 125 mV in the solution containing the mixture of the organic molecules. Obviously, the bimolecular adlayer is still present at the electrode surface in the HER potential regime, hence, resulting in a hindrance of the HER.

Compared to the CVs in HCl solutions containing either only $[H_2TTMAPP]^{4+}$ with peaks at E_1 = -210 mV and E_2 = -420 mV [171,176] or only DBV^{2+} as characterized in chapter 7 [138-140,219] one can see that the red CV in Fig.8.1 is a combination of both. Indeed, the first bump at E = -193 mV coincides with peak P_1 in the CV of the Cu(100) electrode in pure $[H_2TTMAPP]^{4+}$ solution [171] which belongs to the first two-electron transfer step:

$$[H_2TTMAPP(0)]^{4+} + 2e^- + 2H^+ \leftrightarrow [H_4TTMAPP(-II)]^{4+} \qquad (8.1)$$

The peaks P2 and P3 are assigned to the reduction of the viologen dication to the corresponding radical cation and the further reduction of the porphyrin ring, respectively.

In particular, peak P_2 at E = -301 mV with the corresponding wave P_2' at E = -280 mV is attributed to the reduction/oxidation of the adsorbed viologen and/or viologen solution species according to [138].

$$DBV^{2+} + e^- <==> DBV^{\bullet+} \qquad (8.2)$$

This reduced product forms the corresponding dimer- and/or polymer species in solution or at the surface, respectively, following the process:

$$2(or\ n)DBV^{\bullet+} <==> [DBV_2]^{2+}(or\ [DBV_n]^{n+}) \qquad (8.3)$$

Peak P_3 at E = -405 mV arises from two processes, namely the second reduction reaction of the porphyrin molecules [171,176] and chloride desorption [34]. Regarding the reduction step, four more electrons are suggested to be involved [139] according to:

$$[H_4TTMAPP(-II)] + 4H^+ + 4e^- \rightarrow [H_8TTMAPP(-VI)]^{4+} \qquad (8.4)$$

The further reductions of the $DBV^{\bullet+}$ radical mono-cations to the fully uncharged viologen species (DBV^o possibly P_4) is not further considered here because this process is believed to be either out of the copper potential window or within the regime of massive hydrogen evolution and, thus, not detectable.

In the following, the STM work dealing with the adsorption and structural changes of the bimolecular adlayer as a function of electrode potential is presented in detail.

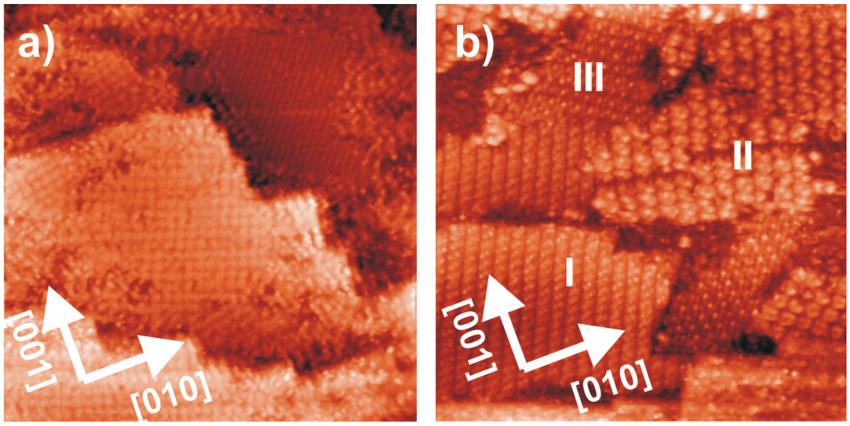

Figure 8.2: Surface morphologies of the binary adlayer structure consisting of $[H_2TTMAPP]^{4+}$ and DBV^{2+} molecules on a chloride modified Cu(100) electrode: a) 107.75 nm x 107.75 nm, U_b = +355 mV, I_t = 0.1 nA, E = -100 mV; b) 61.46 nm x 61.46 nm, U_b = +363 mV, I_t = 0.2 nA, E = +10 mV.

8.2.2. Characterization by in situ STM

8.2.2.1. The binary phase formation

For the adsorption of the binary phase consisting of porphyrin and viologen the electrolyte exchange procedure is routinely performed as described in the

Experimental section in the potential regime from -50 to +50 mV vs RHE, where the stable c(2 x 2)-Cl superstructure on Cu(100) exists and $[H_2TTMAPP]^{4+}$ and DBV^{2+} are thermodynamically stable. After exposing the chloride modified Cu(100) surface to the mixed electrolyte at this potential a highly ordered adlayer is instantaneously formed at the electrode/electrolyte interface. Typical STM images describing the surface morphology and the molecular structure are presented in Fig.8.2. First, the specific angle of 90° at the step-edges (Fig.8.2a) indicates that the chloride anion layer on the Cu(100) electrode is still persistent and unaffected by the presence of the molecular adlayer ontop. A close view on the adsorbate structure shows that this adlayer occurs in three distinct sub-phases denoted as I, II and III, respectively, depicted in Fig.8.2b.

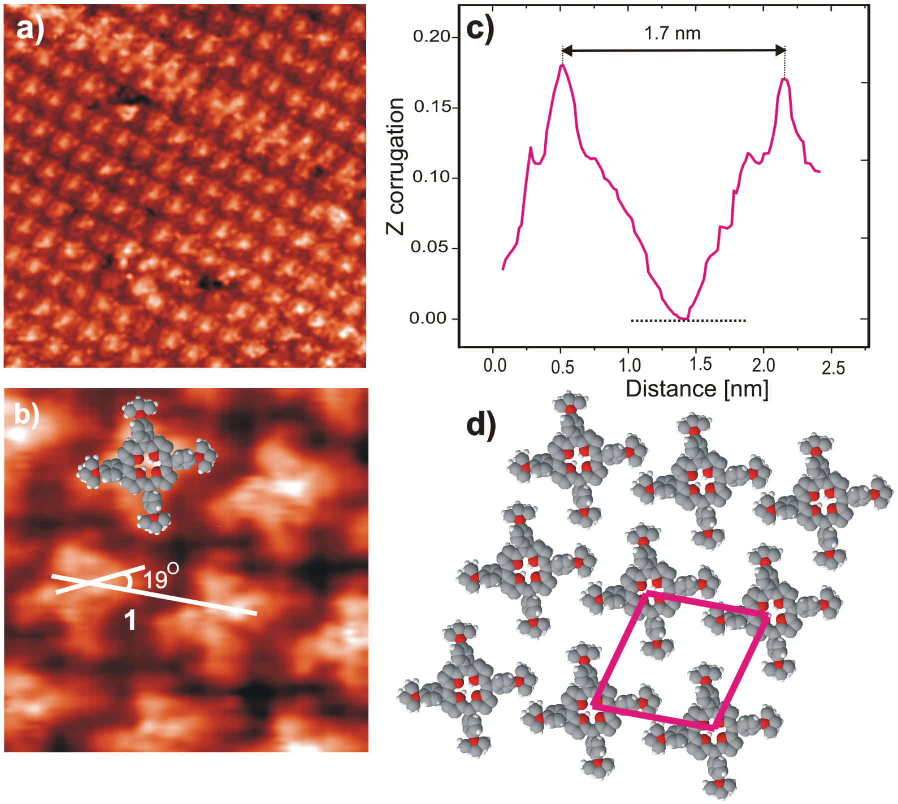

Figure 8.3: Typical medium scale and high resolution STM images of a pseudo square lattice of the $[H_2TTMAPP]^{4+}$ molecules: a) 23.23 nm x 23.23 nm, U_b = +252 mV, I_t = 0.15 nA, E = +10 mV; b) 4.95 nm x 4.95 nm, U_b = +168 mV, I_t = 0.1 nA, E = +20 mV; c) Line profile recorded along line 1 in Fig.8.3b; d) possible model for the square phase on Cl/Cu(100).

On the molecular level, phase I is homogeneously formed only by $[H_2TTMAPP]^{4+}$ molecules (Fig.8.3a). As presented in detail in section 6.3.2, the $[H_2TTMAPP]^{4+}$ molecules are arranged in rows and individual molecules in a row are recognized as a propeller shaped entity and rotated by an angle of 19° with respect to the molecular row as shown in Fig.8.3b. This indicates that porphyrin molecules are flat lying on the chloride layer due to strong electrostatic interactions between the positively charged molecular layer and negatively charged underlying chloride template. The intermolecular distance is calculated using the line profile to be 1.7 ± 0.1 nm as shown in Fig.8.3c. A possible model with a unit cell containing one molecule is proposed for the adsorption of the pure $[H_2TTMAPP]^{4+}$ domains in Fig.8.3d. This structure is identical to the one presented and discussed in chapter 6.

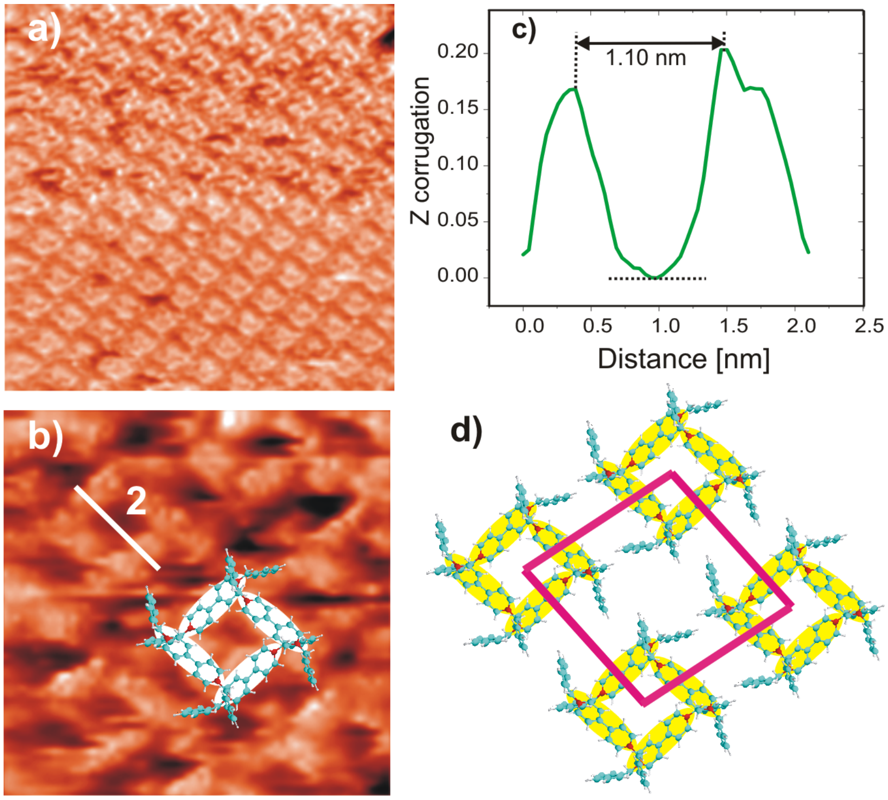

Figure 8.4: Typical medium scale and high resolution STM images of a DBV^{2+} related cavitand phase: a) 30.37 nm x 30.37 nm, U_b = +355 mV, I_t = 0.1 nA, E = +0 mV; b) 7.32 nm x 7.32 nm, U_b = +487 mV, I_t = 0.1 nA, E = +0 mV; c) Line profile recorded along line 2 in Fig.8.4b; d) possible model for the cavitand phase on Cl/Cu(100).

Simultaneously, one also observes pure viologen domains of the so-called DBV^{2+} “cavitand phase” which was previously described in detail by Pham et al. [138,139] and Safarowsky et al. [140]. The cavitand phase of the viologen is built up by square-shaped units of molecular assemblies with pronounced cavities in their centers (Fig.8.4). Each square-shaped unit of the DBV^{2+} pattern consists of four rod-shaped subunits (Fig.8.4b) arranged in a circular manner. On the basis of STM observations and a careful analysis of this arrangement with an intermolecular distance of 1.1 nm (Fig.8.4c) it can be safely concluded that each square unit is built by four individual DBV^{2+} molecule (see model in Fig.8.4b). A possible structure model for this phase is proposed in Fig.8.4d in which a unit cell contents four square shaped units [138-140].

In addition to the two well known phases mentioned above, a new combined phase consisting of both porphyrin and viologen molecules is also observed (denoted as phase III in Fig.8.2) and presented in Fig.8.5. From the STM observations, it can be seen that the combined arrangement comprising both $[H_2TTMAPP]^{4+}$ and DBV^{2+} molecules on the chloride terminated Cu(100) electrode (Fig.8.5a). At sub-molecular resolution, one can realize a homogeneously alternating alignment of $[H_2TTMAPP]^{4+}$ and DBV^{2+} molecules. The $[H_2TTMAPP]^{4+}$ molecules appear as propeller shaped units and the DBV^{2+} molecules show their typical rod shaped appearances (Fig.8.5b). To elucidate these obtained STM results, a line profile is employed to estimate the intermolecular distances between adjacent porphyrin molecules. As a consequence, in comparison with the intermolecular distance in phase I (Fig.8.3c) the length between neighboring porphyrin molecules in phase III (indicated by line 3 and Fig.8.5c) is longer (1.95 nm compared to 1.7 nm). Furthermore, on the basis of the line profile recorded along line 4 in Fig.8.5b it is clear that the length of a rod-shaped DBV^{2+} molecule is approximately 0.77 nm (see detail in Fig.8.5d). Obviously, in the present context, the intermolecular porphyrin spaces in phase III are large enough so that the DBV^{2+} molecules can be accommodated within these spaces resulting in the formation a new binary phase [33]. Again, the electrostatic interaction between the positively charged molecules and the negatively charged chloride lattice, plus hydrogen bonds between the $[H_2TTMAPP]^{4+}$ and the DBV^{2+} molecules are assumed to play a crucial role for the stabilization of this phase III on the chloride pre-covered Cu(100) electrode surface. A molecular arrangement of phase III, which is a truly mixed phase, is proposed by the model shown in Fig.8.5e.

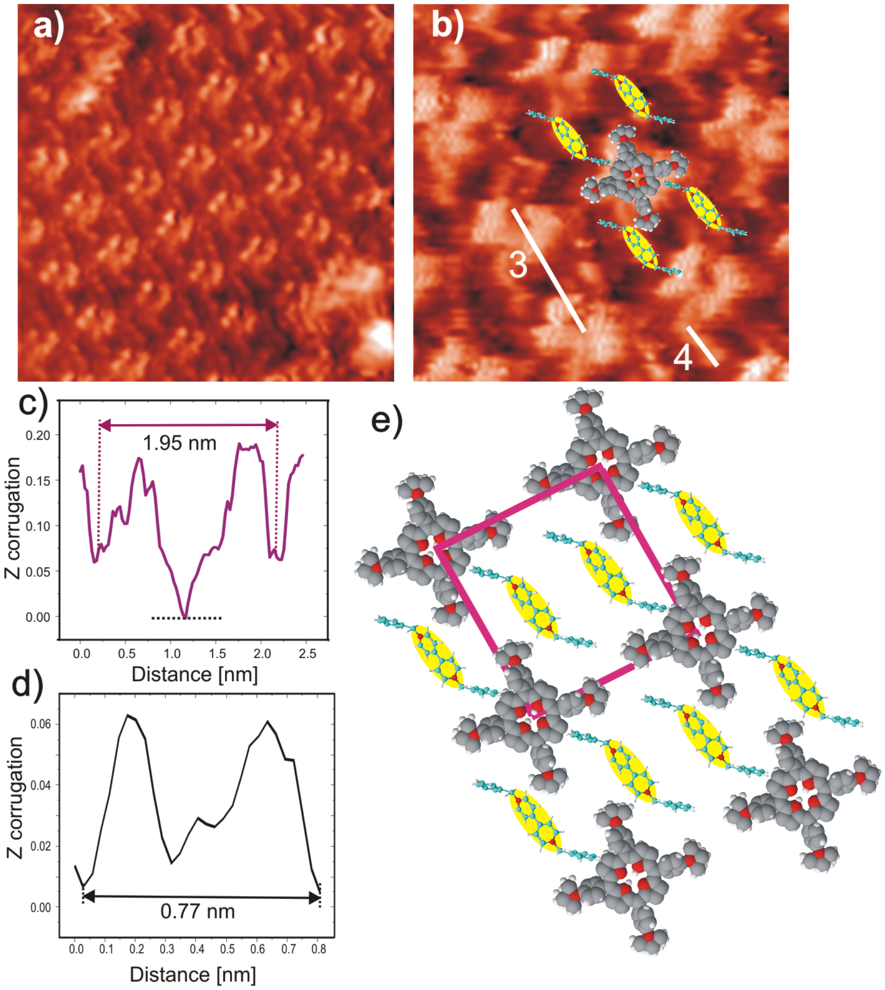

Figure 8.5: Typical medium scale and high resolution STM images of a mixed phase in which the $[H_2TTMAPP]^{4+}$ molecules are recognized as bright squares and the DBV^{2+} molecules as rod shaped entities: U_b = +323 mV, I_t = 0.1 nA, E = +30 mV; a) 12.82 nm x 12.82 nm; b) 5.60 nm x 5.60 nm; Line profile along the line 3 and line 4 in Fig.8.5b are shown in panel c and d, respectively; e) possible model for the mixed phase on Cl/Cu(100).

8.2.2.2. The stacking phase

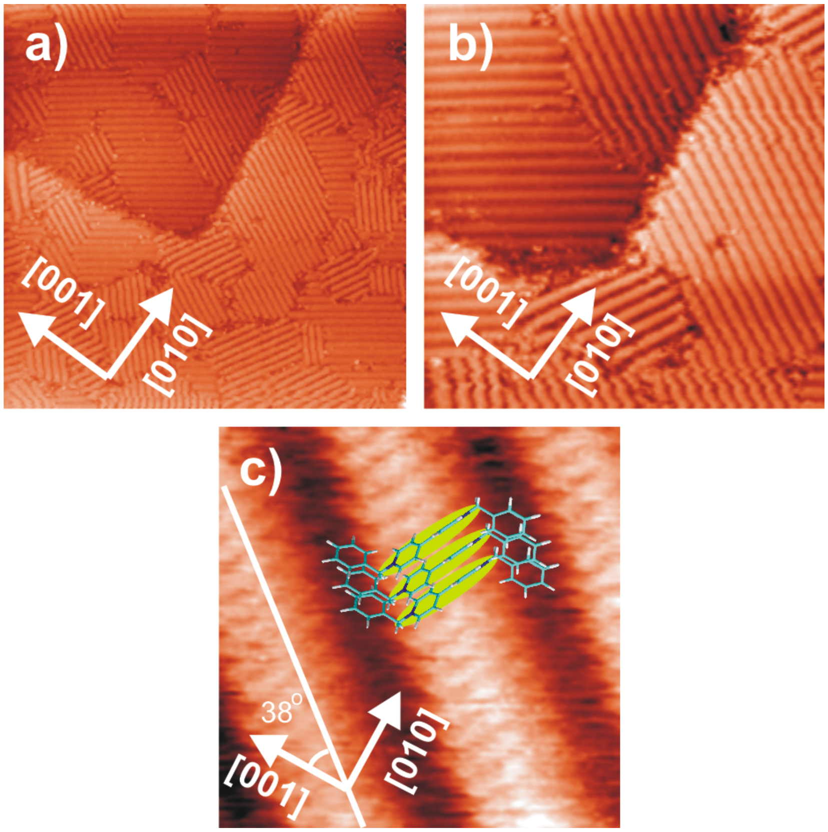

Figure 8.6: Surface morphology, medium scale and high resolution STM images of the stripe pattern phase on Cu(100)-c(2 x 2)-Cl: a) 83.73 nm x 83.73 nm, U_b = +350 mV, I_t = 0.1 nA, E = -300 mV; b) 44.37 nm x 44.37 nm, U_b = +350 mV, I_t = 0.1 nA, E = -300 mV; c) 4.46 nm x 4.46 nm, U_b = +260 mV, I_t = 0.15 nA, E = -310 mV.

Upon lowering the potential to 300 mV vs RHE a stripe pattern is formed based on the radical mono-cationic $DBV^{\bullet+}$ species which originates from the reduction of dicationic DBV^{2+}. A typical surface morphology and high resolution image of the pure stripe pattern is presented in Fig.8.6. On the basis of the observed STM images, one can conclude that the stripes are aligned parallel neither to the surface steps nor to the close-packed copper rows underneath, which are rotated by an angle of 45° with respect to the step-edges. As a result, several mirror domains are observed on large terraces (Fig.8.6a and b). A close view into the individual sub-domain is shown in Fig.8.6c. Each $DBV^{\bullet+}$ molecule is recognized as a bright elongated disc which is assigned to a face to face orientation of the bipyridinium core. The dark ditches observed in the STM image are believed to be a superposition of the benzyl side-groups. For a detailed discussion see the refs. 138-140 and papers cited therein. While the individual $DBV^{\bullet+}$ molecule is rotated by an angle of 14 ± 1° with respect to the stripe direction, the propagation direction of stripes encloses an angle of about 38 ± 2° with the [001] direction of the underlying chloride lattice (Fig.8.6c). The intermolecular distance within a row is calculated from a line profile to be 0.37 ± 0.02 nm (data not shown). This value is in full agreement with a π-stacking assembly of aromatic system [138,139,223] supporting a face to face configuration of the $DBV^{\bullet+}$ monocation radicals.

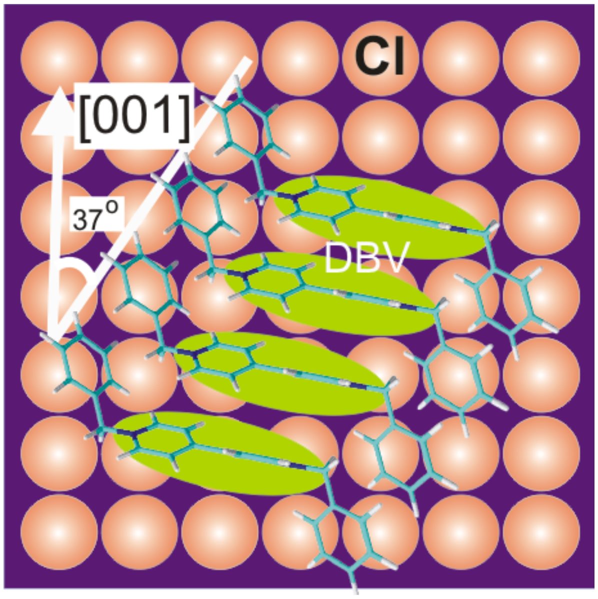

Figure 8.7: Possible structural model of the stripe pattern forming on the Cl/Cu(100) electrode surface showing a deviation of the stripe propagation of 37° with respect to the close packed chloride rows underneath.

On the basis of these observations a structure model describing a single stripe domain is proposed in Fig.8.7. The bipyridinium planes of the $DBV^{\bullet+}$ molecules are suggested to be inclined with respect to the chloride lattice plane and exhibit a trans-conformation [216]. The angle of 37° between the $DBV^{\bullet+}$ molecular rows and the [001] direction as shown in Fig.8.7 is in agreement with the observed result in Fig.8.6c. An insignificant deviation is assigned to slight thermal drift during the measurement. Thus, this stripe phase is identical to the one if $DBV^{\bullet+}$ is alone on the surface.

8.2.2.3. Mixed and coexisting phases/stacking phase transition

The cavitand phase of DBV^{2+} molecules, the pseudo-square phase of $[H_2TTMAPP]^{4+}$ molecules as well as the mixed phase on the c(2 x 2)-Cl/Cu(100) remain stable in the potential range higher than -200 mV vs RHE [138,220]. A change toward lower potential results in the reduction of free base $[H_2TTMAPP]^{4+}$ molecules as well as dicationic DBV^{2+} to the corresponding reduced products, namely, $[H_4TTMAPP(-II)]^{4+}$ and radical monocation ($DBV^{\bullet+}$), leading to a decay of both the mixed and coexisting phases as observed in Fig.8.8. The decay process starts at defect sites and/or domain boundaries marked by white arrows, which serve as active centers for the phase transition taking place on the copper surface. As a result, a stripe pattern gradually replaces the mixed and coexisting phases upon decreasing the electrode potential (Fig.8.8b and c).

Astonishingly, all three phases are displaced by the viologen mono-cation stripe phase. Consequently, the phase transition is completed at about E = -293 mV with the consequence that the viologen radical mono cations completely substitutes the viologen dications and the reduced porphyrin species and forms a perfect stripe phase on the entire chloride precovered Cu(100) electrode surface (Fig.8.8d). Obviously the $DBV^{\bullet+}$ stripe phase is in this potential regime the thermodynamically more stable one. Indeed, the viologen reduction to the corresponding viologen radical monocations causes a reduction of the positive charge on the adsorbed viologens resulting in reduced repulsive electrostatic interactions and, vice versa, increasing corresponding intermolecular interactions.

As a result, the viologen radical monocations, which are known to dimerize in an aqueous solution [33,134] form an ordered array of 1D oligomer and polymer chains of $[DBV_n]^{n+}$ according to eq.8.3. The strong intermolecular bonding due to the π-π interactions between neighboring bipyridinium cores as well as adjacent benzyl side-groups stabilizing the 1D chains on the chloride modified Cu(100) electrode surface are also known from the uncharged HPOG substrate. Pham et al. [221] observed 1D chain formation of the $DBV^{\bullet +}$ molecules also on the bare HOPG electrode surface with sub-molecular resolution. This supports the observed STM images which show a successful competition of the $DBV^{\bullet +}$ molecules on the electrode surface against the $[H_4TTMAPP(-II)]^{4+}$ molecules. In addition, after undergoing the first reduction process the reduced

$[H_4TTMAPP(-II)]^{4+}$ molecules are known to desorb from the surface leaving surface vacancies behind [176] which are occupied by the viologen radical monocations (dimer phase). The potential at which this phase transition occurs with respect to the mixed solution is observed more positively than that in electrolyte containing only DBV [138-139].

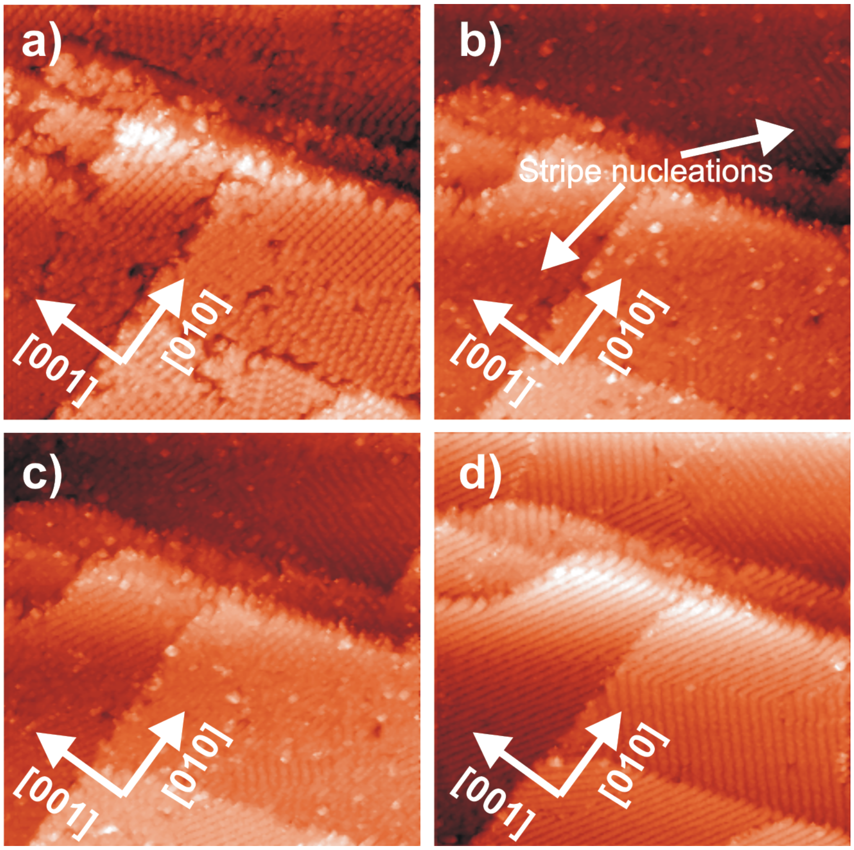

Figure 8.8: Series of STM images showing the surface transition from the mixed adlayer to the single stripe pattern indicating a predominance of $DBV^{\bullet +}$ molecules compared to both the $[H_2TTMAPP]^{4+}$ molecules and its reduction products: 76.82 nm x 76.82 nm, U_b = +336 mV, I_t = 0.1 nA; a) E = -120 mV; b) E = -240 mV; c) E = -273 mV; d) E = -293 mV.

Sweeping backward the potential into the positive regime, a phase transition from the stripe pattern to the mixed and coexisting phases is expected to occur due to the reversible redox process of both porphyrin and viologen molecules [138,176]. Experimentally, a series of STM images showing the decay of the stripe pattern and the subsequent growth of both the mixed and coexisting phases upon increasing the potential from E = -320 mV to E = -100 mV is presented in Fig.8.9. Obviously, the stripe pattern phase is still fully persistent at a potential of E = -320 mV as shown in Fig.8.9a. Disintegration of the stripes starts when the electrode potential has reached a value of E = -240 mV marked as white arrow in Fig.8.9b. As a result, the $DBV^{\bullet+}$ molecular stripes are gradually replaced by the corresponding $[H_2TTMAPP(0)]^{4+}$ and DBV^{2+} molecules in order to restore the bimolecular phases as shown in Fig.8.9c-e. The phase transition process is fully completed at a potential of E = -100 mV, where the new layer consisting of cavitands formed by the DBV^{2+} molecules, the pseudo square phase built up by the corresponding $[H_2TTMAPP(0)]^{4+}$ molecules and the mixed phase is formed (Fig.8.9f). Therefore, from the observed STM results one comes to the conclusion that the composition of the adlayer can be systematically controlled by an adjustment of the electrode potential.

It could be seen that a delicate potential change leads to a radical modification from the 2D ordered binary phase consisting of DBV^{2+} and $[H_4TTMAPP(\text{-II})]^{4+}$ species to the 1D oligomer and polymer single component phase of $DBV^{\bullet+}$ species indicating the dominance of the π-π interactions between the $DBV^{\bullet+}$ monocation radicals. In contrast, these π-π interactions between neighboring and adjacent viologen radical mono-cations are broken upon increasing the electrode potential up to E = -100 mV or more. As a result, the polymeric stripes decay and a new equilibrium allows the bimolecular adsorption as shown in Fig.8.9. The change of the surface charge density at the electrochemical interface leads to modify not only the interaction between molecules and substrate but also between the molecules.

An investigation of binary component adlayers was, in fact, earlier done by Itaya and his coworker [38,224]. The composition of an ordered mixed adlayer of copper(II) octaethyl porphyrin (CuOEP) and cobalt(II) phthalocyanine (CoPc) on an Au(111) and an Au(100) surfaces was found to vary depending on the immersion time. As a consequence the CoPc molecules replaced the CuOEP ones upon increasing the immersion time, such that the latter molecules were completely displaced by the former molecules into the mixed solution.

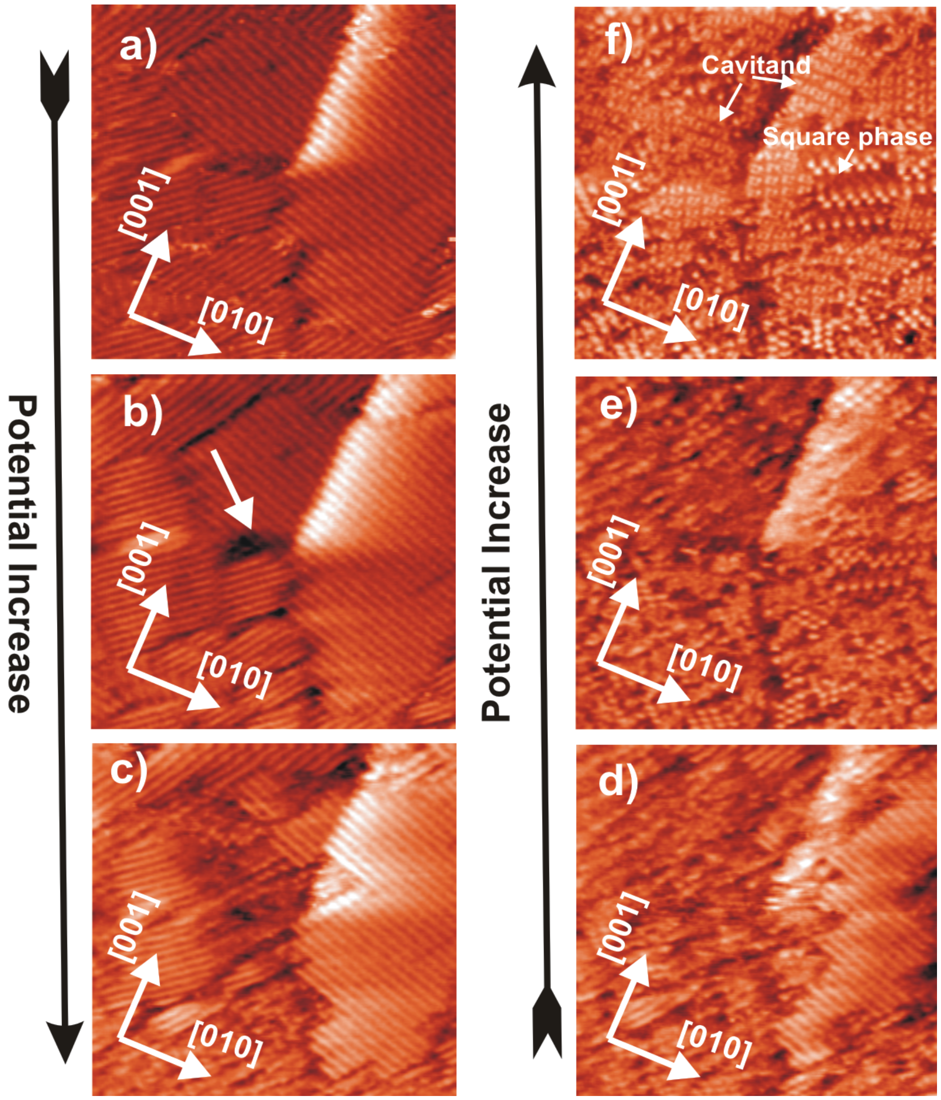

Figure 8.9: Series of STM images showing the decay of the stripe pattern phase and the subsequent growth of the mixed and coexisting phases with increasing potentials: 61.46 nm x 61.46 nm, U_b = +295 mV; I_t = 0.1 nA; a) E = -320 mV; b) E = -240 mV; c) E = -200 mV; d) E = -175 mV; e) E = -130 mV; f) E = -100 mV.

8.2.2.4. Chloride desorption/adsorption induced ordered/disordered phase transition

A further potential sweep reaching peak P_3 (see Fig.8.2) is expected to lead to a further phase transition driven by the desorption of the underlying chloride layer [138,176]. The chloride readsorption takes place upon sweeping the electrode potential in the reverse scan direction passing P_3' in the red CV (Fig.8.2). To clarify this hypothesis a series of STM images is recorded at the same surface area as a function of electrode potential showing, indeed, a decay and a re-growth of the stacking phase as shown in Fig.8.10. The observed STM results show that the preferential sites for activation of this order/disorder phase transition are both step-edges and domain boundaries marked by white arrows as seen in Fig.8.10b. As a consequence, the disordered phase gradually dominates the surface (Fig.8.10c) and the replacement is fully completed when the electrode potential has reached E = -440 mV (Fig.8.10d). A similar template effect leading to an order/disorder phase transition was also investigated by Pham et al. [139].

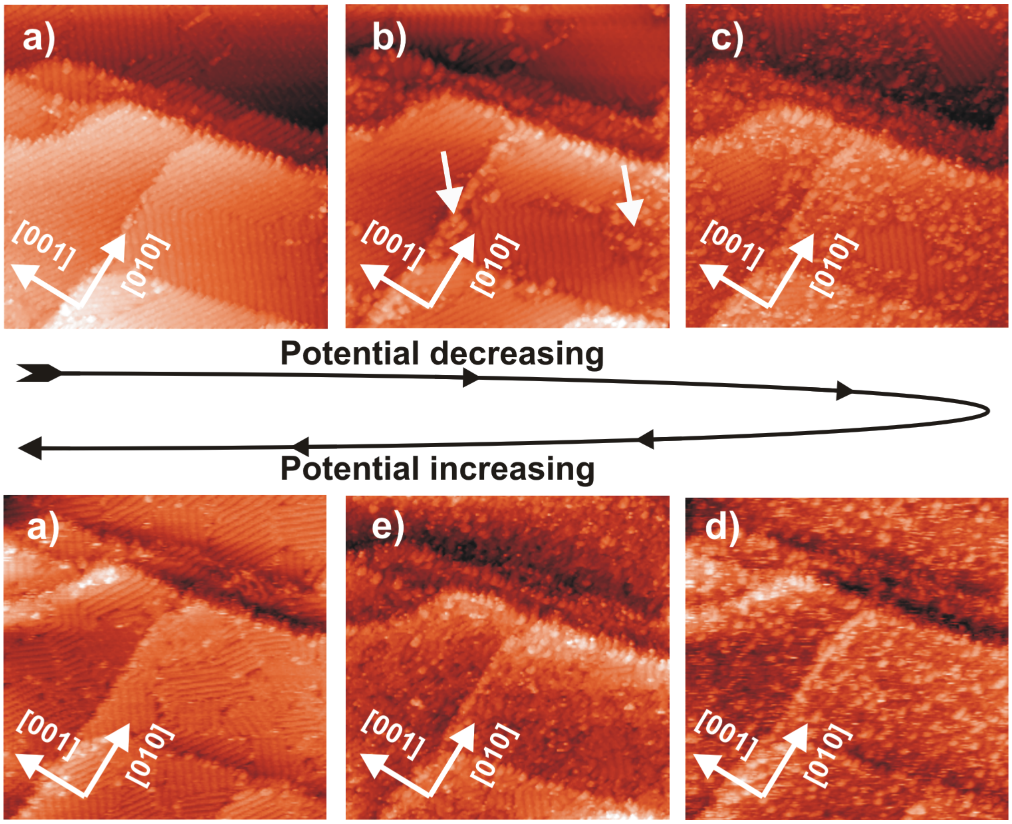

Figure 8.10: Chloride desorption dependent decay of the stripe pattern phase upon reaching the potential range where P_3 appears in the CV: 76.83 nm x 76.83 nm, U_b =

+388 mV, I_t = 0.2 nA; a) E = -355 mV; b) E = -400 mV; c) E = -420 mV; d) E = -440 mV; e) E = -347 mV; f) E = -320 mV.

By sweeping the potential back, the STM observation shows again a dominant competition of the $DBV^{\bullet+}$ molecules over the $[H_4TTMAPP(-II)]^{4+}$ molecules upon restoration of the lateral ordering (Fig.8.10e,f). This observation is consistent with the fact that the $[H_4TTMAPP(-II)]^{4+}$ species are unable to adsorb on the chloride modified Cu(100) at this potential due to the weak electrostatic interaction with the negatively charged chloride lattice underneath.

8.3. Bimolecular adlayer on a chloride terminated Cu(111)

8.3.1. Structural determination

The bimolecular adlayer consisting of $[H_2TTMAPP]^{4+}$ and DBV^{2+} is also examined on a chloride modified Cu(111) electrode surface. As reported in the previous chapters, under non-reactive conditions, i.e. in the double layer regime of the Cu(111) electrode where both molecules have not been reduced yet, the $[H_2TTMAPP]^{4+}$ molecules form a square structure [176], whereas a herring-bone pattern was assigned to the adsorbed DBV^{2+} species on the chloride template [219].

In this section, the self-assembly of the two component system composed of $[H_2TTMAPP]^{4+}$ and DBV^{2+} molecules is addressed as a function of electrode potential and tunneling conditions in order to elucidate the role of the underlying chloride lattice with respect to immobilization and self-organization of the positively charged organic molecules on top. Fig. 8.11 shows such a typical large-scale STM image recorded at E = -100 mV right after the pure supporting electrolyte (10 mM HCl) was replaced by one containing a mixture of the $[H_2TTMAPP]^{4+}$ and DBV^{2+} species. It can be seen that the terrace is fully covered with two randomly distributed phases, namely, a square shaped lattice and a herring-bone pattern. On the basis of these STM results, it becomes evident that the latter phase is assigned to the adsorption of the dication DBV^{2+} molecules, while the $[H_2TTMAPP]^{4+}$ molecules form the square lattice. Apparently, the DBV^{2+} molecular rows run parallel to the substrate steps, whereas the molecular rows of the $[H_2TTMAPP]^{4+}$ molecules are aligned along the $\sqrt{3}$ direction of the chloride lattice. This finding hints that the row arrangement of the DBV^{2+} species is parallel to the close packed rows of the underlying chloride lattice and, hence, is coincident with the $\langle\bar{2}11\rangle$ directions of the copper substrate. Similarly, by alignment along the $\sqrt{3}$ direction compared to the step-edges the $[H_2TTMAPP]^{4+}$ molecular rows run parallel to the close packed rows of the underlying copper lattice, i.e. the $\langle\bar{1}10\rangle$ directions [85,186,219].

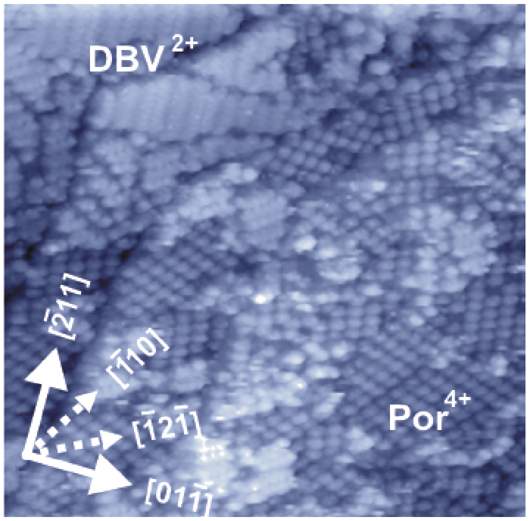

Figure 8.11: Typical large scale STM image showing co-existence phase of the $[H_2TTMAPP]^{4+}$ and the DBV^{2+} molecules: 63.23 x 63.23 nm, U_b = 339 mV, I_t = 0.15 nA, E = -100 mV.

The difference in height between the individual adsorbate domains is taken to identify the individual molecular species. Indeed, the porphyrin molecules are well-known to lie flat on the chloride template [30,31,171,176] resulting in a low corrugation. In turn, the di-cationic DBV^{2+} species exhibits a pronounced non-zero interplanar dihedral angle between the two pyridinium rings of $\Phi = 40.1°$ [33,225] and tend to stand side-on on the surface [216], thereby appearing higher.

Compared to the bimolecular adlayer on Cl/Cu(100), no mixed phase is observed on the chloride modified Cu(111) electrode surface under the same experimental conditions as used in the previous section. It is likely that the difference of the underlying chloride lattice, i.e. square vs. hexagonal arrangement, respectively, results in the absence of the mixed phase. In addition, it is found that the competition between the observed phases strongly depends on the working potential and the applied tunneling conditions. By changing either the electrode potential or the tunneling conditions one can observe a new phase formation due to molecular reduction.

8.3.2. Tunneling conditions dependence

In order to elucidate the competition within the bimolecular adlayer consisting of $[H_2TTMAPP]^{4+}$ and DBV^{2+}, a series of STM images is shown in Fig.8.12 at the same surface area (see step in the lower right corner) taken under different tunneling conditions. Fig.8.12a shows a steady state STM image including two separate highly ordered phases, namely the herring-bone and the square phases. When the tip-sample separation is reduced by either increasing the tunneling current or decreasing the bias voltage the tunneling tip acts as a “brush” sweeping the organic molecules on top away as seen in the lower part in Fig.8.12b and the upper part in Fig.8.12c. This experiment surely guarantees that the binary molecular film is completely swept away from the chloride template surface. For readsorption of the molecules the tunneling tip is retracted by applying the adequate tunneling conditions, i.e. lower tunneling current and higher bias voltage (Fig.8.12c). Astonishingly, the measured terrace is now dominantly covered by herring-bone phase instead of two different phases as observed in Fig.8.12a. On the basis of this observation it can be safely concluded that the $[H_2TTMAPP]^{4+}$ compound is replaced by the DBV^{2+} species upon the restoration. A reasonable interpretation for this visible phenomenon is that the adsorption of the DBV^{2+} molecules on the chloride modified copper electrode is much stronger than that of the $[H_2TTMAPP]^{4+}$ molecules. Additionally, the orientation of the DBV^{2+} molecular rows remains parallel to the step-edge as marked by the white arrow in Fig.8.12d indicating that the formation of the ordered adlayer of the DBV^{2+} molecules is governed by the underlying chloride lattice. The co-existence layer is, therefore, metastable and its equilibration may be triggered by the tunneling tip.

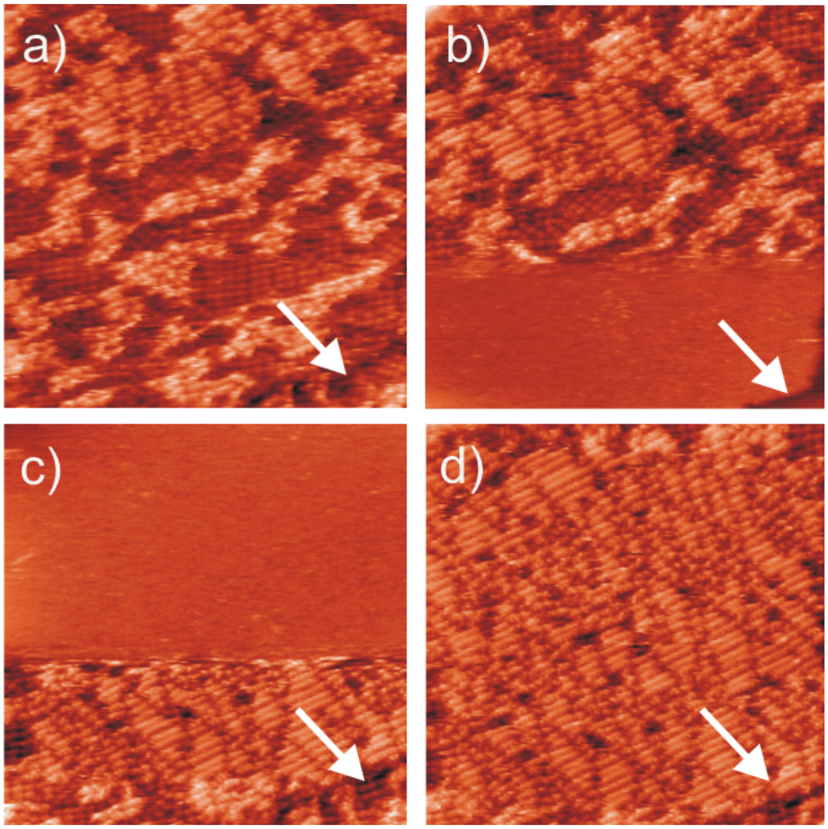

Figure 8.**12:** A series of STM images showing the tip induced selective adsorption between $[H_2TTMAPP]^{4+}$ and DBV^{2+} molecules indicates dominant adsorption of the viologen species: 77.78 x 77.78 nm, E = -19 mV; a) U_b = 360 mV, I_t = 0.1 nA; b-d) U_b = 200 ÷ 300 mV, I_t = 0.1 ÷ 10 nA.

8.3.3. Potential dependence

8.3.3.1. Electrochemical features

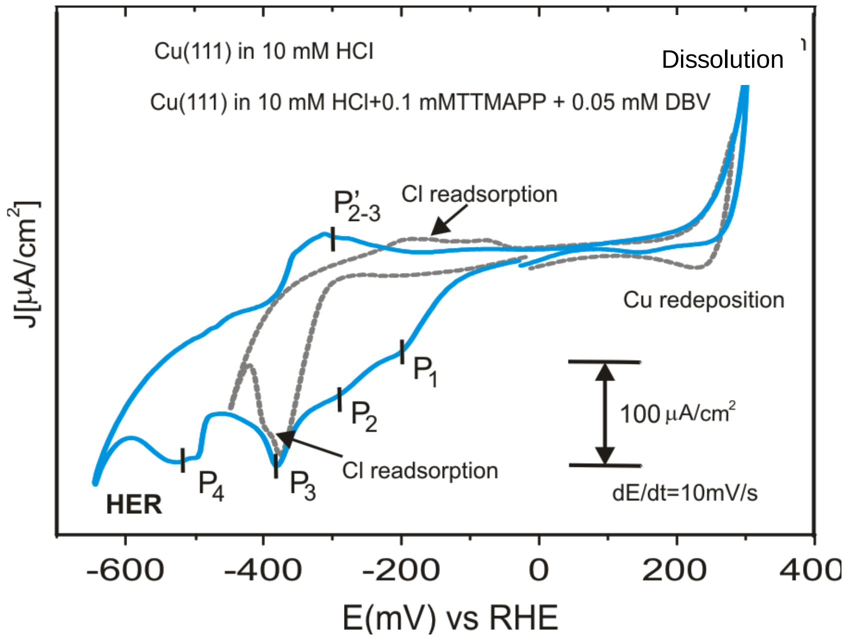

Figure 8.13: Cyclic voltammogram of a Cu(111) electrode in pure hydrochloric acid (dotted grey curve) and in electrolyte containing a mixture of $[H_2TTMAPP]^{4+}$ and DBV^{2+} (blue curve); four cathodic peaks relate to both porphyrin and viologen .reduction; scan rate dE/dt = 10 mV/s.

Similar to the Cu(100) case, an electron transfer and chloride desorption/re-adsorption induced phase transition of the bi-component adlayer as a function of electrode potential is also observed by both cyclic voltammogram and scanning tunneling microscopy measurements. Fig.8.13 describes typical CVs of a Cu(111) electrode in pure supporting electrolyte (dashed back curve) and in electrolyte containing a mixed solution of $[H_2TTMAPP]^{4+}$ and DBV^{2+} molecules. Between the oxidative copper dissolution reaction (CDR) at the anodic limit and the reductive hydrogen revolution reaction (HRE) at the cathodic limit additional chloride desorption/adsorption peaks are also observed as shown in the dashed grey CV [171]. The CV features of Cu(111) in the mixed electrolyte (10 mM HCl + 0.1 mM $H_2TTMAPP$ + 0.05 mM DBV) are rather similar to those of the Cu(100), in which four distinguished cathodic peaks labeled from P_1 to P_4 (blue curve) are attributed to (i) first two-electron transfer step of the porphyrin ligands; (ii) the viologen related reduction process, i.e. from the di-cationic DBV^{2+} to the corresponding radical mono-cationic $DBV^{\bullet +}$; (iii) the chloride adsorption/desorption based order/disorder phase transition, and (iv) the reduction of the radical mono-cations to the fully uncharged viologen species (DBV^{0}), respectively.

8.3.3.2. Potential induced phase transition

In order to clarify the above assumption a series of STM images is taken at different potentials. A phase transition taking place at the electrolyte/substrate interface undergoes the following steps:

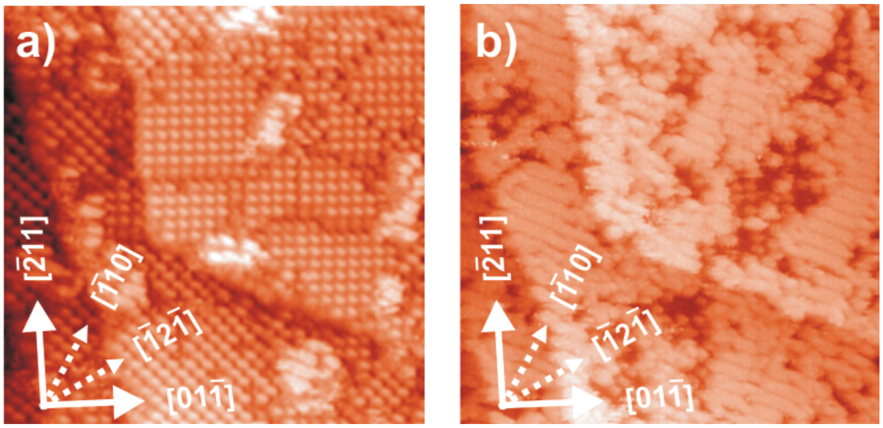

Figure 8.14: Phase transition from the mixture relating to both the $H_2TTMAPP^{4+}$ and DBV^{2+} molecules to the herring-bone structure built up by the DBV^{2+} species only: 63.23 x 63.23 nm, $U_b = 339$ mV, $I_t = 0.15$ nA; a) E = -100 mV; b) E = -235 mV.

- From the bimolecular phase to the herring-bone structure

  The herring-bone structure of the dicationic DBV^{2+} species covers the whole terrace because the square phase of $[H_2TTMAPP]^{4+}$ decays upon sweeping the potential through peak P_1 (Fig.8.14 and 8.15). Obviously, as reported in chapter 6, after overcoming the first two-electron transfer step according to eq.8.1 the porphyrin species is reduced to $[H_4TTMAPP(\text{-II})]^{4+}$ and desorbs from the surface leaving the chloride lattice behind [176]. As a result, the di-cationic DBV^{2+} molecules occupy the vacancies, formed by the $[H_4TTMAPP(\text{-II})]^{4+}$ desorption, on the chloride template (Fig.8.14b and 8.15b). Desorption of the reduced $[H_4TTMAPP(\text{-II})]^{4+}$ molecules is completed at E = -240 mV [176] resulting in an exclusive formation of the observed DBV^{2+} herring-bone pattern (Fig.8.14b).

- Herring-bone/stacking phase transition

The viologen dication based herring-bone structure remains stable in the potential range more positive than E = -240 mV vs RHE, and then decays due to the first reduction of the viologen molecules [139,220]. Namely, sweeping toward more negative potentials leads to a desintegration of the herring-bone film and the growth of the corresponding stripe pattern when the potential reaches the regime of peak P_2, where the dicationic DBV^{2+} species are reduced to the corresponding radical mono-cationic $DBV^{\bullet+}$ molecules (Fig.8.15c,d). Similar to a previous report [219] the herring-bone structure decays and the growth of the stacking phase preferentially occurs at defect points, domain boundaries and step-edges. The stacked phase dominates over the measured terrace at potential required E = -270 mV as seen in Fig.8.15e and f. It becomes evident that the potential required for the phase transition from the herring-bone to the corresponding stacking phase happening in the mixed solution is more positive than that in electrolyte containing only viologen species. For details see ref.219 and papers cited therein. A plausible reason for this observation bases on the fact that desorption of the reduced $[H_4TTMAPP(\text{-II})]^{4+}$ molecules leaves vacancies after undergoing the first reduction. These voids are not filled by the dicationic DBV^{2+} molecules due to co-existence of the radical mono cationic $DBV^{\bullet+}$ molecules in “bulk” solution within this potential regime. These radical mono-cationic $DBV^{\bullet+}$ species are assumed to occupy the free holes on the surface as observed in Fig.8.15c,d. Additionally, the amount of free vacancies upon the first phase transition process rises resulting in an increase of activation centers for the second phase transition step (Fig.8.15c,d). Consequently, the phase transition rate from the herring-bone to the stacking phase is significantly enhanced. On the basis of the STM images, it is found that the dimer phase is also accompanied with the stripe pattern marked by white arrows in Fig.8.15e and in inset figure in Fig.8.15f. This finding is in agreement with the results in chapter 7. The dimer phase was found to appear in company with the stacking at the same potentials when the Cu(111) electrode surface was brought into contact with solution containing only viologen.

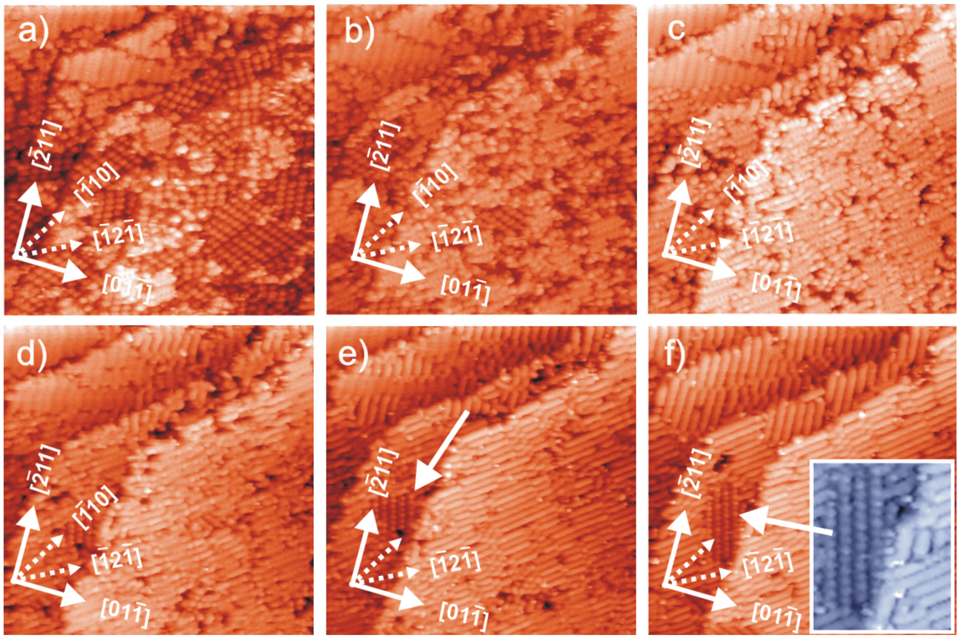

Figure 8.15: Series of STM images showing the decay of the mixed phase and the corresponding growth of alternating stacking pattern: 63.23 x 63.23 nm, U_b = 300 mV, I_t = 0.15 nA; a) E = -160 mV; b) E = -230 mV; c) E = -2350 mV; d) E = -240 mV; e) E = -248 mV; f) E = -270 mV.

- The chloride desorption/readsorption induced disorder/order phase transition is completely similar to that taking place on Cu(100) as mentioned in sub-section 8.2.2.4.
- The phase transition related to the reduction of the radical mono-cations to the fully uncharged viologen species is considered to coincidently occur with the hydrogen evolution reaction and, hence, direct visualization by STM is limited.

A typical molecular scale STM image describing a mixture of the stacked pattern and the dimer phase is displayed in Fig.8.16. Compared to the stripe pattern forming on Cl/Cu(100) the arrangement of the stacked phase on Cl/Cu(111) is more strongly governed by the underlying chloride lattice. Apparently, the stripe rows run parallel to the step-edges and, thus, are aligned along the $\langle\bar{2}11\rangle$ directions of the Cu(111) substrate [186, 220] (Fig.8.16a). From a close-up view into the stacking phase on the Cl/Cu(111) template it could be concluded that the $DBV^{\bullet+}$ molecules in a row are parallel to each other, whereas the arrangement of the $DBV^{\bullet+}$ species in adjacent rows is in opposition

(Fig.8.16b). As a result, the DBV$^{\bullet+}$ molecules form a so-called “zig-zag” structure on the chloride template (see inset molecular model in Fig.8.16b). This finding is in complete agreement with the observations reported for the adsorption of the pure viologen on a chloride modified Cu(111) in chapter 7.

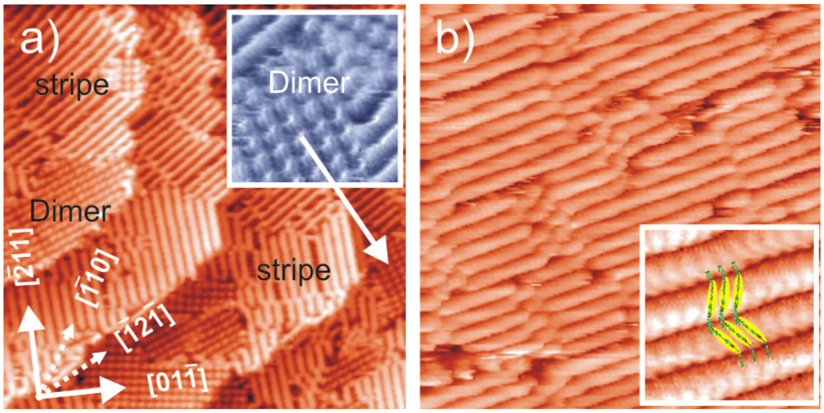

Figure 8.16: a) Typical large scale STM image describing a mixture of stacked pattern and dimer phase: 63.23 nm x 63.23 nm, U_b = 339 mV, I_t = 0.15 nA, E = -100 mV; b) High resolution STM image of the alternating stacking phase indicating the molecular rows run parallel to the ⟨2̄11⟩ directions of Cu(111) substrate; 27.25 nm x 27.25 nm, U_b = 235 mV, I_t = 0.1 nA, E = -285 mV; inset picture showing the molecular orientation within the rows.

The competitive adsorption between $[H_2TTMAPP]^{4+}$ and DBV^{2+} on a chloride terminated Cu(111) electrode reconfirms that the conformation and the phases of the components of a bimolecular system can be controlled by either the tunneling conditions or the potentials.

8.4. Summary

In this chapter, the adsorption of a bimolecular system consisting of $[H_2TTMAPP]^{4+}$ and DBV^{2+} on both chloride modified Cu(100) and Cu(111) electrodes, respectively, has for the first time been examined by using a combination of CV and EC-STM experiments.

On the basis of the CV experiments, we can conclude that the set of peak pairs P_1/P_1', P_2/P_2', P_3/P_3', P_4/P_4' appearing in the CVs in Fig.8.1 and Fig.8.13 is related to the following reactions or processes:

- The peak pair P_1/P_1' is assigned to the first two-electron transfer reduction/re-oxidation of the porphyrin ligands from the $[H_2TTMAPP(0)]^{4+}$ to the corresponding $[H_4TTMAPP(-II)]^{4+}$ species.
- The peaks P_2 and P_4 are related to the first and the second electron transfer reductions from the dicationic DBV^{2+} to the corresponding radical mono cationic $DBV^{\bullet+}$ species, and then to the uncharged DBV^0 molecules, respectively. The peaks P_2' and P_4' are the corresponding re-oxidation steps.
- The last peak pair P_3/P_3' is attributed to the chloride desorption/re-adsorption processes on the surface.

Preliminary assignments of the peaks emerging in the CVs of the Cu(100) and the Cu(111) electrodes are in agreement with the experimental observations by EC-STM. Indeed, in case of the Cl/Cu(100) serving as template and under non-reactive adsorption, the surface is covered by a well-ordered binary molecular adlayer consisting of three distinguishable phases. A square phase is built up only by porphyrin molecules. The second phase is well-known as the so-called “cavitand phase” which is an assembly of squares of four DBV^{2+} molecules. The mixed phase is self-organized from a combination of $[H_2TTMAPP(0)]^{4+}$ and dicationic DBV^{2+} species. By contrast, the bimolecular adlayer of the $[H_2TTMAPP(0)]^{4+}$ and the DBV^{2+} compounds forming on the Cl/Cu(111) template is separated into two “pure” phase, namely, the square phase of the $[H_2TTMAPP(0)]^{4+}$ and the herring-bone phase of the DBV^{2+} molecules, respectively, without forming a mixed phase.

Sweeping through the first reduction peak P_1, the $[H_2TTMAPP(0)]^{4+}$ molecules are reduced to the corresponding $[H_4TTMAPP(-II)]^{4+}$ species. As a result, these reduced species desorb from the surface leaving vacancies behind, which are supposedly occupied by the viologen radical monocations forming the dimer phase. This replacement process is fully completed after the potential passed E = -240 mV in the negative direction. In any case, upon further decreasing the potential toward more negative values, a phase transition from the dicatonic DBV^{2+} based cavitand phase (or dicatonic DBV^{2+} based herring-bone phase) to the corresponding radical monocationic $DBV^{\bullet+}$ stacked phase is observed.

However, the phase transition taking place in this case occurs more positive than that of the pure viologen at the same conditions due to the porphyrin desorption. While the stripes of the stacked phase forming on the Cl/Cu(100) enclose an angle of 38° with respect to the main symmetric axes of the underlying chloride lattice, the propagation of the stripes on the Cl/Cu(111) is aligned parallel to the close packed row of the chloride lattice underneath.

At more negative potentials, passing the chloride desorption peak, an order/disorder phase transition accompanying the chloride desorption/readsorption processes happens. The chloride desorption is considered to occur through the organic viologen molecular adlayer resulting in the formation of an amorphous organic layer. The presence of this amorphous adlayer inhibits the hydrogen evolution reaction (HER) and, hence, a significant hysteresis of the HER to much more negative potentials in the electrolyte containing mixture is observed.

Chapter 9

Summary and Conclusions

Self-assembled layers of organic molecules on solid surfaces have attracted increasing attention in recent years due to their broad applicability in modern material science. The sheer unlimited “design” of the properties of the organic molecules and their well controlled deposition on suitable substrates can lead to functional surfaces with broad applications as catalysts in the field of “green energy”, as devices in state-of-the-art electronics, as sensors and collectors or emitters of light etc. to name only a few. This has motivated surface scientists to apply their broad arsenal of high resolution techniques to investigate the growth mechanisms and collective properties of organic films in order to lay the basis for a rational design of their functionality.

One promising route towards the preparation of organic films is their deposition from solution by dip coating, electrochemical deposition etc. because it extends their realization to organic molecules which are not intact volatile; besides, deposition from solution appears more economic than from the vapor phase in vacuum.

To this end the present thesis aims at making a contribution to the “in-situ characterization of self-assembled organic layers at anion modified metal/electrolyte interfaces”. Specifically, three kinds of redox-active organic molecules were chosen and electrochemically deposited on single crystal copper electrode surfaces. The properties of the resultant films were characterized as a function of the symmetry of the substrate electrode, i.e. on Cu(100) and Cu(111), the preadsorbed anion layer, i.e. chloride, bromide, iodide and sulfate, as well as the electrochemical potential applied to the respective electrode. The following three kinds of redox-active molecules have been chosen:

Metal phthalocyanine (ZnPcPyMe): The self-assembly of this molecule was to be studied on an iodide modified Cu(100) electrode surface. At first, however, it was found that in acidic environment the ZnPcPyMe molecules are transformed into the corresponding metal-free species, i.e. H_2PcPyMe, so that all results presented in this thesis refer to the adsorption of this latter species.

Free base and metal porphyrins (H_2TTMAPP and FeTMPyP): With these molecules, the influence of a number of factors such as the surface symmetry and, especially, the potential induced redox-state on the self-assembly were systematically investigated. The lateral ordering of the H_2TTMAPP molecules on the reactive copper surfaces was studied with sub-molecular resolution, for the first time, while the investigations on the self-assembled layer of the FeTMPyP species extend earlier work.

Dibenzyl-viologen (DBV): Using this molecule, two systems were investigated for the first time, namely (i) the self-assembly of DBV on a chloride modified Cu(111) substrate, in contrast to earlier work on Cu(100) and (ii) the competitive co-adsorption with H_2TTMAPP on Cu(100) and Cu(111), respectively.

In order to achieve an atomistic understanding of the molecular adlayer, a combination of the following three methods was used:

- Cyclic Voltammetry (CV) as a traditional method for the redox chemistry of molecules at metal/electrolyte interfaces as a function of electrode potential.
- In-situ Electrochemical Scanning Tunneling Microscopy (EC-STM) as an atomistically sensitive techniques for surface structure determination and phase behavior of the molecular adlayers,
- Ex-situ X-ray Photoelectron Spectroscopy (XPS) as a supplement method for the correlation of the observed structures with the exact chemical state of the molecules.

9.1. Phthalocyanine adsorbed on an iodide modified Cu(100) surface

The self-assembly of the stable metal-free H_2PcPyMe phthalocyanine species on an iodide terminated Cu(100) surface leads to an ordered adlayer. It is suggested that on the largely uncharged I/Cu(100) surface the adsorption and lateral ordering is dominated by van der Waals interactions both between the organic molecules and the iodide underlayer as well as between the phthalocyanine species themselves.

XPS results

Based on the XPS spectra, the following conclusions are put forward: (i) Although the solution was prepared from ZnPcPyMe-iodide the missing of the Zn 2p signal proves that the zinc atoms in the phthalocyanine rings (ZnPcPyMe) were replaced by hydrogen atoms leading to the adsorption of the corresponding free base phthalocyanine (H_2PcPyMe) in acidic media, and (ii) a co-adsorption of sulfate anions within the H_2PcPyMe layer was also detected by the appearance of the S 2p signal.

Electrochemistry

First, an overview of the electrochemical behavior of H_2PcPyMe was determined employing an HOPG electrode because of its large potential window form -600 to +2200 mV vs RHE. Within the potential regime from +315 to + 800 mV vs. RHE the phthalocyanine molecules adsorb from solution unchanged, i.e. in the $[H_2PcPyMe]^{4+}$ state. In the potential range below +315 mV these molecules undergo several redox reactions. The first redox step to $[H_2PcPyMe]^{3+}$ consists of a one-electron transfer process with cathodic and anodic peak maxima at E = +89 mV and E = +315 mV, respectively. Further reduction processes are observed at -98 mV, -260 mV, and -429 mV, respectively. Since these reduction potentials of the free base phthalocyanine molecules are within the potential range of copper (-500 to +300 mV vs RHE) the corresponding redox steps are also expected to occur once the copper surface is contacted with the electrolyte containing the free base phthalocyanine molecule.

Self-assembled structure

A highly ordered film of ($[H_2PcPyMe]^{4+}$ step is imaged with EC-STM at the electrolyte/Cu(100) interface. The molecules arrange in rows forming a square lattice with the symmetry directions differing from those of both iodide and Cu(100) underneath, namely a characteristic angle of 28 ± 1° between the substrate <011> directions and the lattice vectors of the organic adlayer is observed. Individual molecules can be recognized as a black hollow surrounded by eight bright spots attributed to the pyridyl groups with flat-lying orientation. A square $\left(\sqrt{45}/2 \times \sqrt{45}/2\right)R28^{\circ}$ unit cell is determined with respect to the underlying iodide lattice or $\left(\sqrt{45} \times p\sqrt{45}/2\right)R28^{\circ}$ directly related to the Cu(100) surface. The lattice constants are also figured with $|\vec{a}_2| = |\vec{b}_2| = 1.81$ nm enclosing an angle of 91 ± 2° for the case of p = 2.5. Based on the proposed model, the molecular surface coverage calculated is about 0.048 ML relating to the iodide underneath, or 3.04×10^{13} molecules/cm^2.

9.2. Self-assembly of H_2TTMAPP on anion modified copper surfaces

The adsorption of this free base porphyrin derivative ($[H_2TTMAPP]^{4+}$) on reactive copper surfaces has been investigated for the first time. In particular, the electrochemistry and in-situ visualization of highly ordered layers of the $[H_2TTMAPP]^{4+}$ molecules was studied on different anion modified copper surfaces, namely on Cl/Cu(100), Cl/Cu(111), Br/Cu(111), I/Cu(111) and SO_4/Cu(111).

Electrochemical behavior

Based on the CVs of HOPG in H_2TTMAPP containing acidic electrolyte, first an overview about the redox processes of this molecule is obtained. Within the potential window of HOPG (i.e. from -600 to +2200 mV vs RHE) the H_2TTMAPP species undergoes two successive reduction steps. While the first reduction step taking place at E = -210 mV relates to the first two-electron transfer process, the second one including four electrons in total occurs at a potential with the current peak maximum at E = -420 mV. These two reduction steps are also observed in the potential window of copper dividing this window into two parts as follows: (i) The non reactive regime from -200 to +300 mV where the solution species, i.e.

$[H_2TTMAPP(0)]^{4+}$, remains stable on the surface. More positive of this regime the copper dissolution reaction takes place. (ii) The reactive regime from -500 to -200 mV shows further cathodic peaks relating to the reduction of the $H_2TTMAPP$ molecules, the desorption of the anions from the surfaces, and the hydrogen evolution reaction.

Self-assembled structure under non-reactive conditions

In the non reactive regime, the solution species $[H_2TTMAPP(0)]^{4+}$ adsorbs strongly and forms highly ordered layers on the copper surfaces, the structure of which depends on substrate symmetry and pre-adsorbed anion species.

The influence of the substrate symmetry has been tested by adsorbing the $[H_2TTMAPP(0)]^{4+}$ species on the c(2x2)Cl/Cu(100) and the $c(p \times \sqrt{3})$Cl/Cu(111), respectively. Even though the molecules form a square lattice on both surfaces, the molecular rows of the $[H_2TTMAPP(0)]^{4+}$ adlayer on the Cu(111) run strictly parallel to the close packed rows of the underlying chloride anions, while this is not the case on the Cl/Cu(100) substrate. In addition, the surface coverage is higher on the (111) than on the (100) plane probably due to the higher surface coverage of anions, i.e. the higher charge density, on the Cu(111) surface.

The influence of the nature of the pre-adsorbed anion layer manifests itself by adsorbing $[H_2TTMAPP(0)]^{4+}$ on a Cu(111) surface modified by chloride, sulfate, bromide and iodide. The first two anion layers are negatively charged and, hence, the electrostatic interaction between the porphyrin cations and the chloride and sulfate layers is decisive for the formation of the highly ordered layers of the $[H_2TTMAPP(0)]^{4+}$ species on them. As a result, fully ordered layers of the $[H_2TTMAPP(0)]^{4+}$ molecules are observed on the chloride and the sulfate terminated copper surfaces. Contrarily, the last two anion layers are largely uncharged, so that the adsorption of the positively charged porphyrin layer is governed by van der Waals type interactions. Consequently, the $[H_2TTMAPP(0)]^{4+}$ molecules adsorb quite weakly on the Br/Cu(111) and the I/Cu(111) substrates resulting in the formation of submolayer islands of regular structure, but the relationship between the molecular overlayer and the underlying lattices is unclear.

Influence of the electrode potential

As mentioned above, at negative potentials the adsorbed porphyrin molecules undergo a electrochemical reduction. This change in redox-state is expected to influence the structure of the adlayer. Specifically, by passing the first reduction peak P_1 in the CV of both surfaces, i.e. Cu(100) and Cu(111), in porphyrin containing electrolyte in cathodic direction, a quasi reversible phase transition from the ordered square phase mentioned above to a disordered phase in observed. Since this first two-electron transfer reaction from $[H_2TTMAPP(0)]^{4+}$ to $[H_4TTMAPP(-II)]^{4+}$ reduces the total charge on the molecules, their electrostatic interaction to the anion modified substrate underneath is weakened. As a result, the $[H_4TTMAPP(-II)]^{4+}$ species easily escapes from the surface leaving the disordered layer behind.

In turn, in the anodic regime, first domain ripening within the $[H_2TTMAPP(0)]^{4+}$ layer and then the copper dissolution reaction are observed after shifting the electrode potential positively. Focusing on the latter phenomenon, the presence of the highly ordered layer of porphyrin has no impact on the copper corrosion process. In addition, the incorporation of copper cations, i.e. Cu^{2+}, into the free base porphyrin ($[H_2TTMAPP(0)]^{4+}$) leading to CuTTMAPP does not take place, in contrast to what was previously observed with $[H_2TMPyP]$. It is suggested that this is due to an overall change of the electronic properties between both types of molecules caused by the presence of the four highly polarized trimethylamonium groups, i.e. $(CH_3)_3N^+$.

9.3. FeTMPyP adsorbed on chloride modified Cu(100)

As an example for a metal-porphyrin, the self-assembled structure of FeTMPyP molecules on a chloride terminated Cu(100) surface was successfully investigated here in order to complement previous work on the adsorption of the FeTMPyP on I/Cu(100).

Electrochemical feature:

In aqueous solution, iron porphyrin ($Fe^{III}TMPyP$) exists in several forms depending on the pH value and can undergo several reduction steps relating to the iron center and the π-conjugated ring of the porphyrin, respectively. The first reduction step of the iron center from $Fe^{III}TMPyP$ to $Fe^{II}TMPyP$ involving a one-electron transfer occurs at E = +240 mV vs RHE. The Fe^{II}TMPyP undergoes the next reduction steps at the π-conjugated ring system and the methyl-pyridyl groups at potentials more negative than E = -200 mV. Therefore, within the potential window of Cu(100) the following three regimes can be distinguished: (i) The anodic regime from +200 to +300 mV corresponds to an anodic peak system where the first redox process of the Fe^{III}TMPyP and the copper dissolution reaction occur, (ii) the intermediate regime from -200 to +200 mV where the first reduced product is stable, i.e. Fe^{II}TMPyP, and (iii) the cathodic regime from -450 to -200 mV where the next reduction steps relating to the π-conjugated ring system and the hydrogen evolution reaction take place.

Structure of the adsorbed Fe^{II}TMPyP layer

In-situ EC-STM measurements reveal an ordered self-assembled layer of the Fe^{II}TMPyP species on the chloride modified Cu(100) surface in the intermediate regime. The $[Fe^{II}TMPyP]^{4+}$ molecules arrange in rows building up a square lattice. Individual molecules are recognized as a propeller shape with a protrusion at its center. The square unit cell containing one $[Fe^{II}TMPyP]^{4+}$ molecule can be described by a $\begin{vmatrix} 4 & -1 \\ 1 & 4 \end{vmatrix}$ transformation matrix with respect to the underlying chloride lattice, and the lattice vectors $|\vec{a}_2| = |\vec{b}_2| = 1.53 \pm 0.01$ nm enclose an angle of $93 \pm 2°$. Based on the proposed model, the surface coverage per domain is calculated to be 0.059 ML with respect to the underlying c(2 x 2)-Cl lattice or 2.14×10^{13} molecules/cm^2.

9.4. DBV self-assembly of chloride modified Cu(111)

In order to complement previous work on the adsorption of DBV on Cl/Cu(100) here the self-assembly of DBV was studied on a chloride modified Cu(111) surface using CV and EC-STM measurements.

Electrochemical behavior

In aqueous solution, viologen molecules undergo two reduction steps from viologen dications (DBV^{2+}) to the corresponding viologen monocation-radical ($DBV^{\bullet+}$) and finally to the uncharged molecule (DBV^{0}), respectively. Within the potential window of Cu(111), three reversible pairs of peaks are observed resulting in the distinction of two different regimes, namely the non-reactive regime (from -200 to +300 mV) where the viologen exists as the DBV^{2+} dication on the surface and the reactive regime (from -500 to -200 mV) relating to the reduction processes. The first pair of peaks ($P1_{max}$ = -290 mV, $P1'_{max}$ = -260 mV) is assigned to the first reduction/reoxidation step from the dicationic DBV^{2+} to the corresponding radical cationic $DBV^{\bullet+}$ species, the second pair of peaks ($P2_{max}$ = -375 mV, $P2'_{max}$ = -320 mV) is correlated with the chloride desorption/readsorption processes taking place on the Cu(111) surface and, the last pair of peaks ($P3_{max}$ = -470 mV, $P3'_{max}$ = -460 mV) is assigned to the reduction/reoxidation from the $DBV^{\bullet+}$ species to the uncharged DBV^{0} molecules and the hydrogen evolution reaction.

Ordered adlayer of DBV on Cl/Cu(111):

In the positive regime, the DBV^{2+} dications form a so-called herring-bone phase with two DBV^{2+} molecules per sub-unit. Electrostatic interactions between the negatively charged chloride layer and these dicationic vilologen species are taken to be the major driving force for their adsorption and subsequent lateral ordering on the chloride modified electrode surface. The DBV^{2+} lattice can be described by a (2 x 2p) unit cell with respect to the $c(p \times \sqrt{3})Cl$ structure underneath with lattice constants estimated to be $|\vec{a}_2|$ = 0.83 nm and $|\vec{b}_2|$ = 3.32 nm and enclosing an angle of 88 ± 2°. Each unit cell contains four molecules, and, thus, the surface coverage per domain is calculated to be Θ = 0.25 ML with respect to the underlying chloride lattice or 14.49 molecules/cm^{2}

After passing the first reduction peak, a radical monocation ($DBV^{\bullet+}$) based “zig-zag” staking phase is observed. The π-π interaction between the bipyridinium cores is taken to play the dominant role as the driving force for the *polymerization* of this stripe structure. An ordered dimer phase is also found to coexist with this stacking phase. The unit cell of the zig-zag phase containing two $DBV^{\bullet+}$ molecules corresponds to a (1 x 4)-c(p x $\sqrt{3}$)-Cl mesh with the lattice constants of $|\vec{a}_2|$ = 0.43 ± 0.02 nm and $|\vec{b}_2|$= 2.56 ± 0.02 nm, respectively, and, the $DBV^{\bullet+}$ surface coverage per domain is calculated to be Θ = 0.25 ML with respect to the c(p x √3)-Cl structure serving as the template or 14.30 molecules/cm^2.

An even further decrease of the potential, i.e. passing the second cathodic peak, leads to the desorption of the chloride interlayer. This process starts at step-edges and point defects and is accompanied by the disintegration of the monocationic stripe phase. But this order/disorder transition is reversible, by sweeping back towards positive potentials both chloride re-adsorption and restoration of the stripe phase are observed.

9.5. Bimolecular layer on a chloride modified coppers

Finally, also a two-component adlayer consisting of $[H_2TTMAPP]^{4+}$ and DBV^{2+} molecules forming on a chloride terminated Cu(100) and Cu(111) surface, respectively, using EC-STM measurements was investigated. Such measurements provided insight into the relative stability of different organic adlayers and/or the occurrence of mixed phases.

Electrochemistry

The cyclic voltammograms of the two copper electrodes in hydrochloric acid solution containing both porphyrin and viologen molecules show a drastic deviation from the above described systems containing only one or the other organic species. Close to the hydrogen evolution reaction four pronounced cathodic current peaks are related to reductive electron transfer reactions of both molecules as well as to chloride desorption. The first cathodic peak is assigned to the first porphyrin reduction step, whereas the second peak corresponds to the first electron transfer related reduction from dicationic DBV^{2+} to radical monocationic $DBV^{\bullet+}$. The further cathodic peaks are (i) a superposition of the chloride desorption and the second reduction related to the porphyrin and (ii) the last reduction step from the radical monocationic $DBV^{\bullet+}$ to uncharged DBV^0 molecules, respectively.

Structural characterization

Three separate phases forming on the Cl/Cu(100) surface and two distinct molecular patterns on the Cl/Cu(111) surface are directly observed within the non-reactive regime where both adsorbed molecules retain the same states as in solution, i.e. $[H_2TTMAPP(0)]^{4+}$ and DBV^{2+}, namely the square phase of the $[H_2TTMAPP(0)]^{4+}$ species and the cavitand/herring-bone phase of the DBV^{2+} on Cu(100) and Cu(11) surface, respectively, and the mixed phase on Cu(100).

By moving the electrode potential negatively the mixed and co-existing phases are replaced by the $DBV^{\bullet+}$ stacking phase on both surfaces, Cu(100) and Cu(111). The potential at which this phase transition occurs in the mixed solution is observed more positively than that in electrolyte containing only DBV. The possible explanation is the formation of a metastable phase including the cavitand/herring-bone and dimer phases after the desorption of reduced porphyrin species ($[H_4TTMAPP(\text{-II})]^{4+}$) from the surfaces.

Finally, the competition of molecules on the chloride modified Cu(111) is also investigated using the tunneling tip to trigger equilibration. An irreversible tip-induced removal of the bimolecular layer is observed when “drastic” tunneling conditions are applied. The co-existing phases are replaced by the herring-bone phase after the tunneling tip is retracted.

9.6. Conclusions

Based on the above summarized experimental results with, for instance, $H_2TTMAPP$, and in comparison to previous observations with H_2TMPyP on the same surfaces some general conclusions can be drawn.

1. The shape of the organic molecules seems to be decisive for the structure of the adsorbate lattice. Independent of the substrate symmetry, i.e. on Cu(100) as well as on Cu(111), H_2TMPyP and $H_2TTMAPP$ molecules, both of quadratic shape, form quadratic or rectangular ad-lattices.

2. The size of the organic molecules, obviously for sterical reasons, dictates the molecular density of the ad-lattices. Thus, the densities for H_2TMPyP and $H_2TTMAPP$ on a chloride precovered Cu(100) surface are 4.49×10^{13} and 2.64×10^{13} molecules/cm^2, respectively, i.e. more of the smaller H_2TMPyP molecules fit on the surface. Likewise, on a sulfate precovered Cu(111) surface the H_2TMPyP- and $H_2TTMAPP$-densities are 2.87×10^{13} and 2.46×10^{13}. In turn, the density of $H_2TTMAPP$ molecules on

Cl/Cu(100) and SO_4^{2-}/Cu(100) is rather similar, namely 2.64 x 10^{13} and 2.46 x 10^{13} molecules/cm^2.

3. The charge density on both the adsorbed molecules and the substrate surface, i.e. the electrostatic interaction between both, is an important control parameter.

   On the one hand the molecular density of the H_2TTMAPP layer increases from 2.64 x 10^{13} to 2.80 x 10^{13} molecules/cm^2 when replacing the $c(2 \times 2)$Cl/Cu(100) substrate by the $c(p \times \sqrt{3})$Cl/Cu(111) one, because the density of chloride anions, which are known to adsorb largely ionic, is higher on Cu(111) than on Cu(100). This is also in line with the observation that on Cl/Cu(111) the H_2TTMAPP molecules are aligned with the chloride rows underneath, but not on Cl/Cu(100). In turn, the organic molecules (in cationic form) adsorb weaker on both bromide or iodide precovered copper surfaces, because these two anions form less ionic bonds with copper. Also the observation that H_2TTMAPP forms a rectangular unit cell on SO_4^{2-}/Cu(111) compared to the square unit cell on both Cl/Cu(100) and Cl/Cu(111) surfaces supports the notion that electrostatic interactions play a decisive role. On both Cl/Cu(100) and Cl/Cu(111) all inter-atomic distances between the Cl anions are relative short and equally long. In turn, the distance between SO_4^{2-} anions within the sulfate rows of the quasi $(\sqrt{3} \times \sqrt{7})SO_4^{2-}$ structure on Cu(111) is shorter ($\sqrt{3}$) than between SO_4^{2-} anions in adjacent rows ($\sqrt{7}$). This may be the reason for the rectangular expansion of the H_2TTMAPP unit cell on this surface compared to those on Cl/Cu(100) and Cl/Cu(111).

   On the other hand, electrochemical reduction of the H_2TTMAPP molecules at negative electrode potentials leads to a weakening of the adsorption strength even though the underlying anion density does not change: After the first reductive electron transfer reaction the H_2TTMAPP cations desorb from the Cl/Cu(100) and the Cl/Cu(111) surfaces.

Further attempts to “design” functional organic layers by electrochemical deposition of the molecular constituents may consider these findings.

References

[1] A. D’Amico, C. Di Natale, A. Macagnano, F. Davide, A. Mantini, E. Tarizzo, R. Paolesse, T. Boschi, Biosens. Bioelectron, 13, 711 (1998).

[2] Y. Harima, T. Kodaka, H. Okazaki, Y. Kunugi, K. Yamashita, H. Ishii, K. Seki, Chem. Phys. Lett. 240, 345 (1995).

[3] T.J. Savenije, E. Moons, G.K. Boschloo, A. Goossens, T.J. Schaafsma, Phys. Rev. B 55, 685 (1997).

[4] M.P. Oneil, M.P. Niemczyk, W.A. Svec, D. Gosztola, G.L. Gaines, M.R. Wasielewski, Science 257, 63 (1992).

[5] G. Guillaud, M. Al Sadoun, M. Maitrot, J. Simon, M. Bouvet, Chem.Phys. Lett. 167, p. 503 (1990).

[6] C.C. Leznoff, A.B.P. Lever, *Phthalocyanines Properties and Applications*, Vol.1.VCH. (1989).

[7] A. Louati, M.E. Meray., J.J. Andre, J.Simon, K.M. Kadish, M.Gross and A. Giraudeau, Inorg.Chem, 24, 1175 (1985).

[8] A. Koca, S.B., H.A.Dincer, E. Gonca, Electrochim. Acta, 54, 2684 (2009).

[9] X. Lu, K.W. Hipps., X.D. Wang, U. Mazur, J. Am. Chem. Soc, 118, 7197 (1996).

[10] K.W. Hipps, X. Lu, X.D. Wang, U. Mazur, J. Phys. Chem, 100, 11207 (1996).

[11] X. Lu, K.W. Hipps, J. Phys. Chem. B, 101, 5391 (1997).

[12] D.E. Barlow, K.W.H., J. Phys. Chem. B, 104, 5993 (2000).

[13] S. Zecevic, B.S.-G., E. Yeager, A.B.P. Lever, and P.C. Minor, J. Electroanal. Chem., 196, 339 (1985).

[14] S. Yoshimoto, E.T., K. Suto, Y. Honda, K. Itaya, J. Chem. Phys., 319, 147 (2005).

[15] http://web.uam.es/gruposinv/ftalo/about.htm (accessed May 2010)

[16] F. Remacle, S. Speiser, R.D. Levine, J. Phys. Chem. B, 105, 5589 (2001).

[17] R.K. Lammi, A.A., T. Balasubramanian, R.W. Wagner, D.F. Bocian, D. Holten, J.S. Lindsey, J. Am. Chem. Soc,. 122(31), 7579-7591 (2000).

[18] E. Yeager, Electrochim. Acta, 29, 1527 (1984).

[19] E.D. Sternberg, D.D., C. Bruckner, Tetrahedron, 54, 4151 (1998).

[20] S.P.S. Tita and J. R. Perussi, Brazilian Journal of Medical and Biological Research, 34(10), 1331-1336 (2001).

[21] J. Zhang, A. B. P. Lever, W. J. Pietro; J. Chem. Soc., Faraday Trans., 93(18), 3355-3362 (1997).

[22] Y. He, T. Ye, and E. Borguet, J. Am. Chem. Soc., 124(40), 11964-11970 (2002).

[23] Z. C. Dong, A. S. Trifonov, X. L. Guo, K. Amemiya, S. Yokoyama, T. Kamikado, T. Yamada, S. Mashiko, and T. Okamoto, Surf. Sci., 532-535, 237-243 (2003).

[24] X. L. Guo, Z. C. Dong, A. S. Trifonov, K. Miki, K. Kimura, and S. Mashiko, Appl. Surf. Sci., 241(1-2), 28-32 (2005).

[25] X. L. Guo, Z. C. Dong, A. S. Trifonov, K. Miki, K. Kimura, and S. Mashiko, Appl. Phys. A, 81(2), 367-370, (2005).

[26] F. Buchner, V. Schwald, K. Comanici, H. P. Steinrueck, and H. Marbach, ChemPhysChem, 8(2), 241-243 (2007).

[27] M. Kunitake, N. Batina, and K. Itaya, Langmuir, 11(7), 2337-2340 (1995).

[28] K. Ogaki, N. Batina, M. Kunitake, and K. Itaya, J. Phys. Chem., 100(17), 7185-7190 (1996).

[29] M. Kunitake, U. Akiba, N. Batina, and K. Itaya, Langmuir, 13(6), 1607-1615 (1997).

[30] N.T.M. Hai, K. Wandelt, and P. Broekmann, J. Phys. Chem. C, 112, 10176 (2008).

[31] T.M.H. Nguyen, *Preparation and characterization of copper iodide thin films and organic supramolecular layers at copper/electrolyte interfaces*, PhD dissertation, Bonn, 2007

[32] C. L. Bird and A. T. Kuhn, Electrochemistry of the Viologens, Chem. Soc. Rev.,10, 49-82 (1981).

[33] P. M. S. Monk, *The Viologens: physicochemical properties, synthesis and applications of the salts of 4,4'-bipyridines*,John Wiley and Sons, Ltd., Chichester, UK, 1st edn, (1998).

[34] J. Inukai, Y. Osawa, and K. Itaya; J. Phys. Chem. B, 102(49), 10034 (1998).

[35] H. Imahori, H. Norieda, H. Yamada, Y. Nishimura, I. Yamazaki, Y. Sakata, and S. Fukuzumi; J. Am. Chem. Soc., 123(1), 100-110 (2001).

[36] H. Hosono and M. Kaneko; J. Photochem. Photobio. A: Chemistry, 107, 63-70 (1997).

[37] A.R. Liu, X. Wang, Ch. Nakamura, J. Miyake, N. A. Zorin and D. J. Qian; J. Phys. Chem. C, 112, 1582 -1588 (2008).

[38] Yoshimoto, S.; Higa, N.; Itaya, K., J. Am. Chem. Soc., 126, 8540 (2004).

[39] J. Wang, *Analytical Electrochemistry*, Wiley-VCH, (Copyright @ 2000). ISBNs: 0-471-28272-3 (Hardback) Manual.

[40] H. L. F. Von Helmholtz, Ann. Physik, 7(3), 337-382 (1879)

[41] R. Guidelli and W. Schmickler, Electrochim. Acta, 45, 2317-2338 (2000).

[42] A. Mehlich, *The solid-liquid interface*, Moscow-Bavarian Joint Advanced Student School (MB JASS), 2006. http://www.wsi.tu-muenchen.de/E25/members/Garrido/MB-JASS/AbstractMehlich.pdf (accessed Sept. 2006).

[43] D.C. Grahame, *The electrical double layer and the theory of electrocapillarity*, Chem. Rev. 41, 441-501 (1947).

44] O. M. Magnussen, *Ordered anion adlayers on metal electrode surfaces* Chem. Rev., 102, 679-725 (2002).

[45] K. Kolasinski, Surface science: *Foundations of catalysis and nanoscience,* John Wiley & Sons, Ltd, (2001).

[46] http://www.virginia.edu/ep/SurfaceScience/electron.html (accessed Aug 2010).

[47] J. E. B. Randles, Trans. Faraday Soc., 44(5), 327-338 (1948).

[48] G. Binnig and H. Rohrer, Surf. Sci., 126(1-3), 236-244 (1983).

[49] G. Binnig, H. Rohrer, C. Gerber, and E. Weibel, Appl. Phys. Lett., 40(2), 178-180 (1982).

[50] G. Binnig and H. Rohrer, Scientific American, 253(2), 50-56 (1985).

[51] R. Sonnenfeld and P. K. Hansma, Science, 232, 211-213 (1986).

[52] P. Broekmann, N. Hai, and K. Wandelt, Surf. Sci., 600(18), 3971-3977 (2006).

[53] P. Broekmann, N. T. M. Hai, and K. Wandelt, J. Appl. Electrochem., 36(11), 1241-1252 (2006).

[54] N.T.M. Hai, S. Huemann, R. Hunger, W. Jaegermann, K. Wandelt, and P. Broekmann, J. Phys. Chem. C, 111(40), 14768-14781 (2007).

[55] E. Meyer, H. J. Hug, and R. Bennewitz, *Scanning Probe Microscopy – The lab on a tip, Introduction to Scanning Tunneling Microscopy*. Springer-Verlag Berlin Heidelberg, (2004).

[56] M. Tsukada, K. Kobayashi, N. Isshiki, and H. Kageshima, Surf. Sci. Rep., 13(8), 265–304 (1991).

[57] J. Tersoff and D. R. Hamann, Phys. Rev. Lett., 50(25), 1998-2001 (1983).

[58] J. Tersff and D. R. Hamann, Phys. Rev. B, 31(2), 805-813 (1985).

[59] M. Wilms, *Potentiodynamische Rastertunnelmikroskopie and Fest/Fluessig Grenzplaechen: Apparative Entwicklung and Untersuchung zur Sulfat Adsorption auf Cu(111)*, PhD thesis, University of Bonn, (1999).

[60] K. Oura, V. Lifshits, A. Saranin, A. Zotov, and M. Katayama*, Surface Science An introduction,* Springer-Verlag Berlin Heidelberg, (2003).

[61] M. Wilms, M. Kruft, G. Bermes, and K. Wandelt, Rev. Sci. Instrum., 70(9), 3641-3650 (1999).

[62] K. Besocke, Surf. Sci., 181(1-2), 145-153 (1987).

[63] K. Wandelt and S. Thurgate, *Solid-Liquid Interfaces, Topic Appl. Phys. 85*, Springer-Verlag Berlin Heidelberg, (Copyright @ 2001).

[64] P. Broekmann, *Atomare Struktur und Dynamik von Kupfer/Elektrolyt Grenzflaechen,* PhD thesis, University of Bonn, (2002).

[65] D. Friebel, *In situ STM-Untersuchungen ultraduenner Kupferchalkogenidfilme auf Au(111)-Elektrodenoberflaechen,* PhD thesis, University of Bonn, (2007).

[66] K. Itaya, Prog. Surf. Sci., 58(3), 121-247 (1998).

[67] A. T. Hubbard, Chem. Rev., 88(4), 633-656 (1988).

[68] M. P. Soriaga, Prog. Surf. Sci., 39(4), 325-443 (1992).

[69] J. Clavilier, R. Faure, G. Guinet, and R. Durand, J. Electroanal. Chem., 107(1), 205-209 (1980).

[70] A. Hamelin, *In Modern Aspects of Electrochemistry. No. 16*, New York: Plenum Press, (1985).

[71] S. Motoo and N. Furuya, J. Electroanal. Chem., 167(1-2), 309-315 (1984).

[72] K. Sashikata, N. Furuya, and K. Itaya, J. Vac. Sci. Technol., B, 9(2), 457-464 (1991).

[73] J. H. Schott and H. S. White, J. Phys. Chem., 98(1), 291-296 (1994).

[74] G. M. Brisard, E. Zenati, H. A. Gasteiger, N. M. Markovic, and P. N. Ross, Langmuir, 11(6), 2221-2230 (1995).

[75] D. Briggs and M.P. Seah, *Practical Surface Analysis by Auger and X-ray Photoelectron Spectroscopy*, New York John Wiley and Sons (1985).

[76] http://www.chem.queensu.ca/people/faculty/horton/research.html (accessed Nov. 2011).

[77] C. J. Powell, A. Jablonski, A. Naumkin, A. K-Vass, J.M Conny and J.R. Rumble, J. Electron Spectrosc. Relat. Phenom., 114, 1097-1102, (2001).

[78] T. Mayer, M. Lebedev, R. Hunger and W. Jaegermann, Appl. Surf. Sci. 252, 31-42 (2005).

[79] “Copper.” http://en.wikipedia.org/wiki/Copper (accessed May 2011)

[80] P. C. Andricacos, C. Uzoh, J. . Dukovic, J. Horkans, and H. Deligianni, Ibm J. Kes. Develop., 12, 567–574 (Sept. 1998). http://www.research.ibm com/journal/rd/425/andricacos.pdf (accessed 10 May 2007).

[81] P. M. Vereecken, R. A. Binstead, H. Deligianni, and P. C. Andricacos, Ibm J. Res. and Dev., 49, 3-18 (2005). http://www.research.ibm.com/ journal/rd/491/vereecken.pdf (accessed 10 May 2007).

[82] D. Pletcher, R. Greef, R. Peat, L. Peter, and J. Robinson, *Instrumental methods in electrochemistry,* Southampton Electrochemistry Group, University of Southampton, Copyright @ Horwood Publishing Limited, (2001). ISBN: 1-898563-80-2.

[83] P. Broekmann, M. Anastasescu, A. Spaenig, W. Lisowski, and K. Wandelt, J. Electroanal. Chem., 500(1-2), 241-254 (2001).

[84] M. Kruft, B. Wohlmann, C. Stuhlmann, and K. Wandelt, Surf. Sci., 377-379, 601-604 (1997).

[85] M. Wilms, P. Broekmann, M. Kruft, C. Stuhlmann, and K. Wandelt, Appl. Phys. A, 66, S473-S475 (1998).

[86] M. Wilms, P. Broekmann, C. Stuhlmann, and K. Wandelt, Surf. Sci., 416(1-2), 121-140 (1998).

[87] M. Wilms, P. Broekmann, M. Kruft, Z. Park, C. Stuhlmann, and K. Wandelt, Surf. Sci., 402-404, 83-86 (1998).

[88] C. Safarowsky, A. Spaenig, P. Broekmann, and K.Wandelt, Surf. Sci., 538(3), 137-146 (2003).

[89] L. J. Wan and K. Itaya, J. Electroanal. Chem., 473(1-2), 10-18 (1999).

[90] P. Muller, S. Ando, T. Yamada, and K. Itaya, J. Electroanal. Chem., 467(1-2), 282-290 (1999).

[91] L. J. Wan, T. Suzuki, K. Sashikata, J. Okada, J. Inukai, and K. Itaya, J. Electroanal. Chem., 484(2), 189-193 (2000).

[92] T. Yamada, N. Batina, and K. Itaya, Surf. Sci., 335(1-3), 204-209 (1995).

[93] M. Sugimasa, J. Inukai, and K. Itaya, J. Electroanal. Chem., 554, 285-291 (2003).

[94] M. T. M. Koper, J. Electroanal. Chem., 450(2), 189-201 (1998).

[95] A. Cuesta and D. M. Kolb, Surf. Sci., 465(3), 310-316 (2000).

[96] J. L. Stickney and C. B. Ehlers, J. Vac. Sci. Technol., A, 7(3), 1801-1805 (1989).

[97] W. Polewska, R. J. Behm, and O. M. Magnussen, Electrochim. Acta, 48(20-22), 2915-2921 (2003).

[98] M. R. Vogt, A. Lachenwitzer, O. M. Magnussen, and R. J. Behm, Surf. Sci., 399(1), 49-69 (1998).

[99] P. Broekmann, A. Spaenig, A. Hommes, and K. Wandelt, Surf. Sci., 517(1-3), 123-137 (2002).

[100] A. Hommes, A. Spaenig, P. Broekmann, and K. Wandelt, Surf. Sci., 547(1-2), 239-247 (2003).

[101] B. Obliers, P. Broekmann, and K. Wandelt, J. Electroanal. Chem., 554-555, 183-189 (2003).

[102] A. Spaenig, *Potentialinduzierte Phasenuebergange in anodischen Adsorbatschichten auf niedriginduzierten Kupfereinkristallelektroden,* PhD thesis, University of Bonn, (2004).

[103] M. R. Vogt, F. A. Moller, C. M. Schilz, O. M. Magnussen, and R. J. Behm, Surf. Sci., 367(2), L33-L41 (1996).

[104] S. Huemann, N. T. M. Hai, P. Broekmann, K. Wandelt, H. Zajonz, H. Dosch, and F. Renner, J. Phys. Chem. B, 110(49), 24955-24963 (2006).

[105] P. Broekmann, M. Wilms, and K. Wandelt, Surf. Rev. Lett., 6(5), 907-916 (1999).

[106] P. Broekmann, M. Wilms, A. Spaenig, and K. Wandelt, Prog. Surf. Sci., 67(1-8), 59-77 (2001).

[107] F. Voegtle, *Supramolecular Chemistry: An Introduction*, John Wiley and Sons Ltd, Chichester, UK, 1st edn, (1991).

[108] J. M. Lehn, *Supramolecular Chemistry*, VCH, Weinheim, Germany, 1st edn, (1995).

[109] G.V. Oshovsky, D.N. Reinhoudt, W. Verboom, *Supramolecular Chemistry in Water,* Angewandte Chemie International Edition 46 (14), 2366-2393 (2007).

[110] V. Balzani, M. Venturi and A. Credi, *Molecular Devices and Machines*, Wiley VCH, 1st edn, (2003).

[111] J. M. Lehn, *Supramolecular chemistry-Scope and perspectives. Molecules, supermolecules and molecular devices*, (Nobel Lecture, 8.12.1987), Angew. Chem., Int. Ed. Engl., 27, 89-112 (1988).

[112] K. Ariga and T. Kunitake, *Supramolecular Chemistry- Fundamentals and Application,* Springer-Verlag Berlin Heidelberg, (2006).

[113] G. R. Desiraju, *The Crystal as a Supramolecular Entity - Perpectives in Supramolecular Chemistry*, vol. 2. Baffins Lane, Chichester, West Sussex PO19 1UD, England: John Wiley & Sons Ltd, (Copyright, 1996). ISBN: 0 471950157.

[114] A. E. Kaifer and M. Gomez-Kaifer, *Supramolecular Electrochemistry,* D-69469 Weinheim: WILEY-VCH Verlag GmbH, (Copyright, 2003). 1999, ISBN: 3-527-29597-6.

[115] P. S. Weiss, Nature, 413(6856), 585-586 (2001).

[116] Q. H. Yuan, L. J. Wan, H. Jude, and P. J. Stang, J. Am. Chem. Soc., 127(46),16279-16286 (2005).

[117] R. G. Chapman and J. C. Sherman, Tetrahedron, 53(47), 15911-15945 (1997).

[118] G. M. Whitesides, J. P. Mathias, and C. T. Seto, Science, 254(5036), 1312-1319 (1991).

[119] J. V. Barth, G. Costantini, and K. Kern, Nature, 437(7059), 671-679 (2005).

[120] G. S. Kottas, L. I. Clarke, D. Horinek, and J. Michl, Chem. Rev., 105(4), 1281-1376 (2005).

[121] D. M. Vriezema, M. C. Aragones, J. A. A.W. Elemans, J. J. L. M. Cornelissen, A. E. Rowan, and R. J. M. Nolte, Chem. Rev., 105(4), 1445-1489 (2005).

[122] S. De Feyter and F. C. De Schryver, Chem. Soc. Rev., 32(3), 139-150 (2003).

[123] N.B. McKeown, *Phthalocyanine Materials - Synthesis, Structure and Function*, Cambridge University Press (1998).

[124] C.M. Allen, W.M. Sharman, J.E. van Lier, J. Porphyrins and Phthalocyanines, 5(1) (2001).

[125] R. Bonnett, In: *Chemical Aspects of Photodynamic Therapy*, Gordon and Breach Science, Canada, (2000).

[126] K. Nilson, J. Ahlund, B. Brena, E. Göthelid, J. Schiessling, N. Martensson, C. Puglia, J. Chem. Phys., 127, 114702,(2007).

[127] Y. Naito, T. Matsumoto, K. Sugiura, Y. Sakata, and T. Kawai, Surf. Sci., 487, 534 (2001).

[128] A. Giraudeau, M. El Meray, M. Gross, C. Piechocki, M. Bernard, Analytica Chimica Acta, 251, 39 (1991).

[129] *"Structure of porphyrins"* http://www.porphyrin.net/Heme/iron/porphyrins/porphystruct.html (accessed Nov. 2010).

[130] *"Porphyrin."* http://www.answers.com/topic/porphyrin (accessed Nov. 2010).

[131] J. P. Lei, H. X. Ju, and O. Ikeda, Electrochim. Acta, 49(15), 2453-2460 (2004).

[132] S. M. Chen and S. V. Chen, Electrochim. Acta, 48(27), 4049-4060 (2003).

[133] K. Kobayashi, F. Fujisaki, T. Yoshimina and K. Nik, Bull. Chem. Soc. Jpn., 59(12), 3715-3722 (1986).

[134] K. Arihara, T. Ohsaka and F. Kitamura, Phys. Chem. Chem. Phys., 4(6), 1002-1005 (2002).

[135] T. Lu and T. M. Cotton, J. Phys. Chem., 91(23), 5978-5985 (1987).

[136] B. Kirchner and S. Kossmann, private communication.

[137] T. Sagara and K. Miuchi, J. Electroanal. Chem., 567(2), 193-202 (2004).

[138] D.T. Pham, S.L. Tsay, K. Gentz, C. Zoerlein, S. Kossmann, J.S. Tsay, B. Kirchner, K. Wandelt, and P. Broekmann, J. Phys. Chem. C, 111, 16428-16436 (2007).

[139] D.T. Pham, K. Gentz, C. Zoerlein, N.T.M. Hai, S.L. Tsay, B. Kirchner, S. Kossmann, K. Wandelt, and P. Broekmann, New J. Chem., 30, 1439-1451 (2006).

[140] C. Safarowsky, K. Wandelt, and P. Broekmann, Langmuir, 20, 8261-8269, (2004).

[141] W.S. Caugrey, and .A.H. Corwin, J. Am. Chem. Soc., 77, 1509-1513 (1955).

[142] B. Shah and P. Hambright, J. Inorg. Nucl. Chem., 32, 3420-3422 (1970.

[143] J.F. Moulder, W.F. Stickle, P.E. Sobol and K.D. Bomben, *Handbook of X-ray Photoelectron Spectroscopy*, Perkin Elmer Corp., Eden Prairie, MN (1992).

[144] J.J. Yeh and I. Lindau, *Atomic Data and Nuclear Data Tables*, 32, 1-155, (1985).

[145] S. Huemann, *Elektrochemische preaparation ultraduenner Cadmiumsulfid- und Cadmiumjodid-Filme auf niedrigindizierten Kupfereinkristallelektroden,* PhD-Thesis. University of Bonn, (2007): http://hss.ulb.uni-bonn.de/2008/1303/1303.htm.

[146] T. Sasaki, R.S. Williams, J.S. Wong, D.A. Shirley, J. Chem. Phys. 68, 2718-2724 (1978).

[147] S. Breuer, D.T. Pham., S. Huemann, K. Gentz, C. Zoerlein, R. Hunger, P. Broekmann, K. Wandelt, N. J. Phys., 10, 125033 (2008).

[148] K. Nilson, P. Palmgren, J. Ahlund, J. Schiessling, E. Göthelid, N. Martensson, C. Puglia, M. Göthelid, Surf. Sci., 602, 452-459 (2007).

[149] Y. Alfredsson, B. Brena., K. Nilson, J. Ahlund, L. Kjeldgaard, M. Nyberg, Y. Luo, N. Martensson, S. Sandell, C. Puglia, H. Siegbahn, J. Chem. Phys., 122, 214723 (2005).

[150] A. Kalkan, A. Koca, Z.A. Bayir, Polyhedron, 23, 3155 (2004).

[151] M. Kandaz, M.N.U. Yarasir, A.Koca, O. Bekaroglu, Polyhedron, 21, 225 (2002).

[152] A. Koca, A.R. Ozkaya, M. Selcukoglu, E. Hamuryudan, Elect. Acta, 52, 2683 (2007).

[153] A. Giraudeau, A. Louati, M. Gross, J.J. Andre, J. Simon, C.H. Su, and K.M. Kadish, J. Am. Chem.Soc., 105, 2917 (1983).

[154] R.E. Linder, J.R. Rowlands, and N.S. Hush, Mol. Phys., 21, 417 (1971).

[155] A.M. Schaffer, M. Goutermann, E.R. Davidson, Theor. Chim. Acta, 30, 9-30 (1973).

[156] A.B.P. Lever, S.R. Pickens, P.C. Minor, S. Licoccia, B.S. Ramaswany, K. Magnell, J. Am. Chem. Soc., 103, 6800 (1981).

[157] A.B.P. Lever, P.C. M., Adv.Mol.Rel. and Inter. Processes, 18, 115 (1980).

[158] A.B.P. Lever and E.S.Dodsworth, Chem. Phys. Lett., 112(6), 567 (1984).

[159] J. Zagal, R.K. Sen, E. Yeager, J. Electroanal. Chem., 83, 207 (1977).

[160] A.P. Brown, C. Koval, and F.C. Anson, J. Electroanal. Chem., 72, 379 (1976).

[161] D.W. Clack, N.S. Hush, and J.R. Yandle, Chem. Phys. Lett., 1, 157 (1967).

[162] B.J. Raynor, M. Robson., S.A.M. Torren-Burton, J. Chem. Soc. Dalton Trans., 2360 (1977).

[163] K. Shinoda, W. Shinnoda, C.C. Liew, S. Tsuzuki, Y. Morikawa, M. Mikami, Surf. Sci., 556, 109 (2004).

[164] K. Miyake, Y. Hori., T. Ikeda, M. Asakawa, T. Shimizu, and S. Sasaki, Langmuir, 24, 4708 (2008).

[165] J. M. Gottfried, K. Flechtner, A. Kretschmann, T. Lukasczyk, and H. P. Steinrueck, J. Am. Chem. Soc., 28(17), 5644–5645 (2006).

[166] W. Deng, D. Fujita, T. Ohgi, S. Yokoyama, K. Kamikado, and S. Mashiko, J. Chem. Phys., 117(10), 4995–5000 (2002).

[167] K. Sashikata, T.Sutaga, M. Sugimasa, K. Itaya, Langmuir 14, 2896 (1998).

[168] L.J. Wan, S.Shundo, J. Inukai, K. Itaya, Langmuir, 16, 2164 (2000).

[169] N.T.M. Hai, B. Gašparović, K. Wandelt, P. Broekmann, Surf. Sci. 601, 2597 (2007).

[170] M. Giesen, G. Beltramo, S. Dieluweit, J. Müller, H. Ibach, W. Schmickler, Surf. Sci. 595, 127 (2005).

[171] T.H. Phan and K. Wandelt, Surf. Sci., accepted.

[172] P. Hambright, E. Fleischer, Inorg. Chem. 9, 1757 (1970).

[173] D. L. Langhus, G.S. Wilson, Anal. Chem. 51, 1139 (1979).

[174] B.P, Neri, G.S. Wilson, Anal. Chem. 44, 1002 (1972).

[175] B.P, Neri, G.S. Wilson, Anal. Chem. 45, 442 (1973).

[176] T.H. Phan and K. Wandelt, in preparation

[177] M. C. Richoux, P. Neta, A. Harriman, S. Baral, and P. Hambright, J. Phys. Chem., 90(11), 2462-2468 (1986).

[178] F. G. Bordwell, M. Van Der Puy, N.R. Vanier, J. Org. Chem., 41, 1883 (1976).

[179] J.D. Roberts, R.A. Clement, J.J. Drysdale, J. Am. Chem. Soc., 73, 2181-2183 (1951).

[180] N. Batina, M. Kunitake, and K. Itaya, J. Electroanal. Chem., 405(1-2), 245-250 (1996).

[181] K. Itaya, N. Batina, M. Kunitake, K. Ogaki, Y. G. Kim, L. J. Wan, and T. Yamada, Solid-Liquid Electrochemical Interfaces, 656, 171-188 (1997).

[182] Z. C. Dong, A. Kar, P. Dorozhkin, K. Amemiya, T. Uchihashi, S. Yokoyama, T. Kamikado, S. Mashiko, and T. Okamoto, Thin Solid Films, 438-439, 262-267 (2003).

[183] Z. C. Dong, A. Kar, Z. Q. Zou, T. Ohgi, P. Dorozhkin, D. Fujita, S. Yokoyama, T. Terui, T. Yamada, T. Kamikado, M. N. Zhou, S. Mashiko, and T. Okamoto, Jpn. J. Appl. Phys., Part 1, 41(7B), 4898-4902 (2002).

[184] D. Fujita, T. Ohgi, W. L. Deng, K. Ishige, T. Okamoto, S. Yokoyama, T. Kamikado, and S. Mashiko, Surf. Sci., 493(1-3), 702-707 (2001).

[185] X.-L. Guo, Z.-C. Dong, A. Trifonov, K. Miki, K. Kimura, and S. Mashiko, Appl. Surf. Sci., 241(1-2), 28-32 (2005).

[186] P. Broekmann, M. Wilms, M. Kruft, C. Stuhlmann, K. Wandelt, J. Electroanalyt. Chem., 467, 307-324 (1999).

[187] N.T. M. Hai, S.Furukawa, T. Vosch, S. D. Feyter, P. Broekmann, K. Wandelt, J. Phys. Chem. Chem. Phys.,11, 5422 (2009).

[188] R.G. Jones, M. Kadodwala, Surf. Sci., 370, L219-L225 (1997).

[189] R. D. Jones, D. A. Summerville, and F. Basolo, Chem Res., 79, 139 (1979); Acc. Chem. Res., 10, 265 (1977).

[190] S. Rywkin, C. M. Hosten, J. R. Lombardi, and R. L. Birke, Langmuir, 18(15), 5869-5880 (2002).

[191] A. Bettelheim and T. Kuwana, Anal. Chem., 51(3), 2257-2260 (1979).

[192] D. Solomon, P. Peretz, and M. Faraggi, J. Phys. Chem., 86(10), 1842-1849 (1982).

[193] Y. W. Chi, J. Y. Chen, and K. Aoki, Inorg. Chem., 43(26), 8437-8446 (2004).

[194] G. S. Wilson and B. P. Neri, Ann. N.Y. Acad. Sci., 206, 568 (1973).

[195] R. F. Pasternack, H. Lee, P. Malek, and C. Spencer, J. Inorg. Nucl. Chem., 39, 1865 (1977).

[196] F. L. Harris and D. L. Toppen, Inorg. Chem., 17, 71 (1978).

[197] H. Goff and L. Morgan, Inorg. Chem., 15, 12 (1976).

[198] P. Forshey and T. Kuwana, Inorg. Chem., 20(3), 693 (1981).

[199] R.F. Pasternack and E.G. Spiro, J. Am. Chem. Soc., 100, 968 (1978).

[200] J. Chen, O. Ikeda, T. Hatasa, A. Kitajima, M. Miyake, A. Yamatodani, Electrochem. Comm., 1, 274-277 (1999).

[201] M.S. Rana, K. Tamagake, J. Electroanalyt. Chem., 581, 145-152 (2005).

[202] S.E. Creager, S.A. Rayback, R.W. Murray, J. Am. Chem. Soc.,108, 4225 (1986).

[203] I.R. Paeng, H. Shiwaka, K. Nakamoto, J. Am. Chem. Soc., 110, 1995 (1988).

[204] E. Van Caemelbecke, A. Derbin, P. Hambright, R. Garcia, A. Doukkali, A. Saoiabi, K. Ohkubo, S. Fukuzumi, and K. M. Kadish, Inorg. Chem., 44(11), 3789-3798 (2005).

[205] K. Manandhar, K.T. Park,S. Ma, J. Hrbek, Surf. Sci., 603, 636-640 (2009).

[206] J. Ahlund, J. Schnadt, K. Nilson, E. Gothelid, J. Schiessling, F. Besenbacher, N. Martensson, C. Puglia, Surf. Sci., 601, 3661-3667 (2007).

[207] M.S. Liao, S. Scheiner, J. Comput. Chem., 23, 1391 (2002).

[208] M.S. Liao, S. Scheiner, J. Chem. Phys., 114, 9780 (2001).

[209] S. Yoshimoto, A. Tada, K. Suto, and K. Itaya, J. Phys. Chem. B, 107, 5836-5843 (2003).

[210] P.H. Lippel, R.J. Wilson, M.D. Miler, Ch. Woll, and S. Chiang, Phys. Rev. Lett. 62, 171-174 (1989).

[211] A. Rosa, E. Baerends, J. Inorg. Chem., 33, 584-595 (1994).

[212] Y.X. Diao, Y.X.; M.J. Han, L.J. Wan, K. Itaya, T. Uchida, H. Miyake,A. Yamakata,M. Osawa, Langmuir, 22, 3640 (2006).

[213] T. Dretschkow, T. Wandlowski, Electrochim. Acta, 45, 731 (1999).

[214] M. Jiang, E. Sak, K. Gentz, A. Krupski, K. Wandelt, Chem. Phys. Chem., 17, 1542 (2010).

[215] S.L. Tsay, J.S. Tsay, T.Y. Fu, P. Broekmann, T. Sagara, K. Wandelt, Phys. Chem. Chem. Phys., 12, 14950 (2010).

[216] M. Roefzaad, M. Jiang, V. Zamlinny, K. Wandelt, Electroanalyt. Chem., 662, 219 (2011).

[217] K. Kobayashi, F. Fujisaki, T. Yoshimina, and K.B. Nik, Chem. Soc. Jpn., 59, 3715 (1986).

[218] K. Arihara, T. Ohsaka, F. Kitamura, Phys. Chem. Chem. Phys., 4, 1002 (2002).

[219] T.H. Phan, and K. Wandelt, Unpublished

[220] M. Weck, A.R. Dunn, K. Matsumoto, G.W Coates, E.B. Lobkoysky, R.H. Grubbs, Angew. Chem., Int. Ed., 38, 2741 (1999).

[221] D.T. Pham, *Self-assembly of viologen molecules at metal/electrolyte interfaces under non-reactive and reactive conditions*, PhD thesis, Bonn, (2011).

[222] P. Broekmann , A. Fluegel, C. Emnet, M. Arnold, C. Roeger-Goepfert, A. Wagner, N.T.M. Hai, D. Mayer, Electrochim. Acta, 56, 4724 (2011).

[223] T.H. Phan, and K. Wandelt, In preparation

[225] K. Suto, S. Yoshimoto, and K. Itaya; Langmuir, 22, 10766 -10776 (2006).

[225] C. L. Bird and A. T. Kuhn, Chem. Soc. Rev., 10, 49 (1981).

Acknowledgement

Foremost, I would like to express my particular gratitude to my supervisor Prof. Dr. Dr. h.c. Klaus Wandelt for giving me an opportunity to carry out PhD thesis, for all his financial support, available advices and countless discussions during the recent four years. His counsel is always insightful and presents an effective way to approach a problem that I had not previously considered. Professor Klaus Wandelt himself is the first person who introduced me to the fascinating and rewarding surface electrochemistry. I am deeply grateful for his enormous kindness, patience and for being for me such a wise mentor.

I would like to express my special thanks to Frau Kirschfink for helping me with all administrative formalities during my stay in the Institute of Physical and Theoretical Chemistry, University of Bonn.

I am grateful to Herr Hamed Alaei and Herr Boehmer for helping me to solve some problems with the EC-STM apparatus.

I would be truly ungrateful if I did not acknowledge my fellow Wandelt's group members, both present and past, for all. I would like to thank Stephan Breuer for his help in introducing me to the basics of X-ray photo electron spectroscopy and carrying out XPS measurements at BESSYII, Berlin. My special thanks go to my Vietnamese colleague Dr. Pham Duc Thanh who was instrumental in teaching me how to use the electrochemical scanning tunneling microscopy and for his helpful and fruitful advices in daily life.

I would like to thank the organizers and sponsors of the Vietnamese-German Seminar on Physics and Engineering to give me the opportunity to have a memorable contact with Prof. Dr. Klaus Wandelt.

My sincere thanks go to the Department of Physics and Quinhon University for giving me the opportunity to carry out my PhD studies in Germany.

I would like to thank Prof. Dr. Vo Thach Son who recommended me as a PhD candidate to Prof. Dr. Wandelt.

I wish to express my special gratitude to my parents and my elder brothers and sisters for their unconditionally emotional supports.

Finally, I owe the deepest appreciation and thanks to my beloved wife and son for simply being for me AN KIET and MIEN TRUNG!

Publication list

Papers

1. Thanh Hai Phan and Klaus Wandelt, *“Self-assembly of metal free porphyrin layers at copper-electrolyte interfaces: Dependence on substrate symmetry”*, Surface Science, in press (http://dx.org/10.1016/j.susc.2012.08.013).
2. Phan Thanh Hai, Doan Minh Thuy and Wandelt, Klaus, *“Structures of adsorbed halide anions on a copper electrode studied by in-situ scanning tunneling microscopy”*, Proc. Natl. Conf. Theor. Phys. 36 (2011), pp. 239-247.
3. Tuyet Nga Nguyen, Phi Hung Pham, Xuan Sang Nguyen, Thach Son Vo and Thanh Hai Phan, *Fabrication and properties of ZrO_2 thin film deposited by Dip-coating technique.* Proceedings of the 11th Vietnamese – German Seminar on Physics and Engineering, 2008, pp.219-222.
4. Thanh Hai Phan, Phi Hung Pham, Hoang Thoan Nguyen, Tuyet Nga Nguyen, Xuan Sang Nguyen and Thach Son Vo, *Nano-crystalline ZrO_2 thin film fabricated by spray pyrolysis,* Proceedings of the 5th National Solid-state Conference, 2007, pp. 777-781.

In preparation

5. Thanh Hai Phan and Klaus Wandelt, *“Porphyrin adsorption on a Cu(111) electrode surface: Potential dependent in-situ STM study”*.
6. Thanh Hai Phan and Klaus Wandelt, *“In situ Scanning Tunneling Microscopy of Potential dependent bimolecular component self-assembly consisting of Viologen and Porphyrin at an Electrolyte/Electrode Interface”*.
7. Thanh Hai Phan and Klaus Wandelt, *“Adsorption features and structural transition of dibenzyl viologen adlayer at electrolyte/Cu(111) interface under non-reactive and reactive conditions”.*

8. T.H. Phan, S. Breuer, D.T. Pham; U. Hahn; T. Torres, and K. Wandelt; *"Ordering of phthalocyanine molecules at metal-electrolyte interfaces studied by in-situ STM and XPS"*.

9. Thanh Hai Phan and Klaus Wandelt*, "Electrochemical and structural characterization of Iron Porphyrin at electrolyte/copper interface".*

10. Thanh Hai Phan and Klaus Wandelt, "*Molecular self-assembly at metal-electrolyte interfaces".*

Oral presentations

1. *"Porphyrin adsorption on a Cu(111) electrode surface: Potential dependent in-situ STM studies", Thanh Hai Phan and Klaus Wandelt,* the 220th Electrochemical Society, Boston, US, Oct. 09-14th, 2011.
2. *"Self-assembly of metal free porphyrin layers at copper-electrolyte interfaces: Dependence on substrate symmetry",* Thanh Hai Phan and Klaus Wandelt, The 28th European Conference on Surface Science, Wroclaw, Poland, 28th Aug.- 2th Sep., 2011.
3. *"Adsorption of phthalocyanine molecules on an iodide modified Cu(100) electrode studied by means of in-situ STM and ex-situ XPS"* Thanh Hai Phan; Stephan Breuer; Duc Thanh Pham; Uwe Hahn; Thomas Torres and Klaus Wandelt; DPG Spring Meeting, Dresden – Germany, 13 – 18th March 2011.

Poster presentations

1. *"Ordering of phthalocyanine molecules at metal-electrolyte interfaces".* Thanh Hai Phan, Stephan Breuer, Uwe Hahn, Thomas Torres and Klaus Wandelt, 11th International Conference on Atomically Controlled Surfaces, Interfaces and Nanostructures, St. Petersburg, Russia, Oct. 3-7th, 2011 (presented by Wandelt).

2. *"Adsorption structure of halide anions on a copper electrode studied by in-situ scanning tunneling microscopy"*, Thanh Hai Phan, Minh Thuy Doan and Klaus Wandelt, The 36th National Conference on

Theoretical Physics, Quinhon, Vietnam, Aug. 01th – 04th, 2011 (presented by Doan)

3. *"Adsorption of partially water soluble phthalocyanine on an iodide modified Cu(100) electrode: An in-situ STM study",* Thanh Hai Phan, Stephan Breuer, Uwe Hahn, Thomas Torres and Klaus Wandelt, The 27th European Conference on Surface Science, Groningen, Netherlands, Aug. 29th – Sep. 03th, 2010.

4. *"Atomic structure of adsorbed Zn(II) Phthalocyanine at electrolyte/Cu(100) interface studied by in-situ STM",* Thanh Hai Phan, Stephan Breuer, Uwe Hahn, Thomas Torres and Klaus Wandelt, Summer School: Nanoelectrochemistry, Villars-sur Ollon, Switzerland, Sep. 05th – 09th, 2010.

5. *"Atomic structure of adsorbed Zn(II) Phthalocyanine on a iodide modified Cu(100) electrode"*, Thanh Hai Phan, Uwe Hahn, Thomas Torres and Klaus Wandelt, DPG Spring Meeting, Regensburg, Germany, March 21th-26th, 2010.

6. "*Ordered Zn(II) Phthalocyanine layer at Cu(100)/electrolyte interface: An in-situ STM study"*, Thanh Hai Phan, Uwe Hahn, Thomas Torres and Klaus Wandelt, the 4th International Workshop on Surface Physics, Ladek-Zdrój, Poland, September 20-25, 2009

7. "*Fabrication and properties of ZrO_2 thin film deposited by Dip-coating technique"* Tuyet Nga Nguyen, Phi Hung Pham, Xuan Sang Nguyen, Thach Son Vo and Thanh Hai Phan, The 11th Vietnamese – German Seminar on Physics and Engineering, Nhatrang, Vietnam, March 31th – April 04th, 2008.

8. *"Influence of the process parameters on properties of thin nano-zirconia film by spray pyrolysis deposition",* Tuyet Nga Nguyen, Thanh Hai Phan, Phi Hung Pham, Xuan Sang Nguyen and Thach Son Vo, The First International Workshop on Nanotechnology and Application, Vungtau, Vietnam, Nov. 15-17th, 2007

9. *"Nano-crystalline ZrO_2 thin film fabricated by spray pyrolysis",* Thanh Hai Phan, Phi Hung Pham, Hoang Thoan Nguyen, Tuyet Nga Nguyen, Xuan Sang Nguyen and Thach Son Vo, The 5th National Solid-state Conference, Vungtau, Vietnam, Nov. 12-14th, 2007.